
Implementation and investigation of the impact of different background distributions in gyrokinetic plasma turbulence studies

Alessandro Di Siena



ULM 2019

Implementation and investigation of the impact of different background distributions in gyrokinetic plasma turbulence studies

Alessandro Di Siena

Dissertation zur Erlangung des Doktorgrades
Dr. rer. nat.
an der Fakultät für Naturwissenschaften
der Universität ULM

vorgelegt von
Alessandro Di Siena
aus Napoli, Italia

ULM, 2019

Dekan: Prof. Dr. Peter Dürre

Erstgutachter: Prof. Dr. Joachim Ankerhold

Zweitgutachter: Prof. Dr. Peter Reineker

IPP Betreuer: Dr. Tobias Görler, apl. Prof. Emanuele Poli

Tag der mündlichen Prüfung: 15/11/2019

Ai miei genitori, mio fratello e Saria.

v

Abstract

Abstract

One of the most fascinating projects in the current century is recreating the physical conditions of the center of a Star as an alternative energy source. For this purpose, large temperatures are required (100 million of Kelvin degrees) and the main fuel is found at the so-called plasma state. One of the central issues for fusion energy to be tackled is turbulence, which is destabilized by plasma micro-instabilities. It arises due to the large pressure gradients - from the center to the edge of the device - and strongly reduces plasma confinement and reactor performances. Due to their highly nonlinear features, only very limited solutions can be obtained by solving the basic equations analytically. Therefore, the effect of turbulence on plasma confinement is usually investigated through sophisticated modelling tools, such as gyrokinetic theory. This is a reduced model based on experimentally motivated ordering assumptions allowing approximations of the underlying equations. In the course of this work, the gyrokinetic code GENE, developed at IPP Garching under the guidance of Prof. Dr. Frank Jenko, will be extensively employed and extended.

In the first part of this work, the basic gyrokinetic equations will be re-derived by applying an often employed splitting between fluctuating and equilibrium parts of each quantities. The standard gyrokinetic theory usually considers a locally thermalized background, i.e. a local Maxwellian distribution function. While many examples exist where plasma core turbulence studies could be performed successfully with this particular choice, a more flexible setup is required to capture asymmetries and anisotropies as, for instance, those that exist in energetic particles studies and astrophysical scenarios. The first goal of this work is to replace the local Maxwellian both in the underlying equations and in the source of the gyrokinetic code GENE by a generic background distribution function. The latter could e.g., either be set to analytic expressions or taken from experimental measurements or numerical studies of beam-heated plasma distributions. After verification studies on the extended version of GENE, it is applied in experimentally relevant parameter regimes. The impact of fast ion velocity asymmetries on recent results predicting a significant stabilization of electromagnetic turbulence is investigated.

Abstract

Another part of this work is aimed to understand the basic physical mechanisms involved in the recently discovered beneficial impact of fast particles on plasma confinement. Different stabilizing mechanisms are identified. Fast ions are found to interact with the background microturbulence through a wave-particle resonance mechanism, if the fast ion magnetic drift frequency is close enough to the frequency of the relevant unstable mode. Optimization of the heating schemes and extrapolation to future fusion reactors are also discussed. However, this resonance mechanism can only partially explain the numerical and experimental observations that linked the beneficial energetic particle effect to an increase of the kinetic-to-magnetic pressure ratio. A detailed analysis based on sophisticated energy diagnostics able to capture the full evolution of the free energy of the system is employed. It is found that the nonlinear excitation of subdominant, energetic particle induced modes which are marginally destabilized via energy transfer through different scales and frequencies plays a central role. These modes deplete the energy content of the turbulence driven by thermal species and strongly decorrelate the turbulent complex structures.

Furthermore, in the final part of this work, energetic particle modes which require velocity space asymmetries to be driven are investigated. For the first time, EGAMs (energetic-particle-induced geodesic acoustic modes) are studied with the code GENE. They are coherent structures which oscillate at a fixed frequency. Recently, they have become of particular interest due to the possible interaction between EGAMs and plasma turbulence. In particular, here, the impact of more realistic plasma magnetic geometries on the linear dynamics of these modes is addressed and the findings are applied to a realistic plasma discharge.

Zusammenfassung

Eines der faszinierendsten Forschungsthemen dieses Jahrhunderts ist die physikalischen Bedingung im der Sonne zu reproduzieren, um Energie daraus zu gewinnen. Dazu sind hohe Temperaturen von ca. 100 Millionen Kelvin nötig, bei denen das Material im sogenannten Plasmazustand ist. Die unvermeidliche Entstehung von Turbulenz ist eines der zentralen Probleme auf dem Weg zur Fusionsenergie. Mikroinstabilitäten dabei die durch starke Druckgradienten zwischen der Mitte und dem Rand des Plasmas hervorgerufen werden, reduzieren die Einschlusszeit und damit den Wirkungsgrad der Reaktoren. Durch den nicht-linearen Charakter der Turbulenz sind analytische Lösungen des Systems nur sehr begrenzt möglich. Daher wird Plasmaturbulenz anhand komplexer Modelle wie der gyrokinetischen Theorie untersucht. Die Gyrokinetik ist durch Experimente motiviert und verifiziert und erlaubt es durch Annahmen die Komplexität des Problems zu reduzieren. In dieser Arbeit wird das gyrokinetische Simulationsprogramm GENE, das am IPP Garching unter Leitung von Prof. Dr. Frank Jenko entwickelt wird, erweitert und angewandt.

Im ersten Teil dieser Arbeit werden die gyrokinetischen Gleichung hergeleitet durch eine Trennung der Fluktuationen - und Gleichgewichtsteileder Observablen. In den meisten Fällen wird dabei eine Maxwellverteilung für die Gleichgewichtsverteilungsfunktion angenommen. Während das für viele Szenarien eine valide Annahme ist braucht es ein flexibleres Modell um Asymmetrien und Anisotropien, wie sie beispielweise bei astrophysikalischen Plasmas vorkommen, betrachten zu können. Das erste Ziel dieser Arbeit ist es deshalb in den zugrundeliegenden Gleichungen und dem Quellcode von GENE den Maxwell-Hintergrund durch eine generische Hintergrundverteilungsfunktion zu ersetzen. Diese kann durch analytische Modelle, experimentelle Messungen oder numerische Studien bestimmt werden. Nach den ersten Verifikationen der erweiterten GENE Version wird der Code in experimentell relevanten Szenarios eingesetzt. Der Einfluss der Geschwindigkeitsasymmetrie schneller Ionen auf die Stabilität der elektromagnetischen Turbulenz wird untersucht.

Ein weiterer Teil dieser Arbeit versucht die Mechanismen zu bestimmen, die für den besseren Plasmaeinschluss durch schnelle Teilchen verantwortlich sind. Ver-

schiedene stabilisierende Mechanismen werden gefunden. Schnelle Ionen interagieren mit der Hintergrund-Mikroturbulenz durch einen Welle-Teilchen Resonanzmechanismus, wenn die magnetische Driftfrequenz der schnellen Ionen nah genug an der Frequenz der relevanten instabilen Mode ist. Eine Optimierung der Heizmechanismen und eine Extrapolation zu zukünftigen Fusionsreaktoren wird diskutiert. Allerdings kann dieser Resonanzmechanismus nur teilweise die numerische und experimentelle Beobachtung der Verbesserung des kinetischen zu magnetischen Druckverhältnisses durch schnelle Teilchen erklären. Mithilfe einer Freie-Energie-Diagnostik wird die gesamte zeitliche Entwicklung der freien Energie im System analysiert. Es zeigt sich, dass die nichtlineare Anregung von subdominanten und durch energetische Teilchen induzierten Moden, die durch Energietransfer durch unterschiedliche Skalen und Frequenzen geringfügig destabilisiert werden, eine zentrale Rolle spielt. Diese Moden reduzieren den Energieinhalt der Turbulenz, die von thermischen Spezies angetrieben wird, und dekorrelieren die komplexen turbulenten Strukturen stark.

Darüber hinaus werden im letzten Teil dieser Arbeit energetische Teilchenmoden untersucht, die durch Geschwindigkeitsraumasymmetrien getrieben werden. Mit GENE werden erstmals EGAMs (energetische Partikel-induzierte geodätische akustische Moden) untersucht. EGAMs sind kohärente Strukturen, die bei einer festen Frequenz schwingen und EGAMs sind kürzlich aufgrund der möglichen Wechselwirkung mit der EGAMs und Plasmaturbulenz von besonderem Interesse. Dabei wird insbesondere auf den Einfluss realistischer magnetischer Geometrien des Plasmas auf die lineare Dynamik dieser Moden eingegangen und abschließend ein direkter Vergleich mit experimentellen Beobachtungen durchgeführt.

Contents

Abstract	vi
Zusammenfassung	ix
1 Introduction	1
1.1 Nuclear Fusion	1
1.2 Magnetic confinement	3
1.2.1 Magnetic equilibrium	4
1.3 Plasma modelling	7
1.3.1 Kinetic model	8
1.3.2 Fluid description	9
1.4 Drift instabilities	11
1.4.1 Ion temperature gradient modes	12
1.4.2 Electron temperature gradient modes	15
1.5 Shear Alfvén waves	16
1.5.1 Toroidal Alfvén eigenmodes	18
1.6 Nonlinear turbulence saturation	19
1.6.1 Zonal flow	21
1.6.2 Geodesic acoustic modes	22
1.7 Thesis scope and outline	24
2 Gyrokinetic theory	29
2.1 Basic introduction to gyrokinetic theory	29
2.2 Gyrokinetic ordering	30
2.3 Single particle Lagrangian	31
2.4 One-form formulation	31
2.5 Single particle gyrocenter equation of motion	34
2.6 Vlasov equation for general backgrounds	36
2.7 Field-aligned coordinate system	38

2.8	Normalisation	42
2.9	Velocity moments for general backgrounds	46
2.10	Field equations	48
2.11	Poisson's equation	48
2.12	Ampère's law for $A_{1,\parallel}$	50
2.13	Ampère's law for $A_{1,\perp}$	52
2.14	Solution of the field equations	53
2.15	Observables	54
2.16	Collisions	57
2.17	Non-Maxwellian free energy balance	58
2.18	Chapter summary	61
3	Non-Maxwellian background distributions in GENE: Implementation and verification	63
3.1	Equilibrium distribution functions	63
3.1.1	Maxwellian background	64
3.1.2	Slowing Down background	64
3.1.3	Anisotropic Maxwellian background	67
3.1.4	Symmetric double-bump-on-tail background	70
3.1.5	Numerical backgrounds	71
3.2	Zero-order consistency assessment	73
3.3	Local code verification	74
3.3.1	Microinstability growth rate analysis	75
3.3.2	Transport coefficients	75
3.4	Global code verification	76
3.4.1	Rosenbluth-Hinton test	77
3.4.2	Benchmark with ORB5 code results	80
3.5	Chapter summary	84
4	Non-Maxwellian background effects in local gyrokinetic simulations	85
4.1	JET - low-beta hybrid L-mode plasmas	86
4.2	Equilibrium distribution functions	87
4.3	Linear growth rate and frequency analyses	91
4.3.1	Electromagnetic simulations	91
4.3.2	Electrostatic simulations	94
4.4	Turbulence analysis	95
4.5	Chapter summary	99

CONTENTS

5	Resonant interaction of energetic ions with plasma micro-turbulence	103
5.1	Introduction	104
5.2	Numerical observation - temperature scan	105
5.3	Theoretical simplified model	110
5.4	ITG/energetic particle resonant interaction	112
5.5	Fast particle contribution to energy exchange	116
5.6	Impact of magnetic shear	118
5.7	Influence of energetic ion properties	120
5.7.1	Fast ion charge dependence	121
5.7.2	Fast ion mass dependence	123
5.7.3	Combined effect of fast ion charge and mass	124
5.7.4	Impact of fast ion temperature and density gradients	125
5.7.5	Fast ion distribution function	127
5.8	Impact of finite electromagnetic fluctuations	129
5.9	Nonlinear turbulence results	131
5.10	Fast ion fluxes analysis	135
5.11	ITG-EP resonance effects on ITER standard scenarios	137
5.12	Chapter summary	140
6	Nonlinear electromagnetic stabilisation by energetic ions	143
6.1	Numerical simulations: parameters and results	144
6.2	Real-space and spectral analysis of the electrostatic potential	147
6.2.1	Observations at zero toroidal mode number	150
6.2.2	Observations at finite toroidal mode numbers	156
6.3	Impact of the energetic-particle temperature	159
6.4	Linear analyses - mode identification	161
6.5	Flux-tube approximation of energetic particle modes	164
6.6	Nonlinear energy transfer analysis	167
6.7	Similarity of different discharges	174
6.8	Chapter summary	176
7	Effect of elongation on Energetic-Particle-Induced Geodesic Acoustic Modes	179
7.1	Impact of elongation on linear EGAM dynamic	180
7.2	Reduced gyrokinetic model for the fast ion energy transfer terms	182
7.3	Impact of elongation on resonance position	186
7.4	AUG Experiment based studies	189
7.4.1	Flat density and temperature profiles	191

Contents

7.4.2	Realistic density and temperature profiles	193
7.5	Chapter summary	196
8	Conclusions	199
8.1	Summary	199
8.2	Outlook	202
	Bibliography	205
	Acknowledgement	226
	List of publications	231

Chapter 1

Introduction

The aim of this first chapter is to provide the basics of nuclear fusion and tokamak plasmas in order to create a framework for the work presented in the remainder of the thesis. In particular, a brief overview on the physical requirements for fusion and on the different theoretical models employed to describe a plasma is given as an introduction to the more detailed studies which will follow. Moreover, an overview on the most common and deleterious plasma micro-instabilities, typically destabilized by pressure gradients and magnetic curvature effects, is given by describing their linear (single mode) and nonlinear (multi-mode) dynamics. In this context, the central role of energetic particles on stabilising turbulence is stressed as a motivation for the results shown throughout this work.

1.1 Nuclear Fusion

The fundamental physics principle of nuclear fusion is based on the major discovery that the binding energy (minimum energy required to break an atom in its smaller constituents) has a peaked shape in the atomic mass number with a maximum at ^{56}Fe (see Fig. 1.1). Therefore, nuclear reactions which combine nuclei lighter than ^{56}Fe or break apart heavier ones will generate a net energy release. This resulting energy is larger than the one typically produced in chemical reactions by more than 7 orders of magnitude [2], which makes the possibility of fully exploiting nuclear reactions particularly compelling. Two feasible methods to produce energy have been identified so far. The first is based on the concept of breaking a heavy nucleus into smaller ones and characterizes the principle of fission reactions. The second one, is based on the opposite idea of combining light nucleus into heavier ones. The latter is called nuclear fusion and constitutes the framework of the present work. The first

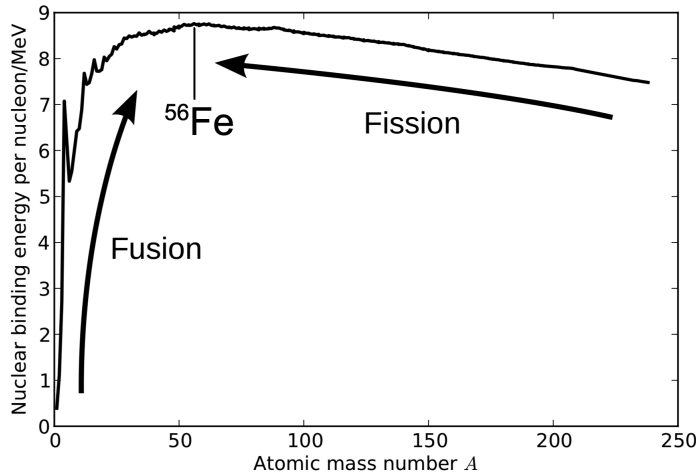


Figure 1.1: Binding energy per nucleon in MeV as a function of the atomic mass number. This picture has been adapted from Ref. [1] with permission from Daniel Told. The energy gain from fusion and fission nuclear reactions is marked by the black arrows.

fission reactor, called Obninsk Nuclear Power Plant was built in 1954, and half a century later, fission is widely used in many countries as an energy source. However, one of its major drawbacks is related to the production of highly unstable atomic nuclei which decay emitting harmful radiations. On the other hand, the feasibility of a fusion reactor is still under active research. The ITER [3, 4] experiment, being built in Cadarache (southern France) should be the first fusion device to produce net energy and maintain fusion for long periods of time. A significant advantage of fusion compared to fission reactors is mainly related to the possibility of generating similar amounts of energy, but with minimal radioactive wastes and without uncontrollable chain reaction risks. However, a major challenge for achieving fusion on Earth is given by the Coulomb repulsion that needs to be overcome to effectively allow light ions to collide and form heavier nuclei. This constraint alone would make fusion reactions prohibitive, requiring kinetic energies of the order of 500keV . However, the quantum mechanic tunneling effect [5] mitigates this energy threshold, allowing finite probability of fusion reactions to occur even if the ions do not possess enough kinetic energy to overcome the Coulomb potential barrier. In a locally thermalized gas, the optimum temperature for fusion turns out to be of the order of 10keV , or equivalently 100 millions of Kelvin (see below). For such high temperatures the reagent mixture, accordingly to classical physics, is completely ionized and a phase

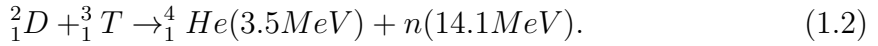
1.2 Magnetic confinement

transition to the so-called plasma state occurs.

To efficiently design a fusion reactor it is essential that the energy produced by fusion reactions $P_f = n^2 \langle \sigma v \rangle \epsilon_\alpha / 4$ exceeds all energy losses, mainly given by bremsstrahlung emission $P_b = c_1 n^2 Z_{\text{eff}} \sqrt{T}$ and diffusive transport $P_D = 3nT/\tau_E$. Here, $c_1 = 5.4 \cdot 10^{-37} \text{ W m}^3 \text{ keV}^{-1/2}$ represents the bremsstrahlung constant, n and T the electron density and temperature, Z_{eff} the effective charge of the plasma, $\langle \sigma v \rangle$ the fusion average cross-section times the particle velocity, ϵ_α the energy of the fusion-born products, while τ_E represents the energy confinement time, i.e. the characteristic time in which the plasma maintains a certain temperature if the heating is switched off. A simple criterion, based on the energy balance between these different terms was derived by Lawson and has since been improved upon [6, 7]. It reads as

$$n\tau_E T = \frac{12T}{\langle \sigma v \rangle \epsilon_\alpha - 4c_1 Z_{\text{eff}} \sqrt{T}}. \quad (1.1)$$

The fusion reaction which maximizes the cross-section $\langle \sigma v \rangle$ in the range of medium temperatures, i.e. $1 < T_i(\text{keV}) < 300$ is given by



Here ${}_1^2D$ and ${}_1^3T$ represent, respectively, the hydrogen isotopes deuterium and tritium. For such a plasma the Lawson criterion has a minimum at $T = 10 \text{ keV}$ at the value

$$n\tau_E T \sim 3.5 \cdot 10^{21} \text{ s} \cdot \text{keV/m}^3 \quad (1.3)$$

The most promising concept to date which is theoretically able to achieve such a triple product is the tokamak. Fig. 1.2 shows the progress of fusion research during the past few decades. Eq. (1.3) gives the condition for a self-sustaining plasma state called ignition. Up to today only a factor ~ 7 is missing and should be bridged by the ITER project, which is supposed to reach values of $n\tau_E T \sim 4 \cdot 10^{21} \text{ s} \cdot \text{keV/m}^3$.

1.2 Magnetic confinement

The tokamak is a toroidal axisymmetric device able to confine the charged particles, which constitute the plasma, through intense magnetic fields. They are generated by external field coils and by currents flowing in the plasma. A schematic tokamak cartoon can be found in Fig. 1.3, which shows the basic tokamak configuration. The main contribution to the magnetic field comes from the toroidal field coils, which generate the toroidal field component. To ensure confinement, a poloidal magnetic

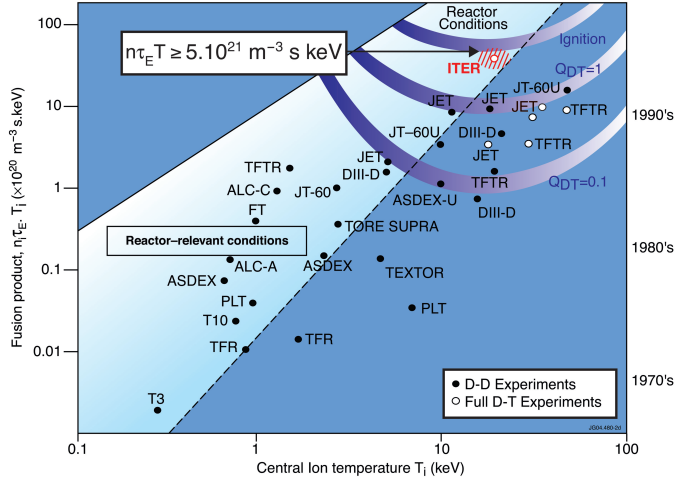


Figure 1.2: Triple product $n\tau_E T$ as a function of the main ion central temperature (expressed in keV) obtained in different experimental plasma discharges. The ITER prediction for a standard scenario is marked in red. This picture is taken from Ref. [8].

field is also needed. In a tokamak it is generated by an externally induced toroidal plasma current [7]. Similar to a standard transformer, this poloidal magnetic field is generated by a time-varying toroidal magnetic field generated by the central solenoid (called primary transformer circuit in Fig. 1.3). Moreover, an additional small contribution to the poloidal magnetic field is also given by a poloidal coil system. The latter is also often employed to modify the plasma shape and position. The superposition of the toroidal and poloidal fields generates complex helical magnetic field lines, as shown in the cartoon of Fig. 1.3.

1.2.1 Magnetic equilibrium

In a tokamak, the plasma is confined through a strong magnetic field \mathbf{B}_0 , which, as discussed previously, is the sum of a toroidal and a poloidal component. It is particularly convenient to describe the magnetic field configuration in a cylindrical coordinate system (R, Z, φ) , shown in Fig. 1.4. Here, R and Z are, respectively, the axial and vertical distance from the center of the toroidal device and φ the toroidal angle. Moreover, the angle θ which lies in the (R, Z) -plane is called poloidal angle. In this general cylindrical coordinate system, the simplest expression for the magnetic

1.2 Magnetic confinement

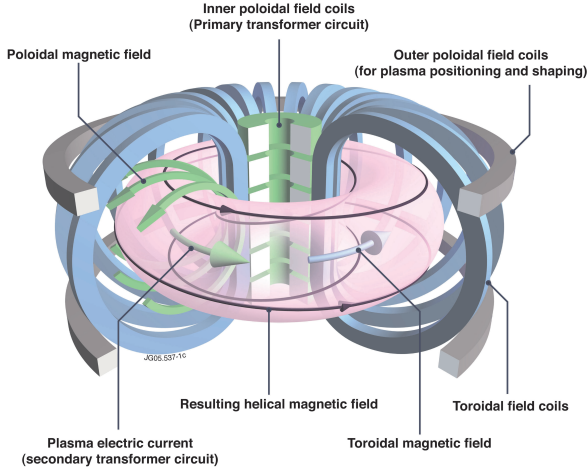


Figure 1.3: Cartoon of a tokamak reactor. The inner central solenoid is the primary winding that induces a toroidal current into the plasma, which represents the secondary winding. The toroidal field coils generate a toroidal magnetic field. A poloidal magnetic field is generated both by external poloidal coils and by a plasma current induced by the central solenoid. This picture is taken from Ref. [9].

field, which preserves the axisymmetric and $\nabla \cdot \mathbf{B}_0 = 0$ properties, can be written in terms of two scalar functions $g(\psi)$ and $\psi(R, Z)$ [10]

$$\mathbf{B}_0 = \mathbf{B}_T + \mathbf{B}_\theta = g(\psi)\nabla\varphi + \nabla\varphi \times \nabla\psi, \quad (1.4)$$

with $\mathbf{B}_T = g(\psi)\nabla\varphi$ and $\mathbf{B}_\theta = \nabla\varphi \times \nabla\psi$, respectively, the toroidal and the poloidal field components. According to the magnetohydrodynamical force balance $\nabla p = \frac{\mathbf{J}}{c} \times \mathbf{B}$ (see Eq. (1.22)), the total plasma pressure p reduces only to a function $p = p(\psi)$, which lies in a plane perpendicular to the magnetic field \mathbf{B}_0 and the current density \mathbf{J} . The function $\psi(R, Z)$ (poloidal flux) can hence be used to uniquely identify surfaces with constant plasma pressure called flux surfaces or magnetic surfaces (one of these surfaces is displayed in Fig. 1.4 and identified through the labels defined below). The poloidal flux is defined through the relation

$$\psi(R, Z) = \frac{1}{2\pi} \int \mathbf{B}_\theta \cdot d\mathbf{S}_\theta. \quad (1.5)$$

Here, $d\mathbf{S}_\theta$ represents the infinitesimal poloidal surface element. The flux surface can also be uniquely specified through the equivalent toroidal coordinate $\psi_T(R, Z)$

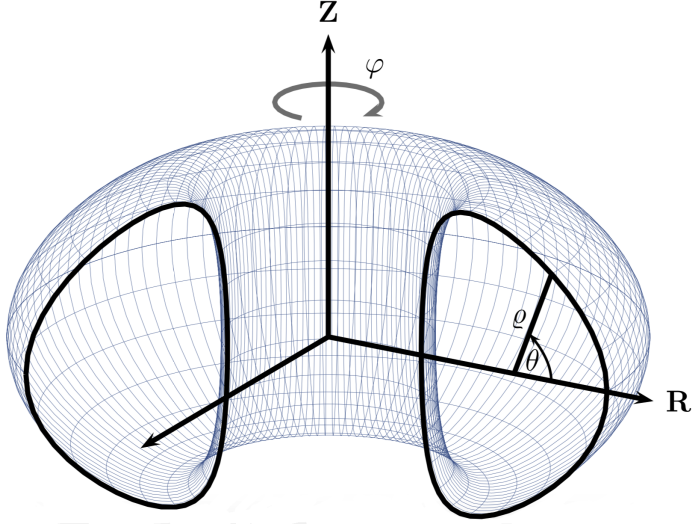


Figure 1.4: Cylindrical coordinate system (R, Z, φ) . Here, θ represents the poloidal angle in the plane (R, Z) . This picture has been adapted from Ref. [11] with permission from Tobias Görler.

(toroidal flux), which is defined as

$$\psi_T(R, Z) = \frac{1}{2\pi} \int \mathbf{B}_T \cdot d\mathbf{S}_T. \quad (1.6)$$

Here, $d\mathbf{S}_T$ represents the infinitesimal toroidal surface element. The ratio between the toroidal and poloidal fluxes measures the change of the pitch of the magnetic field line on different flux surfaces. More precisely, the safety factor q , defined as

$$q = \int_0^{2\pi} \frac{d\psi_T(R, Z)}{d\psi(R, Z)} d\theta, \quad (1.7)$$

expresses the number of toroidal revolutions required for a magnetic field line to complete an angle of 2π in the poloidal plane. The radial derivative of the safety factor is related to the so-called magnetic shear which is defined as

$$\hat{s}(\rho) = \frac{\rho}{q} \frac{dq}{d\rho}. \quad (1.8)$$

Here, ρ represents the radial coordinate, which can be either associated to ψ_T or ψ . In a tokamak device, the poloidal magnetic coil system might also be employed to

1.3 Plasma modelling

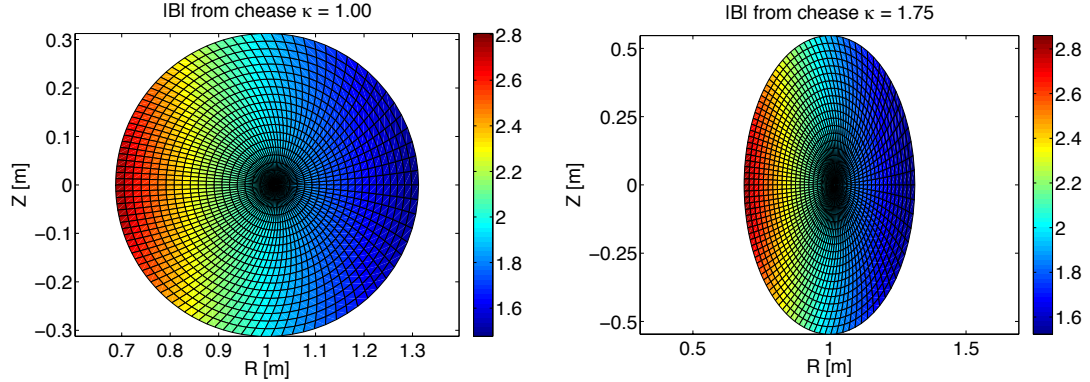


Figure 1.5: Intensity of the equilibrium magnetic field on the poloidal coordinate grid (R, Z) for an elongation a) $\kappa = 1.00$ (circular equilibrium) and b) $\kappa = 1.75$ (elongated equilibrium).

modify the shape of the magnetic configurations. Depending on the tokamak size and on the particular set of coils, different flux-surfaces can be generated. Analytic parametric models able to capture most of the different configurations are very useful. As explained in detail in Ref. [12] each plasma configuration can be expressed in terms of nine different parameters. On the other hand, realistic magnetic configurations exact solutions of the force balance equation (which will be used in chapter 7) can be obtained by numerical solvers like CHEASE [13]. Among the different parameters which characterize the shape of a magnetic configuration, the impact of the so-called elongation κ on the plasma dynamics will be investigated in details in chapter 7. A visual example of different magnetic flux-surfaces obtained by just changing the plasma elongation is given in Fig. 1.5, where it is varied from $\kappa = 1$ (circular plasma) to $\kappa = 1.75$ (elongated plasma).

Recently, a significant improvement of plasma confinement was observed in the tokamak devices TCV (Lausanne, Swiss) and DIII-D (San Diego, USA) and associated only to modifications of the magnetic plasma shape [14, 15]. The theoretical understanding of such experimental results is still under active investigation [16, 17].

1.3 Plasma modelling

The basic plasma dynamics can be studied with several theoretical approaches, each of them based on different approximations [18]. They vary significantly on the ac-

curacy of the physical description and on the complexity of their basic equations. Typically, the more accurate models require more sophisticated mathematical and numerical schemes. Depending on the level of accuracy needed to study the physical system at hand, each of them can provide significant insights. In the following section, a brief introduction to kinetic, fluid and Magnetohydrodynamics (MHD) models is given.

1.3.1 Kinetic model

One of the most comprehensive plasma descriptions is provided by the kinetic theory. It assigns a distribution function f_σ to each species σ in the phase-space (\mathbf{x}, \mathbf{v}) for a given time t . Here, \mathbf{x} and \mathbf{v} represents, respectively, the spatial location and the velocity. The distribution function plays the role of a phase-space density, expressing the number of particles per unit volume $d\mathbf{x}d\mathbf{v}$. It is related to the volume density n_σ and the overall particle number N_σ through the relations

$$n_\sigma(\mathbf{x}, t) = \int d\mathbf{v} f_\sigma(\mathbf{x}, \mathbf{v}, t), \quad (1.9)$$

$$N_\sigma(t) = \int d\mathbf{v} d\mathbf{x} f_\sigma(\mathbf{x}, \mathbf{v}, t). \quad (1.10)$$

By assuming that the dynamics of each particle is affected only by the external electromagnetic Lorentz force $\mathbf{F} = q\mathbf{E} + \mathbf{v} \times \mathbf{B}/c$, their phase-space position changes in the time interval dt as follows

$$\mathbf{x} \rightarrow \mathbf{x}' = \mathbf{x} + \mathbf{v} dt, \quad (1.11)$$

$$\mathbf{v} \rightarrow \mathbf{v}' = \mathbf{v} + \frac{q}{m} \left(\mathbf{E} + \frac{\mathbf{v}}{c} \times \mathbf{B} \right) dt. \quad (1.12)$$

Here, the effect of collisions is neglected.

The Liouville theorem, which states that the distribution function f_σ is constant along the phase-space trajectories (in the absence of collisions), imposes the conservation of the total number of particles in the time interval dt

$$dN' = \int f_\sigma(\mathbf{x}', \mathbf{v}', t + dt) d\mathbf{x} d\mathbf{v} = dN = \int f_\sigma(\mathbf{x}, \mathbf{v}, t) d\mathbf{x} d\mathbf{v}. \quad (1.13)$$

Since the time derivative of the overall number of particles must be preserved at each time step and for each phase-space volume element, the following equation, known as Vlasov equation, must always be fulfilled by the distribution function f_σ

$$\frac{df_\sigma}{dt} = \frac{\partial f_\sigma}{\partial t} + \mathbf{v} \cdot \nabla_x f_\sigma + \frac{q}{m} \left(\mathbf{E} + \frac{\mathbf{v}}{c} \times \mathbf{B} \right) \cdot \nabla_v f_\sigma = 0. \quad (1.14)$$

1.3 Plasma modelling

Here, the property of the electromagnetic Lorentz force $\partial F_i / \partial v_i = 0$ has been applied. It can be shown that by including the effect of collisions in the derivation of Eq. (1.14), an additional term appears at the right hand side, i.e. $(\partial f_\sigma / \partial t)_{coll}$. Eq. (1.14) must be coupled to the Maxwell's equations to obtain a self-consistent description of particles and fields. In particular, the latter affects the particle dynamics which in turn modify the fields evolution. A detailed treatment of particles and fields will be given in chapter 2 for a reduced kinetic model, known as the gyrokinetic model.

1.3.2 Fluid description

One of the great advantages of a kinetic plasma description consists in retaining the full velocity distribution of each plasma species, described by the distribution function $f_\sigma(\mathbf{x}, \mathbf{v})$. This particular approach enables to retain the full information on the velocity dependence of each plasma species with the main drawback of an increase in the complexity of the mathematical and numerical schemes required to solve the kinetic set of equations. However, in many plasma physics applications the velocity information of each plasma species is not required and a kinetic treatment would be unnecessarily expensive. A much simpler approach is rather preferred in which the plasma is represented by its macroscopic quantities (such as density, mean velocity, mean temperature and many others) for which a set of fluid equations is derived. In these cases, each species is considered close to (local) thermal equilibrium and the length scales are assumed larger than the particles mean free path. The basic derivation can be performed starting from the Vlasov equation (Eq. (1.14)) and integrating it over the velocity domain. In terms of the distribution function, the density, the fluid velocity and the averaged-velocity tensor are defined as

$$n_\sigma = \int d\mathbf{v} f_\sigma(\mathbf{x}, \mathbf{v}, t), \quad (1.15)$$

$$\mathbf{V}_\sigma = \frac{1}{n_\sigma} \int d\mathbf{v} f_\sigma(\mathbf{x}, \mathbf{v}, t) \mathbf{v} = \langle \mathbf{v}_\sigma \rangle, \quad (1.16)$$

$$\langle \mathbf{v}_\sigma \mathbf{v}_\sigma \rangle = \frac{1}{n_\sigma} \int d\mathbf{v} f_\sigma(\mathbf{x}, \mathbf{v}, t) \mathbf{v} \mathbf{v}. \quad (1.17)$$

A v -integration leads to the first fluid equation

$$\frac{\partial n_\sigma}{\partial t} + \nabla \cdot n_\sigma \mathbf{V}_\sigma = 0. \quad (1.18)$$

It represents the so-called continuity equation. By multiplying the Vlasov equation by v and integrating over the velocity space, a second fluid equation can be obtained,

which represents the momentum continuity equation. It reads as

$$m_\sigma n_\sigma \frac{\partial \mathbf{V}_\sigma}{\partial t} + m_\sigma n_\sigma (\mathbf{V}_\sigma \cdot \nabla) \mathbf{V}_\sigma = q_\sigma n_\sigma (\mathbf{E} + \frac{\mathbf{V}_\sigma}{c} \times \mathbf{B}) - \nabla \cdot \mathbf{P}_\sigma. \quad (1.19)$$

Here, the second fluid moment (Eq. (1.16)) has been used and the velocity of the fluid element \mathbf{v}_σ has been split in its mean \mathbf{V}_σ and random \mathbf{u}_σ components (with $\langle \mathbf{u}_\sigma \rangle = 0$), respectively as $\mathbf{v} = \mathbf{V}_\sigma + \mathbf{u}_\sigma$. Moreover, the charge of the plasma species σ , i.e. q_σ and the pressure tensor $\mathbf{P}_\sigma = m_\sigma n_\sigma \langle \mathbf{u}_\sigma \mathbf{u}_\sigma \rangle$ (often called Reynolds stress tensor) have been introduced. Similarly, as done previously for the density and momentum continuity equations, an equation for the overall plasma internal energy $E_\sigma = \frac{3}{2} n_\sigma T_\sigma$ can be derived multiplying Eq. (1.14) by v^2 and integrating in velocity space. It reads as

$$\frac{3}{2} n_\sigma \left(\frac{\partial T_\sigma}{\partial t} + \mathbf{V}_\sigma \cdot \nabla T_\sigma \right) + \mathbf{P}_\sigma : \nabla \cdot \mathbf{V}_\sigma + \nabla \cdot \mathbf{q}_\sigma = 0. \quad (1.20)$$

Here, T_σ represents the temperature of the species σ , \mathbf{q}_σ the heat flux and $:$ the tensor product. Eqs. (1.18-1.20) reveal that an infinite hierarchy of fluid equations can be derived from Eq. (1.14), where each of them requires knowledge of a higher order fluid moment. Different criteria to separate such equations and close the fluid description are usually applied in plasma physics and depend strongly on the physical approximations allowed by the selected system. A common simplification involves the pressure tensor description, e.g. by assuming an adiabatic fluid motion or an isothermal behavior. Furthermore, as for the kinetic theory, the fluid equations must always be coupled to the Maxwell's equations to give a complete plasma description. In many reactor relevant plasma scenarios, some reduced fluid model is often employed. The large-scale behaviour and stability of a plasma is described in terms of the ideal MHD theory [19]. It is based on the assumptions that the ion gyro-period and gyro-radius are negligible compared to the characteristic MHD times and scales. Moreover, due to the particularly small electron/ion mass ratio the fluid element velocity and mass are assumed equal to the ion ones and the fluid equations are reduced only to the evolution of the ion fluid equations. The role of electrons is restricted to their contribution to the overall pressure, to ensure quasi-neutrality and to determine the electric field through the Ohm's law. The ideal single fluid MHD equations can be summarized as follows

$$\frac{\partial \rho}{\partial t} + \nabla \cdot \rho \mathbf{V} = 0, \quad (1.21)$$

$$\rho \left(\frac{\partial}{\partial t} + \mathbf{V} \cdot \nabla \right) \mathbf{V} = -\nabla p + \frac{\mathbf{J}}{c} \times \mathbf{B}, \quad (1.22)$$

1.4 Drift instabilities

$$(\frac{\partial}{\partial t} + \mathbf{V} \cdot \nabla)p + \frac{5}{3}p\nabla \cdot \mathbf{V} = 0, \quad (1.23)$$

$$\frac{\partial \mathbf{B}}{\partial t} = \nabla \times (\mathbf{V} \times \mathbf{B}), \quad (1.24)$$

$$\mathbf{J} = \frac{c}{4\pi} \nabla \times \mathbf{B}. \quad (1.25)$$

Here, $\rho = m_i n_i$ represent the mass density, $p = p_e + p_i$ the plasma pressure and $\mathbf{J} = n_i q_i \mathbf{V}_i - n_e e \mathbf{V}_e$ the current density, which is in this model not an independent quantity but related to the magnetic field through Eq. (1.25).

1.4 Drift instabilities

In magnetic confinement plasmas, the presence of steep temperature and density profiles provides free energy to small perturbations, which can grow unstable and generate turbulence in their nonlinear phase. These instabilities develop typically on the spatial scale of the ion Larmor radius ρ_i and involve plasma motion occurring at velocities which are smaller than the thermal velocity by a factor ρ_i/L (where L denotes the typical in-homogeneity scale of the plasma). This is called the drift ordering. For this reason, these instabilities are usually called drift instability or micro-instabilities. A comprehensive description of drift instability can be found in the review paper of Ref. [20].

In the rest of this section, a simple description of the physical mechanism leading to a drift-wave excitation is presented following the discussion in Ref. [21]. Here, a fluid approach is employed (see Eqs. (1.18-1.20)) in the magnetic coordinate system introduced in section 1.2.1 and for a circular magnetic equilibrium. Eqs. (1.18-1.20) can be linearized assuming each quantity as the sum of a constant background equilibrium (denoted by a subscript 0) and a fluctuating counterpart (indicated by a subscript 1). To ensure the closure of the fluid equations, the pressure tensor has been considered isotropic and defined as $\mathbf{P}_\sigma = n_\sigma T_\sigma \hat{1}$, with $\hat{1}$ the unit tensor. Moreover, we assume that the structure of the perturbations is highly anisotropic, i.e. strongly elongated along field lines. This is a particularly good assumption in tokamaks (more specifically in the core) due to the high mobility of the particles along the field lines and it will be employed throughout the rest of this thesis. Moreover the electron inertia is considered negligible compared to the main ion inertia and the electron parallel dynamics is usually reduced to an adiabatic response. Another simplification can be done by enforcing periodic boundary conditions in each direction for every perturbed quantity. Here the so-called local approximation is made and only a small fraction of the perpendicular cross-section is considered. Under this assumption a

constant value of pressure and pressure gradient is considered, allowing the use of periodic boundary conditions in the thin radial domain. The perturbed quantities can therefore be written in Fourier space i.e. $A(\rho, \theta, \varphi) = \sum_{\mathbf{k}} A(k_\rho, k_\theta, k_\varphi) \exp(i\mathbf{k} \cdot \mathbf{x} - i\omega t)$. With these assumptions Eqs. (1.18-1.20), reduce to the so-called Weiland fluid model [22, 23] and they can be rewritten for each species σ as follows

$$\omega \hat{n}_{1,\sigma} + 2\omega_{d,\sigma}(\hat{n}_{1,\sigma} + \hat{T}_{1,\sigma}) = \omega_{d,\sigma} \frac{q_\sigma T_{0,e}}{T_{0,\sigma}} \frac{R}{L_{n,\sigma}} \hat{\phi}_1, \quad (1.26)$$

$$\hat{\omega} \hat{T}_{1,\sigma} + \frac{4}{3} \omega_{d,\sigma} \hat{n}_\sigma + \frac{14}{3} \omega_{d,\sigma} \hat{T}_{1,\sigma} = \omega_{d,\sigma} \frac{q_\sigma T_{0,e}}{T_{0,\sigma}} \frac{R}{L_{T,\sigma}} \hat{\phi}_1, \quad (1.27)$$

Here, the following quantities have been introduced $\omega_{d,\sigma} = -k_\theta T_{0,\sigma}/(q_\sigma B R_0)$ (called magnetic drift frequency), $R/L_{n,\sigma} = -(R_0/n_{0,\sigma}) \partial n_{0,\sigma} / \partial \rho$, $\hat{n}_{1,\sigma} = n_{1,\sigma}/n_{0,\sigma}$, $R/L_{T,\sigma} = -(R_0/T_{0,\sigma}) \partial T_{0,\sigma} / \partial \rho$, $\hat{T}_{1,\sigma} = T_{1,\sigma}/T_{0,\sigma}$ and $\hat{\phi}_1 = e\phi_1/T_{0,e}$ (with e the elementary electron unit charge). In the electrostatic limit, the only field equation that must be solved consistently with Eqs. (1.18-1.20) is the quasi-neutrality condition

$$\hat{n}_{1,e} = \hat{n}_{1,i}. \quad (1.28)$$

The set of three coupled equations, i.e. Eqs. (1.26-1.28), will be applied in the rest of this section to some relevant cases in tokamak plasmas. In particular, the ion-temperature-gradient (ITG) [24, 25] and the electron-temperature-gradient (ETG) [26, 27, 28, 29] modes will be analyzed separately. They are typically considered among the dominant plasma instabilities in many tokamak core conditions and are associated to the main cause of tokamak confinement degradation. Due to the presence of these instabilities particle and energy flows arise, diffusing and convecting plasma and generating complex turbulent patterns.

1.4.1 Ion temperature gradient modes

The ion-temperature-gradient mode is a drift instability driven by the presence of finite main ion temperature gradients above a threshold condition. It has been extensively studied by many authors in both analytical and numerical papers [25, 30, 31, 32, 33, 34, 35]. The discovery of the relevance of the ITG in the magnetic confinement plasma physics community goes back to the '80s, where first experimental evidence of ion-driven turbulence was observed in Doublet III tokamak device in San Diego (USA). In particular, they observed that plasma confinement was saturating at almost one order of magnitude below the so-called neoclassical predictions with significant impact on the plasma performance. A review on neoclassical (i.e. collisional)

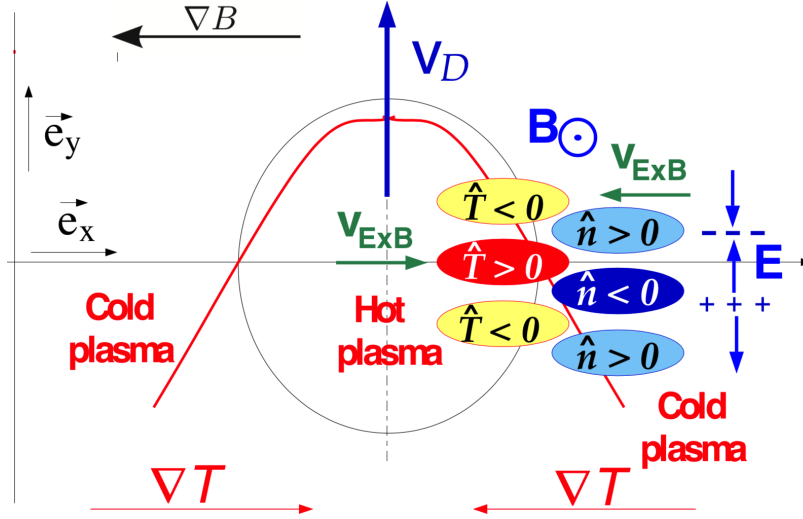


Figure 1.6: Cartoon of the qualitative description of the ion-temperature-gradient (ITG) destabilization in the poloidal plane (R, Z). This picture has been adapted from Ref. [21] with permission from Clemente Angioni.

transport can be found in Ref. [36]. This confinement degradation was attributed to ion-driven turbulence [30, 37]. The mechanism leading to the linear excitation of an ITG can be investigated in the simplified fluid setup introduced previously and summarized in the cartoon of Fig. 1.6. In particular, we take Eqs. (1.26-1.28) and assume $R/L_{n,\sigma} = 0$. The Weiland fluid equations can be written according to Ref. [21] as follows

$$(\omega + 2\omega_{d,\sigma})\hat{n}_{1,\sigma} = -2\omega_{d,\sigma}\hat{T}_{1,\sigma}, \quad (1.29)$$

$$\left(\hat{\omega} + \frac{14}{3}\omega_{d,\sigma} - \frac{4}{3}\frac{2\omega_{d,\sigma}^2}{\hat{\omega} + 2\omega_{d,\sigma}} \right) \hat{T}_{1,\sigma} = \omega_{d,\sigma} \frac{q_\sigma T_{0,e}}{T_{0,\sigma}} \frac{R}{L_{T,\sigma}} \hat{\phi}_1, \quad (1.30)$$

$$\hat{\phi}_1 = \hat{n}_{1,i}. \quad (1.31)$$

Here, we have assumed an adiabatic electron response to any perturbation as mentioned above. Their perturbed density fluctuations can be written (according to the normalization of the previous section) as $\hat{\phi}_1 = \hat{n}_{1,e}$. Due to the toroidal geometry of a tokamak device, the confinement magnetic field \mathbf{B}_0 possesses a gradient ∇B_0 towards the symmetry axis. Eq. (1.29) shows that any ion temperature perturbation leads to a corresponding density fluctuation physically related to the drift of the particles

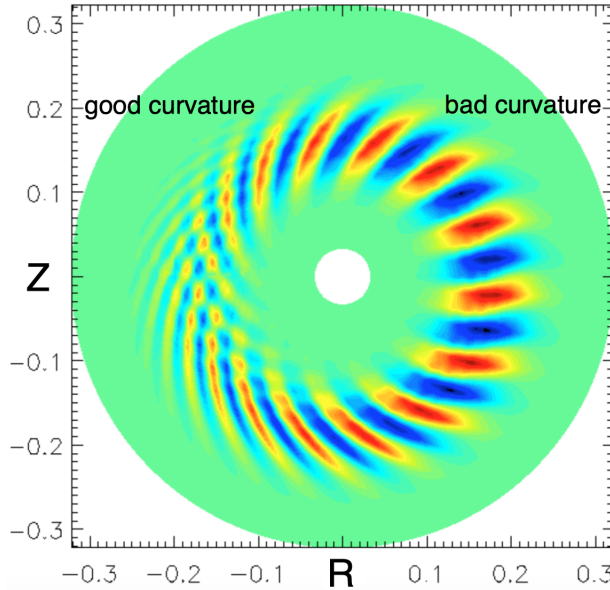


Figure 1.7: Poloidal cross-section of the electrostatic potential in the plane (R, Z). The so-called good and bad curvature regions are specified. This picture has been adapted from Ref. [11] with permission from Tobias Görler.

in the inhomogeneous magnetic field (this drift being proportional to the particle energy). Therefore, a charge separation between ions at different radial locations arises and a fluctuating electric field is generated in the poloidal plane (according to Eqs. (1.30-1.31)). The resulting electric field leads to an $\mathbf{E} \times \mathbf{B}$ drift that enhances and further destabilizes the initial perturbation, which rotates in the poloidal plane with the ion drift frequency $\omega_{d,i}$. A necessary condition to effectively destabilize an ITG mode is that the temperature gradient is parallel to the magnetic field curvature. As shown from the poloidal cross section of Fig. 1.6, this qualitative observation allows us to distinguish between stable (called good curvature) and unstable (called bad curvature) regions, which, respectively, refers to the region where ∇T_i and ∇B are anti-parallel or parallel. This peculiar difference between good and bad curvature regions in the ITG dynamics is also observed in many numerical simulations and in a large variety of different experiments. In Fig. 1.7, for example, a poloidal cross section of the electrostatic potential fluctuations, obtained from a numerical simulation, is shown. Radially elongated structures (typically of the size of the ion Larmor radius $\rho_i = m_i v_\perp / (q_i B)$), often called eddies, are destabilized by

1.4 Drift instabilities

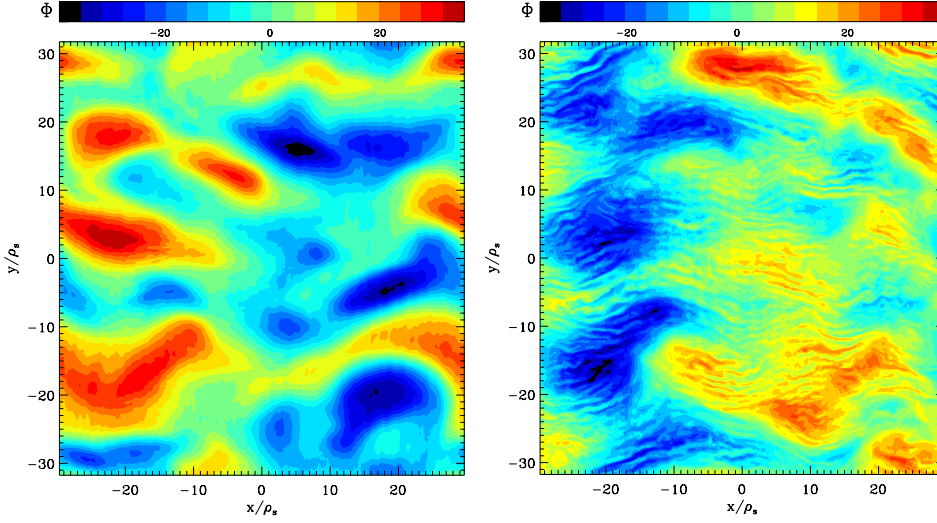


Figure 1.8: Snapshots of the electrostatic potential ϕ_1 in the plane perpendicular to the background magnetic field (x, y) normalised in units of the main ion Larmor-radius for a) an ITG and b) ETG dominated turbulence scenarios. This picture is taken from Ref. [38].

the presence of finite logarithmic temperature gradients, affecting the overall plasma stability. Moreover, Fig. 1.7 reveals that the dominant contribution of the electrostatic potential fluctuations is located in the bad curvature region (consistently with the qualitative predictions of the fluid model previously introduced).

1.4.2 Electron temperature gradient modes

As previously mentioned, another relevant drift instability often observed in many tokamak plasma conditions is the electron temperature gradient (ETG) instability. It is driven unstable by the presence of finite electron temperature gradients at the small electron scale, which is measured by the electron Larmor radius $\rho_e = m_e v_\perp / (|e|B)$. In a linear and electrostatic framework ETGs and ITG modes share similar features. The physical mechanisms leading to their destabilization is the same as explained previously by switching the role of the ions with electrons. In particular, at the typical electron scale, the ion perturbations is adiabatic. The electrons, on the other hand, have to be treated as a kinetic species. In most of the tokamak conditions the spatial and temporal separation between ETGs and ITGs allows us to neglect

the interaction between these two different instabilities. However, it has been shown recently in several works that in some relevant condition their nonlinear coupling might have a substantial role on plasma turbulence [39, 40, 38, 11].

A comparison of the essentially different streamer structures generated by these two different instabilities can be observed in Fig. 1.8. In particular, the fluctuations of the electrostatic potential arising from ETG turbulence generates hyperfine radial streamers compared to the corresponding ITG ones.

1.5 Shear Alfvén waves

In magnetized fusion plasmas a particularly broad range of modes, which differ significantly from the ones previously introduced, can be driven unstable under certain conditions. They are associated with larger scales and higher frequencies than the drift instabilities discussed above. Therefore, they are not responsible for the transport processes of the thermal bulk of the plasma, but they interact rather with energetic particles, which can drive them unstable through resonant wave-particle interactions. In the present section, we restrict the theoretical investigation to the so-called shear Alfvén waves (SAW) [41, 42]. They are electromagnetic plasma oscillations which are destabilized by perturbations along the background magnetic field lines \mathbf{B}_0 and can be thought of as MHD analogous of the oscillation of a string under tension (the string being represented by the magnetic field line). SAW are particularly relevant for the study of energetic particle physics, since their frequency, i.e. ω_{SAW} follows the dispersion relation $\omega_{SAW} = k_{\parallel}v_A$, with $v_A = B_0/\sqrt{4\pi\rho}$ the Alfvén velocity. Here, ρ represents the plasma mass density. For the typical plasma parameters, v_A is comparable to the energetic particle mean velocity, allowing strong wave-particle interaction to occur. In the following, the general SAW dispersion relation is presented in the ideal MHD limit ($E_{1,\parallel} = 0$) for the simplified case of a screw pinch configuration, i.e. with a magnetic equilibrium field \mathbf{B}_0 defined as the sum of a poloidal and field aligned components, i.e. $\mathbf{B}_0 = (0, B_\theta(r), B_z(r))$. By assuming an incompressible plasma and employing the following decomposition of the electrostatic potential, known as ballooning representation

$$\phi_{1,m}(r, \theta, z, t) = \phi_{1,m}(r, t) e^{i(nz/R_0 - m\theta)}, \quad (1.32)$$

1.5 Shear Alfvén waves

the MHD/Maxwell's equations can be recast into the so-called vorticity expression for the electrostatic potential, i.e.

$$\begin{aligned} & \frac{1}{r^2} \frac{\partial}{\partial r} \left[r^3 \left(n - \frac{m}{q(r)} \right)^2 + r^3 \frac{R_0^2}{v_A^2} \frac{\partial^2}{\partial t^2} \right] \frac{\partial}{\partial r} \left(\frac{\phi_{1,m}(r,t)}{r} \right) \\ &= \frac{m^2 - 1}{r^2} \left[\left(n - \frac{m}{q(r)} \right)^2 + \frac{R_0^2}{v_A^2} \frac{\partial^2}{\partial t^2} \right] \phi_{1,m}(r,t) - \left(\frac{\partial}{\partial r} \frac{R_0^2}{v_A^2} \right) \frac{\partial^2}{\partial t^2} \left(\frac{\phi_{1,m}(r,t)}{r} \right). \end{aligned} \quad (1.33)$$

The detailed derivation can be found in Ref. [43, 44]. A solution of Eq. (1.33) can be obtained for large times and reads

$$\phi_{1,m}(r,t) \simeq \frac{1}{t} e^{-i\omega_{SAW}t}, \quad (1.34)$$

with

$$\omega_{SAW}^2(r) = \frac{v_A^2(r)}{R_0^2} \left(n - \frac{m}{q(r)} \right)^2 = v_A^2(r) k_{||}^2(r). \quad (1.35)$$

Here, the parallel wave vector $k_{||} = (m - nq)/qR_0$ has been introduced. Eq. (1.35) represents the SAW dispersion relation. A first observation is that the time asymptotic solution of Eq. (1.33) has an amplitude which decays with the inverse of the time. This collisionless dissipation mechanism is usually called continuum damping [45] and it is associated to the radial dependence of the SAW frequency. In particular, an initial perturbation oscillates with different frequencies at each radial position. This phenomenon, known as phase mixing, decorrelates the radial instability as it propagates along the radial direction acting as an effective damping mechanism.

Moreover, at each radial position (x_0) where the SAW dispersion relation of Eq. (1.35) is fulfilled, the terms inside the squared brackets in Eq. (1.33) vanish and Eq. (1.33) reduces to

$$\omega_{SAW}^2(x_0) \left(\frac{\partial}{\partial r} \frac{R_0^2}{v_A^2} \right) \left(\frac{\phi_{1,m}(x_0,t)}{r} \right) = 0, \quad (1.36)$$

and its solutions become singular. Therefore, the Cauchy theorem is violated and for a fixed $k_{||}(x_0)$ more than one solution is allowed. Fig. 1.9 shows an example of the continuous SAW spectra and its singular solution for the modes (m, n) and $(m + 1, n)$.

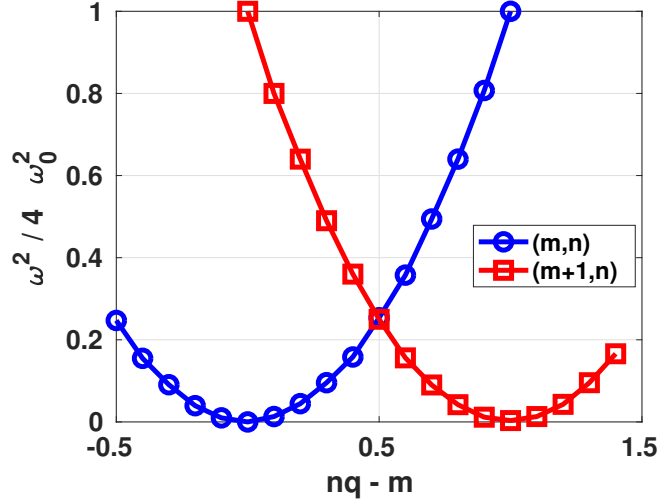


Figure 1.9: Continuous SAW spectra for the modes (m, n) and $(m + 1, n)$ obtained in a screw pinch geometry obtained by solving Eq. (1.35).

1.5.1 Toroidal Alfvén eigenmodes

For real tokamak configurations, the assumption of a screw pinch geometry is only a rough approximation and magnetic curvature effects (induced by the toroidal geometry) need to be taken into account. By considering the gradients of the equilibrium magnetic field, an extra term, responsible for the toroidal mode coupling and proportional to ϵ_0 (defined as the ratio between the minor a and major R_0 radius of the device, i.e. $\epsilon_0 = a/R_0$), appears in the vorticity equation derived previously, which can be written as

$$\begin{aligned} & \frac{1}{r^2} \frac{\partial}{\partial r} \left[r^3 \left(n - \frac{m}{q(r)} \right)^2 + r^3 \frac{R_0^2}{v_A^2} \frac{\partial^2}{\partial t^2} \right] \frac{\partial}{\partial r} \left(\frac{\phi_{1,m}(r, t)}{r} \right) \\ &= \frac{m^2 - 1}{r^2} \left[\left(n - \frac{m}{q(r)} \right)^2 + \frac{R_0^2}{v_A^2} \frac{\partial^2}{\partial t^2} \right] \phi_{1,m}(r, t) - \left(\frac{\partial}{\partial r} \frac{R_0^2}{v_A^2} \right) \frac{\partial^2}{\partial t^2} \left(\frac{\phi_{1,m}(r, t)}{r} \right) \quad (1.37) \\ & - \frac{\partial}{\partial r} \epsilon_0 \frac{R_0^2}{v_A^2} \frac{\partial^2}{\partial t^2} \frac{\partial}{\partial r} [\phi_{1,m+1}(r, t) + \phi_{1,m-1}(r, t)]. \end{aligned}$$

The detailed analytical derivation of Eq. (1.37) is shown in Ref. [43, 44]. A first effect of the toroidicity ϵ_0 consists in coupling different poloidal harmonics, i.e. m

1.6 Nonlinear turbulence saturation

and $m \pm 1$. In the limit of $\epsilon_0 \rightarrow 0$, Eq. (1.37) reduces to the screw pinch case analyzed previously. Eq. (1.37) can be studied in the time asymptotic limit where the SAW dispersion relation of Eq. (1.35) is fulfilled, i.e. by assuming $\omega_0^2 = v_{A,0}^2/4q_0^2R_0^2$. The effect of a finite value for the magnetic plasma toroidicity leads to a system of two coupled equations

$$\frac{\partial}{\partial q_1} \left[\frac{\omega_1}{2\omega_0} - \left(1 - \frac{1}{2m_0 + 1} nq_1 \right) \right] \frac{\partial}{\partial q_1} \phi_{1,m_0} = -\frac{\epsilon_0}{4} \frac{\partial^2}{\partial q_1^2} \phi_{1,m_0+1}, \quad (1.38)$$

$$\frac{\partial}{\partial q_1} \left[\frac{\omega_1}{2\omega_0} - \left(1 - \frac{1}{2m_0 + 1} nq_1 \right) \right] \frac{\partial}{\partial q_1} \phi_{1,m_0+1} = -\frac{\epsilon_0}{4} \frac{\partial^2}{\partial q_1^2} \phi_{1,m_0}. \quad (1.39)$$

They describe the excitation of ϕ_{1,m_0} and ϕ_{1,m_0+1} at $n_0 q_0 = m_0 + 1/2$. In Eqs. (1.38-1.39) the vorticity equation has been Fourier transformed in time and the quantities with a radial dependence have been linearized around the SAW frequency ω_0 , i.e. ($\omega_1 = \omega - \omega_0$) and safety factor q_0 , i.e. ($q_1 = q - q_0$). For the case of finite toroidicity, as shown in Ref. [43, 44], each of the equation for ϕ_{1,m_0} and ϕ_{1,m_0+1} are singular and no real type solutions are allowed in the system in the frequency gap

$$-\frac{\epsilon_0 |\omega_0|}{2} \sqrt{1 - \frac{1}{(2m_0 + 1)^2}} < \omega_1 < \frac{\epsilon_0 |\omega_0|}{2} \sqrt{1 - \frac{1}{(2m_0 + 1)^2}}. \quad (1.40)$$

Inside this frequency gap an eigenfunction associated to a toroidal Alfvén mode, called TAE (toroidal Alfvén eigenmode) peaks. A qualitative description of the TAE linear excitation is given in Ref. [43, 44, 46]. In particular, they can be considered as the result of the beating of two different cylindrical continuum modes, namely the m and $m + 1$, which have the same frequency but propagate in opposite directions. Inside the frequency gaps, these modes are only slightly affected by phase-mixing effects and, therefore, they can be driven unstable from particles moving with mean velocity close to v_A . In particular, for typical tokamak parameters they can be often destabilized by energetic particles generated by auxiliary heating systems like ion-cyclotron heating and neutral beam injection [47, 48, 49, 50]. Moreover, the width of the TAE eigenfunction in the radial direction is proportional to the magnetic toroidicity. Both the drift instabilities and the energetic-particle modes, but particularly the former ones, will play a fundamental role in the studies which are the subject of this thesis.

1.6 Nonlinear turbulence saturation

Plasma instabilities are usually associated with non-negligible radial particle and energy fluxes, which reduce the overall magnetic confinement. In a purely linear

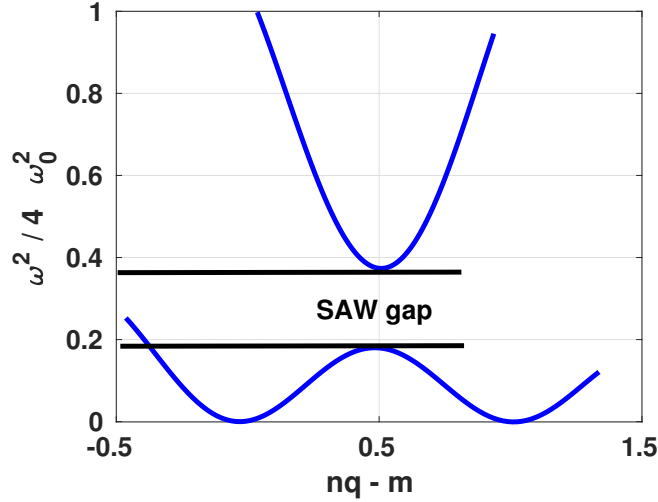


Figure 1.10: Continuous SAW spectra for the modes (m, n) and $(m+1, n)$ obtained in a realistic tokamak geometry. A frequency gap appears due to the effect of magnetic toroidicity.

system, each of these instabilities would grow indefinitely without being affected by any saturation mechanism. In realistic conditions, however, many nonlinear effects contribute to control and in some cases self-regulate plasma turbulence, providing different saturation mechanisms. For the case of resonant modes, for example, it has been shown in several works (see e.g. [51, 52]) that nonlinear effects can redistribute particles in phase-space. In particular, a progressive flattening of the distribution function of the main drive species is often observed and it is related to wave-particle nonlinear interaction. Since the main drive of these resonance modes is provided by the energy-derivatives of their distribution function, a corresponding flattening reflects a reduction of the effective drive term. This first nonlinear saturation mechanism is often associated to a nonlinear modification of the linear mode frequency. This nonlinear effect is called mode chirping and it is usually observed in many plasma experiments, e.g. Ref. [53, 54, 55]. An example of the temporal nonlinear frequency evolution of an EP mode is shown in Fig. 1.11 for a realistic ASDEX Upgrade plasma discharge. The mode disappears as the energetic particle distribution function flattens in phase-space near the resonance position.

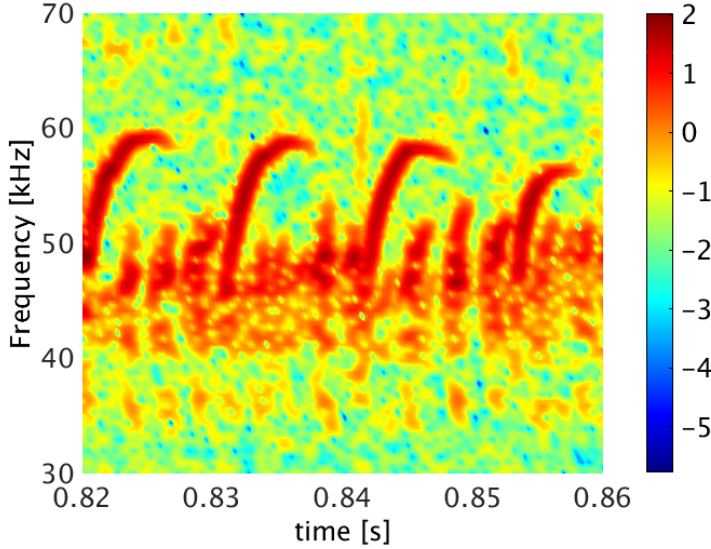


Figure 1.11: Magnetic spectrogram obtained from the AUG discharge #31213.

1.6.1 Zonal flow

As stated previously, one of the most relevant transport channel is attributed to drift instabilities and in particular to ITG turbulence (as previously discussed). As shown in Fig. 1.7 elongated radial structures in the electrostatic potential arise due to the coupling of pressure gradients and magnetic curvature. They are related to the radial turbulent transport. In a tokamak plasma, the main saturation mechanism of ITG turbulence is given by collective plasma flows, usually called zonal flows (ZFs) [56, 57, 58, 59]. They are stationary axisymmetric perturbations which arise due to the presence of radial gradients of the electrostatic potential, i.e. a radial electric field. These produce an effective $v_{E \times B_0}$ velocity directed along the flux-surfaces. It leads to different laminar background flows, whose poloidal rotation velocity changes with the radial position. The effect of ZF on turbulence is qualitatively described in Fig. 1.12. In particular, if a turbulent eddy is part of a radially varying turbulent flow, each fluid element is convected at different velocity. As a result, it gets distorted and sheared, reducing the radial correlation with the other fluid elements of the particular eddy. This decorrelation mechanism leads to a turbulence self-regulation process with an effective energy transfer from the fluctuations to the flow sheared and therefore to a consequent stabilization of the turbulent fluxes. Indeed, axisymmetric perturbations

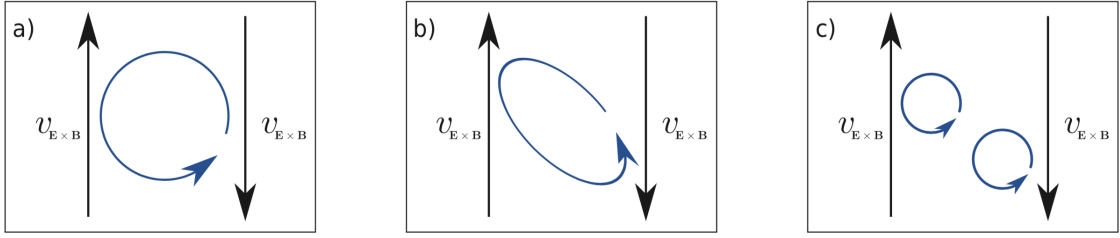


Figure 1.12: Cartoon of the qualitative effect of zonal flow on turbulent eddies. a) A turbulent vortex is destabilized and moves in regions affected by different $v_{E \times B_0}$ velocities, b) its structure is distorted and shared when the zonal flow is strong enough c) It reduces to smaller vortexes, associated to less turbulent transport. This picture is taken from Ref. [17].

cannot actively contribute to radial transport. The term which controls this complex nonlinear coupling is the Reynolds stress tensor, introduced previously in section 1.3.2. However, as the overall energy content of zonal shear flows increases, some of its energy is transferred back to the fluctuating field components. Therefore, a steady-state nonlinear phase requires a balance between the energy flowing from the plasma instabilities to axisymmetric perturbations. Significant progress has been recently made to properly model this nonlinear energy transfer dynamics and the most prominent theory is given by a so-called predator-prey model [60, 61, 62, 63, 64]. A detailed review on shear-flows and its generation mechanisms can be found in Ref. [65, 57].

1.6.2 Geodesic acoustic modes

Finite frequencies axis-asymmetric perturbations are also often observed in tokamak plasmas and numerical simulations. An example is given by the so-called Geodesic-acoustic-mode (GAM), which is characterized by $n = 0$, $m = 1$ density fluctuations. The nature of this mode can be qualitatively captured in the ideal MHD framework [66]. In particular, it arises as the result of the coupling between geodesic curvature terms and sound waves (longitudinal wave propagating along the background magnetic field line). This coupling generates a radial electric field perturbation E_r and therefore a perpendicular $v_{E \times B}$ flow. The GAM oscillatory nature comes from the divergence-free property of the density current $\mathbf{J} = \mathbf{B} \times \nabla p / B^2$. In particular, it is the result of the balancing between the perpendicular geodesic current \mathbf{J}_\perp and its

1.6 Nonlinear turbulence saturation

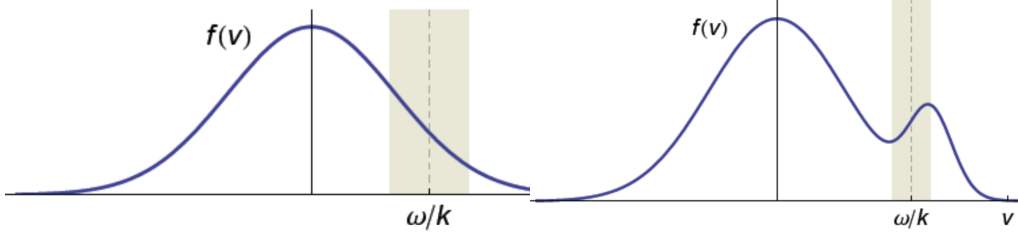


Figure 1.13: Schematic representation of the wave-particle interaction through Landau damping mechanisms for the cases of a) Maxwellian and b) double-bump-on-tail backgrounds. The particles with velocity $v \approx v_\phi = \omega/k$ can exchange energy with the wave. In the case a) more particles are moving at velocities slightly smaller than v_ϕ compared to the number of particles moving at higher velocities and the wave is stabilized. In case b) more particles are moving at velocities slightly higher than $v_\phi = \omega/k$, compared to the number of particles moving at lower velocities and the wave is destabilized

toroidal component \mathbf{J}_{\parallel} . The latter acts to reverse the resulting electric field fluctuations \mathbf{E} to satisfy $\nabla \cdot \mathbf{J}_{\perp} = -\nabla \cdot \mathbf{J}_{\parallel}$. The GAM real frequency can be derived in an ideal MHD framework [66] and it reads as

$$\omega_{GAM} = \sqrt{\frac{2(T_e + \gamma_i T_i)(2q^2 + 1)}{m_i q^2 R_0^2}}. \quad (1.41)$$

with γ_i the adiabatic index of ions, T_e , T_i the electron and ion temperature, m_i the ion mass and R_0 and q , respectively, the tokamak major radius and the safety factor. However, its imaginary part needs to be evaluated within a gyrokinetic/kinetic framework. The MHD model, indeed, does not contain any wave-particle resonance effect, which represents the main damping mechanism of GAM oscillations. In particular, assuming a thermalized system, the background distribution function of ions and electrons is represented by a Maxwellian distribution, i.e.

$$f_s(\mathbf{x}, \mathbf{v}) = \frac{n_{0,s}(\mathbf{x})}{\pi^{3/2} v_{th,s}^3(\mathbf{x})} \exp\left(-\frac{v^2}{v_{th,s}^2}\right). \quad (1.42)$$

Here, $n_{0,s}$ represents the plasma density of the species s and $v_{th,s} = \sqrt{2T_{0,s}/m_s}$ the thermal velocity, with $T_{0,s}$ and $m_{0,s}$ respectively the background temperature and mass. In case a GAM oscillation is excited with phase velocity v_ϕ , an effective

energy exchange between wave and particle occurs if the resonance condition $v \approx v_\phi$ is fulfilled. The particles moving with $v < v_\phi$ will therefore be accelerated taking energy from the wave while the particles moving with $v > v_\phi$ will be decelerated, giving energy to the wave. Since in a Maxwellian plasma the slower particles are more numerous than the faster particles (see Fig. 1.13a)), the resonant interaction results in a net damping, which is well known in the plasma physics community as Landau damping.

In many realistic tokamak plasma scenarios, external heating systems are employed to heat and refuel the plasma. They can generate non-thermalised distributions with shapes similar to the idealized picture of Fig. 1.13b). In this case, the qualitative physical mechanism described above changes and energetic particles can drive geodesic acoustic modes if the thermal damping is overcome. In this case such geodesic acoustic modes are called energetic particle-induced GAM (EGAM) [67, 68, 69, 70, 71, 72] and the parallel velocity anisotropies arising from the non-thermalised fast ion distribution function may lead to an energy transfer from the energetic ions to the EGAM via inverse Landau damping and to a growth of this mode. These unstable modes have also been observed experimentally in different plasma devices and in different plasma conditions at DIII-D [73], LHD [74] ASDEX Upgrade [53] and JET [75]. Furthermore, Ref. [76] contains some first evidence for EGAM excitation by energetic electrons in experiments at HL-2A. Despite significant improvement in the theoretical understanding of the EGAM linear and nonlinear dynamics has already been achieved recently [77, 78, 79], several aspects still need to be addressed in order to be able to understand the whole complex turbulence/ZF nonlinear interaction. Indeed, EGAMs might act on turbulence similarly as ZF, providing additional saturating channel to ion-driven turbulence.

1.7 Thesis scope and outline

Being an almost ubiquitous phenomenon, turbulence with its highly stochastic and nonlinear character is a subject of active research in various fields. In magnetically confined plasma physics, it is of particular interest since it largely determines the radial heat and particle transport and thus the overall confinement. As briefly described in the first section of this introductory chapter, to effectively design a nuclear fusion reactor, the diffusive anomalous transport, along with the other energy losses, needs to be overcome by the energy produced through fusion-born products. Therefore, any insight on possible reductions of the underlying micro-instabilities and/or on modifications of their nonlinear saturation mechanisms can be considered crucial on the way to self-sustained plasma burning and corresponding fusion power

1.7 Thesis scope and outline

plants. As explained in section 1.4 such micro-instabilities are inevitably driven by the typical tokamak steep density and temperature profiles. For the reactor ASDEX Upgrade (Germany), for example, from the plasma center to the periphery (i.e. over roughly one meter) the temperature drops from $1 \cdot 10^8$ to $1 \cdot 10^4$ Kelvin degrees. In this context, recent experimental and numerical studies have shown a particularly interesting link between the presence of fast ions and substantial improvement of energy confinement [80, 81, 82, 83, 84]. In current experiments, these fast particles are produced through external heating systems. For future reactors they will be also partially generated through fusion reactions.

Before the theoretical contribution given by the present work, dedicated studies had already identified a number of possible energetic ion effects on plasma turbulence. In particular, a first direct effect is that fast particles dilute the thermal ion species to ensure the plasma quasi-neutrality [80]. This passive effect reduces the density of thermal ions able to drive diffusive/anomalous transport at the typical ITG-scales and it is usually associated to an improvement of the plasma confinement. Beneficial effects have also been attributed to improvement of the magnetic geometry configurations. In particular, the high energetic particles pressure gradients have been shown to reduce the curvature and magnetic drifts, which are the main drive of drift instabilities [85]. However, the most striking fast ion stabilising mechanism was only observed recently in numerical gyrokinetic simulations in Ref. [84]. In particular, a substantial turbulence reduction was attributed to enhancement of nonlinear electromagnetic effects by energetic ions. These results were also corroborated by a large number of numerical and experimental observations [86, 87, 88]. However, this turbulence stabilization was often observed to be overestimated in numerical gyrokinetic simulations which assumed equivalent Maxwellian backgrounds for the fast particle species, making the extension of such codes to arbitrary distributions particularly compelling. One of the first numerical investigations of a realistic plasma discharge with realistic models for the energetic particle backgrounds was performed in Ref. [89] and it is discussed in course of this thesis work. Despite the extensive progress in the last decade, a detailed understanding of this nonlinear stabilising mechanism was still missing before the comprehensive physical explanation given by Ref. [90] and presented in the course of this dissertation. Moreover, some of the numerical and experimental observations were still in contrast with the aforementioned theoretical fast ion models. For instance, in Ref. [82] a significant variation of the linear ITG growth rates was observed in presence of fast particles in electrostatic simulations, suggesting an additional fast ion interaction mechanism. The latter will be also investigated in detail throughout this dissertation. Here, it is worth mentioning that these numerical results have been obtained by assuming locally thermalized back-

grounds, i.e. a local Maxwellian distribution functions for modelling the energetic particle species. However, as previously discussed, the parallel velocity anisotropies arising from the highly non-thermalised fast ion distribution functions may lead to an energy transfer from the energetic ions to axisymmetric modes, such as EGAMs via inverse Landau damping and to a growth of this mode. Since ITG turbulence mainly saturates via ZFs, any modification of the latter may therefore have a strong impact on transport levels and hence on energy confinement. Hereafter, EGAMs could be another interesting player in this context and need to be properly modelled to have a consistent picture. Therefore, the control of fast ion populations with external heating might open the way to more optimistic scenarios for future fusion devices. However, little is known about the parameter range of relevance of these fast ion effects. This work is therefore dedicated to provide further insights into the beneficial impact of energetic particles on plasma turbulence and to significantly improve the current modelling capabilities. In particular, to extend the numerical schemes of the gyrokinetic code GENE to model anisotropies and asymmetries usually present for highly non-thermalized fast particles.

This work is organized as follows. In chapter 2, a detailed introduction to the reduced kinetic model, i.e. gyrokinetic theory, employed throughout the whole dissertation to investigate the role of energetic ions on turbulence will be presented. In particular, the basic gyrokinetic equations are discussed and derived in the so-called Eulerian framework, i.e. discretized on a fixed grid. This numerical approach is widely used by many gyrokinetic codes in the plasma physics community, such as GENE. The analytic derivation of the basic GENE equations will not only be a mere academic exercise, but will be aimed to extend the gyrokinetic equations, known in literature, for studying the physics of non-thermalized fast particles. A so-called δf -approach is employed and the full distribution function is split into an equilibrium component and in a fluctuating part. The first original contribution of this thesis is that no assumption will be made on the shape of the background F_0 distribution, which, for the case of energetic particles, will contain velocity anisotropies and/or asymmetries. Chapter 3 will be entirely dedicated to provide the essential details on the numerical implementation of the newly derived equations into the gyrokinetic code GENE. Furthermore, first verification studies on the new numerical schemes are performed and the results benchmarked against other codes which present similar features. It is worth mentioning here that, thanks to these code extensions, GENE is the first gyrokinetic code able to study realistic energetic particle models in the full electromagnetic framework retaining the whole radial dependences. The new features of the GENE code will be applied in chapter 4 to analyze a particular plasma with strong fast-ion related turbulence suppression generated in the Joint

1.7 Thesis scope and outline

European Torus (JET). During this study, non-trivial electrostatic energetic particle effects on ITG micro-instabilities are observed which cannot be explained with the conventional assumptions based on pressure profile and dilution. In particular, depending on the heating scheme and, therefore, on the origin of the velocity space asymmetries and anisotropies, fast ions are found to impact plasma micro-instability differently. This represents the second original contribution of this work. Moreover, the study of chapter 4 confirms previous numerical observations on similar plasma discharges performed with simplified fast ion models, where the most relevant fast ion effect was associated to nonlinear and electromagnetic effects. Therefore, the realistic study of chapter 4 motivates more detailed numerical and theoretical analyses. Chapter 5 and 6 will therefore be dedicated to fill the missing gaps and to provide for the first time a consistent picture, respectively, for the electrostatic and electromagnetic fast ion effects on plasma turbulence. In particular, chapter 6 gives for the first time a consistent frame in which to interpret the nonlinear enhancement of the turbulence stabilization observed in the presence of energetic ions. Finally, in chapter 7, the effect of the plasma elongation on the energetic-particle-induced geodesic acoustic mode (EGAM) dynamics is studied with numerical simulations performed with the gyrokinetic codes GENE and ORB5. The full radial dependences of the plasma parameters are retained for this study and the energetic particle species are modelled with realistic analytic models. These findings are applied to the study of an experimental plasma generated in the tokamak reactor ASDEX (Axially Symmetric Divertor Experiment) Upgrade, which is located in Garching (Germany). Conclusions are given in chapter 8 along with an outlook on possible extensions of the results presented in this dissertation.

1. Introduction

Chapter 2

Gyrokinetic theory

In the following chapter, the theoretical framework and basic equations used to investigate turbulence in a magnetized plasma are derived following Ref. [11, 91, 92, 93]. Here, we present an extension of the standard gyrokinetic theory [89] able to account for highly non-thermalised species, generated not only in tokamak plasmas but often observed also in astrophysical scenarios [94, 95, 96]. Other independent derivations of gyrokinetic theory able to capture non-thermal particle properties can be found in Ref. [97, 98, 99, 100, 101]. The assumption in the gyrokinetic δf -theory to consider a locally thermalised background is removed and more flexible distributions can now be considered [89, 102]. The latter might be either analytical or obtained from numerical models [103, 104, 105, 106]. With these modifications it will be possible, as shown in the next chapters, to investigate non-thermal effects with the GENE code for the first time.

2.1 Basic introduction to gyrokinetic theory

The plasma dynamics can be described and modelled with several theoretical approaches, which are based on different approximations. As discussed in chapter 1, the most comprehensive and complete one is the kinetic description, where a distribution function f for each species is introduced and evolved in time in the 6-dimensional space (\mathbf{x}, \mathbf{v}) . The kinetic theory is able to capture, among different physical mechanisms, resonance effects which require the full complex phase space description of the system. Since in a tokamak reactor, as shown in chapter 1, the charged particles are confined through the application of electromagnetic fields, it is essential to study the interaction between particles and fields. The latter affect the particle dynamics which in turn modify the fields evolution. The resulting system of nonlinear

equations needs to be solved self-consistently and can become prohibitively expensive even for the most powerful supercomputers. In this context, it is essential to obtain a reduced kinetic model without losing relevant physics. In the past decades, extensive effort has been spent to optimize the underlying equations and to improve code performances. One of the most prominent reduced kinetic model obtained - employed throughout all the rest of this work - is gyrokinetics [107, 108, 109, 110].

2.2 Gyrokinetic ordering

The analytical derivation of gyrokinetic theory is based on experimentally motivated ordering assumptions allowing approximations which will be used in the rest of this chapter to derive the basic gyrokinetic Vlasov-Maxwell system of equations. Turbulence in the core region of different magnetized plasmas (characterized by high densities and temperatures) usually exhibits general properties, which do not depend on the specific case. In particular, turbulence is usually connected with the following features:

- **Small fluctuations:** In the plasma core, the fluctuation amplitude of any physical observables is considerably smaller than the background counterpart, e.g. $n_1/n_0 \sim \epsilon \ll 1$. This first ordering assumption will be used to simplify the derivation of the basic equations.
- **Anisotropic turbulence:** The turbulence fluctuations are strongly anisotropic. In particular, the turbulence correlation length parallel to the magnetic field lines is commonly several orders of magnitude larger than the perpendicular one, i.e. $k_{\parallel}/k_{\perp} \sim \epsilon \ll 1$. A particularly convenient field-aligned coordinate system which adapts to the elongated structure of turbulence eddies will be used in the next sections to greatly simplify the analytical derivation and optimize the code implementation.
- **Gyrofrequency ordering:** The typical drift-wave frequency ω is much smaller than the ion and electron gyrofrequency $\Omega = qB_0/mc$, i.e. $\omega/\Omega \sim \epsilon \ll 1$. This experimental observation provides the basis for a simplification of the full dynamic description of each particle species. It will be possible to reduce the description of the fast gyromotion to the dynamics of a charged ring and decrease the system dimensionality by one.

2.3 Single particle Lagrangian

2.3 Single particle Lagrangian

The classical equations of motion for a single particle of mass m and charge q in a background magnetic field, described by the vector potential $\mathbf{A}(\mathbf{x})$ and by the scalar potential $\phi(\mathbf{x})$, can be derived from the Lagrangian

$$\mathcal{L}(\mathbf{x}, \mathbf{v}) = \left(m\mathbf{v} + \frac{q}{c}\mathbf{A}(\mathbf{x}) \right) \cdot \dot{\mathbf{x}} - \frac{mv^2}{2} - q\phi(\mathbf{x}). \quad (2.1)$$

Here, \mathbf{x} and \mathbf{v} represent the position and the velocity of the charged particle and c the speed of light.

2.4 One-form formulation

In order to take advantage of the gyrokinetic ordering assumptions, which allow us to simplify the basic equations, it is convenient to introduce the function $d\gamma$ via the action integral \mathcal{S}

$$\mathcal{S} = \int \mathcal{L}(\mathbf{x}, \mathbf{v}) dt = \int d\gamma. \quad (2.2)$$

This approach is known as one-form formulation. In Eq. (2.2) the function $d\gamma = (m\mathbf{v} + \frac{q}{c}\mathbf{A}(\mathbf{x})) \cdot d\mathbf{x} - \left(\frac{mv^2}{2} + q\phi(\mathbf{x}) \right) dt$ has been defined. Assuming that the background quantities are perturbed by small fluctuations, the one-form $d\gamma$ function can be split in an unperturbed and in a fluctuating part, i.e. $d\gamma = d\gamma_0 + d\gamma_1$, with

$$d\gamma_0 = \left(m\mathbf{v} + \frac{q}{c}\mathbf{A}_0(\mathbf{x}) \right) \cdot d\mathbf{x} - \frac{1}{2}mv^2 dt, \quad (2.3)$$

$$d\gamma_1 = \frac{q}{c}\mathbf{A}_1(\mathbf{x}) \cdot d\mathbf{x} - q\phi_1(\mathbf{x}) dt. \quad (2.4)$$

The electrostatic potential $\phi_0(\mathbf{x})$ is not considered, since, in a first approximation, no background electric field is applied in a tokamak reactor and the small background component generated through rotational effects is usually negligible in the plasma core. From the $d\gamma$ functions defined above, it is straightforward to perform a change in the coordinate system known as guiding center transformation [111, 112]. In a strong magnetic field, any charged particle will perform a helical motion along the magnetic field lines. Therefore, it is possible to decompose its dynamics as the motion of the center of gyration \mathbf{X} and the one on its perpendicular plane $\mathbf{r}(\mathbf{X}, \mu, \theta)$. Here, θ represents the gyroangle. The relation between the guiding center coordinate system and the particle coordinates is defined by

$$\mathbf{x} = \mathbf{X} + \mathbf{r}(\mathbf{X}, \mu, \theta), \quad (2.5)$$

2. Gyrokinetic theory

$$\mathbf{v} = v_{\parallel} \hat{b}_0(\mathbf{X}) + v_{\perp}(\mathbf{X}, \mu) \hat{c}(\theta). \quad (2.6)$$

Here, $\mathbf{r}(\mathbf{X}, \mu, \theta) = v_{\perp}(\mathbf{X}) \hat{a}(\theta) / \Omega(\mathbf{X})$ represents the gyroradius, i.e. the distance between the charged particle and the gyrocenter. Furthermore, the unit vectors $\hat{a}(\theta) = \hat{x} \cos \theta - \hat{y} \sin \theta$ and $\hat{c}(\theta) = \frac{\partial}{\partial \theta} \hat{a}(\theta) = -\hat{x} \sin \theta - \hat{y} \cos \theta$ in the Cartesian coordinates $(\hat{x}, \hat{y}, \hat{b}_0)$ have been defined. The gyrokinetic gyrofrequency ordering allows us to greatly simplify the study of the single particle dynamics by assuming the drift wave frequencies to be several order of magnitude smaller than the gyrofrequency. Using this method it is possible to neglect and remove the gyroangle dependence from the single-particle Lagrangian and reduce the dimensionality by one. In order to do so, Eqs. (2.3-2.4) are transformed into the guiding center coordinate system, applying the coordinate transformation defined in Eqs. (2.5-2.6), through the relation

$$\Gamma(\mathbf{X}, \mu, \theta, v_{\parallel})_{\xi} = d\gamma(\mathbf{x}, \mathbf{v})_{\nu} \cdot \mathcal{J}_{\xi}^{\nu}. \quad (2.7)$$

Here, \mathcal{J} denotes the Jacobian of the transformation and $d\gamma = \gamma_{\nu} dx^{\nu}$. Eq. (2.7) is written with the Einstein summation convention. Applying the aforementioned transformation to the unperturbed part $d\gamma_0$ yields for each component

$$\Gamma_{t_0} = -\frac{1}{2} mv_{\parallel}^2 - \mu B_0(\mathbf{X}), \quad (2.8)$$

$$\Gamma_{\mathbf{x}_0} = (mv_{\parallel} \hat{b}_0(\mathbf{X}) + \frac{q}{c} \mathbf{A}_0(\mathbf{X}) + mv_{\perp} \hat{c}(\theta)) \cdot (\hat{\mathbf{1}} + \frac{\partial}{\partial \mathbf{X}} \frac{v_{\perp}(\mathbf{X})}{\Omega(\mathbf{X})} \hat{a}(\theta)), \quad (2.9)$$

$$\Gamma_{v_{\parallel 0}} = 0, \quad (2.10)$$

$$\Gamma_{\theta_0} = (mv_{\parallel} \hat{b}_0(\mathbf{X}) + \frac{q}{c} \mathbf{A}_0(\mathbf{X}) + mv_{\perp} \hat{c}(\theta)) \cdot \frac{v_{\perp}(\mathbf{X})}{\Omega(\mathbf{X})} \hat{c}(\theta), \quad (2.11)$$

$$\Gamma_{\mu_0} = (mv_{\parallel} \hat{b}_0(\mathbf{X}) + \frac{q}{c} \mathbf{A}_0(\mathbf{X}) + mv_{\perp} \hat{c}(\theta)) \cdot \frac{B_0(\mathbf{X})}{mv_{\perp} \Omega(\mathbf{X})} \hat{a}(\theta), \quad (2.12)$$

where $\hat{\mathbf{1}}$ is the unit tensor. It has been assumed that the unperturbed quantities have a slow spatial variation, i.e. $\mathbf{A}_0(\mathbf{x} + \mathbf{r}) \approx \mathbf{A}_0(\mathbf{x})$. As discussed previously, the fast gyroangle dependence can be removed by applying the gyroaverage operator \mathcal{G} defined on the generic function $g(\mathbf{X}, \theta)$ as follows

$$\langle g(\mathbf{X}) \rangle = \mathcal{G}g(\mathbf{X}, \theta) = \frac{1}{2\pi} \oint_0^{2\pi} g(\mathbf{X}, \theta) d\theta. \quad (2.13)$$

2.4 One-form formulation

The dynamics of the single particle reduces, hence, to the study of charged gyro-rings, as discussed in detail in Ref. [11]. The Γ_0 function then reads in the guiding center coordinate system

$$\Gamma_0 = (mv_{\parallel}\hat{b}_0(\mathbf{X}) + \frac{q}{c}\mathbf{A}_0(\mathbf{X})) \cdot d\mathbf{X} + \frac{mv_{\perp}^2(\mathbf{X})}{2\Omega(\mathbf{X})}d\theta - (\frac{1}{2}mv_{\parallel}^2 + \mu B_0(\mathbf{X}))dt. \quad (2.14)$$

The perturbed part of the one-form $d\gamma$ function in the guiding center coordinates can be obtained in a similar way, i.e.

$$\Gamma_{t_1} = -q\phi_1(\mathbf{X} + \mathbf{r}), \quad (2.15)$$

$$\Gamma_{\mathbf{x}_1} = \frac{q}{c}\mathbf{A}_1(\mathbf{X} + \mathbf{r}) \cdot \left(\hat{1} + \frac{1}{\Omega(\mathbf{X})} \sqrt{\frac{\mu}{2mB_0(\mathbf{X})}} \frac{dB_0(\mathbf{X})}{d\mathbf{X}} \hat{a}(\theta) \right), \quad (2.16)$$

$$\Gamma_{v_{\parallel 1}} = 0, \quad (2.17)$$

$$\Gamma_{\theta_1} = \frac{mv_{\perp}(\mathbf{X})}{B_0(\mathbf{X})} \mathbf{A}_1(\mathbf{X} + \mathbf{r}) \cdot \hat{c}(\theta), \quad (2.18)$$

$$\Gamma_{\mu_1} = \frac{1}{v_{\perp}(\mathbf{X})} \mathbf{A}_1(\mathbf{X} + \mathbf{r}) \cdot \hat{a}(\theta). \quad (2.19)$$

The term $\frac{1}{\Omega(\mathbf{X})} \sqrt{\frac{\mu}{2mB_0(\mathbf{X})}} \frac{dB_0(\mathbf{X})}{d\mathbf{X}} \hat{a}(\theta)$ is a second order term in the gyrokinetic ordering parameter ϵ and will be neglected in the following. The perturbed Γ_1 function reads

$$\Gamma_1 = \frac{q}{c}\mathbf{A}_1(\mathbf{X} + \mathbf{r}) \cdot d\mathbf{X} + \frac{\mathbf{A}_1(\mathbf{X} + \mathbf{r}) \cdot \hat{a}(\theta)}{v_{\perp}(\mathbf{X})} d\mu + \frac{mv_{\perp}(\mathbf{X})}{B_0(\mathbf{X})} \mathbf{A}_1(\mathbf{X} + \mathbf{r}) \cdot \hat{c}(\theta) d\theta - q\phi_1(\mathbf{X} + \mathbf{r}) dt. \quad (2.20)$$

The gyroangle dependence of Eq. (2.20) cannot be removed by applying the simple gyroaverage operator introduced previously, since the field perturbations vary on the gyroradius scale. Instead, the more sophisticated approach of the Lie perturbation theory is here employed. More details on the latter approach can be found in Ref. [11, 113, 114, 115]. The gyrocenter one-form expression of Eq. (2.20) becomes

$$\Gamma_1 = \frac{q}{c} \langle \mathbf{A}_1(\mathbf{X} + \mathbf{r}) \rangle \cdot d\mathbf{X} - \left(q \langle \phi_1(\mathbf{X} + \mathbf{r}) \rangle - \frac{q}{c} v_{\perp} \langle \mathbf{A}_1(\mathbf{X} + \mathbf{r}) \cdot \hat{c}(\theta) \rangle \right) dt. \quad (2.21)$$

In the following equations, the position for which every quantity is evaluated is the center of gyration \mathbf{X} . The total Γ function up to the first order in the perturbation theory can be written as

$$\begin{aligned} \Gamma &= \Gamma_0 + \Gamma_1 \\ &= \left(mv_{\parallel}\hat{b}_0 + \frac{q}{c}\mathbf{A}_0 + \frac{q}{c}\bar{\mathbf{A}}_1 \right) \cdot d\mathbf{X} + \frac{\mu mc}{q}d\theta - \left(\frac{1}{2}mv_{\parallel}^2 + q\bar{\phi}_1 + \mu(B_0 + \bar{B}_{1,\parallel}) \right) dt. \end{aligned} \quad (2.22)$$

The equivalence (valid only for the study of a single magnetic surface, i.e. local limit) $qv_{\perp} \langle \mathbf{A}_1 \cdot \hat{c}(\theta) \rangle / c = -\mu \bar{B}_{1,\parallel}$ has been used and is proven analytically in Ref. [93]. Here the overbar indicates that the parallel component of the magnetic field has been gyroaveraged at the particle position \mathbf{x}

$$\bar{B}_{1,\parallel}(\mathbf{X}) = \mathcal{G}B_{1,\parallel}(\mathbf{X} + \mathbf{r}) = \frac{1}{2\pi} \oint_0^{2\pi} B_{1,\parallel}(\mathbf{X} + \mathbf{r}) d\theta. \quad (2.23)$$

Eq. (2.23) is similar to the previously defined Eq. (2.13), with the main fundamental difference that while Eq. (2.23) acts at the particle position \mathbf{x} , Eq. (2.13) applies to the center of gyration \mathbf{X} . Furthermore, the perpendicular component of the vector potential has been neglected in $\bar{\mathbf{A}}_1 = \langle A_{1,\parallel} \hat{b}_0 \rangle$. This approach corresponds to the \parallel -symplectic ($\alpha = 0, \beta = 1$) gyrocenter model of Ref. [91]. To summarize, Eq. (2.22) reads

$$\Gamma = \left(mv_{\parallel} \hat{b}_0 + \frac{q}{c} \mathbf{A}_0 + \frac{q}{c} \bar{A}_{1,\parallel} \hat{b}_0 \right) \cdot d\mathbf{X} + \frac{\mu mc}{q} d\theta - \left(\frac{1}{2} mv_{\parallel}^2 + q\bar{\phi}_1 + \mu (B_0 + \bar{B}_{1,\parallel}) \right) dt. \quad (2.24)$$

2.5 Single particle gyrocenter equation of motion

The one-form formulation is introduced to greatly simplify the derivation of the basic gyrokinetic equations and more easily take advantage of the ordering assumptions discussed previously in section 2.2. In particular, the single particle Lagrangian is transformed from the particle to the guiding center coordinate system. By doing so, the gyroangle is explicitly introduced in the equation of motion and it is averaged out through sophisticated perturbation theory. The full information about the single particle dynamics perpendicular to the background magnetic field is replaced by its averaged contribution. The study of the single particle dynamics reduces, therefore, to the evolution of the particle gyro center and the averaged perpendicular motion. The full dynamics is then approximated by "quasi-particles", i.e. charged rings. According to Eq. (2.22), the single particle Lagrangian associated with the one-form Γ function of Eq. (2.24) reads as

$$\mathcal{L} = \left(mv_{\parallel} \hat{b}_0 + \frac{q}{c} \mathbf{A}_0 + \frac{q}{c} \bar{A}_{1,\parallel} \hat{b}_0 \right) \cdot \dot{\mathbf{X}} + \frac{\mu mc}{q} \dot{\theta} - \left(\frac{1}{2} mv_{\parallel}^2 + q\bar{\phi}_1 + \mu (B_0 + \bar{B}_{1,\parallel}) \right). \quad (2.25)$$

2.5 Single particle gyrocenter equation of motion

The equations of motion in the gyro center coordinate system can be obtained for each coordinate $Z^i = (\mathbf{X}, \mu, v_{\parallel}, \theta)$ from the Euler-Lagrange equation

$$\frac{d}{dt} \left(\frac{\partial \mathcal{L}}{\partial \dot{Z}^i} \right) - \frac{\partial \mathcal{L}}{\partial Z^i} = 0. \quad (2.26)$$

By employing the approximation

$$\nabla \times (\hat{b}_0 \bar{A}_{1,\parallel}) = (\nabla \bar{A}_{1,\parallel}) \times \hat{b}_0 + \mathcal{O}(\epsilon) \approx (\nabla \bar{A}_{1,\parallel}) \times \hat{b}_0, \quad (2.27)$$

which holds true neglecting the background plasma current and electric field and defining

$$\mathbf{A}_0^* = \mathbf{A}_0 + \frac{mcv_{\parallel}\hat{b}_0}{q}, \quad (2.28)$$

$$B_0^* = \nabla \times \mathbf{A}_0^*, \quad (2.29)$$

$$B_{0,\parallel}^* = \hat{b}_0 \cdot (\nabla \times \mathbf{A}_0^*), \quad (2.30)$$

Eq. (2.26) leads to

$$v_{\parallel} = \hat{b}_0 \cdot \dot{\mathbf{X}}, \quad (2.31)$$

$$\dot{\mu} = 0, \quad (2.32)$$

$$\dot{\theta} = \Omega [1 + \frac{q}{B_0} \frac{\partial}{\partial \mu} (\bar{\phi}_1 - \frac{v_{\parallel}}{c} \bar{A}_{1,\parallel} + \frac{\mu}{q} \bar{B}_{1,\parallel})], \quad (2.33)$$

$$\dot{\mathbf{X}} = \frac{\mathbf{B}_0}{B_{0,\parallel}^*} v_{\parallel} + \frac{B_0}{B_{0,\parallel}^*} (\mathbf{v}_E + \mathbf{v}_{\nabla B} + \mathbf{v}_c) \simeq v_{\parallel} \hat{b}_0 + \frac{B_0}{B_{0,\parallel}^*} (\mathbf{v}_E + \mathbf{v}_{\nabla B} + \mathbf{v}_c), \quad (2.34)$$

$$\begin{aligned} \dot{v}_{\parallel} &= \frac{\dot{\mathbf{X}}}{mv_{\parallel}} \cdot \left(q \bar{\mathbf{E}}_1 - \frac{q}{c} \hat{b}_0 \dot{\bar{A}}_{1,\parallel} - \mu \nabla (B_0 + \bar{B}_{1,\parallel}) \right) \\ &= \frac{1}{mv_{\parallel}} \left(v_{\parallel} \hat{b}_0 + \frac{B_0}{B_{0,\parallel}^*} (\mathbf{v}_E + \mathbf{v}_{\nabla B} + \mathbf{v}_c) \right) \cdot \left(q \bar{\mathbf{E}}_1 - \frac{q}{c} \hat{b}_0 \dot{\bar{A}}_{1,\parallel} - \mu \nabla (B_0 + \bar{B}_{1,\parallel}) \right). \end{aligned} \quad (2.35)$$

Here, the $\mathbf{E} \times \mathbf{B}$, the curvature and the grad-B velocities have been defined, respectively, as follows, i.e.

$$\mathbf{v}_E = \frac{c}{B_0^2} (\mathbf{B}_0 \times \nabla \bar{\xi}_1), \quad (2.36)$$

$$\mathbf{v}_c = \frac{v_{\parallel}^2}{\Omega} (\nabla \times \hat{b}_0)_{\perp}, \quad (2.37)$$

$$\mathbf{v}_{\nabla B_0} = \frac{\mu c}{q B_0^2} (\mathbf{B}_0 \times \nabla B_0). \quad (2.38)$$

Furthermore, a modified gyroaveraged potential $\bar{\xi}_1 = \bar{\phi}_1 - \frac{v_{\parallel}}{c} \bar{A}_{1,\parallel} + \frac{\mu}{q} \bar{B}_{1,\parallel}$ is introduced.

Eqs. (2.31-2.35) represent the single particle gyro center equations of motion up to the first order in the gyrokinetic expansion. Eq. (2.32) shows that the magnetic moment is an adiabatic invariant, within the considered limits.

2.6 Vlasov equation for general backgrounds

The gyrokinetic plasma description employs a statistical approach based on the study of a distribution function for each species of the plasma. Its time evolution is determined by the kinetic Vlasov equation

$$\frac{df}{dt} = \frac{\partial f}{\partial t} + \dot{\mathbf{x}} \cdot \frac{\partial f}{\partial \mathbf{x}} + \dot{\mathbf{v}} \cdot \frac{\partial f}{\partial \mathbf{v}} = 0, \quad (2.39)$$

which is coupled to the fields through Maxwell's equations. In case inter-species collisions are considered, Eq. (2.39) is replaced by $df/dt = C(f, f')$ and referred to as Boltzmann equation. Here, $C(f, f')$ represents the Boltzmann collision operator. It will be described in more details in section 2.16.

In the gyrocenter coordinate system for the distribution function $F = F(Z^i) = F(\mathbf{X}, v_{\parallel}, \mu)$, Eq. (2.39) becomes

$$\frac{\partial F}{\partial t} + \frac{\partial Z^i}{\partial t} \frac{\partial F}{\partial Z^i} = 0. \quad (2.40)$$

The single particle one-form formulation, derived in the previous section, can be employed here to obtain an explicit expression for the collisionless Vlasov equation

$$\frac{\partial F}{\partial t} + \dot{\mathbf{X}} \cdot \nabla F + \dot{v}_{\parallel} \frac{\partial F}{\partial v_{\parallel}} = 0. \quad (2.41)$$

Note that F does not depend on the gyrophase θ and the magnetic moment μ is an adiabatic invariant of motion, i.e. $\dot{\mu} = 0$. The time derivative of the gyrocenter position \mathbf{X} and the component of the velocity vector parallel to the background magnetic field v_{\parallel} can be taken from Eqs. (2.34-2.35) with the result

$$\begin{aligned} & \frac{\partial F}{\partial t} + \left[v_{\parallel} \hat{b}_0 + \frac{B_0}{B_{0,\parallel}^*} (\mathbf{v}_E + \mathbf{v}_{\nabla B} + \mathbf{v}_c) \right] \\ & \cdot \left\{ \nabla F - \left[q \nabla \bar{\phi}_1 + \frac{q}{c} \hat{b}_0 \bar{A}_{1,\parallel} + \mu \nabla (B_0 + \bar{B}_{1,\parallel}) \right] \frac{1}{mv_{\parallel}} \frac{\partial F}{\partial v_{\parallel}} \right\} = 0. \end{aligned} \quad (2.42)$$

2.6 Vlasov equation for general backgrounds

An approach often employed in gyrokinetics is the splitting of the distribution function of each species into a background component and in a small fluctuating part, i.e., $F = F_0 + F_1$ (so-called δf approach). While many derivations like the previous one for GENE [113, 93, 11] rely on local Maxwellian distributions, here we relax such an assumption on F_0 . The gyrokinetic δf ordering, i.e., $n_1/n_0 \sim \epsilon \ll 1$, allows us to greatly simplify the numerical solution of Eq. (2.42). It is indeed possible to separate the background time scale variation from the one of the fluctuating quantities through the expansion parameter ϵ . The zeroth order term of the Vlasov equation, which reads as

$$\frac{\partial F_0}{\partial t} = \hat{b}_0 \cdot \left(v_{\parallel} \nabla F_0 - \frac{\mu}{m} \nabla B_0 \frac{\partial F_0}{\partial v_{\parallel}} \right), \quad (2.43)$$

is exactly zero for local Maxwellian backgrounds. Therefore, the right hand side of Eq. (2.43) does not modify F_0 and the zeroth order quantities are constant on the turbulent time scale. This term depends on the non-uniformity of the background magnetic field and it is usually addressed as a mirror force term. For the case of an arbitrary background distribution function, Eq. (2.43) is not necessarily zero and the degree of violation of Eq. (2.43) must be studied case by case (e.g. see section 3.2). The turbulent evolution of the system is determined by the first order term of Eq. (2.43), which reads as

$$\begin{aligned} & \frac{\partial F_1}{\partial t} - \frac{q}{mc} \dot{\bar{A}}_{1,\parallel} \frac{\partial F_0}{\partial v_{\parallel}} + v_{\parallel} \hat{b}_0 \cdot \nabla F_1 \\ & - \left[\hat{b}_0 \cdot \left(\frac{q}{m} \nabla \bar{\phi}_1 \frac{\partial F_0}{\partial v_{\parallel}} + \frac{\mu}{m} \nabla \bar{B}_{1,\parallel} \frac{\partial F_0}{\partial v_{\parallel}} + \frac{\mu}{m} \nabla B_0 \frac{\partial F_1}{\partial v_{\parallel}} \right) \right] \\ & + \frac{B_0}{B_{0,\parallel}^*} (\mathbf{v}_E + \mathbf{v}_{\nabla B} + \mathbf{v}_c) \\ & \cdot \left[\nabla F_0 + \nabla F_1 - (q \nabla \bar{\phi}_1 + \mu \nabla (B_0 + \bar{B}_{1,\parallel})) \frac{1}{mv_{\parallel}} \frac{\partial F_0}{\partial v_{\parallel}} \right] = 0. \end{aligned} \quad (2.44)$$

It is worth mentioning here that the terms of the form

$$(\mathbf{v}_E + \mathbf{v}_{\nabla B} + \mathbf{v}_c) \cdot \left[\nabla F_0 - \mu \nabla B_0 \frac{1}{mv_{\parallel}} \frac{\partial F_0}{\partial v_{\parallel}} \right] \quad (2.45)$$

are of first order in the gyrokinetic expansion parameter ϵ even if they do not contain the perturbed part of the distribution function F_1 . More details can be found in Ref. [93].

Second order terms constitute the so-called parallel nonlinearity, which couples different field components to the perturbed part of the distribution function F_1 as

follows

$$\begin{aligned} \frac{\partial F_2}{\partial t} = & \left\{ v_{\parallel} \hat{b}_0 \cdot \left(q \nabla \bar{\phi}_1 + \frac{q}{c} \dot{\bar{A}}_{1,\parallel} \hat{b}_0 + \mu \bar{B}_{1,\parallel} \right) \right. \\ & \left. + \frac{B_0}{B_{0,\parallel}^*} [\mathbf{v}_E \cdot \mu \nabla B_0 + (\mathbf{v}_{\nabla B} + \mathbf{v}_c) \cdot \nabla (q \bar{\phi}_1 + \mu \bar{B}_{1,\parallel})] \right\} \frac{1}{mv_{\parallel}} \frac{\partial F_1}{\partial v_{\parallel}}. \end{aligned} \quad (2.46)$$

This term is of a higher order in the gyrokinetic expansion compared to the perpendicular $\mathbf{E} \times \mathbf{B}$ nonlinearity for the usual plasma core experiments [116, 117, 118]. However, it can become important for single mode analysis. In particular, it will be shown in chapter 3 that this term can be responsible for the nonlinear chirping phase of finite frequency zonal modes, such as GAMs or EGAMs. In most of the numerical simulations shown in this work this term will be neglected if not stated otherwise to reduce the computational cost the numerical simulations.

2.7 Field-aligned coordinate system

One of the gyrokinetic assumptions is the highly anisotropic feature of plasma fluctuations. The turbulence correlation length parallel to the magnetic field lines is commonly several order of magnitude bigger than the perpendicular one, i.e. $k_{\parallel}/k_{\perp} \ll 1$. It is particularly convenient to adopt a coordinate system with the same property, which allows different grid discretization along these directions - to greatly reduce the computational cost of each simulation. To this aim, a curvilinear coordinate system (x, y, z) with the z -axis aligned to the twisted magnetic field lines - a so called field-aligned coordinate system - is introduced here [10]. According to the standard GENE sign convention, the field-aligned coordinate z is parallel to the background magnetic field and the radial x coordinate is directed outward. Following the same approach of chapter 1, we start defining the magnetic field in the Clebsch representation as

$$\mathbf{B}_0 = \mathcal{C} \nabla x \times \nabla y. \quad (2.47)$$

From the divergence free property of the magnetic field, it follows that \mathcal{C} is a function only of (x, y) . Furthermore, since $\mathbf{B}_0 \cdot \nabla x = \mathbf{B}_0 \cdot \nabla y = 0$ it yields that x and y are constant on field lines. Throughout the remainder of this work, the x and y coordinates are assigned to the radial and binormal directions, respectively; radial refers to $\mathbf{B}_0 \cdot \nabla x$ and binormal to the direction perpendicular to the magnetic field lines and ∇x . Strictly speaking, x and y are orthogonal only at the outboard mid-plane, i.e. $\theta = 0$. The Jacobian in the field-aligned coordinate system is defined

$$\mathcal{J}^{-1} = (\nabla x \times \nabla y) \cdot \nabla z = \frac{\mathbf{B}_0 \cdot \nabla z}{\mathcal{C}}. \quad (2.48)$$

2.7 Field-aligned coordinate system

It is possible to map the field aligned (x, y, z) to the straight-field (ψ, χ, φ) coordinate systems through the transformations

$$x = \mathcal{C}_x(\psi), \quad (2.49)$$

$$y = -\mathcal{C}_y(\psi)[\varphi + |q|(\psi)\chi], \quad (2.50)$$

$$z = \chi. \quad (2.51)$$

Here, $\mathcal{C}_x(\psi)$ and $\mathcal{C}_y(\psi) = \psi_0/|q_0|$ represent the converting functions from the two different coordinate systems and q the safety factor, defined as in Eq. (1.7). Note that they are flux-surface functions. Moreover, ψ_0 and q_0 are the radial coordinate and safety factor at a fixed reference flux surface. By comparing Eq. (1.4) and Eq. (2.47) it is possible to show that the function \mathcal{C} is defined as

$$\mathcal{C} \equiv \frac{1}{2\pi\mathcal{C}'_x\mathcal{C}'_y}, \quad (2.52)$$

where $\mathcal{C}'_x = d\mathcal{C}_x/d\psi$.

To transform the general Vlasov equation of Eq. (2.44) from the gyrocenter to the field-aligned coordinate system for each vector component, it is necessary to introduce the metric tensor g in the contravariant basis $e^{1,2,3} = (x, y, z)$. The latter is defined through the gradients of the coordinate surfaces $g^{ij} = \nabla e^i \cdot \nabla e^j$. The generic scalar functions A and T fulfill the following relations

$$\frac{1}{B_0^2}(\mathbf{B}_0 \times \nabla A) \cdot \nabla T = \frac{g^{xi}g^{yj} - g^{yi}g^{xj}}{\mathcal{C}\gamma_1} \partial_i A \partial_j T, \quad (2.53)$$

$$\mathbf{B}_0 \cdot \nabla A = \frac{\mathcal{C}}{\mathcal{J}} \partial_z A, \quad (2.54)$$

with $\gamma_1 = g^{xx}g^{yy} - g^{yx}g^{xy}$, $\gamma_2 = g^{xx}g^{yz} - g^{yx}g^{xz}$ and $\gamma_3 = g^{xy}g^{yz} - g^{yy}g^{xz}$. Employing Eq. (2.53) and Eq. (2.54), the Vlasov equation for general background distributions in a field-aligned coordinate system can be written as

$$\begin{aligned} & \frac{\partial g_1}{\partial t} + \frac{C}{JB_0} \left\{ v_{||} \partial_z F_1 - \left(\frac{q}{m} \partial_z \bar{\phi}_1 \frac{\partial F_0}{\partial v_{||}} + \frac{\mu}{m} \partial_z B_0 \frac{\partial F_1}{\partial v_{||}} + \frac{\mu}{m} \partial_z \bar{B}_{1,||} \frac{\partial F_0}{\partial v_{||}} \right) \right\} \\ & + \frac{cB_0}{CB_{0,||}^*} \left(\frac{g^{1i}g^{2j} - g^{2i}g^{1j}}{\gamma_1} \right) \left\{ \left[\partial_i \bar{\xi}_1 + \frac{\mu}{q} \partial_i B_0 + \frac{v_{||}^2 m}{q} \left(\frac{\partial_i B_0}{B_0} + \frac{\beta_p}{2} \frac{\partial_i p_0}{p_0} \right) \right] \right. \\ & \left. \cdot \left[\partial_j F_0 + \partial_j F_1 - (q \partial_j \bar{\phi}_1 + \mu \partial_j B_0 + \mu \partial_j \bar{B}_{1,||}) \frac{1}{mv_{||}} \frac{\partial F_0}{\partial v_{||}} \right] \right\} = 0. \end{aligned} \quad (2.55)$$

Here, a modified distribution function $g_1 = F_1 - \frac{q}{mc} \bar{A}_{1,\parallel} \frac{\partial F_0}{\partial v_{\parallel}}$ has been introduced to combine the time derivatives of the perturbed distribution function with the the perturbed parallel component of the vector potential. Furthermore, Eq. (2.53) and Eq. (2.54) have been used to evaluate the scalar product of ∇ with the $\mathbf{E} \times \mathbf{B}_0$, grad-B and the curvature velocities

$$(\mathbf{v}_E \cdot \nabla)_{ij} = \frac{c}{C} \left(\frac{g^{xi} g^{yj} - g^{yi} g^{xj}}{\gamma_1} \right) \partial_i \xi_1 \partial_j, \quad (2.56)$$

$$(\mathbf{v}_{\nabla B} \cdot \nabla)_{ij} = \frac{c\mu}{qC} \left(\frac{g^{xi} g^{yj} - g^{yi} g^{xj}}{\gamma_1} \right) \partial_i B_0 \partial_j, \quad (2.57)$$

$$(\mathbf{v}_c \cdot \nabla)_{ij} = \frac{mc v_{\parallel}^2}{qC} \left(\frac{g^{xi} g^{yj} - g^{yi} g^{xj}}{\gamma_1} \right) \left(\frac{\partial_i B_0}{B_0} + \frac{\beta_p}{2} \frac{\partial_i p_0}{p_0} \right) \partial_j. \quad (2.58)$$

In Eq. (2.58), the curvature velocity has been re-written in terms of the derivatives of the background magnetic field and plasma pressure p_0 through the magneto-hydrodynamic relation $\nabla p_0 = \mathbf{J}_0/c \times \mathbf{B}_0$, obtained from Eq. (1.22) in the limit of stationary solutions. The ratio between the thermal pressure to the magnetic one $\beta_p = 8\pi p_0/B_0^2$ and the plasma current \mathbf{J}_0 have been defined [119]. The general field-aligned Vlasov equation can be further reduced by defining the functions

$$\Gamma_i = \partial_i F_1 - \frac{q}{mv_{\parallel}} \partial_i \bar{\phi}_1 \frac{\partial F_0}{\partial v_{\parallel}} - \frac{\mu}{mv_{\parallel}} \partial_i \bar{B}_{1,\parallel} \frac{\partial F_0}{\partial v_{\parallel}}, \quad (2.59)$$

and

$$\hat{\partial}_i = \partial_i - \frac{\mu \partial_i B_0}{mv_{\parallel}} \frac{\partial}{\partial v_{\parallel}}, \quad (2.60)$$

and by neglecting the field-aligned derivatives of the perturbed quantities (here called G_1) when compared to the radial ones, e.g. $\partial_x G_1 + \frac{\gamma_3}{\gamma_1} \partial_z G_1 \sim \epsilon (1 + \epsilon) \approx \partial_x G_1$. This assumption is justified by the plasma fluctuation anisotropy. For a completely general background distribution function, the Vlasov equation reads in the field-

2.7 Field-aligned coordinate system

aligned coordinate system as

$$\begin{aligned}
& \frac{\partial g_1}{\partial t} + \frac{C}{JB_0} \left\{ v_{\parallel} \Gamma_z - \frac{\mu}{m} \partial_z B_0 \frac{\partial F_1}{\partial v_{\parallel}} \right\} \\
& + \frac{B_0 c}{B_{0,\parallel}^* C} \left\{ - \left[\frac{\mu B_0 + m v_{\parallel}^2}{q B_0} \left(\partial_y B_0 + \frac{\gamma_2}{\gamma_1} \partial_z B_0 \right) \right. \right. \\
& + \frac{v_{\parallel}^2 m}{q} \frac{\beta_p}{2} \frac{\left(\partial_y p_0 + \frac{\gamma_2}{\gamma_1} \partial_z p_0 \right)}{p_0} \hat{\partial}_x F_0 \\
& + \left. \left[\frac{\mu B_0 + m v_{\parallel}^2}{q B_0} \left(\partial_x B_0 - \frac{\gamma_3}{\gamma_1} \partial_z B_0 \right) \right. \right. \\
& + \frac{v_{\parallel}^2 m}{q} \frac{\beta_p}{2} \frac{\left(\partial_x p_0 - \frac{\gamma_3}{\gamma_1} \partial_z p_0 \right)}{p_0} \hat{\partial}_y F_0 \\
& + \left. \left[\frac{\mu B_0 + m v_{\parallel}^2}{q B_0} \left(\frac{\gamma_2}{\gamma_1} \partial_x B_0 + \frac{\gamma_3}{\gamma_1} \partial_y B_0 \right) \right. \right. \\
& + \frac{v_{\parallel}^2 m}{q} \frac{\beta_p}{2} \frac{\left(\frac{\gamma_2}{\gamma_1} \partial_x p_0 + \frac{\gamma_3}{\gamma_1} \partial_y p_0 \right)}{p_0} \hat{\partial}_z F_0 + \partial_x \bar{\xi}_1 \left(\hat{\partial}_y F_0 + \frac{\gamma_2}{\gamma_1} \hat{\partial}_z F_0 \right) \\
& - \partial_y \bar{\xi}_1 \left(\hat{\partial}_x F_0 - \frac{\gamma_3}{\gamma_1} \hat{\partial}_z F_0 \right) + \partial_x \bar{\xi}_1 \Gamma_y - \partial_y \bar{\xi}_1 \Gamma_x \\
& - \left. \left[\frac{\mu B_0 + m v_{\parallel}^2}{q B_0} \left(\partial_y B_0 + \frac{\gamma_2}{\gamma_1} \partial_z B_0 \right) + \frac{v_{\parallel}^2 m}{q} \frac{\beta_p}{2} \frac{\left(\partial_y p_0 + \frac{\gamma_2}{\gamma_1} \partial_z p_0 \right)}{p_0} \right] \Gamma_x \right. \\
& + \left. \left[\frac{\mu B_0 + m v_{\parallel}^2}{q B_0} \left(\partial_x B_0 - \frac{\gamma_3}{\gamma_1} \partial_z B_0 \right) \right. \right. \\
& + \frac{v_{\parallel}^2 m}{q} \frac{\beta_p}{2} \frac{\left(\partial_x p_0 - \frac{\gamma_3}{\gamma_1} \partial_z p_0 \right)}{p_0} \left. \right] \Gamma_y \right\} = 0. \tag{2.61}
\end{aligned}$$

The terms which contain a $y - z$ derivative of the background distribution function (which in a straight field lines geometry can be associated to centrifugal, Corio-

lis effects) are identically zero for a Maxwellian, assuming that the plasma temperatures and densities do not vary along the toroidal and binormal directions, i.e. $\partial_{y,z}n = \partial_{y,z}T = \partial_{y,z}p_0 = 0$. The latter assumption is valid if the poloidal (and/or toroidal for the case of stellarators) asymmetries of the background quantities are neglected. Furthermore, if the equilibrium distribution function F_0 is chosen to be a local Maxwellian, Eq. (2.61) reduces to the Vlasov equation known in literature [112, 92, 119, 120].

The parallel non-linearity can also be re-written in the field-aligned coordinate system. In the simplified electrostatic limit, it becomes

$$\frac{\partial F_2}{\partial t} = \left\{ qv_{||}\hat{b}_0 \cdot \nabla\bar{\phi}_1 + \frac{B_0}{B_{0,||}^*} [\mathbf{v}_E \cdot \mu \nabla B_0 + q(\mathbf{v}_{\nabla B} + \mathbf{v}_c) \cdot \nabla\bar{\phi}_1] \right\} \frac{1}{mv_{||}} \frac{\partial F_1}{\partial v_{||}}. \quad (2.62)$$

By employing the field-aligned representation for the drift-velocities \mathbf{v}_E , $\mathbf{v}_{\nabla B}$, \mathbf{v}_c (defined in Eqs. (2.36-2.38)) and the vector identity $(\mathbf{B}_0 \times \nabla B_0) \cdot \nabla\bar{\phi}_1 = -(\mathbf{B}_0 \times \nabla\bar{\phi}_1) \cdot \nabla B_0$, Eq. (2.62) can be written as

$$\frac{\partial F_2}{\partial t} = \left\{ \frac{q\mathcal{C}}{JmB_0} \partial_z\bar{\phi}_1 + \frac{cB_0}{B_0B_{0,||}^*} [\mathcal{K}_y \partial_y\bar{\phi}_1 + \mathcal{K}_x \partial_x\bar{\phi}_1] \right\} \frac{1}{mv_{||}} \frac{\partial F_1}{\partial v_{||}}. \quad (2.63)$$

In chapter 3 the parallel nonlinear term is benchmarked, for the first time, against the particle-in-cell (PIC) code ORB5 in the electrostatic limit with adiabatic electrons.

2.8 Normalisation

To facilitate the implementation of the general Vlasov-Maxwell coupled equations and improve numerical stability, a normalization is applied to establish dimensionless variables. For this purpose, all the physical quantities are split into a dimensionless value and a dimensional reference part. The latter reduces to the definition of a reference magnetic field B_{ref} , temperature T_{ref} , density n_{ref} , mass m_{ref} , length L_{ref} and the electron charge e . All the other quantities can be derived from the above parameters. In particular, we define the reference velocity $c_{\text{ref}} = \sqrt{T_{\text{ref}}/m_{\text{ref}}}$, frequency $\Omega_{\text{ref}} = eB_{\text{ref}}/m_{\text{ref}}c$ and reference gyroradius $\rho_{\text{ref}} = c_{\text{ref}}/\Omega_{\text{ref}}$. In the GENE code, the reference parameters are often chosen as the electron temperature and density, main ion mass, magnetic field on axis and either the major radius or minor radius of the device. However, different choices are also allowed by the code. With the standard GENE normalization, the derived reference quantities defined previously assume the physical equivalence of the sound speed for c_s , ion gyrofrequency for Ω_{ref} and Larmor radius for ρ_{ref} . Each of the physical quantities of Eq. (2.61) are normalised as follows

2.8 Normalisation

$$\begin{aligned}
x &= \rho_{\text{ref}} \hat{x}, & y &= \rho_{\text{ref}} \hat{y}, & z &= \hat{z}, \\
k_x &= \frac{1}{\rho_{\text{ref}}} \hat{k}_x, & k_y &= \frac{1}{\rho_{\text{ref}}} \hat{k}_y, & k_z &= \hat{k}_z, \\
\gamma_1 &= \hat{\gamma}_1, & \gamma_2 &= \frac{1}{L_{\text{ref}}} \hat{\gamma}_2, & \gamma_3 &= \frac{1}{L_{\text{ref}}} \hat{\gamma}_3, \\
\mathcal{C} &= B_{\text{ref}} \hat{\mathcal{C}}, & v_{\parallel} &= v_{th,j} c_{\text{ref}} \hat{v}_{\parallel}, & \mu &= \frac{T_{\text{ref}}}{B_{\text{ref}}} T_{0,j} \hat{\mu}, \\
B_0 &= B_{\text{ref}} \hat{B}_0, & B_{0,\parallel}^* &= B_{\text{ref}} \hat{B}_0, & t &= \frac{L_{\text{ref}}}{c_{\text{ref}}} \hat{t}.
\end{aligned} \tag{2.64}$$

Here, the radial profiles of each species, e.g. temperature and density, are normalised with respect to the reference position x_0 , i.e. $\hat{T} = T_0(x)/T_0(x_0)$ and $\hat{n} = n_0(x)/n_0(x_0)$. Furthermore, the spatial derivatives of background quantities are assumed to vary on macroscopic scales and hence normalised to L_{ref} . The fluctuating quantities, on the contrary, are assumed to change on a higher order in the gyrokinetic expansion and are normalised to ρ_{ref} . The velocity grids, as shown in Eq. (2.64), have a species dependent normalization. In particular, the parallel velocity coordinate v_{\parallel} is normalized to the thermal velocity of each species $v_{th,j} = \sqrt{2T_{0,j}(x_0)/m_j}$ evaluated at the specific reference position x_0 . The magnetic moment μ is instead normalized to each species temperature $T_{0,j}$ at the reference position x_0 . The particular choice to keep a species dependent normalization in the velocity space allows us to define the same grid box sizes for each species.

The different field components and distribution functions can be written as

$$\begin{aligned}
\phi_1 &= \frac{\rho_{\text{ref}}}{L_{\text{ref}}} \frac{T_{\text{ref}}}{e} \hat{\phi}_1, & A_{1,\parallel} &= \frac{\rho_{\text{ref}}}{L_{\text{ref}}} \rho_{\text{ref}} B_{\text{ref}} \hat{A}_{1,\parallel}, & B_{1,\parallel} &= \frac{\rho_{\text{ref}}}{L_{\text{ref}}} B_{\text{ref}} \hat{B}_{1,\parallel}, \\
F_0(x) &= \frac{n_{\text{ref}} n_{0,j}(x_0)}{c_{\text{ref}}^3 v_{th,j}^3(x_0)} \hat{F}_0(x), & g_1(x) &= \frac{\rho_{\text{ref}} n_{\text{ref}} n_{0,j}(x_0)}{L_{\text{ref}} c_{\text{ref}}^3 v_{th,j}^3(x_0)} \hat{g}_1(x).
\end{aligned} \tag{2.65}$$

Note, that the background distribution function F_0 is still kept as a general function, with the property that must fulfill the zero-order Vlasov equation, i.e. Eq. (2.43). Applying the aforementioned normalisation to Eq. (2.61) yields the dimensionless

Vlasov equation

$$\begin{aligned}
 & \frac{\partial g_1}{\partial t} + \frac{C}{JB_0} \left\{ v_{\parallel} v_{th} \Gamma_z - \frac{\mu v_{th}}{2} \partial_z B_0 \frac{\partial F_1}{\partial v_{\parallel}} \right\} \\
 & + \frac{B_0}{B_{0,\parallel}^*} \left\{ - \left[\frac{T_0 \mu B_0 + 2v_{\parallel}^2}{q B_0} \mathcal{K}_x + \frac{1}{C} \frac{T_0}{q} \frac{v_{\parallel}^2 \beta_{ref}}{B_0^2} \omega_{p,x} \right] \hat{\partial}_x F_0 \right. \\
 & - \left[\frac{T_0 \mu B_0 + 2v_{\parallel}^2}{q B_0} \mathcal{K}_y - \frac{1}{C} \frac{T_0}{q} \frac{v_{\parallel}^2 \beta_{ref}}{B_0^2} \omega_{p,y} \right] \hat{\partial}_y F_0 \\
 & - \left[\frac{T_0 \mu B_0 + 2v_{\parallel}^2}{q B_0} \mathcal{K}_z - \frac{1}{C} \frac{T_0}{q} \frac{v_{\parallel}^2 \beta_{ref}}{B_0^2} \omega_{p,z} \right] \hat{\partial}_z F_0 \\
 & - \frac{1}{C} \partial_x \bar{\xi}_1 \left(\hat{\partial}_y F_0 + \frac{\gamma_2}{\gamma_1} \hat{\partial}_z F_0 \right) + \frac{1}{C} \partial_y \bar{\xi}_1 \left(\hat{\partial}_x F_0 - \frac{\gamma_3}{\gamma_1} \hat{\partial}_z F_0 \right) \\
 & + \frac{1}{C} (\partial_x \bar{\xi}_1 \Gamma_y - \partial_y \bar{\xi}_1 \Gamma_x) + \left[\frac{T_0 \mu B_0 + 2v_{\parallel}^2}{q B_0} \mathcal{K}_x + \frac{1}{C} \frac{T_0}{q} \frac{v_{\parallel}^2 \beta_{ref}}{B_0^2} \omega_{p,x} \right] \Gamma_x \\
 & \left. + \left[\frac{T_0 \mu B_0 + 2v_{\parallel}^2}{q B_0} \mathcal{K}_y - \frac{1}{C} \frac{T_0}{q} \frac{v_{\parallel}^2 \beta_{ref}}{B_0^2} \omega_{p,y} \right] \Gamma_y \right\} = 0. \tag{2.66}
 \end{aligned}$$

Here, the following dimensionless quantities have been defined

$$\begin{aligned}
 \hat{\mathcal{K}}_x &= -\frac{1}{C} \frac{L_{ref}}{B_{ref}} \left(\partial_y B_0 + \frac{\gamma_2}{\gamma_1} \partial_z B_0 \right), \quad \hat{\omega}_{p,x} = -L_{ref} \left(\frac{\partial_y p_0}{p_0} + \frac{\gamma_2}{\gamma_1} \frac{\partial_z p_0}{p_0} \right), \\
 \hat{\mathcal{K}}_y &= \frac{1}{C} \frac{L_{ref}}{B_{ref}} \left(\partial_x B_0 - \frac{\gamma_3}{\gamma_1} \partial_z B_0 \right), \quad \hat{\omega}_{p,y} = -L_{ref} \left(\frac{\partial_x p_0}{p_0} + \frac{\gamma_2}{\gamma_1} \frac{\partial_z p_0}{p_0} \right), \tag{2.67}
 \end{aligned}$$

$$\begin{aligned}
 \hat{\mathcal{K}}_z &= \frac{1}{C} \frac{L_{ref}}{B_{ref}} \left(\frac{\gamma_2}{\gamma_1} \partial_x B_0 + \frac{\gamma_3}{\gamma_1} \partial_y B_0 \right), \quad \hat{\omega}_{p,z} = -L_{ref} \left(\frac{\gamma_2}{\gamma_1} \frac{\partial_y p_0}{p_0} + \frac{\gamma_3}{\gamma_1} \frac{\partial_x p_0}{p_0} \right), \\
 \hat{\partial}_{i\{x,y,z\}} &= -L_{ref} \left(\hat{\partial}_i - \frac{\mu}{2v_{\parallel}} \partial_i B_0 \frac{\partial}{\partial v_{\parallel}} \right), \tag{2.68}
 \end{aligned}$$

and $\beta_{ref} = 8\pi n_{ref} T_{ref}/B_{ref}^2$.

Moreover, the normalized parallel nonlinear term - derived in the electrostatic limit, i.e. $A_{1,\parallel} = B_{1,\parallel} = 0$ - reads as follows

$$\frac{\partial f_2}{\partial t} = \left\{ \frac{qC}{mv_{th} \mathcal{J} B_0} \partial_z \bar{\phi}_1 + \frac{v_{\parallel}}{B_{0,\parallel}^*} [\mathcal{K}_y \partial_y \bar{\phi}_1 + \mathcal{K}_x \partial_x \bar{\phi}_1] \right\} \frac{\partial f_1}{\partial v_{\parallel}}. \tag{2.69}$$

Here, $f_1 = g_1$ for $\beta_e = 0$. The dimensional units can be re-introduced with post-processing tools for direct comparisons with the experimental data. From the normalised Vlasov equation derived above it is possible to identify the different physical

2.8 Normalisation

contributions to the evolution of the perturbed distribution function of each species. In most of the usual tokamak plasma core conditions, turbulence can be studied in the simplified radially local case, i.e. $1/\rho_s^* \rightarrow \infty$. In particular, global effects are neglected to significantly reduce the computational cost of gyrokinetic simulations and the physical investigation is limited to a single magnetic surface. This simplified approach reduces the physical and numerical complexity of the system allowing the use of periodic boundary conditions and a Fourier decomposition in x and y . Eq. (2.66) can hence be written for each wave vector \mathbf{k} as

$$\frac{\partial g_{1,k}}{\partial t} = \mathcal{L}_{\parallel}[f_{1,k}] + \mathcal{L}_D[f_{1,k}] + \mathcal{L}_C[g_{1,k}] + \mathcal{L}_{diss}[f_{1,k}] + \mathcal{L}_{neo} + \mathcal{NL}[g_{1,k}, g_{1,k'}]. \quad (2.70)$$

Here, we have introduced the abbreviations: $\mathcal{L}_{\parallel}[f_{1,k}]$ for the parallel advection term; $\mathcal{L}_D[f_{1,k}]$ for the drive term due to the gradients of background distribution functions; $\mathcal{L}_C[g_{1,k}]$ for the x and y magnetic curvature terms. Moreover, $\mathcal{L}_{diss}[f_{1,k}]$ represents the dissipative terms, i.e. collisions and hyperdiffusivities; \mathcal{L}_{neo} the neoclassical terms and $\mathcal{NL}[g_{1,k}, g_{1,k'}]$ the mode-to-mode nonlinear coupling term which arises from the $\mathbf{E} \times \mathbf{B}_0$ nonlinear interaction. In details, these terms read as follows

$$\mathcal{L}_{\parallel}[f_{1,k}] = -\frac{C}{JB_0} \left\{ v_{\parallel} v_{th} \Gamma_z - \frac{\mu}{2} \partial_z B_0 \frac{\partial F_1}{\partial v_{\parallel}} \right\}, \quad (2.71)$$

$$\mathcal{L}_D[f_{1,k}] = -\frac{1}{\mathcal{C}} \partial_y \bar{\xi}_1 \left(\hat{\partial}_x F_0 - \frac{\gamma_3}{\gamma_1} \hat{\partial}_z F_0 \right), \quad (2.72)$$

$$\begin{aligned} \mathcal{L}_C[g_{1,k}] &= - \left[\frac{T_0}{q} \frac{\mu B_0 + 2v_{\parallel}^2}{B_0} \mathcal{K}_x + \frac{1}{\mathcal{C}} \frac{T_0}{q} \frac{v_{\parallel}^2 \beta_{ref}}{B_0^2} \omega_{p,x} \right] \Gamma_x \\ &\quad - \left[\frac{T_0}{q} \frac{\mu B_0 + 2v_{\parallel}^2}{B_0} \mathcal{K}_y - \frac{1}{\mathcal{C}} \frac{T_0}{q} \frac{v_{\parallel}^2 \beta_{ref}}{B_0^2} \omega_{p,y} \right] \Gamma_y, \end{aligned} \quad (2.73)$$

$$\mathcal{NL}[g_{1,k}, g_{1,k'}] = i \sum_{k'} \left[\left(k_x - k'_x \right) \xi_{1(k-k')} k'_y g_{1,k'} - \left(k_y - k'_y \right) \xi_{1(k-k')} k'_x g_{1,k'} \right]. \quad (2.74)$$

The so-called neoclassical term includes all the remaining terms of the Vlasov equation which do not contain any perturbed quantity. The latter is usually negligible in the tokamak plasma core [121].

2.9 Velocity moments for general backgrounds

In order to self-consistently treat the gyrokinetic Vlasov-Maxwell system of coupled equations, the fluctuating component of the fields must be evaluated from the perturbed distribution function of each plasma species at every time step. Therefore, a general description of the various F_1 velocity space moments appearing in the field equations is presented without making any assumptions on the background distribution function. The general a -th moment in v_{\parallel} and $b/2$ -th in μ (or, more precisely, b -th moment in v_{\perp}) in the guiding centre coordinate system $(\mathbf{X}, \theta, v_{\parallel}, \mu)$ is defined as follows

$$M_{a,b}(\mathbf{x}) = 2^{b/2} \left(\frac{B_0}{m} \right)^{b/2} \int \frac{B_{0,\parallel}^*}{m} \delta(\mathbf{X} + \mathbf{r} - \mathbf{x}) f_1^{gc}(\mathbf{X}, \theta, v_{\parallel}, \mu) v_{\parallel}^a \mu^{b/2} d^3 X dv_{\parallel} d\mu d\theta. \quad (2.75)$$

Here, $f_1^{gc}(\mathbf{X}, \theta, v_{\parallel}, \mu)$ denotes the perturbed distribution function in the guiding centre coordinate system and δ is the Dirac-delta function. The term $B_{0,\parallel}^*/m$ represents the Jacobian associated to the change in the coordinate system. The space transformation used to link the particle coordinates to the guiding centre is $\mathbf{x} = \mathbf{X} + \mathbf{r}(\mathbf{X}, \mu, \theta)$, where \mathbf{r} denotes the gyroradius vector (see Eq. (2.5)). As the time evolution of the perturbed distribution function (Eq. (2.66)) is performed in the gyro centre coordinate system it is necessary to define an operator T^* which transforms F_1 from the gyro centre to the guiding centre coordinate system. Up to the first order in the gyrokinetic expansion, as shown in Ref. [91, 113], the so-called pull-back operator can be written as follows

$$\begin{aligned} f_1^{gc}(\mathbf{X}, \theta, v_{\parallel}, \mu) &= T^* F_1(\mathbf{X}, v_{\parallel}, \mu) \\ &= F_1 + \frac{1}{B_0} \left\{ \left[\Omega \frac{\partial F_0}{\partial v_{\parallel}} - \frac{q}{c} v_{\parallel} \frac{\partial F_0}{\partial \mu} \right] (A_{1,\parallel}(\mathbf{X} + \mathbf{r}) - \bar{A}_{1,\parallel}(\mathbf{X})) \right. \\ &\quad \left. + [q(\phi_1(\mathbf{X} + \mathbf{r}) - \bar{\phi}_1(\mathbf{X})) - \mu \bar{B}_{1,\parallel}] \frac{\partial F_0}{\partial \mu} \right\}. \end{aligned} \quad (2.76)$$

The definition of B_0^* of Eq. (2.29) can be recast in terms of β as

$$\mathbf{B}_0^* = B_0 \left(\hat{b}_0 + \beta_e v_{\parallel} \frac{mv_{th}}{2qB_0^2} \mathbf{J} \right). \quad (2.77)$$

Typically, in magnetic confined plasma β_e is less than few percent and the plasma current is usually small. Therefore, the contribution of the second term in Eq. (2.77)

2.9 Velocity moments for general backgrounds

is neglected. In the rest of this work $B_0^* \simeq B_0$ will be assumed. By performing the integrals over θ and \mathbf{X} and using the previously defined operator, the generic moment of the gyro centre distribution function reduces to

$$\begin{aligned} M_{a,b}(\mathbf{x}) = & \pi \left(\frac{2B_0}{m} \right)^{b/2+1} \int \left\{ \langle F_1(\mathbf{x} - \mathbf{r}) \rangle \right. \\ & + \left(\frac{\Omega}{B_0} \frac{\partial F_0}{\partial v_{||}} - \frac{q}{cB_0} v_{||} \frac{\partial F_0}{\partial \mu} \right) (A_{1,||}(\mathbf{x}) - \langle \bar{A}_{1,||}(\mathbf{x} - \mathbf{r}) \rangle) \\ & \left. + \left[\frac{q}{B_0} (\phi_1(\mathbf{x}) - \langle \bar{\phi}_1(\mathbf{x} - \mathbf{r}) \rangle) - \frac{\mu}{B_0} \langle \bar{B}_{1,||}(\mathbf{x} - \mathbf{r}) \rangle \right] \frac{\partial F_0}{\partial \mu} \right\} v_{||}^a \mu^{b/2} dv_{||} d\mu. \end{aligned} \quad (2.78)$$

Here, a double gyroaveraged operator $\langle \bar{\phi}_1(\mathbf{x} - \mathbf{r}) \rangle$ is introduced. It is defined accordingly to Ref. [93] as follows

$$\begin{aligned} \langle \bar{\phi}_1(\mathbf{x} - \mathbf{r}) \rangle &= \mathcal{G}^\dagger [\phi_1(\mathbf{x} - \mathbf{r})] \mathcal{G} \\ &= \frac{1}{4\pi^2} \oint_0^{2\pi} d\theta \int d\mathbf{X} \delta(\mathbf{X} + \mathbf{r}(\theta) - \mathbf{x}) \oint_0^{2\pi} d\theta' \phi_1(\mathbf{X} + \mathbf{r}(\theta')) d\theta' \end{aligned} \quad (2.79)$$

In normalised units Eq. (2.78) reads

$$\begin{aligned} M_{a,b}(\mathbf{x}) = & n_{\text{ref}} n_0 c_{\text{ref}}^{a+b} v_{th}^{a+b} \frac{\rho_{\text{ref}}}{L_{\text{ref}}} \left\{ \pi B_0^{b/2+1} \int \langle F_1(\mathbf{x} - \mathbf{r}) \rangle v_{||}^a \mu^{b/2} dv_{||} d\mu \right. \\ & + \frac{2q\pi B_0^{b/2}}{mv_{th}} \int \left(\frac{B_0}{2} \frac{\partial F_0}{\partial v_{||}} - v_{||} \frac{\partial F_0}{\partial \mu} \right) (A_{1,||}(\mathbf{x}) - \langle \bar{A}_{1,||}(\mathbf{x} - \mathbf{r}) \rangle) v_{||}^a \mu^{b/2} dv_{||} d\mu \\ & \left. + \pi B_0^{b/2} \int \left[\frac{q}{T_0} (\phi_1(\mathbf{x}) - \langle \bar{\phi}_1(\mathbf{x} - \mathbf{r}) \rangle) - \mu \langle \bar{B}_{1,||}(\mathbf{x} - \mathbf{r}) \rangle \right] \frac{\partial F_0}{\partial \mu} v_{||}^a \mu^{b/2} dv_{||} d\mu \right\}. \end{aligned} \quad (2.80)$$

In the specific case of a Maxwellian background, Eq. (2.80) can be greatly simplified, i.e. the term that multiplies the vector potential is exactly zero [89]. As it will be shown in the next sections, the latter simplification leads to a decoupling between the Poisson and $B_{1,||}$ equations with the parallel component of the Ampère's. This is not necessarily the case for non-Maxwellian distribution functions.

2.10 Field equations

Information on the single plasma species turbulent dynamics can be obtained by solving the Vlasov equation introduced in the previous section. The latter, however, is coupled to the field equations and needs to be solved self-consistently. The analytical derivation of each of these field equations is performed in the next sections. To account for different approaches in treating the gyroaverage operators and boundary conditions, two limits of the gyrokinetic formalism will be studied, i.e. radially local and global. In the former case, the gyroaverage operator \mathcal{G} can be expressed as a diagonal gyromatrix. Periodic boundary conditions are assumed in the radial direction allowing for a Fourier expansion in x . In this limit the gyroaverage operator can be represented in terms of Bessel functions. In particular,

$$\langle \phi_1 \rangle = J_0(\lambda)\phi_1, \quad \langle \bar{\phi}_1 \rangle = J_0^2(\lambda)\phi_1, \quad (2.81)$$

$$\langle A_1 \rangle = J_0(\lambda)A_1, \quad \langle \bar{A}_1 \rangle = J_0^2(\lambda)A_1, \quad (2.82)$$

$$\langle B_{1,\parallel} \rangle = J_0(\lambda)B_{1,\parallel}, \quad \langle \bar{B}_{1,\parallel} \rangle = I_1(\lambda)J_0(\lambda)B_{1,\parallel}, \quad (2.83)$$

with $I_1 = \frac{qv_{th}}{k_{\perp}T_0}\sqrt{\frac{B_0}{\mu}}J_1$ and $\lambda = \frac{k_{\perp}}{\Omega}\sqrt{\frac{2B_0\mu}{m}}$. Furthermore J_0 and J_1 are respectively the zero and first order Bessel functions. See Ref. [93] for the derivation of the previous identities. Furthermore, it will be shown that the equation for $B_{1,\parallel}$ involves significantly more complicated operations to remove the poloidal dependence from the field equation. To simplify the analytical derivation and the numerical implementation, the field equation for $B_{1,\parallel}$ is derived only on a single magnetic surface by assuming periodic radial boundary conditions. The impact of the parallel magnetic fluctuations on the physical results is expected to be negligible for most of the standard tokamak plasma core conditions, as already considered to approximate $B_0 \sim B_{0,\parallel}^*$.

2.11 Poisson's equation

The evolution of the electrostatic field component ϕ_1 is given by the Poisson equation

$$\nabla^2\phi_1(\mathbf{x}) = -4\pi \sum_s q_s n_{1,s}(\mathbf{x}). \quad (2.84)$$

It relates the electrostatic potential ϕ_1 to the total charge density $\rho = \sum_s q_s n_{1,s}$, which can be re-written in terms of the zero-order moment of the perturbed distribution function of each species $M_{0,0}$ as

$$\nabla^2\phi_1(\mathbf{x}) = -4\pi \sum_s q_s M_{0,0,s}(\mathbf{x}). \quad (2.85)$$

2.11 Poisson's equation

For better readability the sum over all the plasma species is omitted in the following. Employing Eq. (2.78) for the $(0, 0)$ velocity space moment a more explicit expression for the Poisson equation can be obtained, which reads

$$\begin{aligned} \nabla_{\perp}^2 \phi_1(\mathbf{x}) = & -\frac{8\pi^2 q B_0}{m} \int \left\{ \langle F_1(\mathbf{x} - \mathbf{r}) \rangle \right. \\ & + \left(\frac{\Omega}{B_0} \frac{\partial F_0}{\partial v_{\parallel}} - \frac{q}{c B_0} v_{\parallel} \frac{\partial F_0}{\partial \mu} \right) (A_{1,\parallel}(\mathbf{x}) - \langle \bar{A}_{1,\parallel}(\mathbf{x} - \mathbf{r}) \rangle) \\ & \left. + \left[\frac{q}{B_0} (\phi_1(\mathbf{x}) - \langle \bar{\phi}_1(\mathbf{x} - \mathbf{r}) \rangle) - \frac{\mu}{B_0} \langle \bar{B}_{1,\parallel}(\mathbf{x} - \mathbf{r}) \rangle \right] \frac{\partial F_0}{\partial \mu} \right\} dv_{\parallel} d\mu. \end{aligned} \quad (2.86)$$

The parallel derivatives have been neglected when compared to the perpendicular ones, i.e. $\nabla^2 \sim \nabla_{\perp}^2$ by assuming the high anisotropy of plasma fluctuations.

Local limit

In the radially local limit, the normalised Poisson field equation including the $B_{1,\parallel}$ contribution reads

$$P\phi_1(\mathbf{x}) + \mathcal{F}A_{1,\parallel}(\mathbf{x}) + \mathcal{T}B_{1,\parallel}(\mathbf{x}) = q\pi n_0 B_0 \int J_0 g_1(\mathbf{x}) dv_{\parallel} d\mu, \quad (2.87)$$

where

$$P = k_{\perp}^2 \lambda_{De}^2 - \frac{\pi q^2 n_0}{T_0} \int (1 - J_0^2) \frac{\partial F_0}{\partial \mu} dv_{\parallel} d\mu, \quad (2.88)$$

$$\mathcal{F} = \frac{2\pi q^2 n_0}{mv_{th}} \int \left[(1 - J_0^2) v_{\parallel} \frac{\partial F_0}{\partial \mu} - \frac{B_0}{2} \frac{\partial F_0}{\partial v_{\parallel}} \right] dv_{\parallel} d\mu, \quad (2.89)$$

$$\mathcal{T} = \pi q n_0 \int \mu J_0 I_1 \frac{\partial F_0}{\partial \mu} dv_{\parallel} d\mu, \quad (2.90)$$

with the previously defined J_0 and I_1 operators and the normalised Debye length $\lambda_{De} = \lambda_{De}/\rho_{ref} = \sqrt{\frac{T_{ref}}{4\pi\rho_{ref}^2 n_{ref} q_{ref}^2}}$.

Global formalism

In the radially global limit, the Poisson field equation can be expressed in normalised units as

$$P\phi_1(\mathbf{x}) + \mathcal{F}A_{1,\parallel}(\mathbf{x}) = q\pi B_0 \int \mathcal{G}(n_0 g_1(\mathbf{x})) dv_\parallel d\mu. \quad (2.91)$$

The parallel component of the perturbed magnetic field $B_{1,\parallel}$ has been neglected, as discussed previously. Here, the following operators have been introduced

$$P = -\nabla_\perp^2 \lambda_{De}^2 - \pi q^2 \int \left[\frac{n_0}{T_0} \frac{\partial F_0}{\partial \mu} \hat{\mathbf{1}} - \mathcal{G}^\dagger \left(\frac{n_0}{T_0} \frac{\partial F_0}{\partial \mu} \right) \mathcal{G} \right] dv_\parallel d\mu, \quad (2.92)$$

$$\mathcal{F} = \frac{2\pi q^2}{m} \left\{ \frac{n_0}{v_{th}} \int \left[v_\parallel \frac{\partial F_0}{\partial \mu} - \frac{B_0}{2} \frac{\partial F_0}{\partial v_\parallel} \right] \hat{\mathbf{1}} dv_\parallel d\mu - \int \mathcal{G}^\dagger \left(v_\parallel \frac{n_0}{v_{th}} \frac{\partial F_0}{\partial \mu} \right) \mathcal{G} dv_\parallel d\mu \right\}, \quad (2.93)$$

where $\hat{\mathbf{1}}$ is the unit tensor. In Eqs. (2.92-2.93) the double gyroaveraged operators acting on the different field components have been replaced with the general expression defined in Eq. (2.79) $\langle \bar{g}(\mathbf{x} - \mathbf{r}) \rangle = \mathcal{G}^\dagger g(x) \mathcal{G}$, which holds true for every fixed k_y mode component. By employing a Maxwellian background distribution function Eqs. (2.87-2.91) reduce to the standard Poisson equation for Maxwellian backgrounds with $\mathcal{F} = 0$ [89].

2.12 Ampère's law for $A_{1,\parallel}$

Using the Coulomb gauge and in the absence of equilibrium electric fields, the Ampère's law for the parallel component of the vector potential $A_{1,\parallel}$ can be written as

$$\nabla_\perp^2 A_{1,\parallel}(\mathbf{x}) = -\frac{4\pi q}{c} M_{1,0}(\mathbf{x}). \quad (2.94)$$

Due to the gyrokinetic ordering, the parallel fluctuations have been neglected when compared to the perpendicular ones. Employing the $(1, 0)$ velocity space moment of Eq. (2.66), the Ampère's law for the parallel component of the vector potential reads

$$\begin{aligned} \nabla_\perp^2 A_{1,\parallel}(\mathbf{x}) &= -\frac{8\pi^2 q}{mc} \int \left\{ \langle F_1(\mathbf{x} - \mathbf{r}) \rangle + \left(\Omega \frac{\partial F_0}{\partial v_\parallel} - \frac{q}{c} v_\parallel \frac{\partial F_0}{\partial \mu} \right) (A_{1,\parallel}(\mathbf{x}) - \langle \bar{A}_{1,\parallel}(\mathbf{x} - \mathbf{r}) \rangle) \right. \\ &\quad \left. + [q(\phi_1(\mathbf{x}) - \langle \bar{\phi}_1(\mathbf{x} - \mathbf{r}) \rangle) - \mu \langle \bar{B}_{1,\parallel}(\mathbf{x} - \mathbf{r}) \rangle] \frac{\partial F_0}{\partial \mu} \right\} v_\parallel dv_\parallel d\mu. \end{aligned} \quad (2.95)$$

This equation is valid for general background distribution functions.

2.12 Ampère's law for $A_{1,\parallel}$

Local limit

In normalised units, Eq. (2.102) becomes

$$\mathcal{L}\phi_1(\mathbf{x}) + \mathcal{H}A_{1,\parallel}(\mathbf{x}) + \mathcal{K}B_{1,\parallel}(\mathbf{x}) = qn_0\pi\beta_{\text{ref}}\frac{B_0v_{th}}{2}\int v_{\parallel}J_0g_1(\mathbf{x})dv_{\parallel}d\mu, \quad (2.96)$$

with the local expression for the previously defined operators

$$\mathcal{L} = \frac{q^2n_0\pi\beta_{\text{ref}}}{mv_{th}}\int \frac{\partial F_0}{\partial\mu}(1 - J_0^2)v_{\parallel}dv_{\parallel}d\mu, \quad (2.97)$$

$$\mathcal{H} = k_{\perp}^2 - \frac{q^2n_0\pi\beta_{\text{ref}}}{m}\int \left[B_0\frac{v_{\parallel}}{2}\frac{\partial F_0}{\partial v_{\parallel}} - v_{\parallel}^2\frac{\partial F_0}{\partial\mu}(1 - J_0^2)\right]dv_{\parallel}d\mu, \quad (2.98)$$

$$\mathcal{K} = \frac{v_{th}}{2}\int J_0I_1v_{\parallel}\mu\frac{\partial F_0}{\partial\mu}dv_{\parallel}d\mu. \quad (2.99)$$

Global formalism

In normalised units, Eq. (2.95) becomes

$$\mathcal{L}\phi_1(\mathbf{x}) + \mathcal{H}A_{1,\parallel}(\mathbf{x}) = q\pi\beta_{\text{ref}}\frac{B_0}{2}\int v_{\parallel}\mathcal{G}(n_0v_{th}g_1(\mathbf{x}))dv_{\parallel}d\mu. \quad (2.100)$$

Here, the following operators have been defined

$$\mathcal{L} = \frac{q^2\pi\beta_{\text{ref}}}{m}\int v_{\parallel}\left[\frac{n_0}{v_{th}}\frac{\partial F_0}{\partial\mu}\hat{\mathbf{1}} - \mathcal{G}^{\dagger}\left(\frac{n_0}{v_{th}}\frac{\partial F_0}{\partial\mu}\right)\mathcal{G}\right]dv_{\parallel}d\mu, \quad (2.101)$$

$$\mathcal{H} = -\nabla_{\perp}^2 - \frac{q^2\pi\beta_{\text{ref}}}{m}\left\{n_0\int\left[B_0\frac{v_{\parallel}}{2}\frac{\partial F_0}{\partial v_{\parallel}} - v_{\parallel}^2\frac{\partial F_0}{\partial\mu}\right]\hat{\mathbf{1}}dv_{\parallel}d\mu + \int v_{\parallel}^2\mathcal{G}^{\dagger}\left(n_0\frac{\partial F_0}{\partial\mu}\right)\mathcal{G}dv_{\parallel}d\mu\right\}. \quad (2.102)$$

Employing a Maxwellian background distribution function, Eqs. (2.96-2.100) reduce to standard Ampère's law for Maxwellian backgrounds, i.e. $\mathcal{L} = \mathcal{K} = 0$ and $A_{1,\parallel}$ decouples from the other field equations [89]. It is worth noting that the $A_{1,\parallel}(\mathbf{x})$ contribution is zero if $\beta_{\text{ref}} = 0$.

2.13 Ampère's law for $A_{1,\perp}$

The equation for the perpendicular component of the vector potential $A_{1,\perp}$ is here derived only on a single magnetic surface, i.e. in the so-called local limit. It can be written in terms of the parallel magnetic fluctuations

$$\begin{aligned} (\nabla \times \mathbf{B}_1)_\perp &= (\partial_y B_{1,\parallel} - \partial_z B_{1,y}) \hat{e}_1 + (\partial_x B_{1,\parallel} - \partial_z B_{1,x}) \hat{e}_2 \\ &= \frac{4\pi}{c} \mathbf{J}_{1,\perp}. \end{aligned} \quad (2.103)$$

Eq. (2.103) can be expressed in terms of the $(0, 1)$ velocity space moment of the perturbed distribution function as

$$\hat{e}_1 \partial_y B_{1,\parallel} + \hat{e}_2 \partial_x B_{1,\parallel} = \frac{4\pi q}{c} \mathbf{M}_{0,1}(\mathbf{x}). \quad (2.104)$$

Here, the parallel derivatives have been once again neglected when compared to the perpendicular ones and the velocity space moment of the perturbed distribution function $\mathbf{M}_{0,1}$ has been written in the poloidal plane

$$\mathbf{M}_{0,1}(\mathbf{x}) = \int \delta(\mathbf{X} + \mathbf{r} - \mathbf{x}) \hat{c}(\theta) T^* F_1 \frac{B_{0,\parallel}^*}{m} v_\perp d^3 X dv_\parallel d\mu d\theta. \quad (2.105)$$

Employing Eq. (2.80) for $\mathbf{M}_{0,1}$ and assuming $B_0^* \simeq B_0$, the perpendicular component of the Ampère's law can be written as

$$\begin{aligned} \hat{e}_1 \partial_y B_{1,\parallel} + \hat{e}_2 \partial_x B_{1,\parallel} &= \frac{8\pi^2 q}{mc} \left(\frac{2B_0}{m} \right)^{\frac{1}{2}} \left\{ B_0 \int \sqrt{\mu} \langle \hat{c}(\theta) g_1(\mathbf{x} - \mathbf{r}) \rangle dv_\parallel d\mu d\theta \right. \\ &\quad + \frac{q}{c} \int \sqrt{\mu} \hat{c}(\theta) \left(\frac{B_0}{m} \frac{\partial F_0}{\partial v_\parallel} - v_\parallel \frac{\partial F_0}{\partial \mu} \right) A_{1,\parallel} dv_\parallel d\mu d\theta \\ &\quad + \frac{q}{c} \int \sqrt{\mu} v_\parallel \hat{c}(\theta) \frac{\partial F_0}{\partial \mu} \langle \hat{c}(\theta) \bar{A}_{1,\parallel} \rangle dv_\parallel d\mu d\theta \\ &\quad \left. + \int \sqrt{\mu} \frac{\partial F_0}{\partial \mu} [q (\hat{c}(\theta) \phi_1 - \langle \hat{c}(\theta) \bar{\phi}_1 \rangle) - \mu \langle \hat{c}(\theta) \bar{B}_{1,\parallel} \rangle] dv_\parallel d\mu d\theta \right\}. \end{aligned} \quad (2.106)$$

Since the background distribution function varies on macroscopic scales, which are assumed to be several order of magnitude larger than the gyroradius, it is possible to perform the following simplification for the gyro averaging $\langle \dots F_0(\mathbf{r} - \mathbf{x}) \rangle = \langle \dots \rangle F_0(\mathbf{r} - \mathbf{x})$. The same property holds for the velocity background distribution

2.14 Solution of the field equations

function derivatives. Eq. (2.106) can hence be greatly simplified. All the terms of the form: $\int_0^{2\pi} \hat{c}(\theta) \psi(\mathbf{x}) d\theta$ vanish and Eq. (2.106) reduces to

$$\begin{aligned} \hat{e}_1 \partial_y B_{1,\parallel} + \hat{e}_2 \partial_x B_{1,\parallel} &= \frac{4\pi q}{c} \left\{ \left(\frac{2B_0}{m} \right)^{\frac{1}{2}} \frac{2\pi B_0}{m} \int \sqrt{\mu} \langle \hat{c}(\theta) g_1(\mathbf{x} - \mathbf{r}) \rangle dv_{\parallel} d\mu d\theta \right. \\ &\quad + \left(\frac{2B_0}{m} \right)^{\frac{1}{2}} \frac{2\pi q}{mc} \int \sqrt{\mu} v_{\parallel} \hat{c}(\theta) \frac{\partial F_0}{\partial \mu} \langle \hat{c}(\theta) \bar{A}_{1,\parallel} \rangle dv_{\parallel} d\mu d\theta \\ &\quad \left. - \left(\frac{2B_0}{m} \right) \frac{2\pi}{m} \int \sqrt{\mu} \frac{\partial F_0}{\partial \mu} [q \langle \hat{c}(\theta) \bar{\phi}_1 \rangle + \mu \langle \hat{c}(\theta) \bar{B}_{1,\parallel} \rangle] dv_{\parallel} d\mu d\theta \right\}. \end{aligned} \quad (2.107)$$

The normalized equation for the parallel magnetic fluctuation $B_{1,\parallel}$ is

$$\mathcal{R}\phi_1(\mathbf{x}) + \mathcal{W}A_{1,\parallel}(\mathbf{x}) + \mathcal{Q}B_{1,\parallel}(\mathbf{x}) = B_0^{\frac{3}{2}} \frac{q\pi n_0 v_{th}}{2k_{\perp}} \beta_{ref} \int \sqrt{\mu} J_1 g_1(\mathbf{x}) dv_{\parallel} d\mu. \quad (2.108)$$

Here, the following operators have been defined

$$\mathcal{R} = q\pi n_0 \int \mu \frac{\partial F_0}{\partial \mu} I_1 J_0 dv_{\parallel} d\mu, \quad (2.109)$$

$$\mathcal{W} = -\frac{qT_0 n_0 \pi}{mv_{th}} \int v_{\parallel} \mu I_1 J_0 \frac{\partial F_0}{\partial \mu} dv_{\parallel} d\mu, \quad (2.110)$$

and

$$\mathcal{Q} = -\frac{1}{\beta_{ref}} + \frac{\pi T_0 n_0}{2} \int \mu^2 I_1^2 \frac{\partial F_0}{\partial \mu} dv_{\parallel} d\mu. \quad (2.111)$$

It is worth noticing that $\mathcal{R} = \mathcal{T}$.

2.14 Solution of the field equations

The field equations involving non-Maxwellian background distribution functions constitute a linear system of three coupled equations. It decouples for the parallel component of the vector potential $A_{1,\parallel}$ only for the case of Maxwellian distributions. In a matrix form, the local field system of equations can be written as $\mathcal{C} \cdot (\phi_1, A_{1,\parallel}, B_{1,\parallel}) = \mathcal{M}$, i.e.

$$\begin{pmatrix} \mathcal{P} & \mathcal{F} & \mathcal{T} \\ \mathcal{L} & \mathcal{H} & \mathcal{K} \\ \mathcal{R} & \mathcal{W} & \mathcal{Q} \end{pmatrix} \cdot \begin{pmatrix} \phi_1 \\ A_{1,\parallel} \\ B_{1,\parallel} \end{pmatrix} = \begin{pmatrix} N_{00} \\ N_{10} \\ N_{01} \end{pmatrix}, \quad (2.112)$$

where the functions

$$N_{00} = q\pi n_0 B_0 \int J_0 g_1(\mathbf{x}) dv_{||} d\mu, \quad (2.113)$$

$$N_{10} = qn_0 \pi \beta_{ref} \frac{B_0 v_{th}}{2} \int v_{||} J_0 g_1(\mathbf{x}) dv_{||} d\mu, \quad (2.114)$$

$$N_{01} = B_0^{\frac{3}{2}} \frac{q\pi n_0 v_{th}}{2k_{\perp}} \beta_{ref} \int \sqrt{\mu} J_1 g_1(\mathbf{x}) dv_{||} d\mu, \quad (2.115)$$

have been defined. It is possible to solve this system of coupled equation through the inversion of the matrix \mathcal{C} as

$$\begin{pmatrix} \phi_1 \\ A_{1,||} \\ B_{1,||} \end{pmatrix} = \frac{1}{det\mathcal{C}} \begin{pmatrix} \mathcal{H}\mathcal{Q} - \mathcal{K}\mathcal{W} & \mathcal{T}\mathcal{W} - \mathcal{F}\mathcal{Q} & \mathcal{F}\mathcal{K} - \mathcal{T}\mathcal{H} \\ \mathcal{K}\mathcal{T} - \mathcal{L}\mathcal{Q} & \mathcal{P}\mathcal{Q} - \mathcal{T}^2 & \mathcal{T}\mathcal{L} - \mathcal{P}\mathcal{K} \\ \mathcal{L}\mathcal{W} - \mathcal{H}\mathcal{T} & \mathcal{F}\mathcal{T} - \mathcal{P}\mathcal{W} & \mathcal{P}\mathcal{H} - \mathcal{F}\mathcal{L} \end{pmatrix} \begin{pmatrix} N_{00} \\ N_{10} \\ N_{01} \end{pmatrix}, \quad (2.116)$$

where

$$det\mathcal{C} = \frac{1}{\mathcal{P}\mathcal{H}\mathcal{Q} + \mathcal{L}\mathcal{W}\mathcal{T} + \mathcal{T}\mathcal{F}\mathcal{K} - \mathcal{P}\mathcal{W}\mathcal{K} - \mathcal{H}\mathcal{T}^2 - \mathcal{L}\mathcal{F}\mathcal{Q}}. \quad (2.117)$$

For a completely general background distribution function each component of the fields is coupled to the others. This system decouples for the $A_{1,||}$ component if a Maxwellian distribution functions is chosen, since $\mathcal{F} = \mathcal{W} = \mathcal{L} = \mathcal{K} = 0$. Furthermore, for equivalent Maxwellian backgrounds $\mathcal{R} = \mathcal{T}$ and the field equations can be written as

$$\begin{pmatrix} \phi_1 \\ A_{1,||} \\ B_{1,||} \end{pmatrix} = \begin{pmatrix} \frac{\mathcal{Q}}{\mathcal{P}\mathcal{Q}-\mathcal{T}^2} & 0 & \frac{\mathcal{T}}{\mathcal{T}^2-\mathcal{P}\mathcal{Q}} \\ 0 & \frac{1}{\mathcal{H}} & 0 \\ \frac{\mathcal{T}}{\mathcal{P}\mathcal{Q}-\mathcal{T}^2} & 0 & \frac{\mathcal{P}}{\mathcal{P}\mathcal{Q}-\mathcal{T}^2} \end{pmatrix} \begin{pmatrix} N_{00} \\ N_{10} \\ N_{01} \end{pmatrix}. \quad (2.118)$$

The schematic solution of the field equations in the radially global case can be written in the same matrix formalism as the local one in the limit of $B_{1,||} = 0$.

2.15 Observables

The solution of the Vlasov equation for each species gives detailed information on the turbulence properties of the system. However, for a more direct comparison between

2.15 Observables

the numerical, analytical results and experimental data, it is necessary to link the perturbed distribution functions to macroscopic observables. The normalized density $n_{1,s}$ and parallel and perpendicular pressure $p_{1,s}$ fluctuations can be derived [122] as

$$n_{1,s} = \int F_{1,s}(\mathbf{x}, \mathbf{v}) d^3 v \equiv M_{0,0}(\mathbf{x}), \quad (2.119)$$

$$p_{1,\parallel,s} = n_{1,\parallel,s} T_{0,\parallel,s} + n_{0,\parallel,s} T_{1,\parallel,s} \equiv \frac{m}{2} \int (v_\parallel - u_{1,\parallel})^2 F_{1,s}(\mathbf{x}, \mathbf{v}) d^3 v, \quad (2.120)$$

$$p_{1,\perp,s} = n_{1,\perp,s} T_{0,\perp,s} + n_{0,\perp,s} T_{1,\perp,s} \equiv \frac{m}{2} \int v_\perp^2 F_{1,s}(\mathbf{x}, \mathbf{v}) d^3 v, \quad (2.121)$$

where the parallel velocity fluctuations

$$u_{1,\parallel} \equiv \frac{1}{n_0} \int v_\parallel F_{1,s}(\mathbf{x}, \mathbf{v}) d^3 v = \frac{M_{10}}{n_0}, \quad (2.122)$$

have been defined. Other important observables usually introduced in gyrokinetic theory are radial particle and heat fluxes. They are linked to plasma confinement and measure the radial particle and energy advection due to the $\mathbf{E} \times \mathbf{B}$ velocity $\mathbf{v}_E = \frac{c}{B_0^2} (\mathbf{B}_0 \times \nabla \xi_1)$. Positive values denote radially outward directed fluxes and hence a consequent degradation in plasma confinement. They are defined as

$$\langle \Gamma_{1,s} \rangle_V = \int \mathbf{v}_{E_{\parallel x}} F_{1,s}(\mathbf{x}, \mathbf{v}) d^3 v, \quad (2.123)$$

$$\langle Q_{1,s} \rangle_V = \frac{m}{2} \int \mathbf{v}_{E_{\parallel x}} v^2 F_{1,s}(\mathbf{x}, \mathbf{v}) d^3 v. \quad (2.124)$$

Here, $\langle \dots \rangle_V$ represents the average over the volume V within a given flux-surface at a given radial position and $\mathbf{v}_{E_{\parallel x}}$, the radial component of the $\mathbf{E} \times \mathbf{B}$ velocity. Eqs. (2.123-2.124) can be expressed in terms of the moments of the perturbed distribution functions and split in the electrostatic and electromagnetic counterparts which (in the local limit) read as

$$\langle \Gamma_{1,s}^{(es)} \rangle_V = -\frac{ik_y}{C} \frac{\rho_{\text{ref}}^2 c_{\text{ref}} n_{\text{ref}}}{L_{\text{ref}}^2} n_0 \phi_{1,k} M_{00}^{*,(es)}, \quad (2.125)$$

$$\langle \Gamma_{1,s}^{(em)} \rangle_V = -\frac{ik_y}{C} \frac{\rho_{\text{ref}}^2 c_{\text{ref}} n_{\text{ref}}}{L_{\text{ref}}^2} n_0 \left[\phi_{1,k} M_{00}^{*,(em)} - v_{th} A_{1,\parallel,k} M_{10}^{*,(em)} + \frac{T_0}{qB_0} B_{1,\parallel,k} N_{00}^{*,(em)} \right], \quad (2.126)$$

2. Gyrokinetic theory

$$\langle Q_{1,s}^{(es)} \rangle_V = -\frac{ik_y}{\mathcal{C}} p_{\text{ref}} c_{\text{ref}} \frac{\rho_{\text{ref}}^2}{L_{\text{ref}}^2} p_0 \left[M_{20}^{*(es)} + M_{02}^{*(es)} \right], \quad (2.127)$$

$$\begin{aligned} \langle Q_{1,s}^{(em)} \rangle_V &= -\frac{ik_y}{\mathcal{C}} p_{\text{ref}} c_{\text{ref}} \frac{\rho_{\text{ref}}^2}{L_{\text{ref}}^2} p_0 \left\{ \phi_{1,k} \left[M_{20}^{*(em)} + M_{02}^{*(em)} \right] \right. \\ &\quad \left. - v_{th} A_{1,\parallel,k} \left[M_{30}^{*(em)} + M_{12}^{*(em)} \right] + \frac{1}{qB_0} B_{1,\parallel,k} \left[N_{20}^{*(em)} + N_{02}^{*(em)} \right] \right\}. \end{aligned} \quad (2.128)$$

Here, all the moments of the perturbed distribution function F_1 - defined in Eq. (2.80) - have been split in an electrostatic $M_{ab}^{(es)}$ (containing ϕ_1) and electromagnetic $M_{ab}^{(em)}$ (containing $A_{1,\parallel}$ and $B_{1,\parallel}$). Furthermore, '*' denotes the complex conjugate and $N_{a,b}$ the modified moments of the perturbed distribution function, defined in normalised units as

$$N_{a,b} = \frac{\rho_{\text{ref}}}{L_{\text{ref}}} p_{\text{ref}} p_0 (c_{\text{ref}} v_{th})^{(a+b)} \pi B_0^{\frac{b}{2}+1} \int dv_{\parallel} d\mu v_{\parallel}^a \mu^{\frac{b}{2}+1} B_0 I_1 h_1. \quad (2.129)$$

In Eq. (2.129), the function I_1 represents the first order modified Bessel function. Moreover, the generalized perturbed distribution function h_1 , often referred to as non adiabatic part of f_1 , has been introduced. For a general background distribution function, it is defined as

$$h_1 = f_1 - \frac{q}{B_0 T_0} \bar{\phi}_1 \frac{\partial F_0}{\partial \mu} - \frac{\mu}{B_0} I_1 \frac{\partial F_0}{\partial \mu} \bar{B}_{1,\parallel} - \frac{qv_{th}}{B_0 T_0} \left(\frac{B_0}{2} \frac{\partial F_0}{\partial v_{\parallel}} - v_{\parallel} \frac{\partial F_0}{\partial \mu} \right) \bar{A}_{1,\parallel}. \quad (2.130)$$

An important property of the radial particle flux on a single magnetic surface is the co-called ambipolarity. By employing the field equations particle flux, it can be shown that

$$\sum_s q_s \Gamma_{1,s} = -\frac{c}{4\pi\mathcal{C}} \sum_{\mathbf{k}} ik_y \left[k_{\perp}^2 |\phi_{1,\mathbf{k}}|^2 - k_{\perp}^2 |A_{1,\parallel,\mathbf{k}}|^2 - |B_{1,\parallel,\mathbf{k}}|^2 \right] = 0. \quad (2.131)$$

From the particle and heat fluxes it is possible to define the corresponding volume averaged diffusivities D_s and χ_s through the Fick's first law for general plasma geometries

$$\langle D_s \rangle_V = -\frac{\langle \Gamma_{1,s} \rangle_V}{\langle g^{xx} \partial_x n_{0,s} \rangle_V}, \quad (2.132)$$

$$\langle \chi_s \rangle_V = -\frac{\langle Q_{1,s} \rangle_V}{\langle g^{xx} n_{0,s} \partial_x T_{0,s} \rangle_V}. \quad (2.133)$$

2.16 Collisions

Here, g^{xx} represents the $\nabla x \cdot \nabla x$ metric coefficient. The flux-surface average of the numerator and denominator of Eqs. (2.132-2.133) is usually performed separately in the code GENE. For the typical tokamak plasma core conditions, no significant difference in the diffusivities estimate is observed if the volume average operator $\langle \dots \rangle_V$ is applied instead on the ratio between the fluxes and the gradients.

2.16 Collisions

The gyrokinetic equation of section 2.6 has been written in the previous sections for a completely general background in a collisionless framework. The binary Coulomb interactions are not expected to play a significant role in the typical plasma core conditions due to the relatively high plasma temperature - usually of the order of few keV - and to be particularly negligible for energetic ions. Nevertheless, they may impact the microinstabilities directly and therefore become relevant in a quantitative comparison between numerical results and experimental measurements. Moreover, collisions might act on the zonal flow amplitude as an effective damping mechanism [123]. To account for such effects, a collision operator $C(F_s, F_{s'})$ is introduced in the following section, which is added to the right hand side of the Vlasov equation. It accounts for the binary interactions between the species s and s' . A detailed description can be found in Ref. [124]. By invoking a separation of the collisional and turbulent time scales, the effect of collisions on the arbitrary non-Maxwellian background distributions is here neglected and Maxwellians are considered for each species in a linearised Landau-Boltzmann collision operator. A more consistent treatment involving a collision operator for arbitrary distributions will be aimed for future studies. The Maxwellian approximation for the background distribution functions significantly simplifies the derivation of an explicit expression for $C(F_s, F_{s'})$, which can be linearised as

$$C(F_s, F_{s'}) = \tilde{C}(F_{1,s}, F_{0,s'}) + \tilde{C}(F_{0,s}, F_{1,s'}) . \quad (2.134)$$

The general operator $\tilde{C}(F_s, F_{s'})$ can be re-written as the sum of a diffusion \mathbf{D} and a dynamical friction \mathbf{R} operators as

$$\tilde{C}(F_s, F_{s'}) = \frac{\partial}{\partial \mathbf{v}} \cdot \left(\mathbf{D} \cdot \frac{\partial}{\partial \mathbf{v}} - \mathbf{R} \right) F_s, \quad (2.135)$$

with

$$\mathbf{D} = \nu_c \frac{\partial^2}{\partial \mathbf{v} \partial \mathbf{v}} \int F_s \left| \mathbf{v}_s - \mathbf{v}_{s'} \right| d^3 v_{s'}, \quad (2.136)$$

$$\mathbf{R} = 2 \frac{\partial}{\partial \mathbf{v}} \int \frac{F_{s'}}{|\mathbf{v}_s - \mathbf{v}_{s'}|} d^3 v_{s'}. \quad (2.137)$$

Here, ν_c represents the so-called collision frequency, which is defined as

$$\nu_c = \frac{2\pi q_s^2 q_{s'}^2}{m_s m_{s'}} \ln \Lambda_c \quad (2.138)$$

and $\ln \Lambda_c$ is the Coulomb logarithm [125].

In the gyrokinetic code GENE, different collision operators can be employed. The simplest one is pitch-angle scattering, which can be obtained from Eq. (2.135) in the limit of infinitely heavy ions (thereby neglecting the energy transfer from electrons to ions through collisions). This rough assumption limits the physical applicability of such an operator and is usually employed only for benchmarks with other codes. A more sophisticated expression for the collision operator is given by the linearized Landau-Boltzmann form. This model fulfills the particle, momentum, and energy conservation properties. However, in nonisothermal scenarios, the free energy dissipation property breaks and non-physical energy transfer from the particle background distributions to their perturbations might occur. The Sugama collision operator [126] is able to account for collisions in nonisothermal systems including, moreover, finite Larmor radius (FLR) corrections. More details on the underlying equations and their respective numerical implementation in the GENE code can be found in Ref. [93, 124, 127].

2.17 Non-Maxwellian free energy balance

The contribution of each plasma species to the overall linear and nonlinear dynamics can be investigated by studying the time evolution of the system's free energy. It is defined, analogously to the standard fluid theory, as the sum of a kinetic E_k (first right-hand-side term below), field E_w (second right-hand-side term below) and entropy \mathcal{S} (last right-hand-side term) contributions. Here, the subscript s is omitted for simplicity. The free energy is defined as follows

$$E_{fe} = \int d\mathbf{x} d\mathbf{v} F(\mathbf{x}, \mathbf{v}) \frac{mv^2}{2} + \int d\mathbf{x} \frac{E^2 + B^2}{8\pi} - T_0 \int d\mathbf{x} d\mathbf{v} F(\mathbf{x}, \mathbf{v}) \log F(\mathbf{x}, \mathbf{v}). \quad (2.139)$$

Here, F represents the total distribution function of the species s , \mathbf{E} and \mathbf{B} , respectively, the electric and magnetic field. It can be shown (see Ref. [128, 129, 130] for the detailed derivation) that by applying the δf approach and keeping only first order terms in Eq. (2.139), the sum of the entropy and kinetic parts reduces to

2.17 Non-Maxwellian free energy balance

$E_k + \mathcal{S} = T_0 \int d\mathbf{x} d\mathbf{v} f_1^2 / (2F_0)$. In the following sections, we will refer to this term as a kinetic contribution to the overall energy balance - in the sense that it depends on the perturbed distribution function f_1 . Eq. (2.139) can then be written as

$$E_{fe} = T_0 \int d\mathbf{x} d\mathbf{v} \frac{f_1^2}{2F_0} + \int d\mathbf{x} \frac{E^2 + B^2}{8\pi}. \quad (2.140)$$

Here, f_1 is the perturbed first order distribution function. By analyzing Eq. (2.140) and its time derivative, it is possible to identify the leading terms in the destabilization or stabilisation of the typical tokamak plasma instabilities. In particular, the different terms that contribute mostly to the increase/decrease of the overall system free energy can be investigated in detail, providing relevant physical insights on the scenario at hand. For example, by studying the energy terms in phase-space ($v_{||}, \mu$) velocity resonances and trapped particle effects can be easily recognized. In the gyrokinetic formalism, the kinetic and field energy terms can be written - see Ref. [128, 129, 130] for more details - as

$$E_k = \left\langle \int d\mu dv_{||} \pi B_0 n_0 T_0 \frac{|g_{1,k}|^2}{2F_0} \right\rangle_z, \quad (2.141)$$

$$E_w = \left\langle \int d\mu dv_{||} \frac{\pi}{2} B_0 n_0 q \bar{\xi}_{1,k}^* g_{1,k} \right\rangle_z, \quad (2.142)$$

with the z-average

$$\langle A(z) \rangle_z = \frac{\int \mathcal{J}(z) A(z) dz}{\int \mathcal{J}(z) dz}. \quad (2.143)$$

Here, \mathcal{J} is the Jacobian in the field-aligned coordinate system defined in Eq. (2.48). The time derivative of Eqs. (2.141-2.142) represents the free energy balance equation, which determines the energy flow during the whole simulation. It can be shown - see Ref. [128, 129, 130] for more details - that the time derivative of Eqs. (2.141-2.142) can be written as

$$\frac{\partial E_k}{\partial t} = \left\langle \int d\mu dv_{||} \pi B_0 n_0 T_0 \frac{g_{1,k}^* \partial_t g_{1,k}}{2F_0} \right\rangle_z, \quad (2.144)$$

$$\frac{\partial E_w}{\partial t} = \left\langle \int d\mu dv_{||} \frac{\pi}{2} B_0 n_0 q \bar{\xi}_{1,k}^* \partial_t g_{1,k} \right\rangle_z. \quad (2.145)$$

2. Gyrokinetic theory

Employing the schematic decomposition of the first order Vlasov equation (Eq. (2.66)), it is possible to identify the contribution of each term and each species to the total free energy exchange as follows

$$\frac{\partial E_{fe}}{\partial t} = E_{\mathcal{L}_{\parallel}} + E_{\mathcal{L}_D} + E_{\mathcal{L}_C} + E_D + E_{NL}. \quad (2.146)$$

Here, the parallel advection, the drive, the curvature, the dissipative and nonlinear terms are given as

$$E_{\mathcal{L}_{\parallel}} = \left\langle \int d\mu dv_{\parallel} \frac{\pi}{2} B_0 n_0 \left(\frac{T_0 g_{1,k}^*}{F_0} + q \bar{\xi}_{1,k}^* \right) \mathcal{L}_{\parallel} \right\rangle_z, \quad (2.147)$$

$$E_{\mathcal{L}_D} = \left\langle \int d\mu dv_{\parallel} \frac{\pi}{2} B_0 n_0 \left(\frac{T_0 g_{1,k}^*}{F_0} + q \bar{\xi}_{1,k}^* \right) \mathcal{L}_D \right\rangle_z, \quad (2.148)$$

$$E_{\mathcal{L}_C} = \left\langle \int d\mu dv_{\parallel} \frac{\pi}{2} B_0 n_0 \left(\frac{T_0 g_{1,k}^*}{F_0} + q \bar{\xi}_{1,k}^* \right) \mathcal{L}_C \right\rangle_z, \quad (2.149)$$

$$E_{NL} = \left\langle \int d\mu dv_{\parallel} \frac{\pi}{2} B_0 n_0 \left(\frac{T_0 g_{1,k}^*}{F_0} + q \bar{\xi}_{1,k}^* \right) \mathcal{NL} \right\rangle_z. \quad (2.150)$$

The nonlinear, i.e. E_{NL} , and the parallel advection, i.e. $E_{\mathcal{L}_{\parallel}}$, terms vanish when summed over all the k wave vector components. In the gyrokinetic formalism the overall cross-scale energy nonlinearly transferred is conserved, since the free energy acts as a nonlinear conserved quantity. This property of the nonlinear transfer term comes from the Poisson bracket symmetry properties as shown in Ref. [128, 129, 130, 131, 40, 132]. However, it is possible to rewrite Eq. (2.150) in terms of a nonlinear transfer function \mathcal{T}_{fe}

$$\begin{aligned} E_{NL} &= \left\langle \int d\mu dv_{\parallel} \frac{\pi}{2} B_0 n_0 \left(\frac{T_0 g_{1,k}^*}{F_0} + q \bar{\xi}_{1,k}^* \right) \mathcal{NL} \right\rangle_z \\ &= \left\langle \sum_{k',k''} \mathcal{T}_{fe}^{k',k''} \right\rangle_z, \end{aligned} \quad (2.151)$$

which is defined as follows

$$\mathcal{T}_{fe}^{k,k'} = \sum_s \Re e \left\{ \int dz dv_{\parallel} d\mu \pi B_0 h_{1,s}^{k,*} \frac{n_s T_s}{F_{0,s}} \left[(\mathbf{k}' \times \mathbf{k}'') \cdot \frac{\mathbf{B}_0}{|B_0|} \right] \left(\bar{\xi}_{1,s}^{k'} g_{1,s}^{k''} - \bar{\xi}_{1,s}^{k''} g_{1,s}^{k'} \right) \right\}. \quad (2.152)$$

2.18 Chapter summary

Here, $h_{1,s}^k$ represents the non-adiabatic part of the perturbed distribution function f_1 , defined for a general background distribution function as in Eq. (2.130). This term represents the nonlinear energy transfer between the mode k and the mode k' . From the Poisson and Ampère's equations, the field components are linear functions of the distribution function $g_{1,k}$ and Eq. (2.151) is multiplied by $g_{1,k'}$. Therefore, the nonlinear energy transfer is a cubic function of $g_{1,k}$ and it can be expressed as a triadic nonlinear coupling between the modes k , k' and $k - k'$. Since the coupling condition $k + k' + k'' = 0$ is satisfied, the triad transfer is an symmetric function of k and k' , i.e. $\mathcal{T}_{fe}^{k,k'} = \mathcal{T}_{fe}^{k',k}$.

From the energy relation of Eqs. (2.141-2.145), it is also possible to compute the most unstable linear growth rate γ through the time variation of the kinetic and potential energy, as shown in Ref. [133, 134, 128, 135], by the relation

$$\gamma = -\frac{1}{E_w} \sum_s \frac{\partial E_{k,s}}{\partial t}. \quad (2.153)$$

Eq. (2.153) allows one to distinguish between the contribution of each species s to the total growth rate, by removing the sum over all the species and studying each term separately. Positive (negative) values of $\partial E_{k,s}/\partial t$ indicate that the plasma species considered is giving (taking) energy to (from) the electrostatic field component with a consequent growth (damping) of the mode. Eq. (2.153) will be used in the following chapters to investigate the impact of energetic ions on the overall energy terms.

2.18 Chapter summary

In the present chapter, a brief introduction to gyrokinetic theory and its underlying equations has been provided. The analytic derivation of this reduced kinetic model partially follows the enlightening work of Brizard and Hahm [91]. The latter is specifically applied to obtain the basic equations solved by the GENE code as previously done in Ref. [11, 91, 93]. However, the main difference to these previously published works is that here no assumption has been made on the background distribution function. In particular, the gyrokinetic Vlasov-Maxwell coupled equations have been re-derived for a completely arbitrary background distribution function in the electromagnetic case. This more flexible setup is required to capture asymmetries and anisotropies as, for instance, in the presence of energetic particles and astrophysical scenarios. In the next chapter a benchmarking effort, involving both the local and the global versions of the extended version of the GENE code will be presented and discussed.

Chapter 3

Non-Maxwellian background distributions in GENE: Implementation and verification

The numerical details of the non-Maxwellian background implementation in the gyrokinetic code GENE are provided in the present chapter. As mentioned previously, the δf approach of splitting the full distribution function for the solution of the Vlasov-Maxwell equations allows the separation of the time-independent background, i.e. F_0 with the small fluctuating part, namely F_1 . In order to capture the asymmetries and anisotropies arising from the different heating schemes, e.g. ICRH and NBI in velocity and space, different background F_0 components are now supported by the code. The full description of the new non-Maxwellian equilibrium distributions is provided here. First verification studies on the extended version of GENE are performed and the results benchmarked against other codes which present similar features.

3.1 Equilibrium distribution functions

In the previous chapter the basic δf gyrokinetic equations have been re-derived for a completely arbitrary background distribution function without any specification for the shape of F_0 . Here, all the possible choices implemented in the gyrokinetic code GENE in the course of the present work are specified. A large variety of different background distribution functions are now supported, which can be either analytical, namely slowing down, anisotropic Maxwellian and double bump-on-tail, or numerical. Furthermore, as shown in the previous chapter, to completely describe

3. Non-Maxwellian background distributions in GENE: Implementation and verification

a background distribution function, not only F_0 but also its radial profile is needed to extract $\hat{\partial}_x F_0$ on the whole radial domain or on the single magnetic surface of interest, respectively, for the global or local solvers. The velocity space derivatives of the analytic backgrounds are computed analytically while a third order Lagrangian scheme has been used to compute them from the numerical backgrounds.

3.1.1 Maxwellian background

The most basic plasma background, often employed in any gyrokinetic simulations, is the (equivalent) Maxwellian distribution function defined, on the GENE grid, as follows

$$F_{0,M} = \frac{n_0}{\pi^{3/2} v_{th}^3} \exp \left\{ -\frac{v_{||}^2}{v_{th}^2} - \frac{\mu B_0}{T_0} \right\}. \quad (3.1)$$

Here, $v_{th} = (2T_0/m)^{1/2}$ represents the thermal velocity. Eq. (3.1) allows to describe fully thermalised species with no velocity anisotropy. It can approximate the bulk main ion and electron species in the absence of any external heating scheme particularly well. All the gyrokinetic equations significantly simplify for the basic Maxwellian plasma background. As shown in details in the previous chapter, a meaningful example is that the field equations for ϕ_1 , $B_{1,||}$ and $A_{1,||}$ decouple, due to the $v_{||}$ -symmetry of Eq. (3.1). The radial derivative of the equivalent Maxwellian distribution function reads

$$\hat{\partial}_x F_{0,M} = \frac{F_{0,M}}{n_0} \partial_x n_0 + \frac{F_{0,M}}{T_0} \partial_x T_0 \left(\frac{mv_{||}^2/2 + \mu B_0}{T_0} - \frac{3}{2} \right). \quad (3.2)$$

By employing the GENE normalisation, the Maxwellian plasma background and its radial derivative can be written as

$$F_{0,M} = \frac{1}{\pi^{3/2}} \exp \left\{ -v_{||}^2 - \mu B_0 \right\}, \quad (3.3)$$

$$\hat{\partial}_x F_{0,M} = \frac{F_{0,M}}{n_0} \partial_x n_0 + \frac{F_{0,M}}{T_0} \partial_x T_0 \left(v_{||}^2 + \mu B_0 - \frac{3}{2} \right). \quad (3.4)$$

3.1.2 Slowing Down background

The first analytic non-Maxwellian distribution function implemented in GENE is the velocity-space-isotropic slowing down background of Ref. [89, 102, 136, 99, 137, 100]. It is a solution of the Fokker-Planck equation with an isotropic delta-function particle

3.1 Equilibrium distribution functions

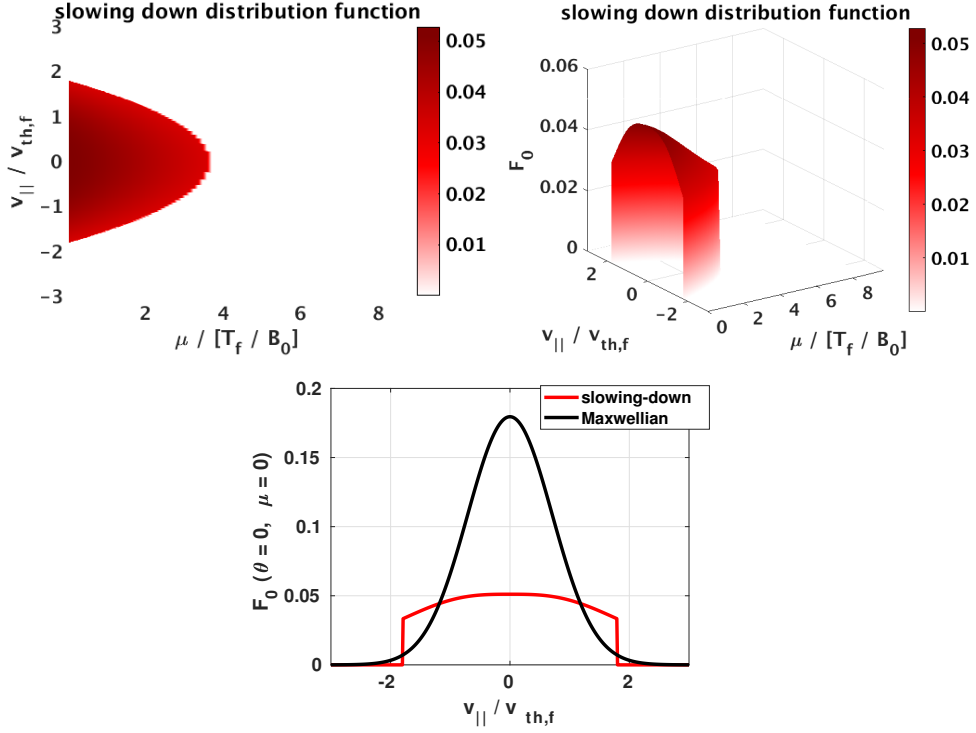


Figure 3.1: a) Contour and b) 3D plots of the slowing down distribution function defined in Eq. (3.7) for the reference parameters $T_f = 81.5T_e$, $v_c = 5.81v_{th,f}$ and $E_f = 22.4T_f$ at $\theta = 0$. c) Comparison of the slowing down distribution function with an equivalent Maxwellian at $\theta = \mu = 0$.

source. The details about its analytic derivation can be found in Ref. [136]. It reads as

$$F_{0,s} = \frac{n_0}{\frac{4}{3}\pi \log \left[1 + \left(\frac{v_\alpha}{v_c} \right)^3 \right]} \frac{\Theta(v_\alpha - v)}{v_c^3 + v^3}, \quad (3.5)$$

where, E_α is the birth energy, which defines the velocity v_α as $v_\alpha = \sqrt{2E_\alpha/m_\alpha}$. Moreover, $v_c = \sqrt{2T_e/m_e} \left(\frac{3\sqrt{\pi}}{4} \sum_{ions} \frac{n_i m_e q_i^2}{n_e m_i} \right)^{1/3}$ represents the crossover velocity and Θ the Heaviside step function. The slowing down distribution function of Eq. (3.5) is a particularly good first order analytic approximation to model fusion born alpha particles, which are not expected to have anisotropies in the velocity space and which are generated at the specific energy $E_\alpha = 3.5\text{MeV}$. Moreover, such distribu-

3. Non-Maxwellian background distributions in GENE: Implementation and verification

tion can also be employed to model externally injected beam ions with only small velocity anisotropies and generated at a particularly narrow energy range. The radial derivative of Eq. (3.5) is directly linked to the drive term contribution in the Vlasov equation and can be easily computed to

$$\hat{\partial}_x F_{0,s} = \frac{F_{0,s}}{n_0} \partial_x n_0 + \left[\frac{v_\alpha^3}{(v_c^3 + v_\alpha^3) \log \left(1 + \left(\frac{v_\alpha}{v_c} \right)^3 \right)} - \frac{v_c^3}{v^3 + v_c^3} \right] \left(\frac{3}{2T_e} \partial_x T_e + \frac{1}{n_i} \partial_x n_i - \frac{1}{n_e} \partial_x n_e \right) F_{0,s}. \quad (3.6)$$

The radial derivative component of the magnetic field B_0 vanishes from the definition of $\hat{\partial}_x = \partial_x - \frac{\mu \partial_x B_0}{mv_{\parallel}} \frac{\partial}{\partial v_{\parallel}}$. Eq. (3.6) shows that for a slowing down distribution function, $\hat{\partial}_x F_{0,s}$ is defined through the ion and electron temperature and density gradients. The background plasma, namely the ions and electrons act as a drag term to the energetic ions, affecting the radial profile of the slowing down F_0 distribution. The interplay between ion/electron drag interaction with the energetic beam is discussed in detail in Ref. [136] and is regulated by the crossover velocity v_c . By employing the normalisation of chapter 2 the adimensional F_0 and $\hat{\partial}_x F_{0,s}$ read as

$$F_{0,s} = \frac{3\Theta \left[\sqrt{\frac{E_\alpha}{T_\alpha}} - \sqrt{v_{\parallel}^2 + \mu B_0} \right]}{4\pi \log \left(1 + \left(\frac{v_\alpha}{v_c} \right)^3 \right) \left(\left(\frac{v_c}{v_{th,\alpha}} \right)^3 + (v_{\parallel} + \mu B_0)^{3/2} \right)}, \quad (3.7)$$

$$\begin{aligned} \hat{\partial}_x F_{0,s} = & \frac{F_{0,s}}{n_0} \partial_x n_0 + \left[\frac{1}{\left(1 + \left(\frac{v_c}{v_\alpha} \right)^3 \right) \log \left(1 + \left(\frac{v_\alpha}{v_c} \right)^3 \right)} \right. \\ & \left. - \frac{\left(\frac{v_c}{v_{th,\alpha}} \right)^3}{v^3 + \left(\frac{v_c}{v_{th,\alpha}} \right)^3} \right] \left(\frac{3}{2T_e} \partial_x T_e + \frac{1}{n_i} \partial_x n_i - \frac{1}{n_e} \partial_x n_e \right) F_{0,s}. \end{aligned} \quad (3.8)$$

A visual example of the velocity space structure of the normalised slowing-down distribution function implemented in GENE is given in Fig. 3.1 for the generic plasma parameters $T_f = 81.5T_e$, $v_c = 5.81v_{th,f}$ and $E_f = 22.4T_f$. It is necessary at this point

3.1 Equilibrium distribution functions

to define the slowing down distribution function temperature. The latter can be rigorously defined only through the second order moment of the equivalent Maxwellian background distribution function i.e.

$$\int v^2 F_{0,\text{Max}} d^3v = \int v^2 F_{0,\text{non-Max}} d^3v. \quad (3.9)$$

In particular, for thermal species (therefore described by a Maxwellian background) the temperature is uniquely defined by the full width at half maximum of the Gaussian distribution. By doing so, any free parameter related to possible anisotropies is then determined by the aforementioned constraint. Employing the slowing down distribution function defined in Eq. (3.7) into Eq. (3.9), the following definition for the slowing down temperature is derived

$$T_s = \frac{2I_4}{3I_2} E_\alpha, \quad (3.10)$$

where

$$I_2 = \frac{1}{3} \log \left(\frac{1 + \left(\frac{v_c}{v_\alpha} \right)^3}{\left(\frac{v_c}{v_\alpha} \right)^3} \right), \quad (3.11)$$

and

$$I_4 = \frac{1}{2} - \left(\frac{v_c}{v_\alpha} \right)^2 \left\{ \frac{1}{6} \log \left(\frac{1 - \frac{v_c}{v_\alpha} + \left(\frac{v_c}{v_\alpha} \right)^2}{\left(1 + \frac{v_s}{v_\alpha} \right)^2} \right) + \frac{1}{\sqrt{3}} \left[\frac{\pi}{6} + \arctan \left(\frac{2 - \frac{v_s}{v_\alpha}}{\sqrt{3} \frac{v_c}{v_\alpha}} \right) \right] \right\}, \quad (3.12)$$

have been defined.

3.1.3 Anisotropic Maxwellian background

In many different plasma scenarios, velocity space anisotropies might arise from the heating schemes and magnetic configurations. For the case of externally heated particles, for example, a preferential injection angle can increase the number of particle moving along specific directions, generating asymmetries along $v_{||}$ and between $v_{||}$ and μ (v_\perp). For correctly modelling such scenarios and the resulting background distribution function of the energetic ions, an anisotropic and asymmetric background

3. Non-Maxwellian background distributions in GENE: Implementation and verification

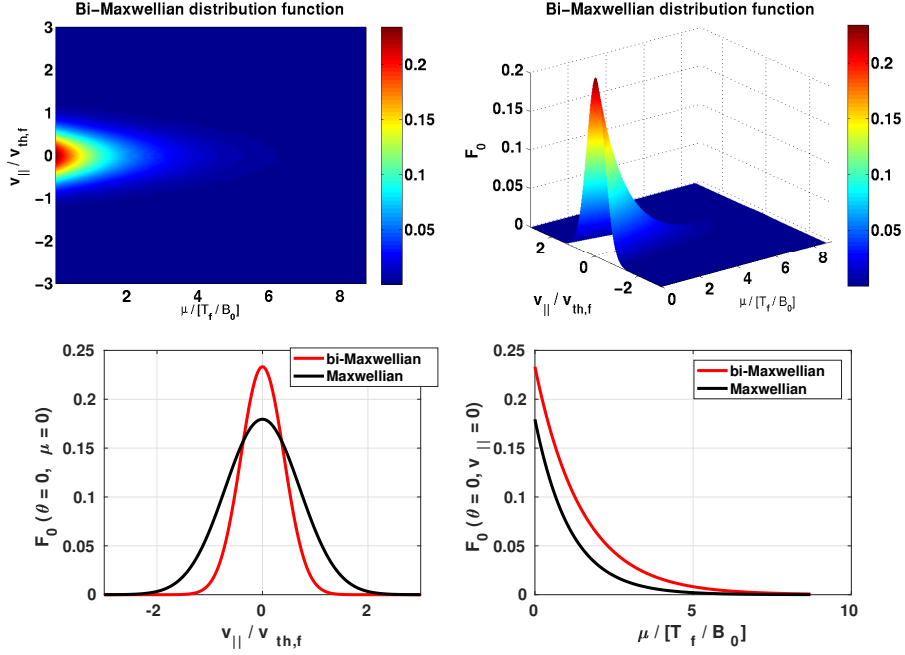


Figure 3.2: a) Contour and b) 3D plots of the anisotropic Maxwellian distribution function defined in Eq. (3.19) for the reference parameters $T_{\perp} = 9.2T_e$, $T_{\parallel,+} = T_{\parallel,-} = 2.3T_e$ and $T_0 = 6.9T_e$ at $\theta = 0$. Comparison of the anisotropic Maxwellian distribution function with an equivalent Maxwellian at c) $\theta = \mu = 0$ and d) $\theta = v_{\parallel} = 0$

is required. To this aim the F_0 distribution function of Ref. [102, 138] has been implemented in the code GENE, namely

$$F_{0,aM} = \frac{2n_0 \exp\left(-\frac{\mu B_0}{T_{\perp}}\right)}{\pi^{3/2} (v_{th,-} + v_{th,+}) v_{th,\perp}^2} \left\{ \exp\left(-v_{\parallel}^2/v_{th,-}^2\right) [1 - \Theta(v_{\parallel})] + \exp\left(-v_{\parallel}^2/v_{th,+}^2\right) \Theta(v_{\parallel}) \right\}. \quad (3.13)$$

Here, $T_{\parallel,+}$ and $T_{\parallel,-}$ are respectively the positive and negative parallel temperature, while T_{\perp} is the perpendicular temperature. The different thermal velocities are defined through the above defined temperatures, i.e. $v_{th,+} = (2T_{\parallel,+}/m)^{1/2}$, $v_{th,-} = (2T_{\parallel,-}/m)^{1/2}$ and $v_{th,\perp} = (2T_{\perp}/m)^{1/2}$. In the limit of $T_{\parallel,+} = T_{\parallel,-}$, Eq. (3.13) reduces to a bi-Maxwellian distribution function. The latter can often be considered a good

3.1 Equilibrium distribution functions

first order approximation to radio-frequency heated energetic ions, as will be shown in chapter 4. Furthermore, in the limit of $T_{\parallel,+} = T_{\parallel,-} = T_{\perp}$, Eq. (3.13) turns into a Maxwellian distribution function. The radial derivative of the anisotropic Maxwellian of Eq. (3.13) is

$$\begin{aligned}\hat{\partial}_x F_{0,aM} &= \frac{F_{0,aM}}{n_0} \partial_x n_0 - \frac{F_{0,aM}}{2(v_{th,-} + v_{th,+})} \left[\frac{v_{th,-}}{T_{\parallel,-}} \partial_x T_{\parallel,-} + \frac{v_{th,+}}{T_{\parallel,+}} \partial_x T_{\parallel,+} \right] \\ &\quad + \frac{mv_{\parallel}^2}{2} \left[\frac{F_{0,aM}^+}{T_{\parallel,+}^2} \partial_x T_{\parallel,+} + \frac{F_{0,aM}^-}{T_{\parallel,-}^2} \partial_x T_{\parallel,-} \right] - \frac{F_{0,aM}}{T_{\perp}} \partial_x T_{\perp} \\ &\quad + \frac{F_{0,aM} \mu B_0}{T_{\perp}} \left[\frac{1}{T_{\perp}} \partial_x T_{\perp} - \frac{1}{B_0} \partial_x B_0 \right] - \frac{\mu \partial_x B_0}{mv_{\parallel}} \partial_{v_{\parallel}} F_{0,aM}.\end{aligned}\quad (3.14)$$

where, the functions

$$F_{0,aM}^+ = \frac{2n_0 \exp\left(-\frac{\mu B_0}{T_{\perp}}\right)}{\pi^{3/2} (v_{th,-} + v_{th,+}) v_{th,\perp}^2} \left\{ \exp\left(-v_{\parallel}^2/v_{th,+}^2\right) \Theta(v_{\parallel}) \right\}, \quad (3.15)$$

and

$$F_{0,aM}^- = \frac{2n_0 \exp\left(-\frac{\mu B_0}{T_{\perp}}\right)}{\pi^{3/2} (v_{th,-} + v_{th,+}) v_{th,\perp}^2} \left\{ \exp\left(-v_{\parallel}^2/v_{th,-}^2\right) [1 - \Theta(v_{\parallel})] \right\}, \quad (3.16)$$

have been defined. The normalised expression for Eq. (3.13) and for its radial derivative read as

$$F_{0,aM} = \frac{2 \exp\left(-\frac{\mu B_0}{\tau_{\perp}}\right)}{\pi^{3/2} (\sqrt{\tau_{\parallel,-}} + \sqrt{\tau_{\parallel,+}}) \tau_{\perp}} \left\{ \exp\left(-v_{\parallel}^2/\tau_{\parallel,-}\right) [1 - \Theta(v_{\parallel})] + \exp\left(-v_{\parallel}^2/\tau_{\parallel,+}\right) \Theta(v_{\parallel}) \right\}, \quad (3.17)$$

$$\begin{aligned}\hat{\partial}_x F_{0,aM} &= \frac{\partial_x n_0}{n_0} F_{0,aM} - \frac{\partial_x T_{\parallel,-}}{T_{\parallel,-}} \left[\frac{\sqrt{\tau_{\parallel,-}} F_{0,aM}}{2(\sqrt{\tau_{\parallel,-}} + \sqrt{\tau_{\parallel,+}})} - v_{\parallel}^2 \frac{F_{0,aM}^-}{\tau_{\parallel,-}} \right] \\ &\quad - \frac{\partial_x T_{\parallel,+}}{T_{\parallel,+}} \left[\frac{\sqrt{\tau_{\parallel,+}} F_{0,aM}}{2(\sqrt{\tau_{\parallel,-}} + \sqrt{\tau_{\parallel,+}})} - v_{\parallel}^2 \frac{F_{0,aM}^+}{\tau_{\parallel,+}} \right] \\ &\quad - \frac{\partial_x T_{\perp}}{T_{\perp}} \left(1 - \frac{\mu B_0}{\tau_{\perp}} \right) F_{0,aM} - \partial_x B_0 \mu \left(\frac{F_{0,aM}}{\tau_{\perp}} + \frac{\partial_{v_{\parallel}} F_{0,aM}}{2v_{\parallel}} \right).\end{aligned}\quad (3.18)$$

Here, the normalised temperatures $\tau_{\parallel,+} = T_{\parallel,+}/T_0$, $\tau_{\parallel,-} = T_{\parallel,-}/T_0$ and $\tau_{\perp} = T_{\perp}/T_0$ have been introduced. The functions $F_{0,aM}^+$ and $F_{0,aM}^-$ have been normalised as

3. Non-Maxwellian background distributions in GENE: Implementation and verification

Eq. (3.13). The anisotropic Maxwellian temperature and temperature gradients are defined, as shown previously from the slowing down background, through the relation of Eq. (3.9), namely

$$T_0 = \frac{T_{\parallel,+} + T_{\parallel,-} - \sqrt{T_{\parallel,+}}\sqrt{T_{\parallel,-}}}{3} + \frac{2T_{\perp}}{3}, \quad (3.19)$$

$$\partial_x T_0 = \frac{\partial_x T_{\parallel,+} + \partial_x T_{\parallel,-} - \frac{1}{2}\sqrt{\frac{T_{\parallel,+}}{T_{\parallel,-}}}\partial_x T_{\parallel,-} - \frac{1}{2}\sqrt{\frac{T_{\parallel,-}}{T_{\parallel,+}}}\partial_x T_{\parallel,+}}{3} + \frac{2\partial_x T_{\perp}}{3}. \quad (3.20)$$

For the limit $T_{\parallel,+} = T_{\parallel,-} = T_{\parallel}$, Eqs. (3.19-3.20) reduce to the well known expressions which relate the bi-Maxwellian to the equivalent Maxwellian temperature and temperature gradients, i.e. $T_0 = \frac{T_{\parallel}+2T_{\perp}}{3}$ and $\partial_x T_0 = \frac{\partial_x T_{\parallel}+2\partial_x T_{\perp}}{3}$. An example of the anisotropic Maxwellian distribution function defined in Eq. (3.17) on the GENE normalised grid is provided in Fig. 3.2 for the reference parameters $T_{\perp} = 9.2T_e$, $T_{\parallel,+} = T_{\parallel,-} = 2.3T_e$ and $T_0 = 6.9T_e$.

3.1.4 Symmetric double-bump-on-tail background

Another analytic background distribution function implemented in the code GENE is the symmetric double bump-on-tail distribution function of Ref. [70, 77, 78, 139]. It is the superposition of two shifted Maxwellian distribution functions and reads as

$$F_{0,b} = \frac{1}{2} \frac{n_0}{(2\pi T_{0,b}/m)^{3/2}} \left[\exp\left(-\frac{(v_{\parallel} - \bar{v}_{\parallel})^2}{2T_{0,b}/m} - \frac{\mu B_0}{T_{0,b}}\right) + \exp\left(-\frac{(v_{\parallel} + \bar{v}_{\parallel})^2}{2T_{0,b}/m} - \frac{\mu B_0}{T_{0,b}}\right) \right], \quad (3.21)$$

where \bar{v}_{\parallel} represents the magnitude of the shift in both positive and negative v_{\parallel} . The bump on tail background can model externally injected beams at a specific energy with no asymmetry in the magnetic moment direction and with the same amount of particles moving along the magnetic field lines in both directions. The F_0 distribution of Eq. (3.21) is particularly suited for studying energetic-particle induced geodesic acoustic modes (EGAMs), whose drive (through inverse Landau damping) requires parallel velocity anisotropies. The radial derivative of Eq. (3.21) is

$$\hat{\partial}_x F_{0,b} = \left\{ \frac{\partial_x n_0}{n_0} + \frac{\partial_x T_{0,b}}{T_{0,b}} \left[\frac{mv_{\parallel}^2/2 + \mu B_0}{T_{0,b}} - \frac{3}{2} - \frac{mv_{\parallel}\bar{v}_{\parallel}}{T_{0,b}} \arctan\left(\frac{mv_{\parallel}\bar{v}_{\parallel}}{T_{0,b}}\right) \right] \right\} F_{0,b} - \frac{\mu \partial_x B_0}{v_{th,f}} \left(\frac{F_{0,b}}{T_{0,b}} + \frac{\partial_{v_{\parallel}} F_{0,b}}{2v_{\parallel}} \right). \quad (3.22)$$

3.1 Equilibrium distribution functions

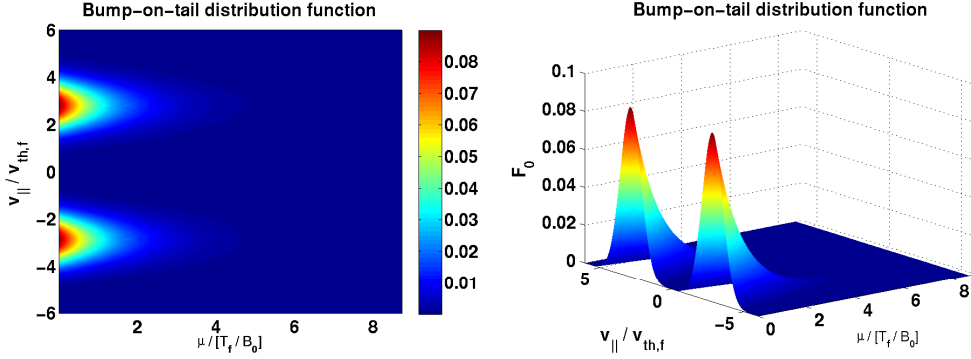


Figure 3.3: a) Contour and b) 3D plots of the bump-on-tail distribution function defined in Eq. (3.23) for the reference parameters $\bar{v}_{\parallel} = 2.83$ at $\theta = 0$.

By employing the GENE normalisation, F_0 and the drive term can be written respectively as follows

$$F_{0,b} = \frac{\hat{n}_0}{\left(\pi \hat{T}_{0,b}\right)^{3/2}} \exp\left[-\frac{v_{\parallel}^2 + \bar{v}_{\parallel}^2 + \mu B_0}{\hat{T}_{0,b}}\right] \cosh\left(\frac{2v_{\parallel}\bar{v}_{\parallel}}{\hat{T}_{0,b}}\right), \quad (3.23)$$

$$\begin{aligned} \hat{\partial}_x F_{0,b} = & \left\{ \frac{\partial_x n_0}{n_0} + \frac{\partial_x T_{0,b}}{T_{0,b}} \left[\frac{v_{\parallel}^2 + \mu B_0}{\hat{T}_{0,b}} - \frac{3}{2} - 2v_{\parallel}\bar{v}_{\parallel} \arctan\left(\frac{2v_{\parallel}\bar{v}_{\parallel}}{\hat{T}_{0,b}}\right) \right] \right\} F_{0,b} \\ & - \mu \partial_x B_0 \left(\frac{F_{0,b}}{\hat{T}_{0,b}} + \frac{\partial_{v_{\parallel}} F_{0,b}}{2v_{\parallel}} \right). \end{aligned} \quad (3.24)$$

As previously done for the slowing down and anisotropic Maxwellian, an equivalent temperature can be defined through the second order moment of the bump-on-tail distribution function. The following relation can be derived

$$T_0 = T_{0,b} \left(1 + \frac{2\bar{v}_{\parallel}^2}{3} \right). \quad (3.25)$$

3.1.5 Numerical backgrounds

As previously mentioned, GENE has been extended to also support numerical background distribution functions, which might be provided from heating codes such as

3. Non-Maxwellian background distributions in GENE: Implementation and verification

\hat{s}	q	T_e/T_i	R/L_{T_i}	R/L_{T_e}	R/L_{n_e}	r/R	$k_\theta \rho_i$
0.8	1.4	1.0	6.9	6.9	2.2	0.18	0.5

Table 3.1: Cyclone base background plasma and magnetic geometry parameters.

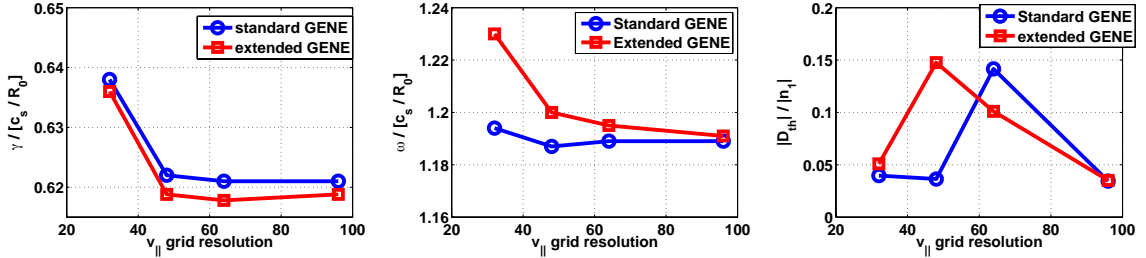


Figure 3.4: Comparison of the linear a) growth rates, b) frequencies and c) thermo diffusion coefficients between the standard and extended GENE codes. The main deuterium and electrons are modelled with an analytic Maxwellian for the standard code and with an ad-hoc numerical Maxwellian for the extended ones.

NEMO/SPOT [103] for NBI injected particles and/or TORIC/SSFPQL [105, 106], SELFO [104] for ICRF heated particles. For each of the distribution functions extracted from the aforementioned codes, interface routines have been created to respectively map the numerical backgrounds into the GENE space-velocity grids. As for the analytic distribution functions both the F_0 and its radial numerical derivative are required by the code to run in both the local and global limits. The equivalent temperature of the numerical backgrounds is also extracted by the second order moment of F_0 as explained in the previous sections. A first simple verification test on these new numerical schemes can be performed by comparing the linear observables (growth rate, frequencies and thermo-diffusion coefficients) obtained with the standard (analytic Maxwellian) and extended GENE code versions. For the latter, however, each species is modelled with an ad-hoc numerical Maxwellian interpolated on the GENE coordinate grid. The same procedure has been used for the radial derivative of the background distribution functions for each species. The simulations are performed in a circular geometry on a single magnetic surface in the simple electrostatic limit. The plasma parameters correspond to the so-called Cyclone Base Case (CBC) [140] and are summarized in table 3.1. The CBC are base parameters often employed in code-code gyrokinetic comparisons characterized by strong ITG turbulence. Fig. 3.4 shows a first comparison of growth rates, frequencies and

3.2 Zero-order consistency assessment

thermo diffusion coefficients normalised to the density fluctuations with the standard version of GENE for different v_{\parallel} grid resolutions at $(x, z, \mu) = (23, 32, 32)$. A significantly good agreement with the standard GENE code is achieved for all the observables with differences of the order of maximum $\sim 7\%$, except for the thermo diffusion coefficient at $n_{v_{\parallel}} = 48$. It reduces to $\sim 2\%$ when the v_{\parallel} resolution is increased. A further improvement, for each $n_{v_{\parallel}}$, in the linear observables comparison can be achieved by increasing the (v_{\parallel}, μ) box sizes, reducing the truncation errors of the velocities integrals of the numerical backgrounds. Moreover, no significant differences in any observable have been observed starting from a magnetic moment discretization of $n_{\mu} = 32$.

3.2 Zero-order consistency assessment

An important assumption made in the previous chapter for the analytical derivation of the gyrokinetic non-Maxwellian Vlasov equation is the time independent property of the background distribution function F_0 . It comes directly from the δf splitting of the full distribution function, assuming that the lowest order term of the basic Vlasov equation, namely

$$\frac{\partial F_0}{\partial t} - \hat{b}_0 \cdot \left(v_{\parallel} \nabla F_0 - \frac{\mu}{m} \nabla B_0 \frac{\partial F_0}{\partial v_{\parallel}} \right) = 0, \quad (3.26)$$

always vanishes. The latter is identically zero for Maxwellian (defined in Eq. (3.1)) and slowing down (defined in Eq. (3.5)) backgrounds and no evolution of the equilibrium quantities is allowed. All the zeroth order quantities can therefore be considered time independent on the turbulent time scale. On the contrary, for the case of more general backgrounds which may, for instance, stem from heating codes considering both kinetic effects and collisions, Eq. (3.26) is not necessarily zero and the degree of violation of the assumed time scale separation must be studied case by case. However, it is worth noting that the F_0 provided by heating codes is not the solution of the simple Eq. (3.26), where the equilibrium is established only by the mirror force, namely left hand side of Eq. (3.26). Instead, the numerical backgrounds are the steady-state solutions of the more complex Fokker-Planck equation which also includes collisions and sources/sinks. These distribution functions represent the equilibrium between the fast ion excitation (or birth) process and the collisions, and hence they are not expected to be modified on turbulence timescales. With the assumption that the time scale characteristic of the mirror force, defined as

$$\tau_{F_0} = F_0 / (dF_0/dt), \quad (3.27)$$

3. Non-Maxwellian background distributions in GENE: Implementation and verification

\hat{s}	q	T_e/T_i	R/L_{T_i}	R/L_{T_e}	R/L_{n_e}	r/a	R/a
0.8	1.4	1.0	6.0	6.0	3.0	0.5	3.0

Table 3.2: Background plasma and magnetic geometry parameters employed in Ref. [99, 102].

is much faster than the collisional one, it is possible to reduce the study of evolution of the numerical background by solving Eq. (3.26). For the specific cases of an anisotropic Maxwellian, defined in Eq. (3.17) and a bump-on-tail distribution, defined in Eq. (3.23), the zero order characteristic time τ_{F_0} can be estimated analytically and reads respectively

$$\frac{\partial F_{0,aM}}{\partial t} = -\mu \partial_z B_0 \left(\frac{F_{0,aM}}{\tau_\perp} - \frac{F_{0,aM}^-}{2\tau_{\parallel,-}} - \frac{F_{0,aM}^+}{2\tau_{\parallel,+}} \right), \quad (3.28)$$

$$\frac{\partial F_0}{\partial t} = -\mu \partial_z B_0 \left(\frac{F_{0,b}}{\hat{T}_{0,b}} + \frac{\bar{v}_\parallel}{v_\parallel} \frac{\hat{n}_0}{\left(\pi \hat{T}_{0,b}\right)^{3/2}} \exp \left[-\frac{v_\parallel^2 + \bar{v}_\parallel^2 + \mu B_0}{\hat{T}_{0,b}} \right] \sinh \left(\frac{2v_\parallel \bar{v}_\parallel}{\hat{T}_{0,b}} \right) \right). \quad (3.29)$$

In both Eqs. (3.28-3.29) the characteristic time τ_{F_0} becomes more relevant as the background anisotropy - in one case controlled by τ_{\perp} and in the other by \bar{v}_\parallel - increases. This result is consistent with the numerical observations of Ref. [78].

3.3 Local code verification

In the framework of verification of the newly implemented terms in the extended version of the gyrokinetic code GENE, supporting non-Maxwellian distribution functions, first benchmark studies were performed against published results obtained with the gyrokinetic codes GS2 and GKW [99]. These codes are able to include and model energetic ions with a slowing down distribution function in electrostatic simulations. In this section, the plasma scenario of Ref. [99, 102] is considered. It is a plasma with thermal Deuterium, electrons and fusion-born alpha particles modelled with the slowing down distribution function of Eq. (3.7). The main parameters are summarized in table 3.2 and have the property to closely approximate the values obtained by GLF23 at mid-radius for an ITER standard scenario. For all the results shown in this section, the linear mode number analyzed is $k_y \rho_s = 0.18$, which corresponds to the typical scale length of ITG eddies in nonlinear turbulence simulations.

3.3 Local code verification

3.3.1 Microinstability growth rate analysis

The first analysis shown here concerns the study of the most unstable growth rates and frequencies for different concentrations of slowing down alpha particles in linear electrostatic simulations. The bulk plasma temperature is set to a realistic ITER mid-radius value, i.e. $T = 10\text{keV}$ in a collisionless plasma [3]. Due to fusion reactions, the alpha particles are generated at the specific energy of $E_\alpha = 3.5\text{MeV}$, which corresponds - according to Eq. (3.10) - to an equivalent temperature of $T_\alpha/T_e = 81.5$. The numerical grid resolutions employed for this linear analysis is $(x, z, v_{||}, \mu) = (21, 48, 124, 68)$. This particularly high velocity grid discretization is required to fully resolve the slowing-down energy cutoff. Fig. 3.5 shows a remarkable agreement between the GENE and GS2 [141, 28] linear results for each concentration of the energetic alpha particles with a relative difference between the GENE and the GS2 results of $\sim 5\%$. As explained in details in Ref. [99, 102], the alpha particles are not found to affect the overall main ITG drive and almost constant growth rates are observed up to an alpha particle charge concentration of $q_\alpha n_\alpha/n_e \sim 0.02$, which is almost two times the expected alpha particle concentration at the plasma mid radius in an ITER standard scenario. Although α particles are fully retained in the solution of the Vlasov-Maxwell coupled equations, their dynamics is negligible and they behave almost as a passive species, i.e. do not affect the overall electrostatic potential and hence the ITG dispersion relation. The minor linear impact of energetic alpha particles on the linear electrostatic growth rates is demonstrated by the relatively small changes in γ for an increase in the alpha particle density up to 20%, namely $\sim 30\%$.

3.3.2 Transport coefficients

To further corroborate the previous benchmark analysis against the codes GS2 and GKW [142, 143], the linear electrostatic comparison with the non-Maxwellian version of the GENE code has been extended to the study of the alpha particle diffusivity for the specific choice of $n_\alpha/n_e = 2.5 \cdot 10^{-4}$ and for different values of the bulk electron temperature T_e . As it will be shown in detail in chapter 5, the particle flux of each plasma species s can be decomposed in a quasi-linear framework in terms of a diffusion $D_{n,s}$, thermal diffusion $D_{T,s}$ and roto-diffusion $V_{p,s}$ coefficients [144, 145] as follows

$$\frac{R\Gamma_s}{n_s} = \frac{RD_{n,s}}{L_{n,s}} + \frac{RD_{T,s}}{L_{T,s}} + RV_{T,s} \quad (3.30)$$

Similarly to Ref. [99, 102], the α particle thermal diffusivity $D_{T,\alpha}$ is computed for each T_e value by subtracting the particle flux contribution at the specific choice of

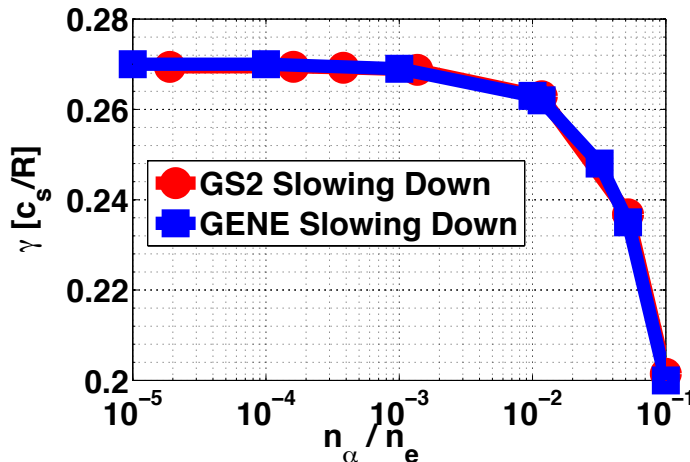


Figure 3.5: a) GENE (blue line) and GS2 (red line) growth rates as a function of the α particles charge density concentration plotted in logarithmic scale.

$k_y \rho_s = 0.18$ from the one obtained with zero density gradients. The numerical GENE results obtained by modelling the alpha particles with an equivalent Maxwellian and a slowing down are shown in Fig. 3.6 and compared with the ones of Ref. [99]. The GENE grid resolution has been kept fixed with respect to the one used in the previous section, namely $(x, z, v_{||}, \mu) = (21, 48, 124, 68)$. Compared to the other code, a very good agreement is observed for each value of the electron temperature considered, with differences only of the order of few percentage, namely $\leq 6\%$. These results corroborate the previous growth rate comparison and prove the correct analytical derivation and numerical implementation of the electrostatic local GENE solver. It is worth noting that compared to GS2 and GKW, the gyrokinetic code GENE has been extended, as extensively shown in the previous chapters, to support arbitrary analytic and numerical non-Maxwellian backgrounds in both electrostatic/electromagnetic and local/global limits.

3.4 Global code verification

The global version of the non-Maxwellian GENE code is tested in the following section with electrostatic simulations. First the relaxation dynamics of an initial electrostatic perturbation, artificially excited into the system, is investigated with Rosenbluth-Hinton tests [56]. In particular, only the axis-symmetric (zonal) compo-

3.4 Global code verification

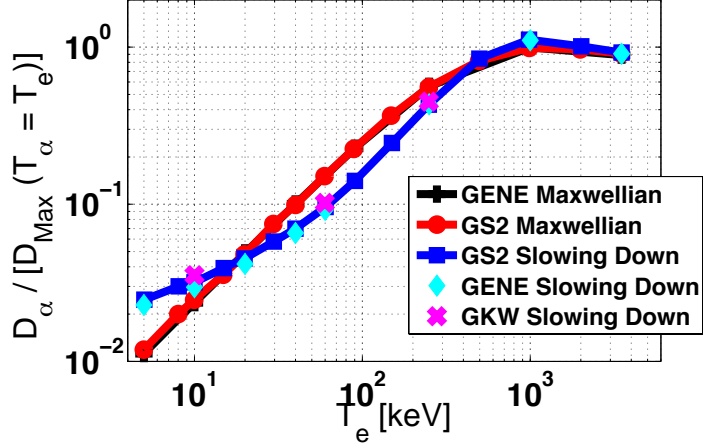


Figure 3.6: GENE (cyan line), GS2 (blue line) and GKW (magenta cross) α particles diffusivity for slowing down distribution function and GENE (black line), GS2 (red line) α particles diffusivity for equivalent Maxwellian distribution function normalised to the diffusivity of thermal helium plotted in logarithmic scale.

nent of electrostatic field ϕ_1 is retained and evolved in time. The correct description of the zonal flows, as discussed in chapter 1, is of great importance for the study of turbulent systems, since ZF represents the primary nonlinear saturation mechanism for most drift-wave instabilities, e.g. ITGs. Furthermore, the reduced physics model allows us to compare the numerical results of such linear tests with analytic predictions. These analyses are performed in the absence of any energetic ion species and the results are compared with the ones obtained with the standard version of the code. In the final part of this section, linear growth rates, frequency and radial structure of an electrostatic potential of an EGAM are also compared with the ones obtained with the gyrokinetic code ORB5 [146, 147]. The energetic ions are modelled with the bump-on-tail distribution function of Eq. (3.23).

3.4.1 Rosenbluth-Hinton test

The first global verification analysis concerns the study of the time evolution of the zonal component - namely $n = m = 0$ - of the electrostatic potential ϕ_1 after an initial perturbation of the form $\phi_1(\rho_{pol}, t = 0) \sim \sin(\pi\rho_{pol})$. Here, $\rho_{pol} = \sqrt{\psi/\psi_{edge}}$ represents the radial coordinate with values in $[0, 1]$ and ψ the poloidal flux, as

3. Non-Maxwellian background distributions in GENE: Implementation and verification

defined in Eq. (1.5). In the absence of collisions and assuming flat profiles, the only damping mechanism acting on the zonal flow is Landau damping and the amplitude of the initialized signal reduces with time. The zonal component of ϕ_1 oscillates at the characteristic geodesic acoustic mode (GAM) frequency. Although such mode is damped, its amplitude reaches a non-zero stationary mean value A_r , which can be analytically estimated in a simple circular plasma geometry with a large aspect ratio through the well known relation derived by Rosenbluth-Hinton [56], namely

$$A_r = \frac{1}{1 + 1.6q(x)^2 / \sqrt{x/R_0}}. \quad (3.31)$$

The residual level A_r , along with the frequency and damping rate of the GAM oscillations determine the complete time evolution of ϕ_1 , averaged over the circular flux surfaces, according to the following expression

$$\frac{\phi_1(x, t)}{\phi_1(x, t = 0)} = (1 - A_r) e^{(-\gamma_{GAM} t)} \cos(\omega_{GAM} t) + A_r. \quad (3.32)$$

Here, ω_{GAM} and γ_{GAM} represent, respectively, the characteristic GAM frequency and damping rate, which can be extracted through a logarithmic fit of the time evolution of ϕ_1 at each specific radial position. In the limit of $t \rightarrow \infty$, Eq. (3.32) reveals that the GAM oscillations are damped away and $\phi_1(x, t)/\phi_1(x, t = 0) \rightarrow A_r$. To test the newly implemented Vlasov-field solver for general F_0 backgrounds, first analysis are performed comparing the GAM frequency, damping rate and residual levels obtained with the new extended version of GENE with the analytic predictions of Ref. [56, 148, 149] and Eq. (3.31) at the center of the radial box in a collisionless plasma. Here, the main ions are modelled with a Maxwellian distribution function. This simple verification study is particularly meaningful to test the new numerical schemes employed in the Vlasov-field solver, which now performs all the integrals and some of the derivatives of F_0 numerically. For this analysis, the inverse aspect ratio $\epsilon (= a/R_0)$ is fixed to 0.3125, with $R_0 = 1\text{m}$ and $a = 0.3125\text{m}$. The magnetic field on axis is equal to $B_0 = 1.9\text{T}$ with a constant safety factor $q = 2$. All the radial profiles employed in this section are flat and electrons are treated as an adiabatic species. The numerical resolution in the grids $(x, z, v_{||}, \mu)$ is set respectively to $(128, 48, 128, 48)$ and the box length is chosen to be $(L_{v_{||}}, L_\mu) = (4v_{th}, 10T_0/B_0)$. The time traces of the electrostatic potential are plotted in Fig. 3.7 for three different values of ρ^* , namely $\rho^* = 1/64$, $\rho^* = 1/128$ and $\rho^* = 1/256$. A particularly good agreement is achieved between the numerical results and the analytic predictions for all the values of ρ^* .

3.4 Global code verification

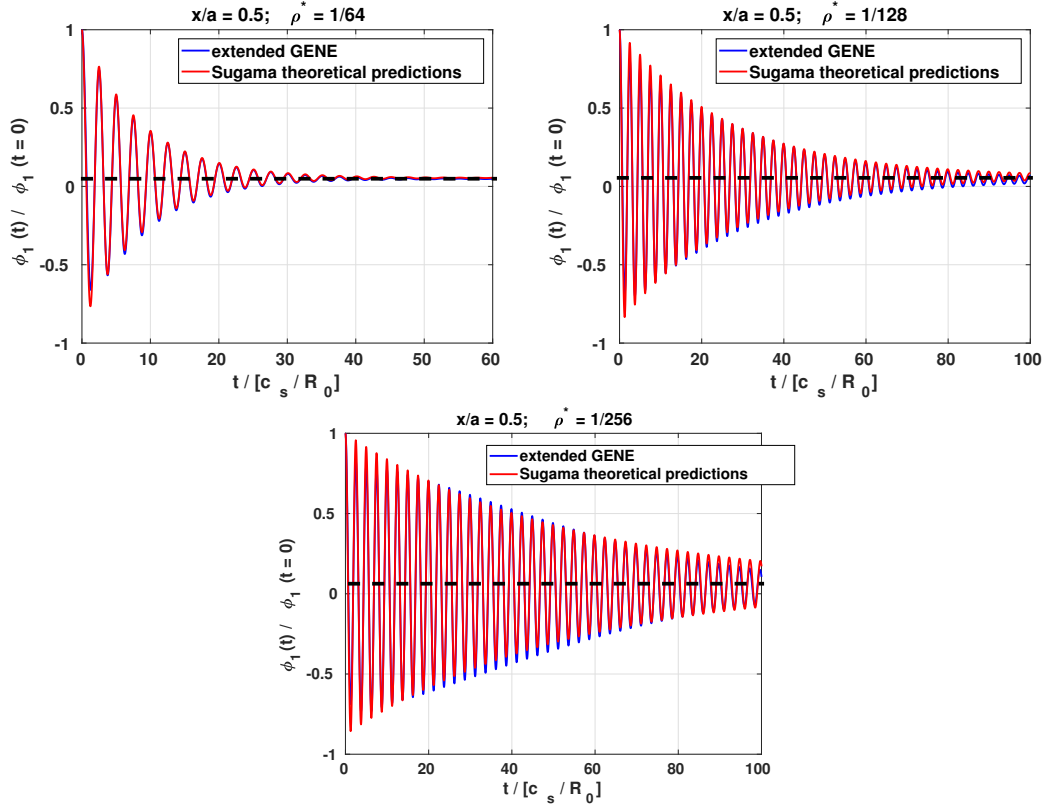


Figure 3.7: Comparison of the time traces of the electrostatic potential at $\rho_{pol} = 0.5$ between the extended version of GENE (blue line) and the analytic predictions of Ref. [148, 149] (red line) for a) $\rho^* = 1/64$, b) $\rho^* = 1/128$ and c) $\rho^* = 1/256$. The black dotted line indicates the residual as predicted by Rosenbluth and Hinton in Eq. (3.31).

3. Non-Maxwellian background distributions in GENE: Implementation and verification

3.4.2 Benchmark with ORB5 code results

The new global version of the non-Maxwellian code GENE is also tested and benchmarked against the gyrokinetic particle-in-cell (PIC) code ORB5. Here, an energetic ion species is included in the simulations and modelled with the bump-on-tail distribution function of Eq. (3.23) with a symmetric shift of $\bar{v}_{\parallel} = 2.83$ in GENE normalised units. A local Maxwellian is maintained for the main (thermal) ion species. The particular choice of the background distribution function for the energetic particle species allows inverse Landau damping mechanisms to occur and possibly excite an EGAM if the drive overcomes the thermal damping. In the following section, the EGAM growth rates and frequencies are investigated for different fast particle concentrations and different magnetic circular geometries. Electrons are considered adiabatic and at $t = 0$ a density perturbation of the form $n_1(\rho_{pol}, t_0) \sim \sin(\pi\rho_{pol})$ is initialized. Dirichlet boundary conditions are applied in the radial direction. As already done in the previous section for the Rosenbluth-Hinton testes, the growth rates and frequencies are obtained through a logarithmic fit of the time evolution of ϕ_1 at the radial position $\rho_{pol} = 0.5$.

EGAM growth rates, frequency and radial structure

The numerical simulations presented in this section are performed with analytical circular magnetic equilibria [150] and in a collisionless plasma. The inverse aspect ratio $\epsilon (= a/R_0)$ is fixed to 0.3125, with $R_0 = 1\text{m}$ and $a = 0.3125\text{m}$. The magnetic field on axis is equal to $B_0 = 1.9\text{T}$. Furthermore, to facilitate the numerical comparison and restrict the numerical analysis to only the EGAM excitation and dynamics, flat temperature and density profiles have been considered. The radial coordinate goes from $\rho_{pol} = [0.05, 0.95]$. The EP and bulk ion temperatures ($T_e = T_i = T_{EP}$) are fixed by the choice of $\rho^* = \rho_s/a$, with $\rho_s = \sqrt{T_e/m_i}/\Omega_i$ and $\Omega_i = qB_0/mc$. To extend the numerical comparison to different plasma setups, two different values of ρ^* have been used, i.e. $\rho^* = 1/64$ and $\rho^* = 1/128$. In Fig. 3.8 the EGAM growth rates and frequencies obtained for different energetic ion concentrations at $\rho_{pol} = 0.5$ are compared between GENE and ORB5 for a flat q -profile = 3, i.e. shear = 0 and for $\rho^* = 1/64$ and $\rho^* = 1/128$. The theoretical values of the EGAM frequencies and growth rates have been taken from Ref. [78], in which an analytic EGAM dispersion relation is derived for a background bump-on-tail distribution function. The differences between the GENE and ORB5 results are of the order of 7% for $\rho^* = 1/64$, which reduce to $\sim 5\%$ for ρ^* , i.e. $\rho^* = 1/128$. The agreement between the codes improves even further if the value of the flat q -profile is reduced to 2, as it is shown in Fig. 3.9 for the EGAM growth rates and frequencies. The small discrepancy in

3.4 Global code verification

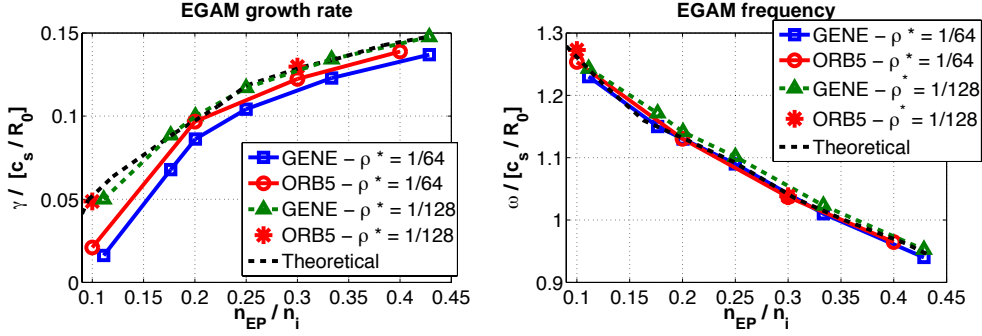


Figure 3.8: EGAM frequencies and growth rates for $q = 3$ and $\rho^* = 1/64$; $\rho^* = 1/128$. Reproduced from [139], with the permission of IAEA.

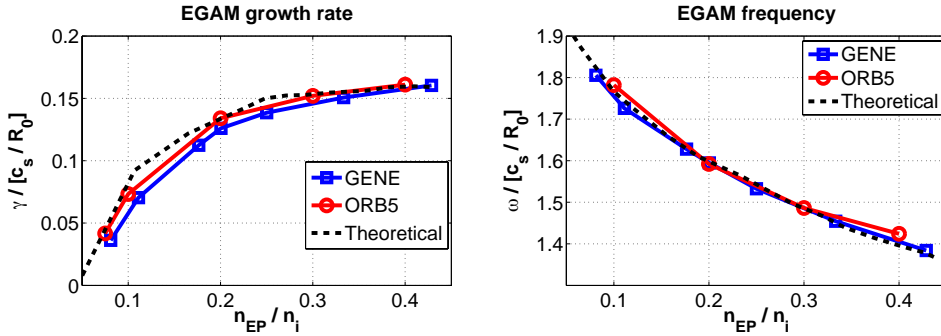


Figure 3.9: EGAM frequencies and growth rates for $q = 2$ and $\rho^* = 1/64$. Reproduced from [139], with the permission of IAEA.

the linear EGAM growth rates and frequencies between GENE and ORB5 might be related to slightly different implementations of finite-Larmor-radius effects. For this specific geometry, i.e. $q = 2$, and for the fast ion concentration of $n_{EP}/n_e = 0.2$, a comparison of the radial structure of the perturbed electrostatic potential obtained with GENE and ORB5 is shown in Fig. 3.10 for $t = 0$ and $t = 268.1$ in units of c_s/R_0 . The time $t = 268.1c_s/R_0$ corresponds to a maximum of the electrostatic potential. This time has been chosen after an initial transient phase, and therefore gives a characteristic indication of the radial structure of the well-formed mode. A good agreement between the codes is observed. In particular, and a slight shift of the radial position of the peak is found. The latter corresponds to a lack of radial symmetry caused by the finite aspect ratio. More details can be found in Ref. [139].

3. Non-Maxwellian background distributions in GENE: Implementation and verification

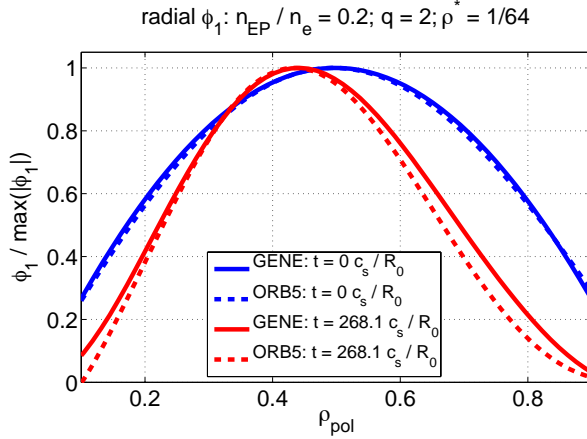


Figure 3.10: Comparison of the radial structure of the electrostatic potential ϕ_1 between GENE (continuous line) and ORB5 (dotted line) for the case $n_{EP}/n_e = 0.2$, $q = 2$ and $\rho^* = 1/64$. Reproduced from [139], with the permission of IAEA.

Nonlinear EGAM wave-particle and wave-wave interaction

Another meaningful test case for the global version of the non-Maxwellian GENE code consists in the study of the nonlinear EGAM dynamics, excited by the velocity space anisotropies of fast particle population. In particular, the nonlinear interaction of the $n = 0$ mode with itself and with the energetic ions is investigated with GENE and the results are compared with the ones obtained with ORB5. As discussed in chapter 2 the parallel nonlinearity is usually a second order term in the gyrokinetic ordering. However, in certain parameter regimes it might become particularly relevant and strongly modify the linear mode dynamics. In particular, it is possible to separate the different nonlinear physical mechanisms in wave-particle and wave-wave nonlinear interactions [72]. The nonlinear wave-particle interaction can be studied by including the nonlinear term only in the energetic particle Vlasov equation and neglecting it for the thermal main ion species. For a particle-in-cell code as ORB5 this means that the energetic particles are evolved along the trajectories which include perturbed terms associated with the EGAM electric field, whereas the bulk ions follow the unperturbed trajectories. By retaining the parallel nonlinearity in the thermal ion Vlasov equation, the wave-particle and wave-wave terms are both included. For this analysis only the $n = 0$ mode is retained and the energetic parti-

3.4 Global code verification

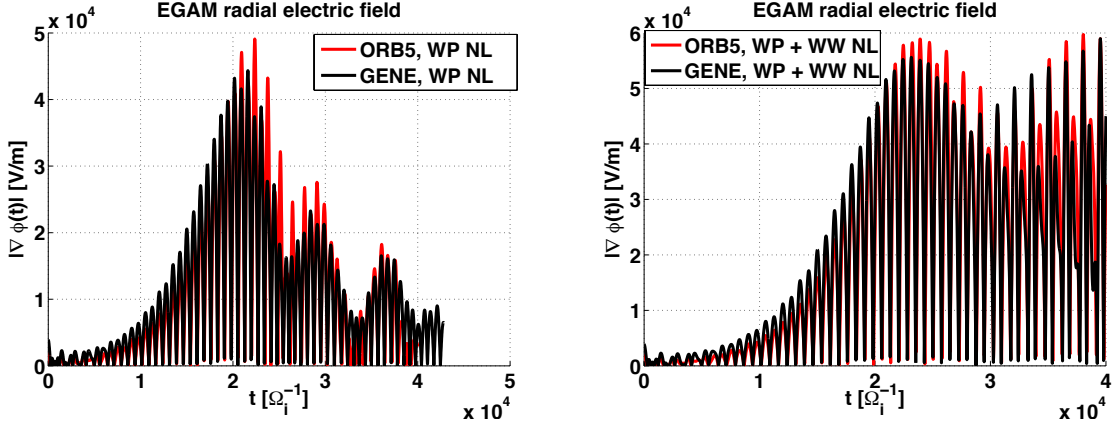


Figure 3.11: Comparison of the radial electric field at the position $\rho_{pol} = 0.5$ between GENE (black line) and ORB5 (red line) for the case $n_{EP}/n_e = 0.1$, $q = 2$ and $\rho^* = 1/128$ retaining a) only the wave-particle (WP) and b) both wave-particle and wave-wave (WW) nonlinearities.

cles are modelled with a bump-on-tail distribution functions with a symmetric shift in the parallel velocity of $\bar{v}_{\parallel} = 2.83$ in GENE units. The physical parameters as well as the numerical grid discretization are the same as the ones employed in the previous section with a flat safety factor profile of $q = 2$, $\rho^* = 1/128$ and a fast particle concentration of $n_f/n_e = 0.1$. Furthermore, the electrons are considered adiabatic. Fig. 3.11 shows the comparison of the radial electric field at the position $\rho_{pol} = 0.5$ obtained with GENE and ORB5 retaining the wave-particle (WP) and/or wave-particle, wave-wave (WW) nonlinearities. Both the codes observe a first linear phase, which does not depend on the particular nonlinear term considered, where the radial electric field grows exponentially with time reaching the value $|\nabla\phi_1| \sim 5 \cdot 10^4$. However, as soon as the linear EGAM eigenmode is fully developed, a nonlinear chirping phase (briefly introduced in chapter 1) is identified, which leads to the mode saturation. Moreover, in the case only the wave-particle nonlinearity is retained, the mode amplitude is observed to decrease with time. Fig. 3.11 shows a particularly good agreement between the GENE and ORB5 nonlinear results with only small differences in the amplitude of the radial electric field of the order of 8%.

3.5 Chapter summary

The gyrokinetic turbulence code GENE has been modified to consider arbitrary background distributions in the full electromagnetic case. While the basic derivation of the extended set of equations has been presented in chapter 2, a detailed description of the new background distributions intrinsically supported by the code has been provided in the first part of this chapter. In particular, analytical approximations to the realistic backgrounds, i.e., slowing down, bi-Maxwellian and bump-on-tail, and distributions obtained from numerical fast ion models have been introduced. Afterwards, dedicated benchmarks have been performed to test the new numerical schemes and verify the basic model against other codes which present similar features and with theoretical predictions. In particular, single magnetic surface comparisons with GS2 and GKW have been shown for an ITER standard scenario in the electrostatic limit for slowing-down distributed α particles. Furthermore, the radially global version of the non-Maxwellian GENE code has also been verified with numerical (Rosenbluth-Hinton) test and with further inter-code comparisons on the EGAM physics.

Chapter 4

Non-Maxwellian background effects in local gyrokinetic simulations

In present-day tokamak experiments, fusion-relevant temperatures are achieved via external heating systems, such as neutral beam injection (NBI) and ion cyclotron resonance heating (ICRH). The former is also used to externally drive an internal current and refuel the plasma. These schemes can generate energetic tails in the distribution functions of the heated species. The impact of these velocity (v_{\parallel}, μ) anisotropies and/or asymmetries on plasma turbulence still needs to be fully understood and investigated, since most of the studies employ Maxwellian backgrounds. In the present chapter, based on the results published in Ref. [102, 89], a particular JET plasma with strong fast-ion related turbulence suppression is revised with the new GENE code capabilities described in detail in the previous chapters. In particular, analytic approximations to the realistic fast ion distributions, i.e. slowing down and bi-Maxwellian, and numerical backgrounds, e.g. extracted from specialized heating modelling codes like SPOT/NEMO [103] (for the NBI particles) and SELFO [104] or TORIC/SSFPQL [105, 106] (for the ICRH ions) are employed. The impact of such highly non-thermalized distributions on both the linear (growth rates and frequencies) and the nonlinear (main ion, electron heat/particle fluxes and zonal flow amplitude) observables is studied.

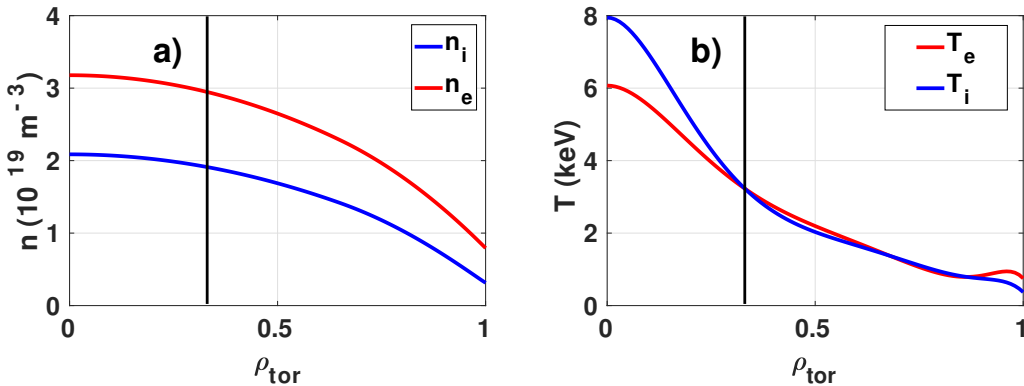


Figure 4.1: Radial profiles of main ion (blue line) and electron (red line) a) temperature and b) density reconstructed by CRONOS simulations for the JET discharge #73224. The black vertical line marks the radial position $\rho_{\text{tor}} = 0.33$, i.e. where the flux-tube simulations have been performed. Adapted from [89], with the permission of AIP Publishing.

4.1 JET - low-beta hybrid L-mode plasmas

Taking advantage of the new features of the gyrokinetic code GENE introduced in chapters 2 and 3, an experimental discharge associated to significant fast ion stabilisation is here investigated. In particular, the Carbon wall (C-wall) low-confinement mode (L-mode) plasma #73224 has been selected and extensively studied. The choice of this plasma discharge is motivated by its relevance in the plasma physics community. The first numerical evidence of the substantial effect of energetic particles in suppressing turbulence was demonstrated in Ref. [84] by performing gyrokinetic simulations for this particular JET discharge. The experiment was performed with vacuum toroidal magnetic field $B_T \approx 3.3\text{T}$ and plasma current $I_p \approx 2\text{MA}$. The safety factor q , defined in chapter 1 in Eq. (1.7), at the normalized poloidal flux $\sqrt{\psi/\psi_{\text{edge}}} = 0.95$ is equal to 6. Such large value is required close to the plasma edge region to avoid the destabilization of MHD instabilities. The heating power consisted of 3.5MW of ICRH in ${}^3\text{He}-D$ minority scheme and of 1.5MW of NBI. Furthermore, the ICRH power was deposited on-axis. The plasma was composed of bulk thermal Deuterium, electrons and Carbon impurities and of fast NBI Deuterium and ICRH ${}^3\text{He}$. An accurate description of this discharge can be found in Ref. [84, 151, 152].

The numerical gyrokinetic analyses presented in this chapter are performed by including experimental geometry, collisions (described by the Landau-Boltzmann oper-

4.2 Equilibrium distribution functions

R	\hat{s}	q	T_e/T_i	R/L_{T_i}	R/L_{T_e}	R/L_{n_e}	ν^*
3.1	0.5	1.7	1.0	9.3	6.8	1.3	0.038
n_{fD}	$n_{^3He}$	T_{fD}	$T_{^3He}$	$R/L_{T_{fD}}$	$R/L_{T_{^3He}}$	$R/L_{n_{fD}}$	$R/L_{n_{^3He}}$
0.06	0.07	9.8	6.9	3.2	23.1	14.8	1.6

Table 4.1: Parameters at $\rho_{\text{tor}} = 0.33$ for the JET L-mode discharge #73224 according to Ref. [84, 86]. Here, T represents the temperature normalized to the electron one, $R/L_{T,n}$ the normalized logarithmic temperature and density gradients and ν^* the electron-ion collision frequency normalized to the trapped electron bounce frequency.

ator introduced in chapter 2 in Eq. (2.135)), electromagnetic fluctuations and kinetic electrons. The magnetic geometry and the nominal plasma parameters, taken in the quasi-stationary state at flattop, are summarized in table 4.1 and the radial thermal density and temperature profiles, reconstructed by CRONOS [153] simulations, are shown in Fig. 4.1. The numerical simulations of this discharge are performed in the local flux-tube approximation at $\rho_{\text{tor}} = 0.33$. At this particular radial position a significant steepening of the main ion temperature profile is observed (see Fig. 4.1). It can be related to a reduction in the particle and energy fluxes and therefore to a substantial turbulence suppression. Here, the local approach appears to be justified given the low values of the ion Larmor radius normalized to the tokamak minor radius ρ_i/a , with $\rho_i = (T_i/m_i)^{1/2}/\Omega$, namely $\rho^* = 1/450$ for thermal ions and $\rho_{fast,D}^* = 1/150$, $\rho_{^3He}^* = 1/200$, respectively, for fast deuterium and helium. Therefore, global effects, involving a wider radial domain are here assumed to be negligible and not considered.

4.2 Equilibrium distribution functions

The equilibrium background distributions employed to model each plasma species of the JET L-mode plasma previously introduced are here described. In particular, a local Maxwellian is assumed for the bulk thermal species (i.e. ions and electrons). It is defined in chapter 3 in Eq. (3.1) and it reads

$$F_{0,M} = \frac{n_0}{\pi^{3/2} v_{th}^3} \exp\left(\frac{-mv_{||}^2/2 - \mu B_0}{T_0}\right). \quad (4.1)$$

Here, m is the particle mass, T_0 the equilibrium temperature, n_0 the particle density, $v_{th} = (2T_0/m)^{1/2}$ the thermal velocity and B_0 the equilibrium magnetic field. The fast ion species, on the other hand, are modelled here with the more sophisticated

4. Non-Maxwellian background effects in local gyrokinetic simulations

non-Maxwellian backgrounds introduced already in chapter 3. Thanks to these code extensions, based on the more general gyrokinetic formulation of chapter 2, GENE is able to support a large variety of different distribution functions which can be either analytical or numerical. By exploiting this feature, it is possible to capture individual asymmetries and anisotropies in the distribution function arising from the different heating schemes, which for the JET plasma at hand are both ICRH ^3He and NBI fast deuterium. In order to rigorously model the highly non-thermalized fast ions species, accurate numerical backgrounds, obtained with the SPOT/NEMO code for the NBI and the TORIC/SSFPQL and SELFO/LION+FIDO codes for the ICR-heated ions, are here employed. A detailed description on the underlying equations and numerical schemes employed by each of these codes can be found in Ref. [103, 104, 105, 106]. When the distribution function of the fast ion species is calculated with Monte Carlo methods such as SPOT/NEMO and SELFO, irregularities of the distribution functions may appear due to the finite number of test particles (markers) used in the each run, which is limited by its high computational cost. These irregularities lead to a significant increase in the error of the velocity space derivatives required by the extended version of the GENE code to correctly describe the non-Maxwellian gyrokinetic equations, as shown in chapter 2. In the analyses shown in this chapter they have been reduced by applying a 3D Gaussian filters, known as Weierstrass transformation. In more detail, the smoothed distribution functions were the result of a convolution integral, in each dimension, with a Gaussian kernel, which preserves boundaries but reduces the high-frequency components. In Fig. 4.2a) the numerical SPOT/NEMO distribution function for the NBI fast Deuterium, obtained with 4191 markers, is shown on the GENE $v_{\parallel} - \mu$ grid. A velocity space structure similar to a slowing down distribution can be identified with a cut-off velocity $v_{\parallel,c} \sim 1.5$. Furthermore, a strong velocity anisotropy between co-passing and counter-passing fast particles is observed. In the next section linear analyses are performed studying the impact of the different backgrounds on the more unstable growth rates and frequencies. Regarding the NBI fast deuterium, the results obtained with the numerical SPOT/NEMO distribution function are compared to the ones obtained with the analytic slowing-down derived in Ref. [136] and, e.g., used in Ref. [99] for modelling fusion born alpha particles. The latter is a solution of the Fokker-Planck equation with an isotropic delta-function particle source defined in chapter 3 in Eq. (3.5), i.e.

$$F_{0,s} = \frac{3n_0}{4\pi \log \left(1 + \frac{v_{\alpha}^3}{v_c^3} \right) [v_c^3 + v^3]} \Theta(v_{\alpha} - v). \quad (4.2)$$

4.2 Equilibrium distribution functions

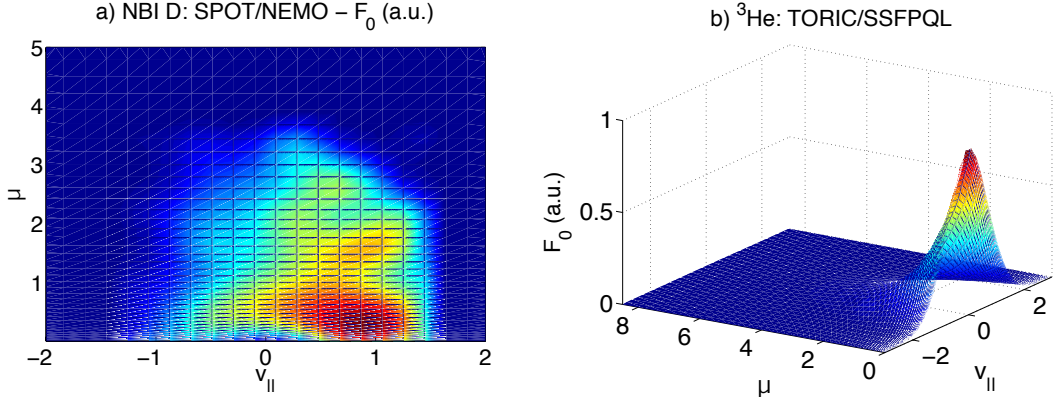


Figure 4.2: Numerical distribution functions on the (v_{\parallel}, μ) velocity grid - integrated along the field-aligned coordinate - extracted from a) NEMO/SPOT for the NBI deuterium and b) TORIC/SSFPQL for the ICRH ${}^3\text{He}$. Reproduced from [89], with the permission of AIP Publishing.

Here, the birth velocity is defined through the birth energy E_α as $v_\alpha = (2E_\alpha/m_\alpha)^{1/2}$, while $v_c = v_{th,e} \left(\frac{3\sqrt{\pi}m_e}{4} \sum_{\text{main ions}} \frac{n_i z_i^2}{n_e m_i} \right)^{1/3}$ represents the crossover velocity. Furthermore, Θ is the Heaviside step function. This isotropic background distribution is able to well capture some features of the realistic numerical background, such as the birth and cut-off velocities. However, it lacks to describe any effect related to velocity anisotropy, such as co-passing and counter-passing particles.

For the case of the ICRH ${}^3\text{He}$, on the other hand, the numerical distribution functions extracted from TORIC/SSFPQL and SELFO are used both in the linear and turbulence analyses presented in the study of this JET plasma. The here employed SPOT/NEMO and SELFO numerical distribution functions had already been used in Ref. [84] to calculate the fast ion profiles for the equivalent Maxwellian distribution function, respectively, for the NBI and ICRH-driven fast ions. In Fig. 4.2b) the phase space structure of ${}^3\text{He}$ distribution function extracted from TORIC/SSFPQL is shown on the GENE coordinate grid. No significant difference with the SELFO background is observed (not shown here). Similar to the NBI fast Deuterium, which has been approximated by a slowing down distribution (see Eq. (4.2)), an analytical approximation is employed for the ICRH generated ${}^3\text{He}$. In particular, the bi-Maxwellian distribution function defined in chapter 2 in Eq. (3.17) in the limit

4. Non-Maxwellian background effects in local gyrokinetic simulations

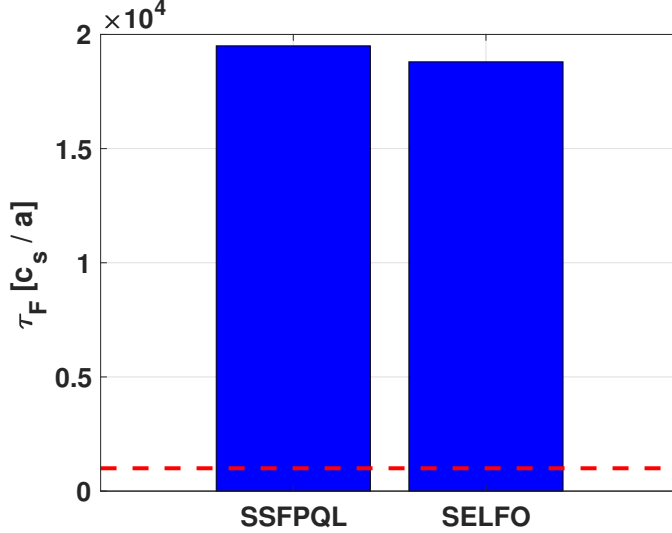


Figure 4.3: Comparison between the characteristic time scale of variation τ_{F_0} , defined in Eq. (3.27), and the average time range of GENE nonlinear simulations - red dotted line - in units of c_s/a . Adapted from [89], with the permission of AIP Publishing.

$T_{\parallel,+} = T_{\parallel,-}$, i.e.

$$F_{0,aM} = \frac{n_0}{\pi^{3/2} v_{th,\parallel} v_{th,\perp}^2} \exp\left(-v_{\parallel}^2/v_{th,\parallel}^2 - \frac{\mu B_0}{T_{\perp}}\right), \quad (4.3)$$

is used to account for the velocity space anisotropies arising from the ICRH heating. Here, T_{\parallel} and T_{\perp} are respectively the parallel and perpendicular temperatures. The $T_{\perp}/T_{\parallel} = 2.2$ and $L_{T_{\parallel}}/L_{T_{\perp}} = 3$ anisotropies have been extracted from SELFO simulations and are consistent with the ones evaluated with TORIC/SSFPQL. Furthermore, the fast particle temperatures have been defined, accordingly to the discussion in chapter 3, as the second order moment of the numerical distribution functions [99, 137], namely

$$\frac{3}{2} T_f = \frac{\int v^2 F_{0,\text{numerical}} d^3 v}{\int F_{0,\text{numerical}} d^3 v}. \quad (4.4)$$

One of the major constraints on the analytic derivation of chapter 2 is set by Eq. (2.43). The time scale of background distribution variations $\tau_{F_0} = F_0/(\partial F_0/\partial t)$, defined in Eq. (3.27), described by the zeroth order Vlasov equation should always be well separated from the turbulent time scale. The separation between turbulence time scale and time evolution of F_0 is explained in detail in section 3.2. For the anal-

4.3 Linear growth rate and frequency analyses

yses at hand, τ_{F_0} is evaluated for the numerical distributions employed throughout this study and compared with the averaged time required for GENE simulation to reach a steady-state equilibrium. Corresponding results are shown in Fig. 4.3 and demonstrate that the average time - normalized to c_s/a - required in the GENE non-linear simulations (dotted red line) to reach a saturated turbulence state is several order of magnitudes smaller than τ_{F_0} . Therefore, if F_0 is perturbed, it reaches a new equilibrium on a much longer time scale than the one turbulence needs to reach saturation for all the background distributions here considered. They can thus be assumed, with good approximation, constant in time.

4.3 Linear growth rate and frequency analyses

In this section, the impact of the more realistic distribution functions on the ITG micro-instability is addressed with dedicated electrostatic and electromagnetic GENE simulations. As already described in chapter 2, the electromagnetic field equations include finite magnetic field perturbations (i.e. $A_{1,\parallel}$ and $B_{1,\parallel\parallel}$), which are artificially suppressed in the simplified electrostatic limit. In this specific case, the only field evaluated is the electrostatic potential ϕ_1 . The effect of each of these different field components on the linear ITG physics can be investigated separately, allowing to characterize "electromagnetic" (which require finite magnetic field perturbations) and "electrostatic" (which do not require finite magnetic field perturbations) mechanisms. Although an accurate comparison with experiments can only be made with fully nonlinear analyses (see next sections), it is still possible to extract valuable information regarding the expected nonlinear sensitivity of the ITG dominated physics on the different fast ion backgrounds in a linear framework. The studies of Ref. [102], extended afterwards in Ref. [89] by including growth rates and frequencies obtained with the fast-ion numerical distribution functions are presented in this section. To resolve the fine velocity-space structure of the numerical backgrounds, 68 points have been used for both the v_\parallel and the μ GENE grids with simulations box sizes of respectively (3, 9) in normalized units. For the analytic backgrounds, 32 v_\parallel points and 48 μ points have been found to be sufficient.

4.3.1 Electromagnetic simulations

In the following paragraph, linear gyrokinetic simulations are performed retaining finite β_e electromagnetic fluctuations. First, possible effects of the NBI fast Deuterium on frequency and growth rate of the instability are studied in Fig. 4.4 for different $k_y \rho_i$ values or equivalently for different toroidal mode numbers n . The

4. Non-Maxwellian background effects in local gyrokinetic simulations

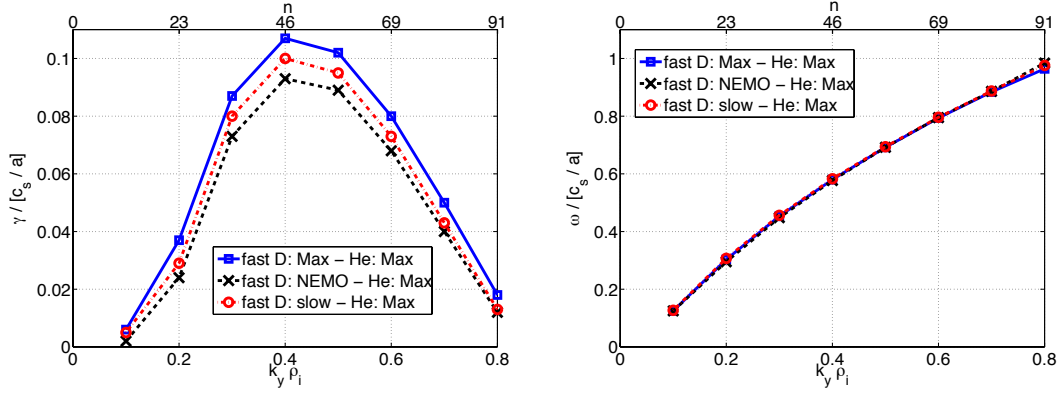


Figure 4.4: GENE calculation of the a) linear growth rates and b) frequencies against $k_y \rho_i$ (toroidal mode numbers n) for different distribution functions for the fast deuterium. Electromagnetic fluctuations are included at the nominal value of $\beta_e = 0.0033$. Reproduced from [89], with the permission of AIP Publishing.

latter is defined as follows

$$n = \mathbb{I} \left(\frac{k_y C_y L_{\text{ref}}}{\rho_{\text{ref}}} \right). \quad (4.5)$$

Here, $\mathbb{I}(A)$ represents the integer of A , C_y and ρ_{ref} are, respectively, a geometrical curvature coefficient (defined in chapter 2 in Eq. (2.50)) and the reference value of ρ_s (defined in chapter 2 in section 2.8). The growth rates and frequencies have been normalized to c_s/a with $c_s = (T_e/m_i)^{1/2}$. A low sensitivity to the change of the fast Deuterium distribution function is observed. The velocity space anisotropies, well captured only by the numerical NEMO/SPOT distribution, do not significantly modify the linear results and only a relative difference of a few percent, i.e. $\lesssim 10\%$, is observed. The slowing down distribution function seems to be a better approximation for the numerical NEMO/SPOT results than the local Maxwellian. Furthermore, for this specific choice of fast Deuterium parameters, lower growth rates are found with the more realistic distributions. A similar analysis can be performed for the ICRF-heated ^3He . All the thermal plasma species have been modelled with a local Maxwellian while the NBI fast Deuterium background is either described by a Maxwellian or a slowing down, which has been found to be the best analytical approximation to the NEMO/SPOT distribution. In Fig. 4.5, linear growth rates and frequencies are displayed for different ^3He backgrounds. A striking observation is that, contrarily to the previous results for fast deuterium, the ICRH ^3He has a significant impact on the linear ITG physics and differences of $\sim 50\%$ are observed.

4.3 Linear growth rate and frequency analyses

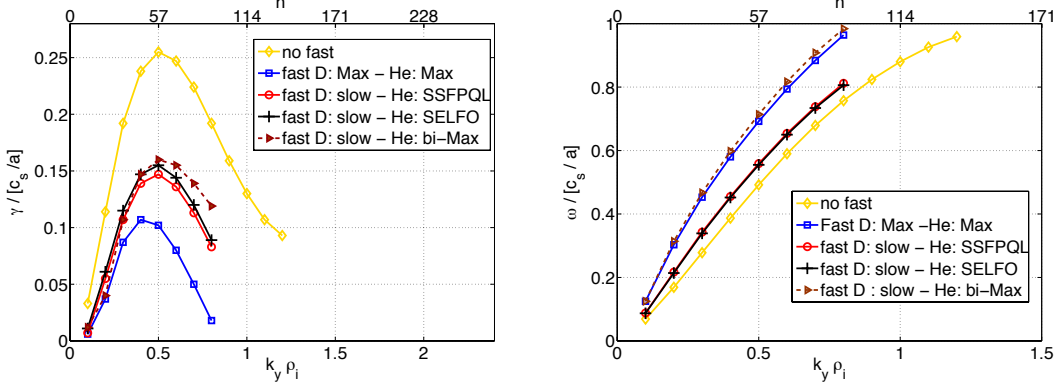


Figure 4.5: GENE calculation of the a) linear growth rates and b) frequencies against $k_y \rho_i$ (toroidal mode numbers n) for the fast ^3He . Electromagnetic fluctuations are included at the nominal value of $\beta_e = 0.0033$. Reproduced from [89], with the permission of AIP Publishing.

Moreover, with the more realistic ^3He distribution functions a weakening of the still substantial fast ion stabilisation is observed. Fig. 4.5 also contains simulation results without fast ion effects for reference. These have been obtained by consistently modifying the pressure gradient. The dominance of the kinetic effects on setting the difference between "with" and "without" fast ions has been well established from dedicated scans involving turning on and off the various physics effects (modification of drift frequency, Shafranov shift, kinetic effects) in previous work on similar discharges [154]. These results are consistent with experimental observations [83] and predict an overestimation of equivalent-Maxwellian fast-ion stabilisation for these nominal plasma parameters. According to quasilinear models an increase in the linear growth rates might lead to a relative increase of the nonlinear fluxes, greatly improving the agreement with experiments. This is further discussed in section 4.4. Furthermore, an excellent agreement between the linear results obtained with TORIC/SSFPQL and SELFO is shown in Fig 4.5. The bi-Maxwellian has been found to be a good analytical approximation for the growth rate analysis to the numerical distributions in the low $k_y \rho_i \sim 0.1 - 0.3$ wave number range, where most of the transport typically originates in nonlinear ITG simulations.

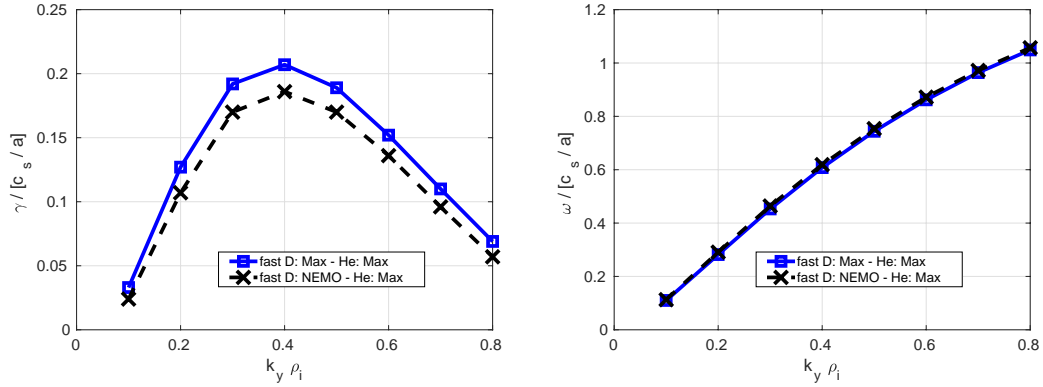


Figure 4.6: GENE calculation of the a) linear growth rates and b) frequencies against $k_y \rho_i$ for different distribution functions for the fast deuterium. Only electrostatic fluctuations are considered.

4.3.2 Electrostatic simulations

Finite β_e (electromagnetic) effects are known to lead to a progressive stabilization of the linear ITG mode with increasing β_e [155, 156]. In order to separate electromagnetic from possible electrostatic fast ion effects, the impact of the more realistic energetic particle backgrounds on the linear ITG growth rates and frequencies is also investigated in the electrostatic limit, i.e. by artificially setting $\beta_e = 0$. In this specific case, the only field component evaluated is the electrostatic potential ϕ_1 . This simplified setup allows a reduction of the physical complexity of the system and gives more insights into the effects of energetic particles on plasma microturbulence by characterizing further differences between NBI and ICRH fast ions. Similarly as for the full electromagnetic setup, the GENE growth rates and frequencies are shown for different $k_y \rho_i$ values modelling all the plasma species with a local Maxwellian and the NBI fast Deuterium with the numerical (NEMO/SPOT) distribution. No significant difference in the linear results is observed in Fig. 4.6 by changing the fast Deuterium distribution function also in the electrostatic limit (ca. $\lesssim 10\%$). The linear analyses shown in this section reveal that the linear results concerning the NBI fast particle species are only slightly affected by the presence of velocity space anisotropies. This picture changes significantly for the ICRF-heated ^3He . In Fig. 4.7, linear growth rates and frequencies are displayed for different ^3He backgrounds neglecting, however, electromagnetic fluctuations. An interesting observation is that the results obtained with the numerical backgrounds differ qualitatively from the Maxwellian ones even

4.4 Turbulence analysis

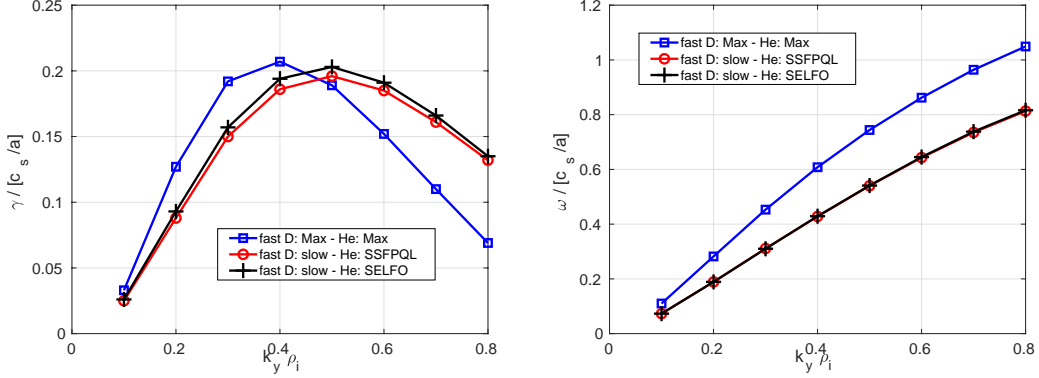


Figure 4.7: GENE calculation of the a) linear growth rates and b) frequencies against $k_y \rho_i$ for different distribution functions for the fast ^3He . Only electrostatic fluctuations are considered.

in the absence of any finite β_e effects. In particular, velocity-space anisotropies of the more realistic numerical backgrounds act on the ITG growth rates differently at each $k_y \rho_s$ scale respect to reference Maxwellian linear results. Most importantly, this analysis reveals that the ^3He and the NBI fast Deuterium affect the thermal ITG mode in different ways. In particular, non-trivial electrostatic fast ion effects, not explainable in the usual dilution framework (which is introduced in section 1.7 and is the only electrostatic fast particle effect known before our studies [133]) play here a significant role. A detailed explanation for the fast-ion turbulence stabilization discussed above will be given in the next chapters taking as reference case the JET L-mode discharge presented here. The different role of fast ions produced by NBI and ICRH heating is also elucidated in chapter 5.

4.4 Turbulence analysis

The impact of more realistic fast-ion distribution functions on the turbulent transport of the low-beta JET discharge #73224 was also studied with GENE nonlinear simulations. The physical parameters are the same as in table 4.1. The radial box size is $175\rho_i$ and the minimum finite $k_y \rho_i$ is set to 0.05. We used 192 grid points in radial direction, 48 modes in the binormal direction and 32 points along the field line. As for the linear simulations, a high velocity space resolution is required to resolve the fine velocity structure of the non-Maxwellian distribution functions. In

4. Non-Maxwellian background effects in local gyrokinetic simulations

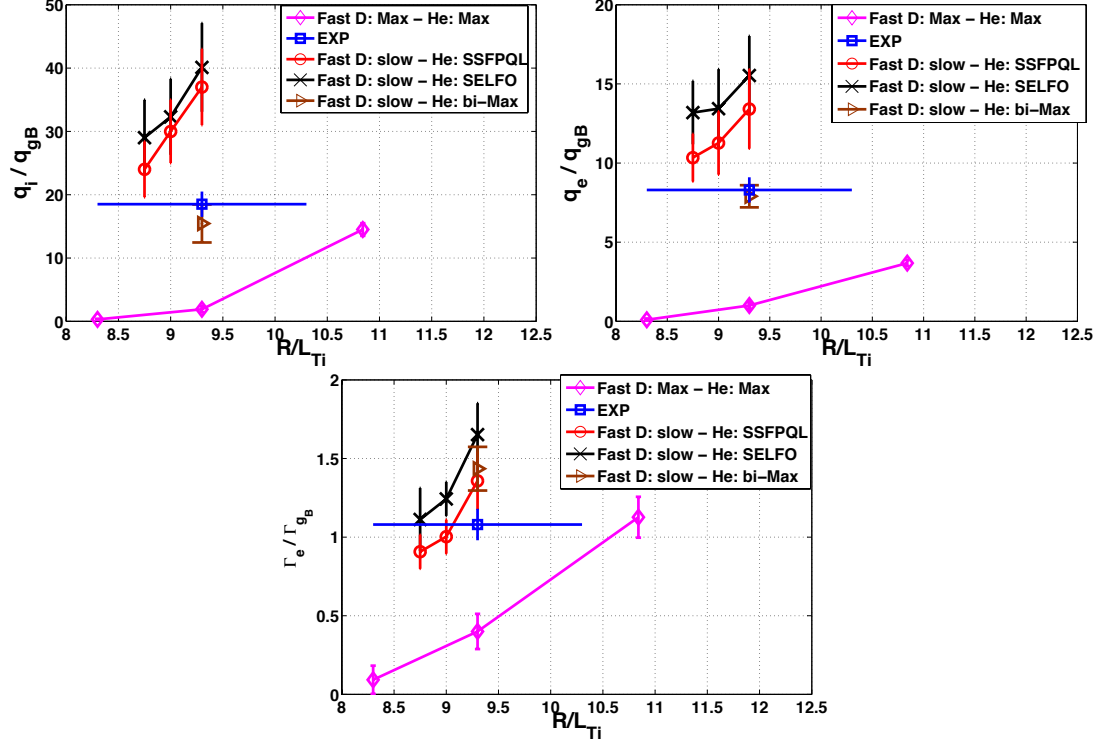


Figure 4.8: Time-averaged nonlinear a) main ion, b) electron heat and c) particle flux in GyroBohm units for different main ion temperature gradients and fast ion distribution functions. Reproduced from [89], with the permission of AIP Publishing.

velocity space, 68 Gauss-Laguerre points and 68 equidistant symmetric grid points have been used for the numerical distributions and 48, 32 for the analytical backgrounds for resolving respectively the μ and the v_{\parallel} space with a (μ, v_{\parallel}) box size of respectively (9, 3) in normalized units. The first nonlinear analysis presented in this section aims at studying the main ion and electron fluxes. In Ref. [157], it has been shown that a reasonable agreement between the numerical and the experimental values - extracted from CRONOS interpretative simulations - could only be achieved by including (in the numerical simulations) fast ions, which were modelled through an equivalent Maxwellian distribution. However, the experimental fluxes were matched only by an increase of the main ion temperature gradient of $\sim 20\%$, which may be due to an overestimation of the fast particle stabilizing effects at the nominal plasma parameters. In Fig. 4.8 a comparison between the nonlinear results

4.4 Turbulence analysis

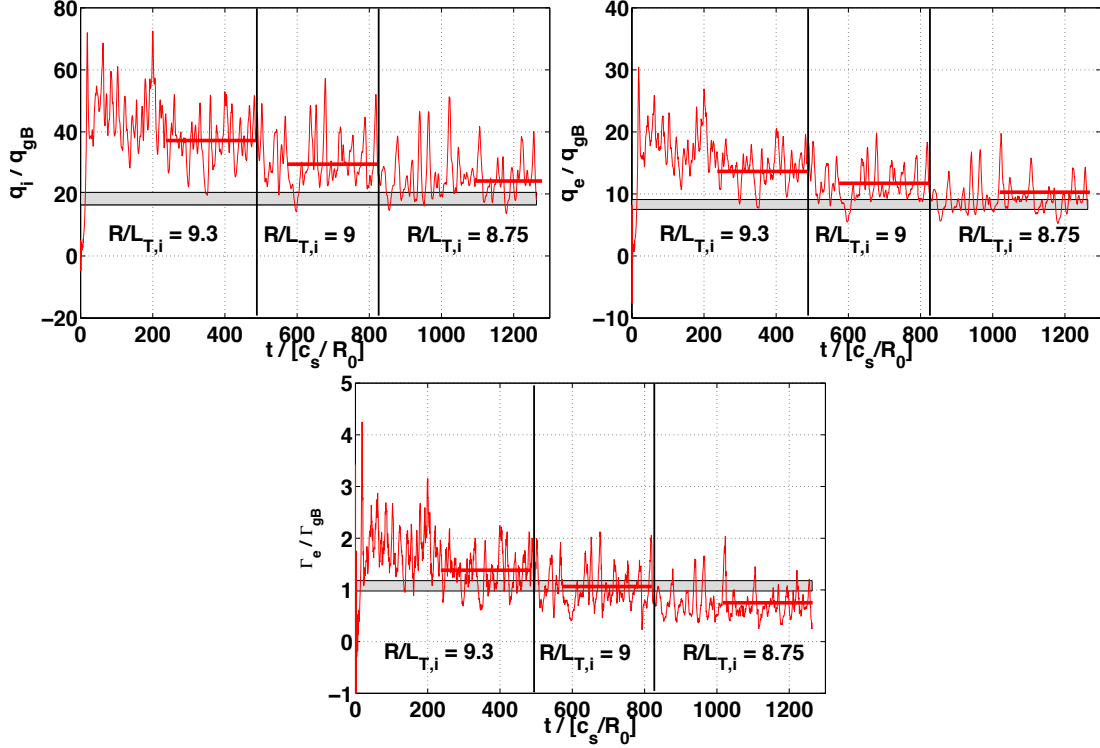


Figure 4.9: Time trace of the nonlinear a) main ion, b) electron heat and c) particle flux in GyroBohm units for different main ion temperature gradients for the case: slowing down fast deuterium and TORIC/SSFPQL fast helium. The gray area denotes the experimental value within error bars. Reproduced from [89], with the permission of AIP Publishing.

obtained with the more realistic fast ion distribution functions and their analytic approximations is shown for values of the main ion temperature gradients inside the experimental error bars. In order to keep the same notation as in Ref. [84, 151, 152], the particle and heat fluxes are normalised, respectively, to $\Gamma_{gB} = v_{th,i}\rho_i^2n_i/R_0^2$ and $Q_{gB} = v_{th,i}\rho_i^2n_iT_i/R_0^2$. Furthermore, the NBI fast deuterium has been modelled either with a local Maxwellian or with a slowing down distribution function. The values of the fluxes are computed as a time-average over the saturated state of the simulations. A significantly better agreement between numerical and experimental results is achieved with the more realistic distribution functions for the fast ion population. The experimental results are well reproduced by GENE simulations inside the temperature gradient error bars with both analytical (slowing down, bi-Maxwellian)

4. Non-Maxwellian background effects in local gyrokinetic simulations

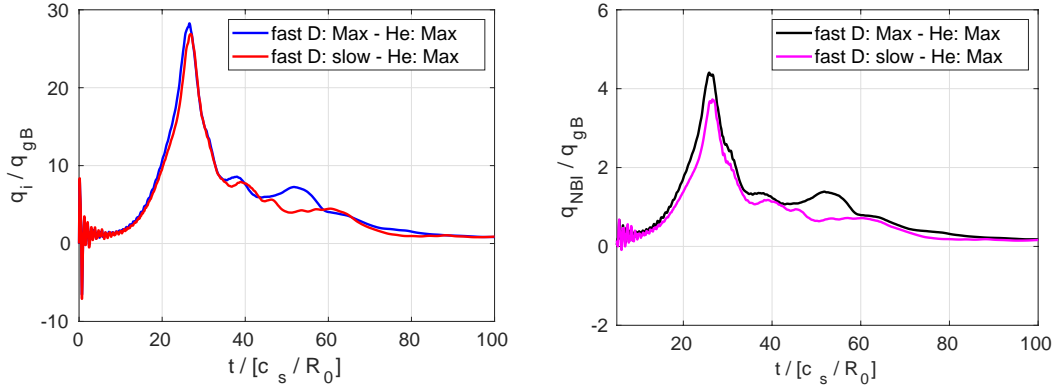


Figure 4.10: Time trace of the nonlinear a) main ion and b) NBI heat fluxes in GyroBohm units for the cases of slowing down and numerical (NEMO/SPOT) fast deuterium backgrounds at $R/L_{Ti} = 9.3$.

and numerical (SSFPQL/TORIC-SELFO) backgrounds. In line with the linear results, a corresponding "weakening" of the (still significant) fast ion stabilisation is observed and the bi-Maxwellian distribution is confirmed to be a good approximation to the more realistic backgrounds for the range of parameters here employed. In Fig. 4.9 the time trace of the main ion and electron fluxes obtained with slowing down NBI fast deuterium and numerical TORIC/SSFPQL helium is shown with the corresponding average value used for Fig. 4.8. Furthermore, a good agreement between nonlinear GENE analyses based on TORIC and SELFO could also be established. The NEMO/SPOT equilibrium was numerically challenging in the full nonlinear GENE turbulence studies. An increased number of markers is most likely required in NEMO/SPOT simulations in order to obtain a smoother numerical distribution compared to the coarse function with 4191 test particles used in this analysis. However, as shown in the previous sections, no significant difference is expected by employing the numerical backgrounds for the NBI fast deuterium. This lack of sensitivity of the numerical results on the NBI equilibrium function, based on a linear analysis, is also confirmed by GENE nonlinear turbulence simulations. Fig. 4.10 shows the time traces of the ITG-driven heat fluxes for the cases a Maxwellian or a slowing down distributions are employed to model the NBI particles. All the other species have been described with Maxwellian distribution functions. In particular, Fig. 4.10 reveals that the simulations saturate at similar steady-state values with differences of less than 3%.

4.5 Chapter summary

The impact of the different fast ion distribution functions on the nonlinear transport levels can be further investigated through the study of the zonal flow structure. It has been shown in several publications [158, 57, 159] and described in chapter 1, that zonal flows - as one of the major turbulence nonlinear saturation mechanisms - can play a significant role in the reduction of turbulent fluxes. In gyrokinetic simulations, zonal flow activity is often measured through the $E \times B$ shearing rate (defined as the radial derivative of bi-normal component of the $E \times B$ velocity) as follows

$$\omega_{\text{ZF}} = \frac{\partial}{\partial x} v_{E \times B}|_y = \frac{d^2 \phi_{\text{ZF}}}{d^2 x}. \quad (4.6)$$

Here, ϕ_{ZF} is the zonal (i.e. constant on a flux surface) component of the electrostatic potential. In Fig. 4.11, the ratio between ω_{ZF} , averaged over all the k_x mode components, and the linear growth rate at the $k_y \rho_s$ of the transport flux maximum is shown for different values of the main ion temperature gradients and for the different fast ion distribution functions used in the nonlinear analysis of Fig. 4.8. A qualitative inverse dependence between $\langle \omega_{\text{ZF}} \rangle_{k_x} / \gamma_{\text{lin}}$ and the turbulent flux levels is observed in Fig. 4.11. The zonal flow activity increases with a decrease of the main ion temperature gradients and lower fluxes are observed in GENE numerical simulations. These results suggest that the zonal flows are also affected by the more realistic fast-ion distribution functions and they are overestimated in the case of equivalent Maxwellian distributed fast ions. Although more realistic descriptions of the energetic particle species seem to affect the fast ion stabilisation of the thermal fluxes, a basic understanding of these results is still partially missing even in the limit of Maxwellian backgrounds. A prominent example, which is addressed in chapter 6, is the significant enhancement of the fast particle stabilising effects when nonlinear mode-to-mode coupling terms and electromagnetic fluctuations are both considered, as shown in Fig. 4.12. This beneficial effect is approximately a factor of 2 larger than the linear one and leads in this case to a relative reduction of ca. 97% of the electrostatic fluxes. To remove any other stabilising effect not related to nonlinear and electromagnetic fluctuations, in Fig. 4.12 the external shearing rate generated due to toroidal rotation is neglected.

4.5 Chapter summary

In the present chapter, first results obtained with the extended version of the gyrokinetic code GENE, supporting arbitrary backgrounds, are presented. In particular, a previous study of a low beta JET plasma with significant fast ion stabilisation is revised with more realistic distribution functions for the fast ion population. The

4. Non-Maxwellian background effects in local gyrokinetic simulations

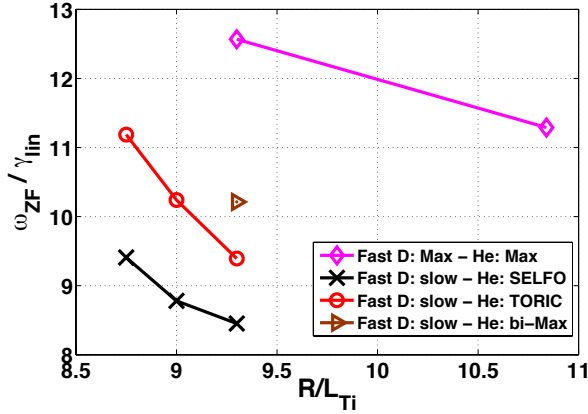


Figure 4.11: Time- k_x averaged $E \times B$ shearing rate normalised to the linear growth rate at the k_y of the transport flux maximum for different main ion temperature gradients and for different fast ion distributions. Reproduced from [89], with the permission of AIP Publishing.

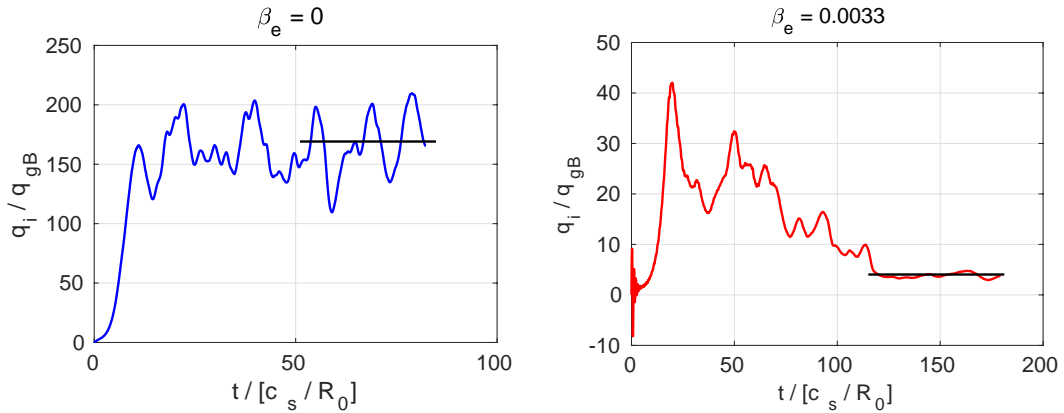


Figure 4.12: Time trace of the nonlinear main ion heat flux in GyroBohm units by employing Maxwellian distribution functions for each species at $R/L_{Ti} = 9.3$ and: a) $\beta_e = 0$ and b) $\beta_e = 0.0033$. The black line in each plots denotes the time averaged saturated values. Note that the external shearing rate is not considered here.

4.5 Chapter summary

bulk plasma is composed by Deuterium, electron and Carbon impurities, while the fast particles are NBI fast deuterium and ICRH heated ^3He . Electromagnetic effects, collisions and experimental geometry are taken into account in the simulations.

In the linear analysis it is found that with the more realistic distribution functions, the fast ion stabilisation still holds, even if it is weakened. This is in line with previous nonlinear findings (based on equivalent-Maxwellian backgrounds for the fast-ion species) where gradients higher than the nominal ones had to be employed in order to match the experimental heat fluxes in the presence of fast particles [84]. The impact of the different non-Maxwellian backgrounds is studied separately on each fast ion species and a lack of sensitivity to the NBI fast ion distribution is observed. On the contrary, the choice of the ^3He background distribution - particular, its anisotropies and asymmetries - has a stronger impact on the linear results than the fast deuterium backgrounds. Moreover, linear analyses have shown non-trivial electrostatic fast particles effects on ITG micro-instability which cannot be explained by the standard dilution theory. Dilution does not depend on the particular velocity-structure of the energetic particle distribution but only on their background density.

The weakening of the energetic particle stabilisation with the more realistic background is also confirmed by GENE nonlinear simulations. An improved agreement between the experimental and numerical results is achieved for the main ion and electron fluxes at the nominal plasma parameters when more realistic fast-ion distribution functions are employed. Additionally, for the range of parameters considered here, the bi-Maxwellian and the slowing down distributions are shown to be good approximations for the fast helium and deuterium numerical backgrounds. A good agreement between nonlinear GENE results obtained using TORIC/SSFPQL and SELFO distribution functions is confirmed. This analysis provides further element of confidence on the reliability of these two codes and verify their basic models. In particular, beside the different numerical schemes and underlying equations, self-consistent energetic particle backgrounds are obtained. Preliminary studies suggest that the choice of the background distribution function has also an impact on the level of zonal-flow activity.

Chapter 5

Resonant interaction of energetic ions with plasma micro-turbulence

The numerical investigation shown in the previous chapter, based on the JET L-mode discharge #73224, has shown electrostatic and electromagnetic non-trivial energetic particle effects on the ITG growth rates. In particular, even when electromagnetic fluctuations have been neglected, the GENE results differed significantly from the theoretical expectations, which predict only dilution effects. Moreover, the different fast particle species, i.e. NBI fast deuterium and ICRH ^3He , have been shown to act differently on the thermal ITG. For this reason, chapter 4 motivates a deeper analysis on the interaction between fast particles and plasma instabilities in the electrostatic limit which is here tackled. The electrostatic fast particle stabilisation is studied with both numerical simulations and a reduced Vlasov theoretical model. To better understand this electrostatic energetic ion mechanism, equivalent Maxwellian backgrounds are first employed to model fast ions. Only afterwards this assumption is relaxed and the effects of anisotropies and asymmetries on the linear results is discussed. The present study shows that significant stabilisation of micro-turbulence can be achieved even neglecting any electromagnetic fluctuations and in a linear/quasi-linear framework. It is found that fast particles can actively modify the Poisson field equation (even at low fast particle density and high temperatures) through a resonance mechanism with the main instability. The main dependences of such mechanism are investigated and the validity of the simplified model here developed is discussed. The latter can well reproduce the numerical findings and can easily be used for future extrapolations and interpretations.

5.1 Introduction

Before the theoretical and numerical works of Ref. [133, 90], the main fast particles electrostatic effect on the plasma micro-turbulence was expected to be dilution [80]. As briefly described in chapter 1, the zeroth order quasineutrality condition is indeed passively modified by the presence of fast particles. In particular, the density of thermal ions able to drive anomalous transport at the typical ITG-scales is reduced with a consequent improvement of plasma confinement. This effect depends only on the fast particles charge concentration and it is independent from the velocity structure of the energetic particle backgrounds. In a low fast ion density regime, their dynamics is not expected to contribute to the perturbed electrostatic potential and often in gyrokinetic simulations the fast particle trace approximation is used to reduce the computational effort [160, 137]. The trace assumption consists in neglecting the energetic ion contribution to the perturbed field equations (however retaining the effect of dilution) and treating them only as passive tracers. It is justified by the hypothesis that fast particles are much more energetic than the bulk plasma and for low fast particle density the interaction with the thermalised species is practically negligible. However, as already predicted by Holland and co-authors [82] even at low fast particle density there might be a strong interaction with the background microturbulence. A significant difference in the linear growth rates obtained with another gyrokinetic code called GYRO [161] was indeed observed between cases of active (retaining fast ions in the perturbed Poisson equation) and passive (neglecting fast ions in the perturbed Poisson equation) fast particle species, suggesting an additional interaction mechanism which can not be explained by dilution. However, no physics explanation for this behaviour was given up to now.

In the following chapter, the parameter range of validity of the trace approximation and the dynamic effect that fast particles might have on the plasma micro-instability are discussed for the realistic low-beta JET discharge analyzed in chapter 4. It is found that fast particles can contribute to the development of plasma micro-turbulence and modify the main ion response to temperature and density gradients even at low density and high fast particle temperatures through a linear wave-particle resonance mechanism [99, 138, 133, 90]. This dynamic effect depends strongly on the fast particles species and parameters and is observed also including electromagnetic fluctuations. Despite the essentially linear nature of the resonant interaction, a corresponding nonlinear analysis is also performed here and its main dependences captured with a quasi-linear model. Both numerical results obtained with the gyrokinetic code GENE and a reduced theoretical Vlasov-Poisson model are presented in this chapter.

5.2 Numerical observation - temperature scan

One of the main parameter which characterizes energetic particles is their particularly large equivalent temperature T_f . Therefore, a numerical analysis that might provide significant insights over the nature of the peculiar electrostatic fast ion results observed in the previous chapter requires a temperature scan over the energetic particle temperature. For this reason, in this first section of this chapter, linear electrostatic simulations are performed with the gyrokinetic code GENE by varying the temperature of the fast ion species from the values $T_f \sim T_e$ to $T_f \sim 40T_e$. The code is used as an initial value solver, initializing a perturbation at a fixed wave number and studying the linear growth rate and frequency of the unstable mode solution. The plasma parameters considered for this analysis are the same employed in chapter 4 (see table 4.1). They are taken from the JET L-mode hybrid discharge with both NBI-deuterium and ICRF heated ^3He [151, 152] and with substantial fast ion effects [84]. We used 32 grid points in radial direction and 24 points along the field line. In velocity space, 32 points and 24 equidistant symmetric grid points have been used for resolving, respectively, the μ and the v_{\parallel} space with a (μ, v_{\parallel}) box size of respectively (9, 3) in normalized units. The simulations are performed in the same flux-tube domain of chapter 4, justified by the small Larmor-radius-to-minor-radius ratio which evaluates to $\rho_i^* = 1/450$ for thermal ions and $\rho_{f,D}^* = 1/150$; $\rho_{^3\text{He}}^* = 1/200$, respectively, for fast deuterium and helium. All simulations shown in this chapter are electrostatic, unless noted otherwise and employ a realistic Miller [12] equilibrium.

The linear growth rates normalized to c_s/a - with a minor radius of the device - are shown in Fig. 5.1 as a function of (a) the fast ^3He and (b) the fast deuterium temperature. All the linear simulations presented here are performed at a fixed wave number of $k_y\rho_s = 0.5$. The linear ITG growth rates are found to be strongly affected by the different fast particle temperatures and this effect cannot be explained in the usual dilution framework, which predicts a dependence only on the fast particle charge concentration. Furthermore, a striking observation is the different temperature behaviour between the various fast particle species. In particular, a sharp growth rate reduction, with a maximum stabilisation of $\sim 60\%$ at $T_f \sim 12T_e$, is found for the ICRH helium, which becomes less significant by further increasing the fast particle temperature. On the contrary, the fast deuterium shows a slowly monotonic growth-rate reduction with $\sim 25\%$ at $T > 39T_e$. The black cross in each graph corresponds to the linear electrostatic growth rates for the nominal fast particles temperatures. Regarding the mode frequencies, smaller changes are observed in Fig. 5.2, with a relative variation of $\sim 15\%$ for the helium case and $\sim 7\%$ for the fast deuterium one. Furthermore, Fig. 5.2 reveals a different fast particle temperature

5. Resonant interaction of energetic ions with plasma micro-turbulence

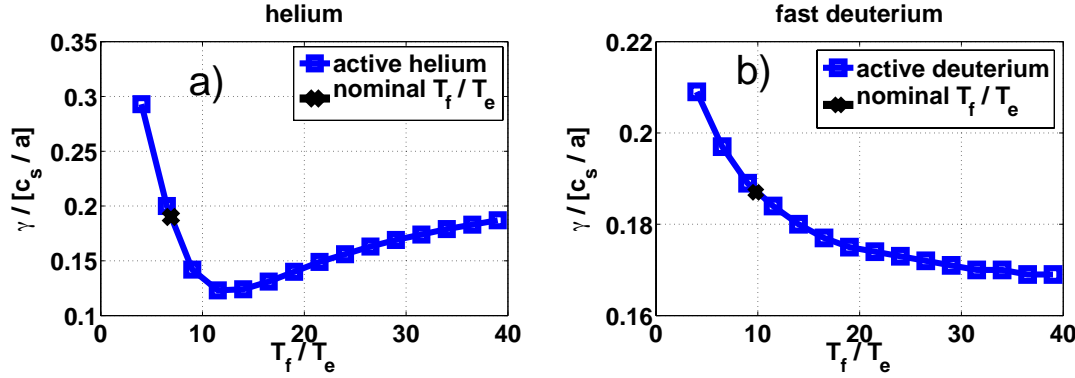


Figure 5.1: GENE calculations of the linear growth rates as a function of the fast particle temperature in the five species setup: a) fast helium temperature scan; b) fast Deuterium temperature scan. The black-cross shows the nominal fast particle temperature.

behaviour compared to the growth rate analysis shown previously. Therefore, these interesting results trigger several questions that need to be addressed in the rest of this chapter:

1. What is the electrostatic physical mechanism responsible for the ITG growth rate/frequency temperature dependences observed in Figs. 5.1-5.2?
2. Why does the beneficial fast ion effect on the ITG growth rates depend on the nature of the energetic particle species?
3. Can this new fast ion stabilizing effect be optimized in view of future fusion reactor like ITER? and what are the key fast particle parameters?

To facilitate the analyses required to answer each of the previous points, only a single fast particle species – e.g., either NBI fast deuterium (in the following called deuterium setup) or ICRH 3He (in the following called helium setup) – will be retained at a time while the bulk plasma is composed of deuterium and electrons. All the physical parameters are kept the same as the one of table 4.1 even in the reduced setups. Carbon impurities are not expected to significantly impact the linear dynamic and will be neglected. In Fig. 5.3 the same qualitative temperature dependences found in Fig. 5.1 for the full realistic case are observed. For the 3He setup, a pronounced growth rate reduction of about $\sim 50\%$ at $T_f \sim 12T_e$ is found compared

5.2 Numerical observation - temperature scan

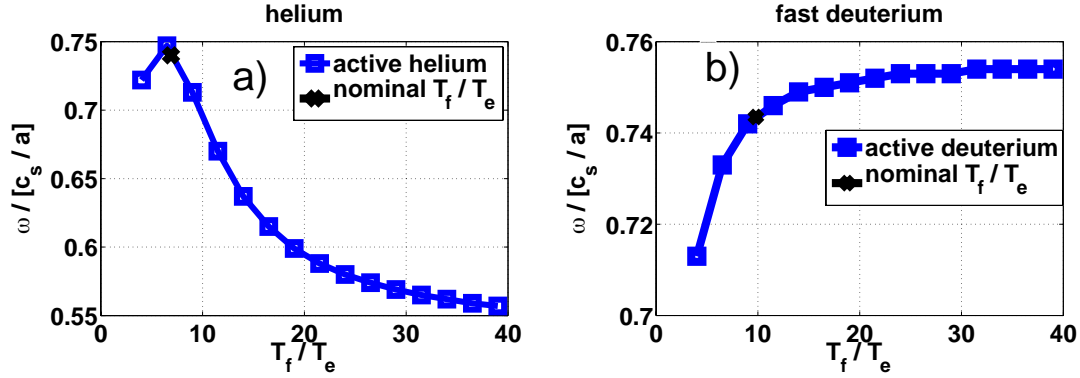


Figure 5.2: GENE calculations of the linear frequencies as a function of the fast particle temperature in the five species setup: a) fast helium temperature scan; b) fast Deuterium temperature scan. The black-cross shows the nominal fast particle temperature.

to the case without fast particles and of about $\sim 30\%$ compared to a pure dilution case. The latter is obtained neglecting fast ions only in the perturbed quasineutrality equation. For the fast deuterium case a slowly monotonic growth-rate reduction is observed of about $\sim 20\%$ at $T_f > 39T_e$. The fast particles add a positive contribution (with respect to the dilution case) to the main ITG drive which rapidly decays to zero when the fast particle temperature is increased. In both cases, dilution is recovered at very high temperatures. This result could imply that highly energetic fusion alpha particles, i.e. $T_f \sim 80T_e$, may be described by dilution only. However, due to the particularly large α -particle temperature, a radially global approach (retaining the full radial dependences) is most likely required. Furthermore, Fig. 5.3 also contains simulation results without fast ion effects for reference. These have been obtained by consistently modifying the overall geometrical pressure gradient. The dominance of the kinetic effects on setting the difference between with and without fast ions has been well established from dedicated scans involving turning on and off the various physics effects (modification of drift frequency, Shafranov shift, kinetic effects) in previous work on similar discharges [154]. As for the full five species analysis shown previously, the mode frequency is found to have a weaker dependence on the fast particle temperature compared to the growth rates. The active fast particle contribution to the main ITG dynamic is investigated also through the study of the phase angle between the electrostatic potential and main ion density perturbation. As explained in detail in Ref. [11], is often studied to characterize the main drive of

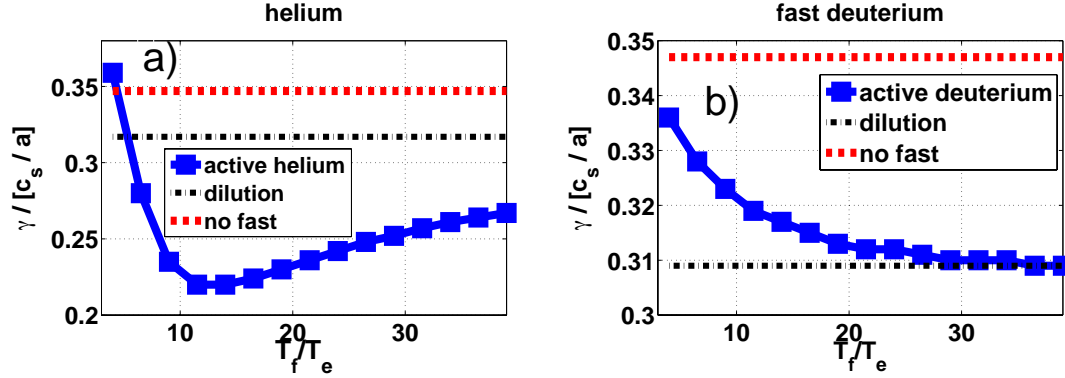


Figure 5.3: GENE calculations of the linear growth rates as a function of the fast particle temperature in the three species reduced setup: a) fast helium temperature scan; b) fast Deuterium temperature scan. The black-dotted and red lines show, respectively, the dilution and the no fast particle growth rates. Reproduced from [133], with the permission of IAEA.

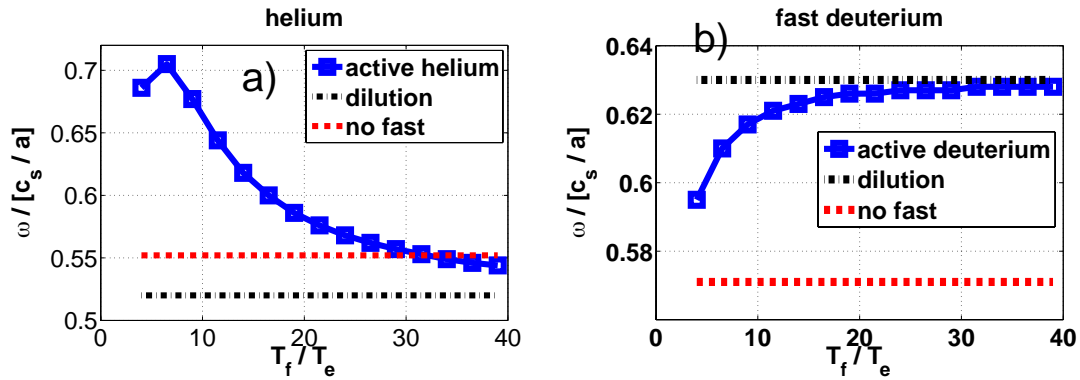


Figure 5.4: GENE calculations of the linear frequencies as a function of the fast particle temperature in the three species reduced setup: a) fast helium temperature scan; b) fast Deuterium temperature scan. The black-dotted and red lines show, respectively, the dilution and the no fast particle frequencies.

5.2 Numerical observation - temperature scan

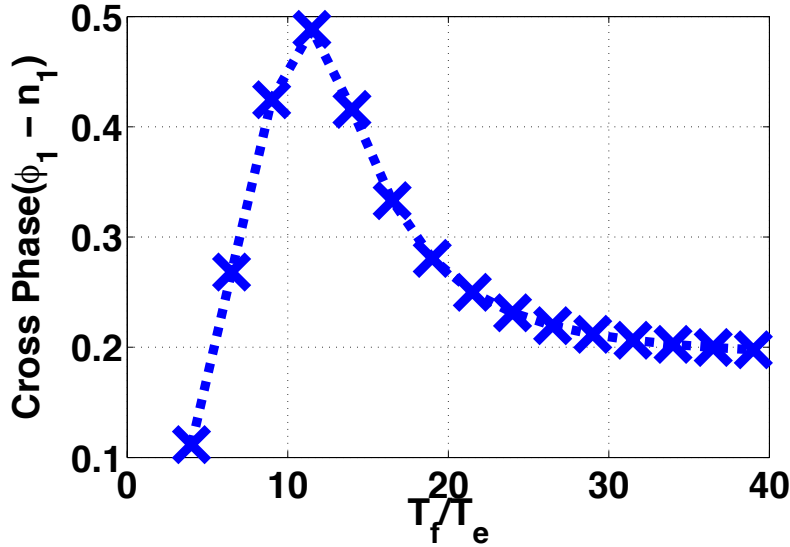


Figure 5.5: GENE calculation of the cross phase (in rad) between the perturbed electrostatic potential and the main ion density perturbation for different fast particle temperatures. It is taken at $z = 0$ performing a time average. Adapted from [90], with the permission of AIP Publishing.

typical micro-instabilities. For example, if it is close to multiples of π the main ion species are not expected to contribute to the linear drive (for example in a purely ETG scenario). On the other hand a maximum contribution is predicted if the phase relation is zero. Therefore, the study of the phase angle can be used as a measure of the fast particle stabilization on the ITG. In Fig. 5.5 the numerical cross phase between the main ion density perturbation and the electrostatic field is shown for different fast ion temperatures. In case of no active interaction between the fast particles and the main drive of the ITG instability, a constant cross phase would be expected for different fast particle temperatures. However, a non constant behaviour is observed from Fig. 5.5. The fast particles can significantly modify the electrostatic field ϕ_1 . The maximum of this interaction for the Deuterium - Electrons - fast helium setup is again observed around 12 times the electron temperature. In correspondence of this temperature, the fast helium can strongly contribute to the main instability modifying the electrostatic field both in terms of magnitude and phase. In case of passive fast particles a zero cross phase angle between ϕ_1 and $n_{i,1}$ is obtained.

5.3 Theoretical simplified model

The linear, electrostatic numerical setup employed in the previous section allows a further investigation of the energetic particle effects on plasma micro-turbulence with a simplified analytic model. As discussed in chapter 2, the most unstable linear growth rates are computed in GENE by consistently solving the Vlasov equation for each plasma species and the electrostatic field component ϕ_1 . Fast ion effects on the most unstable linear mode are hence represented by modifications of the thermal species response to any initial perturbation in the normalized Poisson field equation (see Eq. (2.87)). Here, the energetic particle contribution is determined by the zeroth-order moment of their perturbed distribution function $F_{1,f}$. It evolves in time accordingly to the Vlasov equation (see Eq. (2.66)). In the electrostatic, i.e. $\bar{A}_{1,\parallel} = \bar{B}_{1,\parallel} = 0$ and collisionless limit, it can be written in the GENE field aligned coordinate system (x, y, z) as follows

$$\begin{aligned} \frac{\partial F_1}{\partial t} = & -\frac{C}{JB_0} v_{th} v_{\parallel} \left[\partial_z F_1 - \frac{q}{2T_0 v_{\parallel}} \partial_z \bar{\phi}_1 \frac{\partial F_0}{\partial v_{\parallel}} \right] + \frac{C}{JB_0} v_{th} \frac{\mu}{2} \partial_z B_0 \frac{\partial F_1}{\partial v_{\parallel}} \\ & + \frac{T_0}{q} \left(\frac{\mu B_0 + 2v_{\parallel}^2}{B_0} \right) \mathcal{K}_x \hat{\partial}_x F_0 - \frac{T_0}{q} \left(\frac{\mu B_0 + 2v_{\parallel}^2}{B_0} \right) \mathcal{K}_y \partial_y F_1 \\ & + \left[\frac{1}{2v_{\parallel}} \frac{\partial F_0}{\partial v_{\parallel}} \left(\frac{\mu B_0 + 2v_{\parallel}^2}{B_0} \right) \mathcal{K}_y - \frac{1}{C} \hat{\partial}_x F_0 \right] \partial_y \bar{\phi}_1 \\ & - \frac{T_0}{q} \left(\frac{\mu B_0 + 2v_{\parallel}^2}{B_0} \right) \mathcal{K}_x \partial_x F_1 + \frac{1}{2v_{\parallel}} \frac{\partial F_0}{\partial v_{\parallel}} \left(\frac{\mu B_0 + 2v_{\parallel}^2}{B_0} \right) \mathcal{K}_x \partial_x \bar{\phi}_1. \end{aligned} \quad (5.1)$$

The neoclassical terms have been neglected, since they are not expected to affect the time evolution of $F_{1,f}$ and furthermore evolve entirely independently in the flux-tube limit. The individual right hand side terms of Eq. (5.1) are hence the parallel advection, the trapped particle, the radial (x) and bi-normal (y) curvature and the background drive. The contribution of each of the terms of Eq. (5.1) to the overall stabilising fast-ion effect observed in Figs. 5.1-5.5 can be investigated by artificially removing them from the gyrokinetic fast particle Vlasov equation directly in the code GENE. Fig. 5.6 demonstrates that the trapped fast-particle, the parallel dynamic and the radial curvature terms play only a minor role in the linear ITG growth rate suppression for the ${}^3\text{He}$ setup. These results are consistent with previous observations in different plasma regimes [138]. A simplified electrostatic linear Vlasov equation for the fast ion species, can then be written by removing the negligible terms as

5.3 Theoretical simplified model

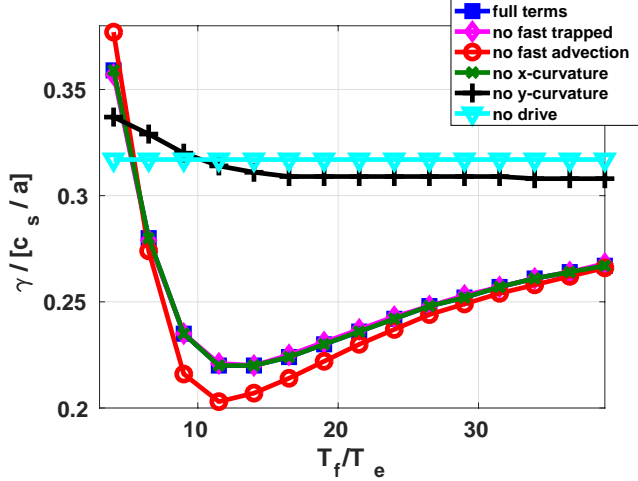


Figure 5.6: GENE calculation of the linear ITG growth rates obtained by artificially suppressing terms in the fast particle Vlasov equation. Reproduced from [90], with the permission of AIP Publishing.

follows

$$\frac{\partial F_1}{\partial t} = -\frac{T_0}{q} \left(\frac{\mu B_0 + 2v_{||}^2}{B_0} \right) \mathcal{K}_y \partial_y F_1 + \left[\frac{1}{2v_{||}} \frac{\partial F_0}{\partial v_{||}} \left(\frac{\mu B_0 + 2v_{||}^2}{B_0} \right) \mathcal{K}_y - \frac{1}{C} \hat{\partial}_x F_0 \right] \partial_y \phi_1. \quad (5.2)$$

Employing a plane wave ansatz for the perturbed quantities, i.e. the electrostatic potential ϕ_1 and the perturbed distribution function F_1 , of the form

$$\phi_1(x, y, z) = \sum_{k_x, k_y} \phi_1(k_x, k_y, z) e^{-i\omega t + i(k_x x + k_y y)}, \quad (5.3)$$

the following simplified Vlasov equation for each wave vector \mathbf{k} and frequency $\omega = -\omega_r + i\gamma$ can be derived

$$F_{1,f} = \frac{k_y \bar{\phi}_1 \left[\frac{1}{2v_{||}} \frac{\partial F_0}{\partial v_{||}} \left(\frac{\mu B_0 + 2v_{||}^2}{B_0} \right) \mathcal{K}_y - \frac{1}{C} \hat{\partial}_x F_0 \right]}{\omega_r - i\gamma + \frac{T_f}{q} \left(\frac{\mu B_0 + 2v_{||}^2}{B_0} \right) k_y \mathcal{K}_y}. \quad (5.4)$$

The real frequency ω_r is defined with a minus sign to account for the default sign convention in GENE where positive values indicate modes propagating in the ion

diamagnetic-drift direction. Furthermore, for all the simulations performed in this chapter, the term $\partial F_0 / \partial v_{\parallel} \mathcal{K}_y (\mu B_0 + 2v_{\parallel}^2) / (2v_{\parallel} B_0)$ is found to be negligible if compared to $(\hat{\partial}_x F_0) / C$ and is erased for the rest of the theoretical analysis. Although a simplified isotropic Maxwellian distribution function is employed throughout most of this chapter to model the energetic particle population, Eq. (5.4) is written for a general background distribution function F_0 . For the specific choice of an equivalent Maxwellian distribution, the x - and v_{\parallel} -derivative terms evaluate to

$$\hat{\partial}_x F_M = \left[\frac{R}{L_n} + \frac{R}{L_T} \left(v_{\parallel}^2 + \mu B_0 - \frac{3}{2} \right) \right] F_M, \quad (5.5)$$

and

$$\frac{1}{2v_{\parallel}} \frac{\partial F_M}{\partial v_{\parallel}} = -F_M \quad (5.6)$$

in normalized units.

5.4 ITG/energetic particle resonant interaction

The physical mechanism responsible for the interaction between fast particles and linear ITG instability can be investigated with the simplified model derived in the previous section. From Eq.(5.4) it is obvious that the main contributions to the fast particles' F_1 come from the background drive term (temperatures and density gradients), i.e. $\hat{\partial}_x F_0$ and from the y -curvature term. Similar results are also observed in different plasma regimes and numerical setups [99, 138]. Moreover, Eq. (5.4) suggests that a certain fraction of fast particles can "resonate" with the background micro-instability, where with the term "resonance" we denote that the real part of the denominator of Eq. (5.4) is zero, i.e.

$$\omega_r = -\frac{T_0}{q} \left(\frac{\mu B_0 + 2v_{\parallel}^2}{B_0} \right) k_y \mathcal{K}_y. \quad (5.7)$$

This condition corresponds to the minimum of the denominator of Eq. (5.4) and hence to the maximum fast ion response in the Poisson's equation. Furthermore, it is worth noting that the drive term in the numerator of Eq.(5.4) does not depend on the fast particle temperature and is fixed by the magnetic geometry and by the fast particle gradients. A wave-particle interaction can then be expected if the ITG mode frequency is close enough to the fast particle magnetic-drift frequency. In order for this condition to occur, the y -curvature term \mathcal{K}_y must be negative. A

5.4 ITG/energetic particle resonant interaction

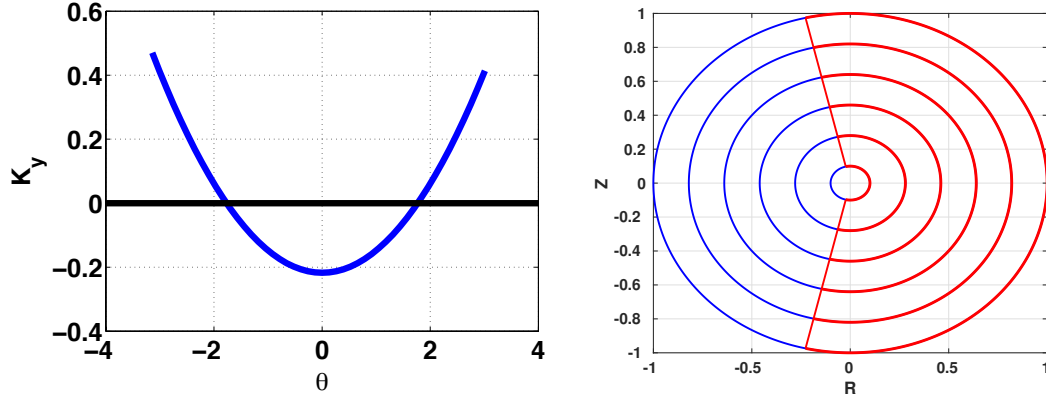


Figure 5.7: a) Toroidal geometrical coefficients K_y extracted from GENE for different binormal angles. In the GENE field aligned coordinate system, the y direction corresponds to the toroidal coordinate. The black line corresponds to $K_y = 0$; b) Circular concentric flux-surfaces in the straight-field line coordinate system. The poloidal region marked in red denotes the values where $K_y < 0$.

range of the straight-field line angle θ can be identified where $K_y < 0$ (typically on the low-field-side (LFS), also called "bad-curvature" region of Fig. 1.7). According to Eqs. (5.4-5.7), Fig. 5.7a) shows that, for the parameters of the JET discharge studied in chapter 4, no resonant interaction can occur if $\theta \leq -1.8$ or $\theta \geq 1.8$, i.e. beyond the zeroes of K_y . The velocity and poloidal dependence of the wave-fast particle resonance can be investigated with both the reduced Vlasov model and the numerical GENE results in the 3He setup. For this analysis the numerical simulations have been performed neglecting collisions, their role is found to be negligible for the resonant fast particle stabilisation mechanism studied here. In Fig. 5.8 the real part of F_1/ϕ_1 is shown in the $v_{\parallel} - \theta$ plane for different values of the magnetic moment μ . The analysis of F_1/ϕ_1 allows a direct comparison between the numerical and the analytical results. The latter, indeed, cannot describe the evolution of field component ϕ_1 , which requires the full dispersion relation. In the case of large values of μ the resonance position is found for values of θ which are close to K_y . Small values of K_y and v_{\parallel} are needed in presence of high μ in order for the fast particle magnetic-drift frequency to match the linear ITG mode frequency (see Fig. 5.8b)). A decrease in the magnetic moment leads to a respective increase of the values of v_{\parallel} and K_y required for the resonance (Fig. 5.8a)), which is found for a broad range of $v_{\parallel} - \theta$ values with a maximum at $\theta = 0$. These results are perfectly reproduced by the reduced Vlasov model, Fig. 5.8c)-d). The aforementioned studies aim at

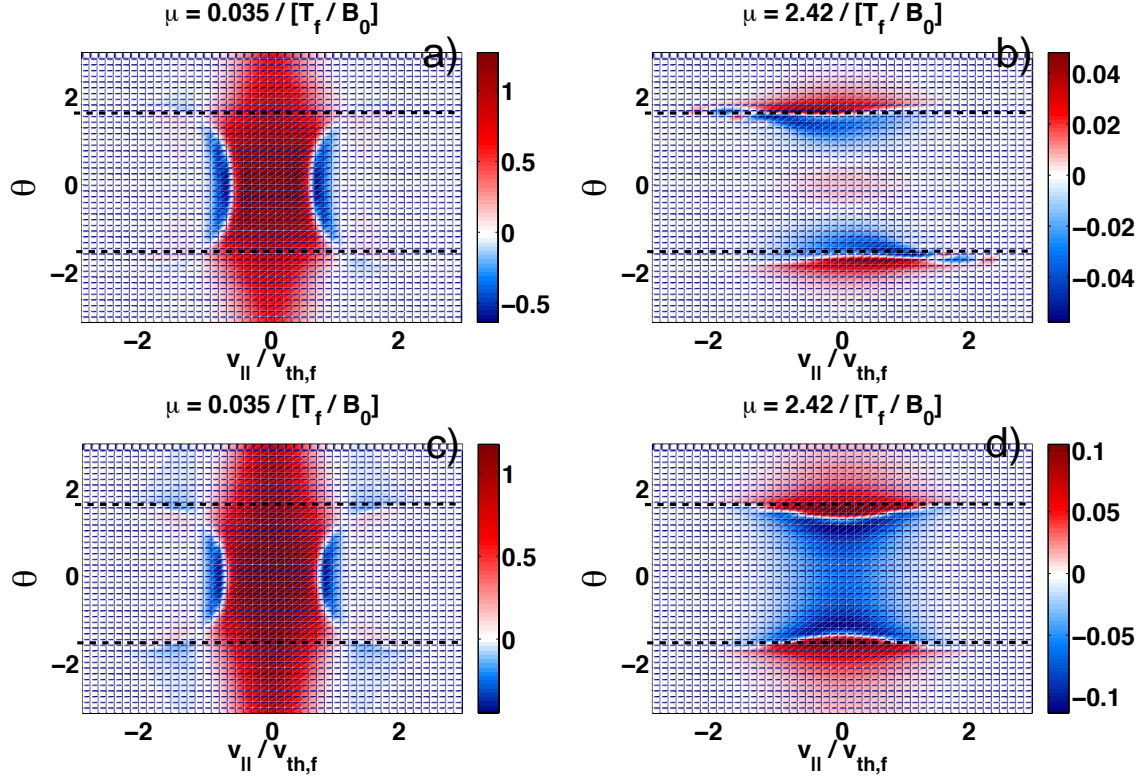


Figure 5.8: Real part of the ratio F_1/ϕ_1 obtained from GENE linear electrostatic simulations for different values of magnetic moment: a) $\mu = 0.035$; b) $\mu = 2.42$ and from the reduced Vlasov model for different values of magnetic moment: c) $\mu = 0.35$; d) $\mu = 2.42$ in the $v_{\parallel} - \theta$ space. Figures a) and b) are reproduced from [133], with the permission of IAEA.

5.4 ITG/energetic particle resonant interaction

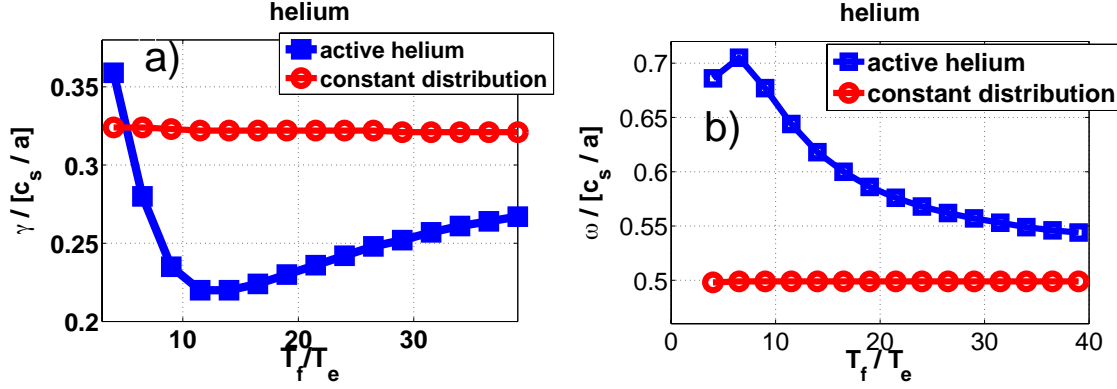


Figure 5.9: GENE calculations of the linear growth rates a) and frequencies b) as a function of the fast particle temperature in the three species setup for the case of a Maxwellian fast helium background (Blue line) and for a constant fast helium background (Red line).

demonstrating the presence of a wave-fast particle interaction and describing its main dependences. This interaction has similar features to the ion Landau Damping. The fast ion resonance, however, depends not only on the particle velocities, but also on the magnetic geometry and on the fast particles temperature and charge. Fast particles with velocity comparable to the phase velocity of the mode can interact with it and a net energy transfer between the wave (linear micro-instability) and the fast particle population might occur. This energy exchange is modified by the magnetic geometry, in particular by the y -curvature term. According to this picture, no interaction is expected in the presence of an energy-independent fast particle distribution function. In Fig. 5.9 linear growth rates are shown for different fast helium temperatures, modelling the fast particles background distribution function with the constant distribution function $F_0 = n_0 / (l_v l_\mu)$. Here, n_0 represents the fast particle density and l_v and l_μ , respectively, the extension of the simulation box in the $v_{||}$ and μ directions. These results are compared with the linear growth rate obtained with a Maxwellian distribution function (Fig. 5.3). As expected, constant growth rates are observed. The constant background F_0 can also be obtained from a slowing down distribution function with small birth energy.

5.5 Fast particle contribution to energy exchange

According to the reduced Vlasov model developed in the previous section, a resonance between energetic particles and micro-turbulence is expected if the linear frequency of the bulk-ion mode approaches the fast ion magnetic-drift frequency. Correspondingly, a net energy transfer between wave and particles occurs. Both the direction and magnitude of the energy exchange can be investigated for each values of the fast particle temperature through the time evolution of the system free energy E_{fe} . The latter, as shown in chapter 2, is defined as the sum of the kinetic E_k (see Eq. (2.141)) and field E_w (see Eq. (2.142)) contributions [134, 128]. The time derivative of E_{fe} represents the free energy balance equation, which determines the energy flow in the whole simulation. As shown in detail in Refs. [128, 129] and in chapter 2, the potential (see Eq. (2.145)) and kinetic (see Eq. (2.144)) parts of the overall energy balance can be written as

$$\frac{\partial E_k}{\partial t} = \sum_s \Re \left\{ \int dz d\mu dv_{||} \frac{\pi B_0 n_{0,s} T_{0,s}}{F_{0,s}} F_{1,s}^{k,*} \frac{\partial F_{1,s}^k}{\partial t} \right\}, \quad (5.8)$$

$$\frac{\partial E_w}{\partial t} = \sum_s \Re \left\{ \int dz d\mu dv_{||} \pi B_0 q_s n_{0,s} \bar{\phi}_1^{k,*} \frac{\partial F_{1,s}^k}{\partial t} \right\}. \quad (5.9)$$

An effective linear growth rate [135], related to the exponential growth of the main plasma micro-instability, can be defined starting from Eqs. (5.8-5.9),

$$\gamma = \sum_s \gamma_s = \frac{1}{E_w} \sum_s \frac{\partial E_{w,s}}{\partial t}. \quad (5.10)$$

This definition allows a separation of the contribution of each species (s) to the overall linear growth rate and to identify resonance effects in phase space by studying the velocity ($v_{||}, \mu$)-kernel of γ_s . Here, positive (negative) values of γ_s indicate that the plasma species considered is giving (taking) energy to (from) the electrostatic field component with a consequent growth (damping) of the mode. A reduced expression for the energetic particle contribution to the growth rate γ_f can be derived by employing the plane wave ansatz defined in the previous section and the simplified fast ion perturbed distribution function $F_{1,f}$ of Eq. (5.4), namely

$$\gamma_f = -\frac{1}{E_{pot}} \left\{ \int dz dv_{||} d\mu \pi n_f J_0^2 |\phi_1^k|^2 T_f (2v_{||}^2 + \mu B_0) k_y^2 \mathcal{K}_y \frac{\gamma}{\mathcal{C}} \right\}$$

5.5 Fast particle contribution to energy exchange

$$\frac{\left[\frac{R}{L_{n,f}} + \frac{R}{L_{T,f}} \left(v_{\parallel}^2 + \mu B_0 - \frac{3}{2} \right) \right] F_M}{\left(\omega_r + \frac{T_f}{q_f} \left(\frac{\mu B_0 + 2v_{\parallel}^2}{B_0} \right) k_y \mathcal{K}_y \right)^2 + \gamma^2}. \quad (5.11)$$

The resulting expression reveals that the energetic ion contribution to the overall energy production or dissipation is maximized in correspondence to the minimum of the denominator of Eq. (5.4), therefore leading - potentially - to substantial modifications of the bulk instability. As explained in the previous section, the bi-normal curvature term \mathcal{K}_y must be negative in order to fulfill the resonance condition of Eq. (5.7) in ITG-dominated scenarios. A first direct consequence of this observation is that the sign of γ_f is entirely determined by the radial derivative of the energetic particle background distribution function. For the case of an equivalent Maxwellian background, the latter depends strongly on the energetic particle temperature and density gradients. A detailed analysis on these parameters is presented in section 5.7.4. For small values of T_f , the fast ion magnetic-drift frequency $\omega_{d,f}$ is usually smaller in magnitude than the mode frequency and no significant resonance effects are expected. A negative and hence stabilising contribution of the fast particle to the overall growth rate is predicted from the reduced model presented in this section, for values of the fast particle energy satisfying $v_{\parallel}^2 + \mu B_0 < 3/2$. This contribution becomes destabilizing for fast particle energies $v_{\parallel}^2 + \mu B_0 > 3/2$. This is also confirmed in actual GENE simulation results. Fig. 5.11a), shows indeed that the resonance position identified by the reduced Vlasov model, i.e. Eq. (5.7) (black line), moves in velocity space as the fast ion temperature is increased. It should be noted that this shift of the resonance curve is due to the fact that it is expressed in terms of the normalized velocities. Higher temperatures lead hence to smaller normalized values of v_{\parallel} and μ satisfying the resonance condition. The resonance significantly modifies the structures of γ_f maximizing the background drive term contribution. The maximum stabilisation is then expected in correspondence of the fast ion temperature which brings the resonance to the minimum of the background drive term. This picture is clarified by the schematic cartoon of Fig. 5.10. As shown in Figs. 5.11a)-c), this temperature is identified for $T = 12T_e$ which is in agreement with the numerical GENE results. A further increase in the fast particle temperature moves the resonance to smaller energies, which leads to a less effective stabilization.

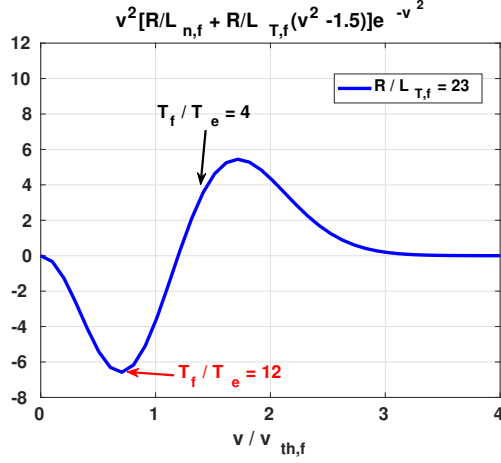


Figure 5.10: Cartoon of the helium drive term contribution in Eq. (5.11) connected with the wave-fast particle resonance for the logarithmic energetic ion gradient $R/L_{T,f} = 23$. The resonance position at $T_f = 4T_e$ and $T_f = 12T_e$ are indicated as reference, respectively, by a black and red arrow.

5.6 Impact of magnetic shear

The wave-fast ion resonance mechanism described in the previous sections depends strongly on the binormal y -curvature term \mathcal{K}_y . It localizes the resonant interaction in phase space and sets a threshold condition for the particle to interact with the ITG-drift wave (as shown in Fig. 5.8). In this section, the role of \mathcal{K}_y will be further analyzed by changing the value of the magnetic shear \hat{s} , i.e. the radial derivative of the safety factor q on the flux surface of interest (see definition in Eq. (1.8)). An analytic approximation for \mathcal{K}_y is given in the limit of a simple shifted circular (often called s- α) geometry and reads $\mathcal{K}_y \sim -\cos(z) - \hat{s}z \sin(z)$, with z field-aligned coordinate [138]. This definition shows that the main geometrical parameter which determines the shape of the y -curvature term \mathcal{K}_y is the magnetic shear and it does not affect the amplitude of \mathcal{K}_y at $z = 0$. The s- α approximation is able to reproduce shifted circular magnetic equilibrium. However, it lacks other magnetic-flux surface shaping contributions, such as elongation, triangularity. Therefore, in many realistic studies aiming to reproduce the experimental observations, more accurate geometrical models are required, e.g. Miller (briefly introduced in chapter 1).

In Fig. 5.12 the analytical predictions of \mathcal{K}_y in the s- α and Miller models are compared. A qualitative good agreement is observed. Nevertheless, the simplified

5.6 Impact of magnetic shear

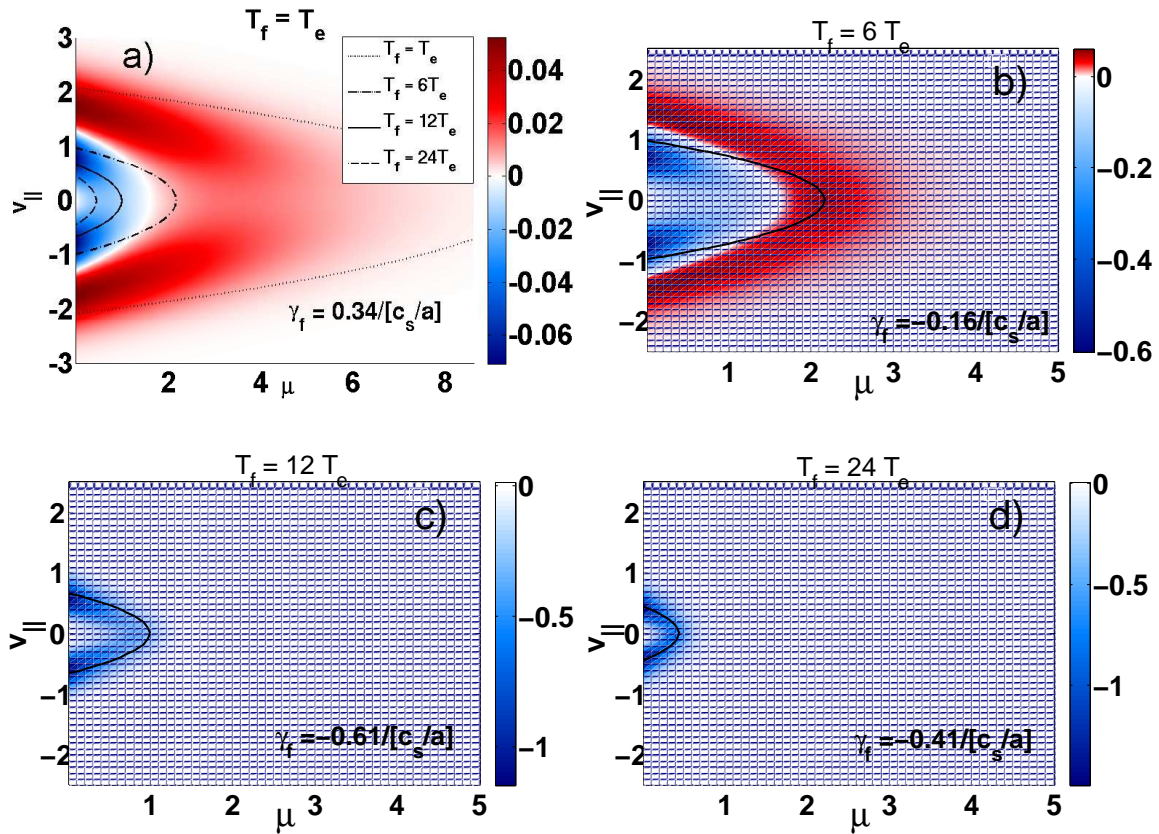


Figure 5.11: Converged fast particle γ_f velocity space structure from GENE at low field side for a) thermal, b) $T_f = 6T_e$, c) $T_f = 12T_e$ and d) $T_f = 24T_e$ helium. The black contour lines indicate the resonance positions according to the reduced Vlasov model for different temperature ratios. The corresponding value of the velocity space averaged growth rate contribution is included in the lower right of each plot. Figures a) and c) are reproduced from [133], with the permission of IAEA.

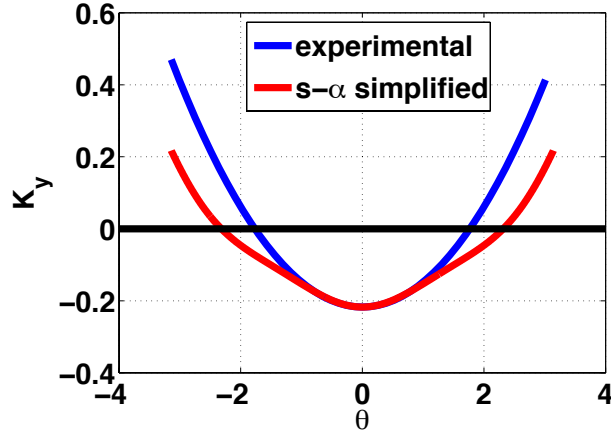


Figure 5.12: Toroidal geometrical coefficients K_y extracted from GENE (blue line) and an analytic first order approximation (red line) for different binormal angles. The black line corresponds to $K_y = 0$.

analytic model slightly overestimates the position of the zeroes of K_y , as shown in Fig. 5.12. To analyze the impact of the magnetic shear on the linear ES resonant microturbulence suppression observed previously, linear simulations have been performed in the simplified helium setup for different values of the magnetic shear and fast ion temperatures. Since the change in the magnetic geometry also affects the thermal ITG, to investigate the relative effect of the shear only on the resonance stabilisation, the linear growth rates have been normalised to the ones obtained in the case without fast ions. They are shown in Fig. 5.13. The strongest fast particle stabilisation can be observed for $s = -0.4$. As shown in Fig. 5.13b), a decrease in the magnetic shear leads indeed to a further localization of the wave-particle resonance in the bad curvature region strengthening the fast ion contribution to the linear growth rates [90]. The thermal ITG is maximum at $z = 0$. The contribution of the triangularity, q profile and other geometric coefficients is not expected to significantly affect the fast particle dynamic and the resonance mechanism.

5.7 Influence of energetic ion properties

In the previous sections, the resonance mechanism presented in this chapter has been described with a reduced model able to capture the main dependences observed in the GENE linear simulations. According to this model, the wave-fast ion stabiliza-

5.7 Influence of energetic ion properties

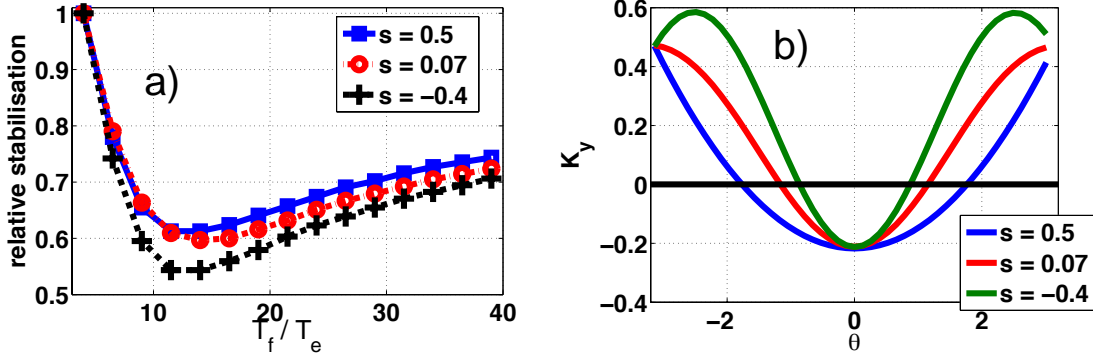


Figure 5.13: a) GENE calculation in the Deuterium - Electron - fast helium setup of relative fast ion stabilization for different values of the magnetic shear. Growth rates are normalised to the value at $T_f = 4T_e$. Normalization factors: $\gamma_{s=0.5} = 0.359c_s/a$, $\gamma_{s=0.07} = 0.315c_s/a$, $\gamma_{s=-0.4} = 0.252c_s/a$; b) Different toroidal geometrical coefficients K_y extracted from GENE for each value of the shear. The black line corresponds to $K_y = 0$. Detailed information about the Miller equilibria can be found in Ref. [86]

tion is the result of a wave-fast-ion resonance term, which maximizes the otherwise negligible energetic particle contribution in the Poisson equation. Eq. (5.7) shows that the phase space position of the resonance depends on the charge and mass of the energetic particle species. Aiming for further exploitation of the stabilizing effect, it is hence obvious to explore the impact of the various fast ion properties. Therefore, numerical scans over the fast particles charge (in electron-charge units), mass (in deuterium-mass units) and over different temperature and density radial profiles are performed in the present section, comparing to reference parameters given in table 4.1. Moreover, the analytic predictions of the reduced model, derived in the previous sections, will be further validated.

5.7.1 Fast ion charge dependence

The first parameter analyzed here is the fast particle charge. It directly affects the magnetic-drift frequency and thus the phase-space position of the wave-fast particle resonance. Moreover, it enters in the field equation as a weight to the energetic particle density perturbation and modifies the fast particle Larmor radius corrections. The dependence of the fast particle resonant stabilization on the energetic ion charge is investigated in this section with linear electrostatic simulations. The reference phys-

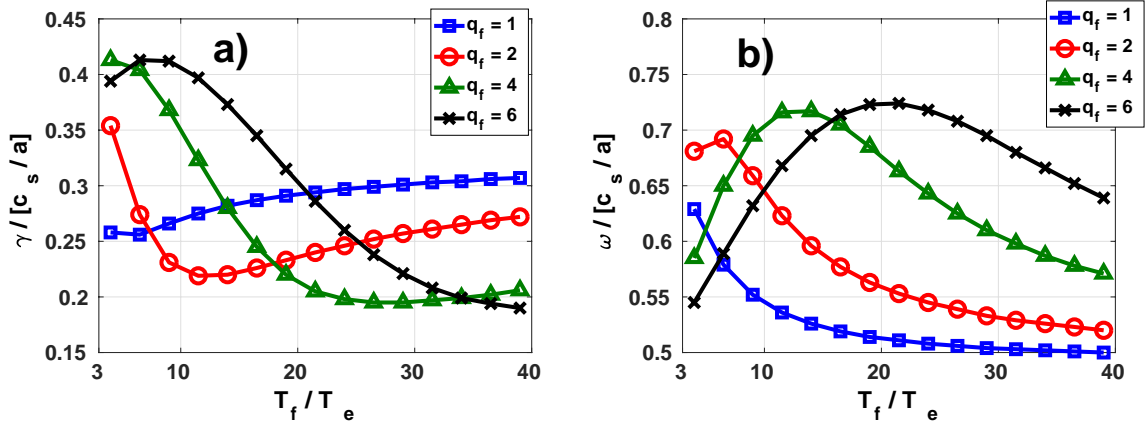


Figure 5.14: a) Growth rates and b) frequencies as a function of the fast particle temperature T_f/T_e and charge q_f (expressed in units of the proton charge) at $k_y\rho_s = 0.5$. The fast particle charge concentration is fixed to $q_f n_f = 0.14n_e$. Reproduced from [90], with the permission of AIP Publishing.

ical parameters are the same as in Tab. 4.1 for each value of the fast particle charge employed throughout this section, which is the only parameter changed. Moreover, the charge concentration is always kept fixed to the value $q_f n_f = 0.14n_e$. The choice of keeping a constant charge concentration is particularly convenient to isolate the charge dependence of the resonance mechanism from other electrostatic physical effects, i.e. mainly dilution. Fig. 5.14 shows the temperature behaviour of the linear ITG growth rates and frequencies for different values of q_f . It reveals that the charge of fast particles can significantly affect the growth rate, with relative changes up to 50%. The real frequency, on the other hand, experiences weaker modifications of about 20%. In particular, the strongest linear growth rate reduction is observed for the largest energetic particle charge, which is consistent with the reduction of the argument of the zero order Bessel functions. For the same charge concentration, an increase in the fast ion charge is hence reflected in a corresponding increment in the energetic particle contribution in the Poisson field equation and thus to an increase of its beneficial effect. However, arbitrarily high charge would be unrealistic in experimental conditions and a corresponding optimization would need to consider further limitations. Another interesting observation is that the energetic particle temperature corresponding to the minimum of the linear growth rates moves towards higher values as the fast ion charge increases. This result is in agreement with the theoretical

5.7 Influence of energetic ion properties

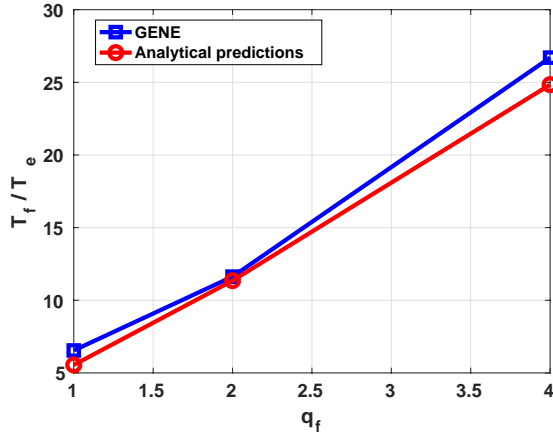


Figure 5.15: Comparison of the numerical (GENE - blue line) and analytic predictions (red line) of the fast ion temperature corresponding to the most stable linear growth rate for different fast particle charge. The fast particle charge concentration is fixed to $q_f n_f = 0.14 n_e$. Reproduced from [90], with the permission of AIP Publishing.

predictions of the reduced model of Eq. (5.4), (5.7). In the limit for which the mode frequency is only slightly affected by the change in the fast particle charge, Eq. (5.7) imposes a constraint over the fast ion temperature required to fulfill the resonance interaction, i.e. the ratio T_f/q_f must be kept constant. Fig. 5.15 shows a particular good agreement between the numerical GENE results and the analytic prediction of the optimal fast ion temperature which maximizes the ITG linear suppression. The frequencies used in the analytic model are taken from the GENE simulations.

5.7.2 Fast ion mass dependence

A second parameter which characterizes different fast ion species is their mass (m_f), which is not expected to significantly affect the resonance position according to the reduced theoretical model presented previously. Nevertheless, it enters in the argument of the Bessel functions. In particular, an increase in m_f leads to larger finite Larmor radius effects and thus to smaller energetic particle contributions to the overall electrostatic field. The impact of the mass on the linear growth rates and frequencies is shown in Fig. 5.16. The physical parameters are the same of Tab. 4.1 and the charge concentration is kept to $q_f n_f = 0.14$. As predicted, the magnitude

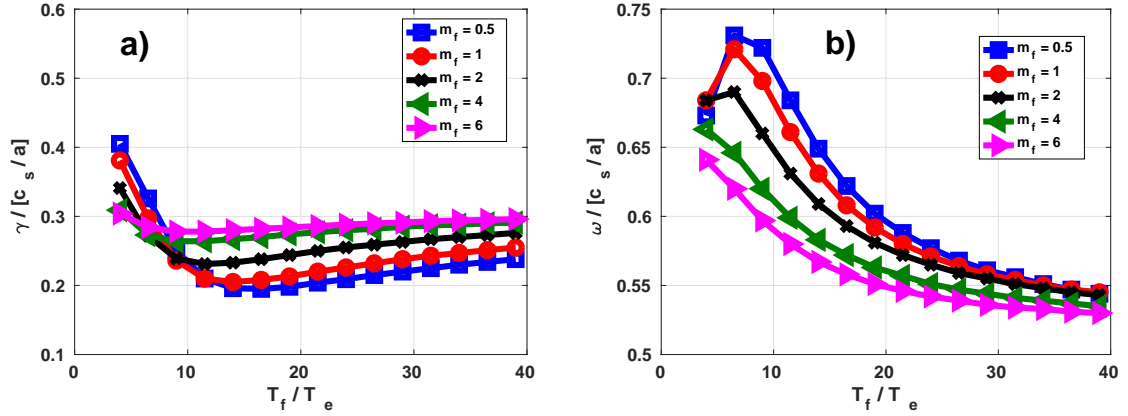


Figure 5.16: a) Growth rates and b) frequencies as a function of the fast particle temperature T_f/T_e and mass m_f (expressed in units of the deuterium mass) at $k_y\rho_s = 0.5$. The fast particle charge concentration is fixed to $q_f n_f = 0.14 n_e$. Reproduced from [90], with the permission of AIP Publishing.

of the linear ITG growth rate reduction decreases by increasing the fast particle mass and almost disappears for the value of $m_f = 6$. Moreover, Fig. 5.16 shows only minor modifications on the fast ion temperature related to the more effective ITG stabilization. These results are in agreement with the theoretical predictions, where only minor modifications are expected due to changes in the real frequency ω_r of the more unstable mode. Therefore, an enhancement of the ITG fast particle stabilisation through resonant effects is predicted for ions with smaller mass. These results align well with the experimental need to use light energetic ions. Indeed, for a fixed injected external power, ions with smaller inertia can be more easily accelerated at specific energies.

5.7.3 Combined effect of fast ion charge and mass

The identification of the fast particle species which maximizes the ITG/fast-ion beneficial interaction is addressed in this section. The balance of the complex effects of mass - that increases the argument of the Bessel function as $\sqrt{m_f}$ - and charge - which impacts on the position of the resonance and reduces the argument of the Bessel function- is investigated. Fig. 5.17 shows the linear temperature dependences of growth rates in a three species setup with deuterium, electron and different fast ion species, considered as ^2D , ^3He , ^7Li and ^9Be . Here, the fast particle charge con-

5.7 Influence of energetic ion properties

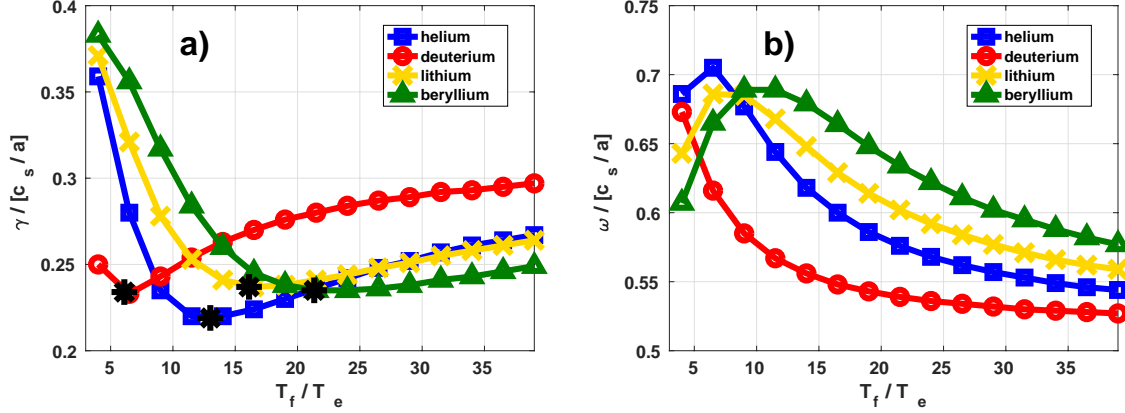


Figure 5.17: a) Growth rates and b) frequencies as a function of the fast particle temperature T_f/T_e for different fast ion species at $k_y\rho_s = 0.5$. The fast particle charge concentration is fixed to $q_f n_f = 0.14 n_e$. Reproduced from [90], with the permission of AIP Publishing.

centration is fixed at $q_f n_f = 0.14$. The parameters are the same as in Tab. 4.1 and the bi-normal wave number is chosen at the maximum ITG growth rate, namely $k_y\rho = 0.5$. Fig. 5.17 reveals that the minimum growth rates change significantly with the fast particle species. In particular, at $T_f < 9T_e$, the minimum ITG linear growth rate is observed for the fast deuterium. In the range between $9 < T_f/T_e < 20$ helium shows the highest stabilization while lower growth rates are observed for beryllium at higher temperature. In Fig. 5.17 the black cross on each line corresponds to maximum fast ion stabilization predicted with Eq. (5.7). The predicted fast ion temperature related to the maximum stabilization and the numerical GENE results are in perfect agreement. Only minor modifications on the ITG mode frequencies are instead observed. As already mentioned before, these results depend significantly on the fast particles temperature, density gradients and on the magnetic geometry. The numerical analysis presented in this section relies on the assumption that the different energetic particle species have the same gradients and have the same impact on the plasma geometry.

5.7.4 Impact of fast ion temperature and density gradients

As shown previously, the maximum stabilization is found when the helium temperature is such that the drift velocity of the mode matches the minimum in the drive

5. Resonant interaction of energetic ions with plasma micro-turbulence

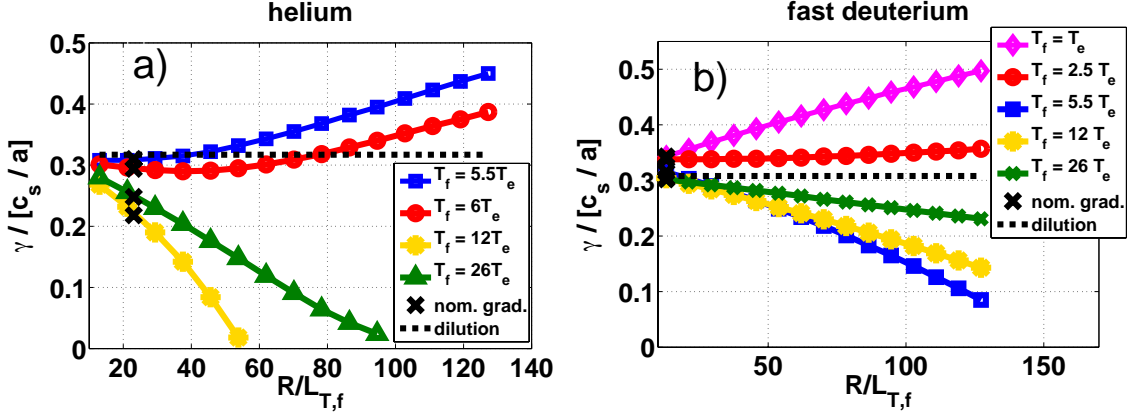


Figure 5.18: Growth rates obtained from GENE for different fast helium a) and fast deuterium b) temperature and temperature gradients. The black dotted lines indicate the pure dilution results. Figure a) is reproduced from [133], with the permission of IAEA.

term as expressed by Eqs. (5.5-5.11). This particularly favorable region in phase-space is found for the parameters used in this section around $T_f/T_e = 12$. The findings in Fig. 5.3a) can therefore be interpreted both qualitatively and quantitatively as results of the combined drive and wave-fast ion interaction on the helium contribution of the overall growth rate. Moreover, from Eq. (5.11) a relation between the fast particle density and temperature gradients and the ITG mode stabilization can be established. In order to maximize the resonant stabilization and have a large fast particle induced negative contribution to the ITG growth rate the relation $\eta_f^{-1} = \frac{R}{L_n} / \frac{R}{L_T} < 1.5$ must be fulfilled. This condition is obtained in the limit of zero fast particle energy (i.e. $v \rightarrow 0$) and corresponds to the minimum condition in order to establish a negative drive. As the ratio of the density and temperature gradients decreases, the fast particle resonant stabilization becomes more significant. This result is in agreement with the limited stabilizing effect due to fast deuterium ions apart from dilution, as observed in Fig. 5.1b), since the ratio $\eta_f^{-1} \sim 5$ in this case and the fast deuterium drive term is positive for all energies. According to the model described before, the stabilizing effect of the fast particles requires at the same time that (a) the minimum of the background drive term (see Eqs. (5.5-5.11)) is negative (this being controlled by the ratio η_f^{-1}) and (b) the wave-fast-ion resonance and this negative region of the background drive overlap in phase space (the effect being maximum if the propagation velocity of the mode matches the minimum of the

5.7 Influence of energetic ion properties

drive). In Fig. 5.18a) it is shown that, for the case of small fast particle temperatures $T < 6T_e$, the wave-fast ion resonance coincides with positive values of the drive in phase space (see Fig. 5.10). An increase in the temperature gradients therefore leads to a fast ion induced destabilization, by increasing the positive drive contribution. However, as soon as the fast ion resonance approaches the threshold condition identified above, i.e. $v_{\parallel}^2 + \mu B_0 < 3/2$, the fast helium contribution to the linear growth rate becomes negative and a strong ITG stabilization is observed. The latter increases with $R/L_{T,f}$ and is maximized for $T = 12T_e$, where even a full ITG mode suppression is achieved at high temperature gradients (see Fig. 5.10). In Fig. 5.18b) the fast particle temperature gradient scan is shown also for the fast deuterium setup employing the corresponding parameters of table 4.1. The fast deuterium can behave quite similar to fast helium if the temperature gradient exceeds the nominal density gradient value. If this condition is fulfilled, a significant linear ITG suppression is achieved even with NBI heated fast deuterium. Negative, i.e. stabilising, regions in phase space can be formed and their effect can be maximized by properly adjusting the resonance interaction region, as shown for the temperatures $T_f > 4T_e$. For smaller temperatures the resonance increases the positive drive contribution with a consequent overall destabilization. The fast particle temperature which corresponds to the strongest stabilisation is $T_f = 5.5T_e$.

To summarize, the analysis shown in the present section demonstrates that the shape of the fast particle temperature profile represents a key parameters in maximizing the resonance effect discussed in this chapter. All the numerical scans confirm the expectations of the reduced model presented in section 5.3. Moreover, the possibility of stabilizing ITG micro-instability through resonance mechanism with fast particles is not only limited to Ion Cyclotron (IC) heating schemes. Therefore, the proper optimization of energetic particle temperatures and temperature gradients needs to become a central target in any discharge design in the presence of fast particles.

5.7.5 Fast ion distribution function

The physics of the ITG-fast particle resonance interaction strongly depends also on the background distribution function employed to model the energetic ion population. According to the resonance condition identified with the reduced analytic model of Eq. (5.7), the position of the resonance in phase space is not supposed to be affected by a change in F_0 . The fast particle response, i.e. the numerator of Eq. (5.4), on the contrary, is mainly determined by the radial derivative of the equilibrium distribution function and the negative/positive contributions to the linear growth rate might be significantly modified by the different background drive terms. The tem-

perature, which corresponds to the strongest linear growth rate reduction and the overall micro-instability suppression can be partially controlled by an optimization of the shape of F_0 and its radial derivative (i.e. by optimizing η_f^{-1}), which are set by the external heating schemes. In the present section, the linear ITG growth rates are studied in the helium setup by employing the bi-Maxwellian distribution function, defined in Eq. (3.17) for the energetic particle species. It has been shown in chapter 4 that the bi-Maxwellian background is a good first order analytic approximation to the numerical F_0 extracted from the codes TORIC/SSFPQL and SELFO for the discharge at hand. As discussed in detail in chapter 3, the fast particle temperature can be rigorously defined only through the second order moment of an equivalent Maxwellian background distribution function, which can be related to the experimental pressure. For the case of the bi-Maxwellian backgrounds, it is possible to define an effective temperature by imposing the bi-Maxwellian pressure to be equal to the Maxwellian one. The parallel to the perpendicular anisotropy is then fixed by fulfilling the aforementioned constraint, namely

$$T_f = \frac{T_{\parallel} + 2T_{\perp}}{3}. \quad (5.12)$$

Linear growth rates are shown for different fast particle temperatures and compared with the ones obtained using a Maxwellian distribution function. In Fig. 5.19a) a first analysis is performed by studying only the effect of the temperature anisotropies on the resonant stabilisation, keeping $\omega_{T_{\parallel}} = \omega_{T_{\perp}}$. Here, $\omega_{T_{\parallel}} = R_0/T_{\parallel}(\partial T_{\parallel}/\partial x)$ and $\omega_{T_{\perp}} = R_0/T_{\perp}(\partial T_{\perp}/\partial x)$, with R_0 major radius of the device. Depending on the ratio between parallel and perpendicular temperatures, a stronger/weaker stabilisation is observed compared to the Maxwellian case. In particular, further stabilisation is achieved by increasing the parallel temperature with respect to the perpendicular one. In Fig. 5.19b) it is shown that the temperature gradient anisotropy can also enhance the resonance stabilisation. The results shown in Fig. 5.19 can be explained by the reduced analytic model developed in this chapter. As shown in Fig. 5.20a) for the case of $T_f = 12T_e$, which corresponds to the case of the strongest stabilisation for the Maxwellian distribution function, a decrease in the ratio T_{\parallel}/T_{\perp} moves the beneficial region of the bi-Maxwellian drive to smaller values of v_{\parallel} . The resonance position, identified by the black line, is not affected by the choice of the bi-Maxwellian distribution function and cannot match the minimum of the negative drive for this specific choice of T_f . The contribution of the fast helium to the overall growth rate is then less stabilising, as shown in Fig. 5.20b) by actual GENE simulations. On the other hand, an increase in the parallel temperature for these specific parameters, leads to a better superposition between resonance and minimum of the negative drive contribution, as shown in Fig. 5.20b). The role of the temperature gradient

5.8 Impact of finite electromagnetic fluctuations

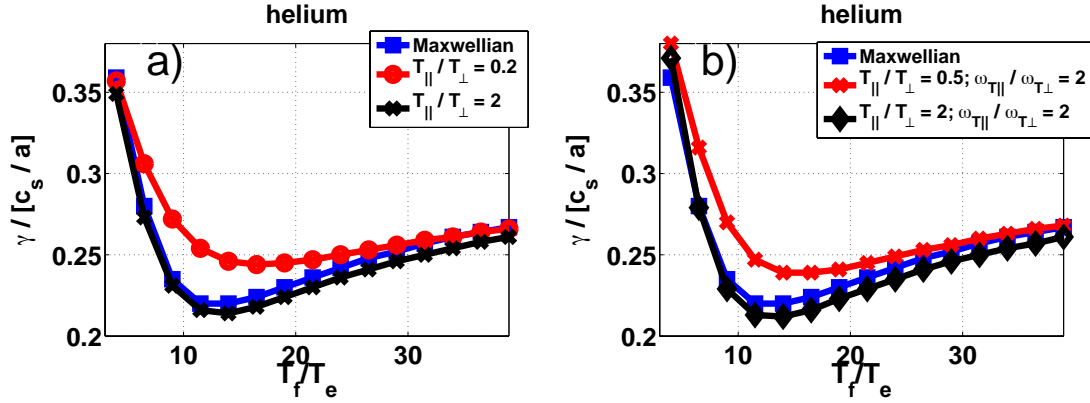


Figure 5.19: GENE calculations of the linear growth rates as a function of the fast particle temperature in the three species reduced setup. The fast particle distribution functions are modelled with a Maxwellian and a bi-Maxwellian backgrounds for a) $\omega_{T_{\parallel}} = \omega_{T_{\perp}}$ and $\omega_{T_{\parallel}} = 2\omega_{T_{\perp}}$.

anisotropies is analogous to that of the temperatures. The phase angle analysis of the main ion density perturbation and the electrostatic potential of Fig. 5.21 confirms that the wave-fast particle interaction for the case $T_{\parallel}/T_{\perp} = 0.2$ and $\omega_{T_{\parallel}} = \omega_{T_{\perp}}$ occurs for higher fast particle temperature. Furthermore, we observe a weaker dephasing compare to the Maxwellian results, which is related to a weaker wave-fast particle interaction.

5.8 Impact of finite electromagnetic fluctuations

All the previous results can be generalized including electromagnetic fluctuations. In Fig. 5.22 linear growth rates are shown for different fast particle temperatures for a fixed ratio of the plasma pressure to the magnetic pressure of $\beta_e = 0.33\%$. The linear electromagnetic growth rates follow the same behaviour as the electrostatic ones for both the fast deuterium and fast helium setups. The electrostatic resonance stabilisation is not visibly affected by the presence of the finite beta, which brings an additional constant stabilisation at each fast particle temperature. Furthermore, the wave-fast ion resonance related linear growth rate relative reduction is of the same order of magnitude as the electromagnetic one, showing that the combination of the two mechanisms can yield a significant microturbulence suppression.

5. Resonant interaction of energetic ions with plasma micro-turbulence

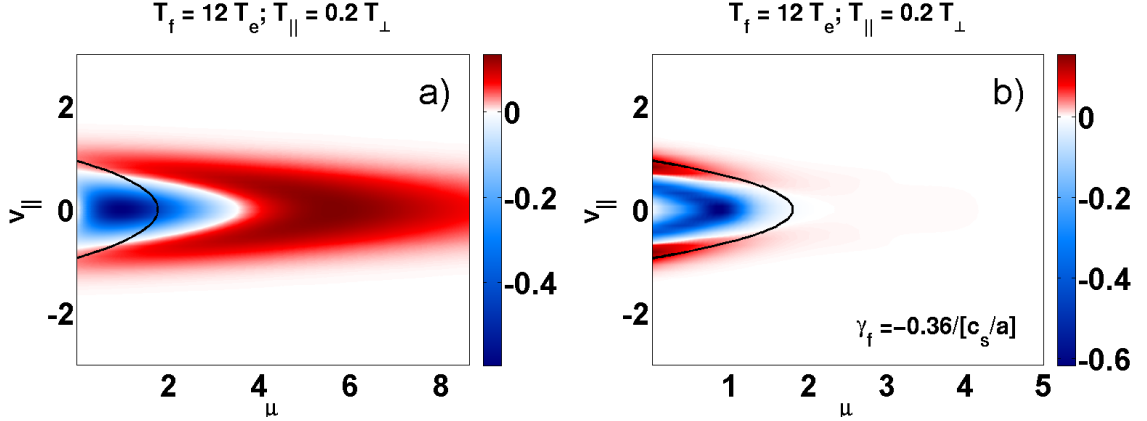


Figure 5.20: a) Analytic radial derivative of a bi-Maxwellian distribution function and b) converged fast particle γ_f velocity space structure with a bi-Maxwellian background for the fast helium from GENE at low field side for $T_f = 12T_e$, $T_{\parallel} = 0.2T_{\perp}$ and $\omega_{T_{\parallel}} = \omega_{T_{\perp}}$. The black contour lines indicate the resonance positions according to the reduced Vlasov model. The corresponding value of the velocity space averaged growth rate contribution is included in the lower right of the GENE plot.

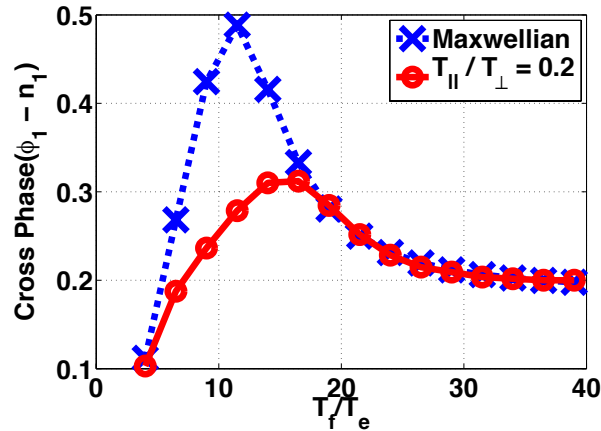


Figure 5.21: GENE calculation of the cross phase (in rad) between the perturbed electrostatic potential and the main ion density perturbation for different fast particle temperatures. The fast particle distribution function has been modelled with a Maxwellian (blue line) and a bi-Maxwellian (red line) background with $T_{\parallel} = 0.2T_{\perp}$ and $\omega_{T_{\parallel}} = \omega_{T_{\perp}}$. It is taken at $z = 0$ performing a time average.

5.9 Nonlinear turbulence results

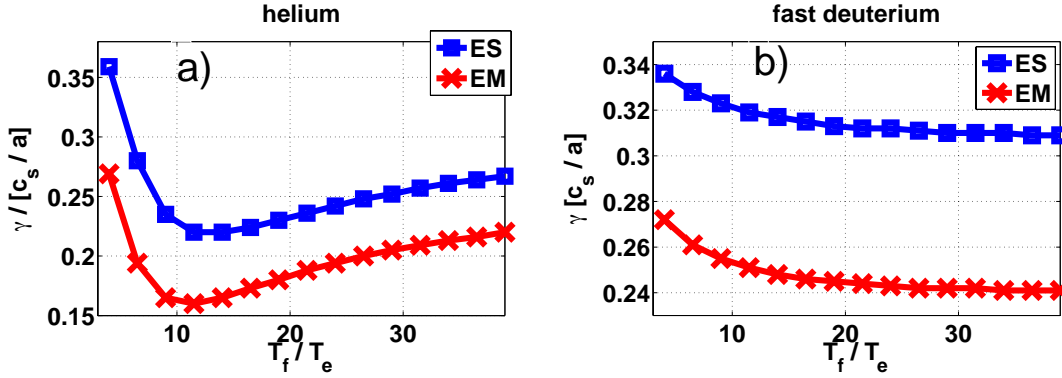


Figure 5.22: Electrostatic (blue line) and electromagnetic $\beta = 0.33\%$ (red line) linear growth rates for different fast particle temperature in the three species setup with a) deuterium-electron-fast helium b) deuterium-electron-fast Deuterium. Figure a) is reproduced from [133], with the permission of IAEA.

5.9 Nonlinear turbulence results

In this section, nonlinear GENE turbulence simulations are performed in the 3 species setup (deuterium - electrons - fast helium). In particular, the wave-fast ion resonance stabilizing mechanism, shown previously on the linear ITG physics, will be extended to nonlinear turbulence simulations. The main quantity to be investigated is the main ion heat flux. Typically, in tokamak scenarios dominated by bulk ion-scale turbulence, the ion heat flux represents the main source of energy confinement degradation. As explained in detail in chapter 2, it measures the energy flowing along the radial direction. Positive or negative values are related respectively to outward or inward energy flows. Depending on the specific plasma parameters, in ITG dominated turbulence scenarios the main ion heat flux is usually larger than the one of the other species by almost of a factor of 5-10 (see for example Fig. 5.24). In the next section, the energetic particle heat flux will also be investigated in detail with the help of reduced quasi-linear models.

The physical parameters employed for the nonlinear analyses at hand are the same as indicated in table 4.1. The radial box size is $175\rho_s$ and the minimal $k_y\rho_i$ is set to 0.05. Moreover, 192 and 48 grid points are used, respectively, in the radial and bi-normal directions. Along the field line 24 points were used. In velocity space, 20 points and 32 equidistant symmetric grid points have been used for resolving respectively the μ and the $v_{||}$ space. The impact of fast particles on the main ion

heat flux is shown in Fig. 5.23 for different fast particle temperatures. The ion heat flux corresponds to time-averaged value over the saturated state of the simulations, and is expressed in gyroBohm $Q_{gB} = v_{th,i}\rho_i^2 n_e T_i / R_0^2$ normalised units.

A strong stabilisation can be observed in the nonlinear simulations. Indeed, an increase in the fast particle temperature produces a net reduction of the main ion turbulent transport. This stabilisation is maximized for $T_f = 24T_e$. With a further increase in the latter parameter an increase of Q_i is observed. The fast particle temperature behaviour of the main ion heat flux can be compared to the growth rates reduction shown in the linear analysis. Indeed, both linear and nonlinear results have a similar fast particle temperature dependency. In Fig. 5.23 the nonlinear main ion heat flux and the linear growth rates relative reductions are shown. For the linear simulations $k_y\rho_s$ is set to 0.2. The latter has been identified as the dominant linear mode in the nonlinear simulations for the nominal fast particle temperature. The linear and nonlinear relative reductions are of the same order of magnitude. Moreover, the nonlinear fast particle temperature which corresponds to the maximum stabilisation is well identified by the linear simulations. By comparing the linear results shown in Fig. 5.23 for the bi-normal wave mode number $k_y\rho_s = 0.2$ with the ones of Fig. 5.3 for $k_y\rho_s = 0.5$ it is possible to observe that the fast particle temperature related to the maximum stabilisation decreases with $k_y\rho_s$. This numerical result is consistent with the reduced model developed in the previous sections. Assuming only a weak dependence of the real ITG frequency with $k_y\rho_s$, the resonance condition of Eq. (5.7), imposes a constraint between T_f and $k_y\rho_s$, which are inversely proportional. A decrease in $k_y\rho_s$ leads to a consequent increase in the fast particle temperature related to the maximum stabilisation in order to match the mode frequency. The time traces of the thermal and energetic ion heat fluxes is shown for three different fast particle temperatures in the electrostatic limit in Fig. 5.24. A striking observation from Fig. 5.24 is the change in sign of the fast particle heat flux spectra by increasing T_f/T_e from 6.9 to 24. In this regards a detailed investigation is postponed to the next section. At this point, tests regarding the simulation sanity and, in particular, the correct bi-normal box size and resolution have to be performed. Therefore, the heat flux spectra $Q_s(k_y)$ is studied for each species s at $T_f = 6.9T_e$ and $T_f = 24T_e$ in Fig. 5.25. This analysis reveals that the heat flux contribution of each species is well resolved for both simulations. In particular, the maximum contribution of each species does not coincide with the minimum value of $k_y\rho_s$ and the heat flux spectra decays smoothly to zero at large k_y . A striking observation is the shift of the peak of the heat flux spectra towards larger $k_y\rho_s$ as the energetic particle temperature is increased. At $T_f = 6.9T_e$ it is indeed located at $k_y\rho_s = 0.2$ and moves to $k_y\rho_s = 0.3$ for $T_f = 24T_e$. This temperature dependence of bi-normal scale associated with the

5.9 Nonlinear turbulence results

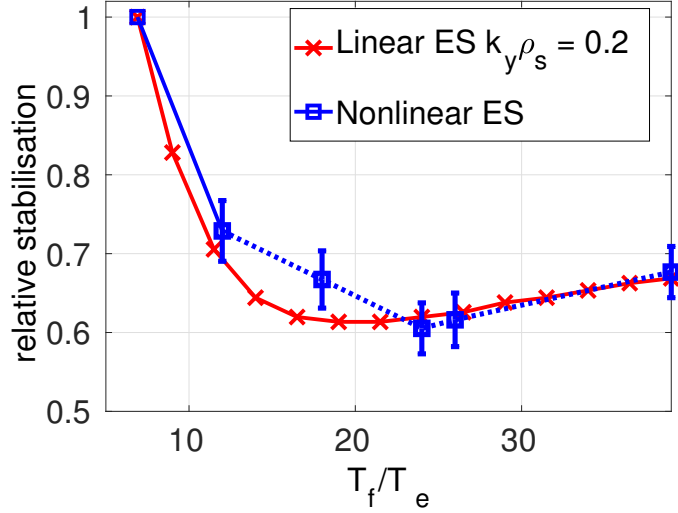


Figure 5.23: Relative nonlinear main ion heat fluxes and linear growth rates at $k_y \rho_s = 0.2$ reduction for different helium temperatures relative to the nominal values at $T_f/T_e = 6.9$, i.e. $\gamma^{\text{nom}} = 0.163 c_s/a$, $q_{i,\text{ES}}^{\text{nom}}/q_{\text{gB}} = 275.37$.

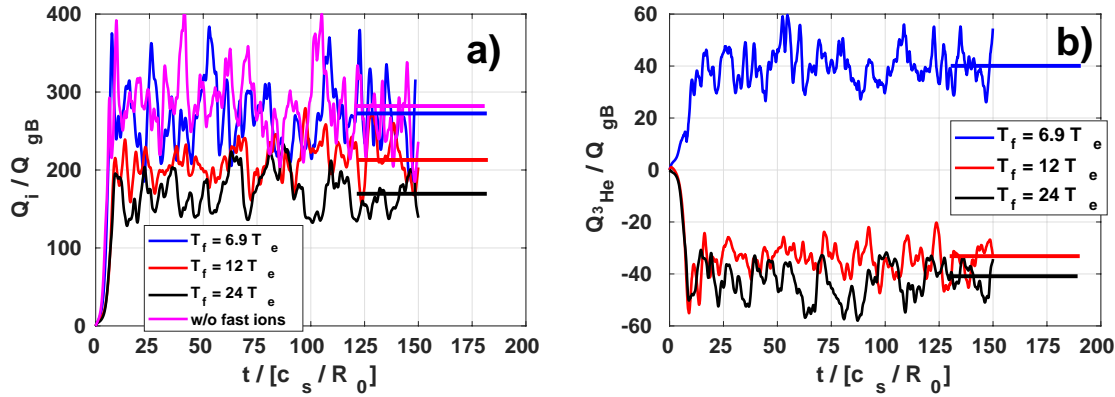


Figure 5.24: Time trace of the nonlinear a) main ion, b) fast ion heat flux in GyroBohm units for different energetic particle temperature T_f/T_e and for the case with only thermal species. Reproduced from [90], with the permission of AIP Publishing.

5. Resonant interaction of energetic ions with plasma micro-turbulence

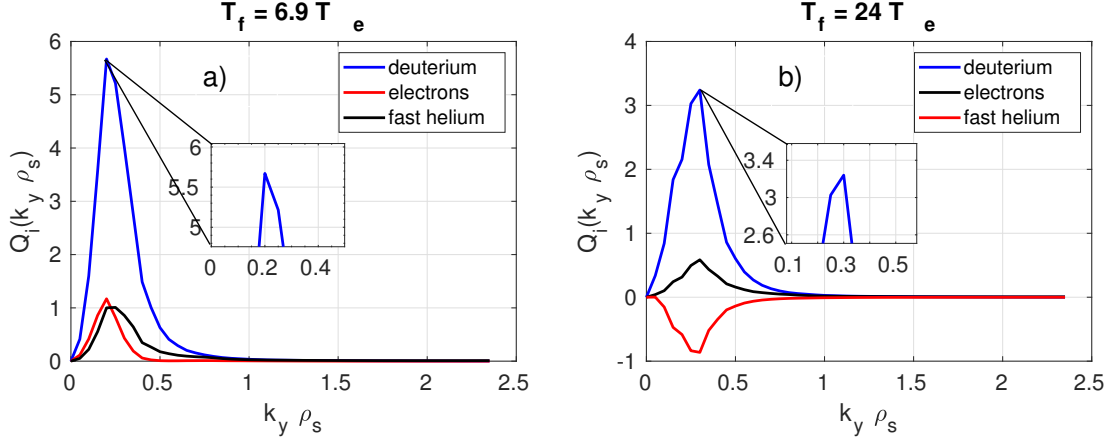


Figure 5.25: Bi-normal heat flux spectra contribution of bulk ions, electrons and energetic particles for a) $T_f = 6.9 T_e$ and b) $T_f = 24 T_e$ averaged over k_x and in the time domain $t = [150 - 400] c_s/a$.

maximum heat flux contribution is consistent with the wave-fast particle resonance mechanism described in this chapter. In particular, as discussed in Ref. [90], the temperature of the energetic particles corresponding to the highest linear stabilization varies significantly with the bi-normal wave vector ($k_y \rho_s$). Hence, at a fixed temperature, each scale undergoes a different resonant stabilization significantly affecting the shape of the bi-normal heat flux spectra.

Another striking observation is the nonlinear behavior of the cross phase relation (α) between the electrostatic potential and the main ion density perturbation. During the investigation of section 5.2 the linear cross phase was shown to be a function of the fast particle temperature and to be strongly affected by resonance effects between the main ITG mode and the energetic particles. Similar results are also observed in turbulent regimes in Fig. 5.26, where the cross phase function $\chi(\alpha, k_y \rho_s)$ obtained for $T_f = 24 T_e$ is compared to the one without energetic particles. It is measured at $z = 0$ and is obtained by performing a time average in the steady-state domain $t/[c_s/R_0] = [25 - 150]$. Fig. 5.26 reveals that χ , which peaks as the nonlinear drive at $k_y \rho_s \sim 0.2$, is zero ($\alpha = 0$) if energetic particles are neglected. However, consistently with the linear results shown in Figs. 5.1-5.4, it increases significantly for the case $T_f = 24 T_e$. In particular, each scale undergoes a different dephasing, consistently with the linear results on Fig. 5.5.

5.10 Fast ion fluxes analysis

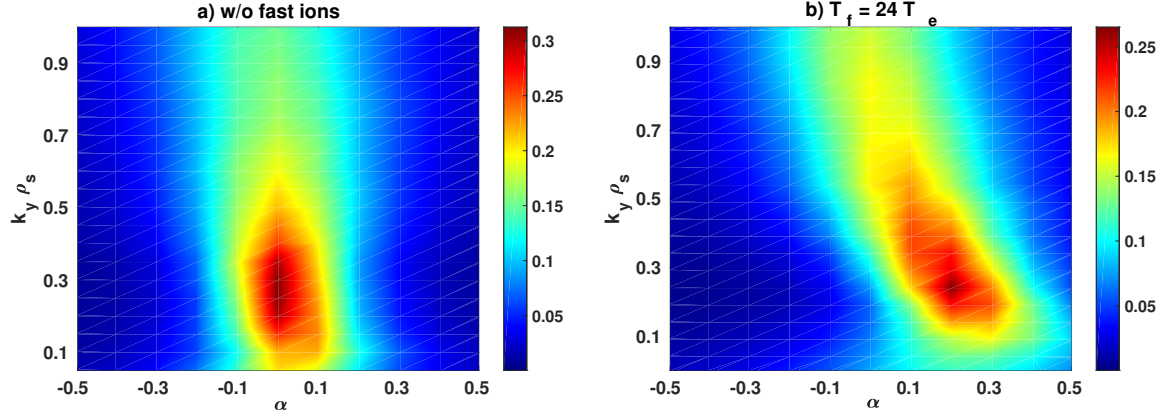


Figure 5.26: Nonlinear cross phase (in rad) between the perturbed electrostatic potential and the main ion density perturbation at different $k_y \rho_s$, a) removing and b) including energetic particles at $T_f = 24 T_e$. It is taken at $z = 0$ and in the steady-state time domain $t/[c_s/R_0] = [25 - 150]$. Reproduced from [90], with the permission of AIP Publishing.

5.10 Fast ion fluxes analysis

The resonant interaction between energetic particles and ITG micro-instability is not significantly affected by cross-scale coupling. The change in sign of the fast ion heat flux observed in Fig. 5.24 can be qualitative and quantitative captured even in the simplified single mode framework presented previously. This observation allows a derivation of a quasi-linear description - following the analytic derivation of Ref. [144, 145] - able to explain the temperature dependences of the energetic particle steady-state heat flux. In the gyrokinetic formalism, the radial component of the heat flux is defined as

$$Q_{1,f} = \frac{m}{2} \int v_E^x v^2 F_{1,f}(\mathbf{x}, \mathbf{v}) d^3 v, \quad (5.13)$$

where v_E^x represents the radial component of the $E \times B$ velocity, namely $v_E^x = \frac{c}{B_0^2} (\mathbf{B}_0 \times \nabla \bar{\phi}_1)_x$. As discussed in details in chapter 2, Eq. (5.13) can be rewritten in

5. Resonant interaction of energetic ions with plasma micro-turbulence

the GENE field-aligned coordinate system as follows

$$Q_{1,f} = -\Re \left\{ \sum_k \pi B_0 \frac{c}{C} i k_y \int \left(v_{\parallel}^2 + \frac{2B_0\mu}{m_f} \right) \left[J_0 \phi_1^k F_1^{k,*} + \frac{q_f}{B_0} (1 - J_0^2) |\phi_1^k|^2 \frac{\partial F_0}{\partial \mu} \right] dv_{\parallel} d\mu \right\}. \quad (5.14)$$

Here, the field-aligned representation of the radial component of the $E \times B$ velocity $v_E^x = -\frac{c}{C} \partial_y \bar{\phi}_1$ has been employed. The radial fast particle heat flux can be further computed by means of the reduced Vlasov equation derived in Eq. (5.4), which in normalized units reads

$$\begin{aligned} Q_{1,f}/Q_{gB} &= \frac{\pi B_0 n_f T_f}{C^2} \sum_{k_y} k_y^2 |\phi_1^k|^2 \gamma^k \int J_0^2 (v_{\parallel}^2 \\ &\quad + \mu B_0) \frac{\left[\frac{R}{L_{n,f}} + \frac{R}{L_{T,f}} (v_{\parallel}^2 + \mu B_0 - \frac{3}{2}) \right] F_M}{\left(\omega_r + \frac{T_f}{q_f} \left(\frac{\mu B_0 + 2v_{\parallel}^2}{B_0} \right) k_y \mathcal{K}_y \right)^2 + \gamma^2} dv_{\parallel} d\mu. \end{aligned} \quad (5.15)$$

Here, Eq. (5.15) is expressed in gyroBohm units. Following a similar approach as in Refs. [144, 145] for the particle flux, Eq. (5.15) can be written in a quasi-linear framework as the sum of a off-diagonal diffusion D_n - proportional to the fast particle density gradient - and a diagonal-diffusion D_T - due to the presence of temperature gradients, i.e.

$$Q_{1,f}/(n_f T_f Q_{gB}) = D_n \frac{R}{L_{n,f}} + D_T \frac{R}{L_{T,f}}. \quad (5.16)$$

Here, the pure convection is neglected [145]. The quasi-linear decomposition of Eq. (5.16) can be easily identified in the reduced expression for the energetic particle heat flux derived in Eq. (5.15). The diffusion operators can hence be written as

$$D_n = \frac{\pi B_0 n_f T_f}{C^2} \sum_{k_y} k_y^2 |\phi_1^k|^2 \gamma^k \int \frac{J_0^2 (v_{\parallel}^2 + \mu B_0) \frac{R}{L_{n,f}} F_{0,M}}{\left(\omega_r + \frac{T_f}{q_f} \left(\frac{\mu B_0 + 2v_{\parallel}^2}{B_0} \right) k_y \mathcal{K}_y \right)^2 + \gamma^2} dv_{\parallel} d\mu. \quad (5.17)$$

$$\begin{aligned} D_T &= \frac{\pi B_0 n_f T_f}{C^2} \sum_{k_y} k_y^2 |\phi_1^k|^2 \gamma^k \int J_0^2 (v_{\parallel}^2 + \mu B_0) \frac{\frac{R}{L_{T,f}} (v_{\parallel}^2 + \mu B_0 - \frac{3}{2}) F_{0,M}}{\left(\omega_r + \frac{T_f}{q_f} \left(\frac{\mu B_0 + 2v_{\parallel}^2}{B_0} \right) k_y \mathcal{K}_y \right)^2 + \gamma^2} dv_{\parallel} d\mu. \end{aligned} \quad (5.18)$$

5.11 ITG-EP resonance effects on ITER standard scenarios

The above decomposition of the radial component of the fast particle heat flux reveals that the sign of the diffusion term depends on the sign of the density gradient. For the parameters employed throughout this work it is always positively defined, i.e. directed outward. Moreover, the sign of the thermo-diffusion term depends on the energetic particle temperature gradient and on the velocity space quantity $v_{\parallel}^2 + \mu B_0 - 3/2$. Its structure is of the same form as Eq. (5.11). Therefore, the resonance mechanism can affect the quasi-linear expression for $Q_{1,f}$ similarly as discussed previously for the linear contribution of the energetic ions to the total growth rate γ_f . Assuming positive values for $R_0/L_{T,f}$, a positive (outwards) fast particle heat flux is expected when the linear contribution of the most unstable mode in the turbulence simulations is destabilizing. Negative fluxes, on the other hand, are expected in cases where the resonance moves to smaller energies in velocity space, therefore maximizing the negative contribution of the energetic particle drive. These theoretical predictions are in agreement with the GENE nonlinear results of Fig. 5.24. Fig. 5.27 shows that the fast particle heat flux changes sign when the resonance position moves in phase space through more favorable regions, as discussed in the previous sections for the linear growth rate analysis. In Fig. 5.27 the velocity space averaged growth rate contribution, normalized to the thermal deuterium one, is included in the lower right of each plots.

5.11 ITG-EP resonance effects on ITER standard scenarios

Finally the possible impact of the wave-fast ion resonance stabilisation is analyzed for an ITER standard scenario with ${}^3\text{He}$ ICRH minority heating. As explained in chapter 1, ITER is the first prototype of a nuclear fusion reactor. Each physical mechanism, able to suppress turbulent transport and hence to increase its performances is therefore extremely valuable and need to be fully exploited. In this section, the initial phase of an ITER discharge is considered before the L-H transition [162]. This selected time slice is particularly favorable for ICRH external heating mechanisms. The ion and electron temperatures are still low enough to allow to the ${}^3\text{He}$ minority to absorb almost entirely the ICRF waves and to generate a consistent population of fast ${}^3\text{He}$ with steep profiles. In later stages of the discharge, the bulk temperatures will increase above 15 keV and the ICRF external waves are predicted to be absorbed by the Tritium and electron populations to the detriment of the fast ${}^3\text{He}$. Its profiles will flatten and no resonant wave-fast particle mechanisms will be allowed. In this section, linear and nonlinear GENE flux-tube simulations are per-

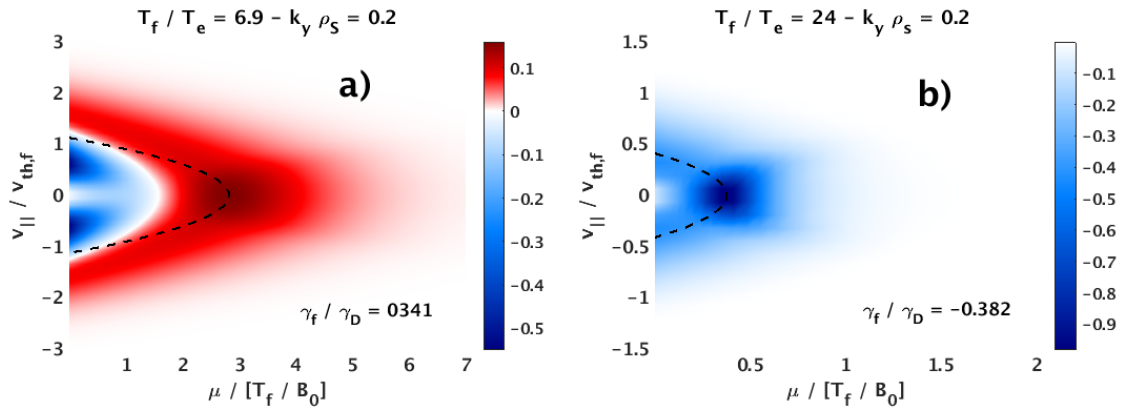


Figure 5.27: Converged fast particle γ_f velocity space structure obtained from GENE at $z = 0$ for the $k_y \rho_s$ more relevant in turbulence simulations, i.e. $k_y \rho_s = 0.2$. The energetic particle temperature is taken as a) $T_f = 6.9 T_e$ and b) $T_f = 24 T_e$. The black contour lines indicate the resonance positions according to the reduced Vlasov model. Moreover, the velocity space averaged growth rate contribution, normalized to the thermal deuterium one, is included in the lower right of each plots. Reproduced from [90], with the permission of AIP Publishing.

5.11 ITG-EP resonance effects on ITER standard scenarios

R/m	\hat{s}	q	T_D	T_T	R/L_{T_D}	R/L_{T_T}
6.2	0.27	1.12	0.74	0.74	1.96	1.87
n^3He	R/L_{n^3He}	R/L_{n_T}	R/L_{n_D}	R/L_{n_e}	R/L_{T_e}	ν^*
0.03	0.6	0.6	0.6	0.6	1.26	0.0

Table 5.1: Parameters for ITER standard scenario ($\rho_{\text{tor}} = 0.32$). Here, T denotes the temperature normalized to the electron one, $R/L_{T,n}$ the normalized logarithmic temperature and density gradients, \hat{s} the magnetic shear and ν^* the electron-ion collision frequency normalized to the trapped electron bounce frequency.

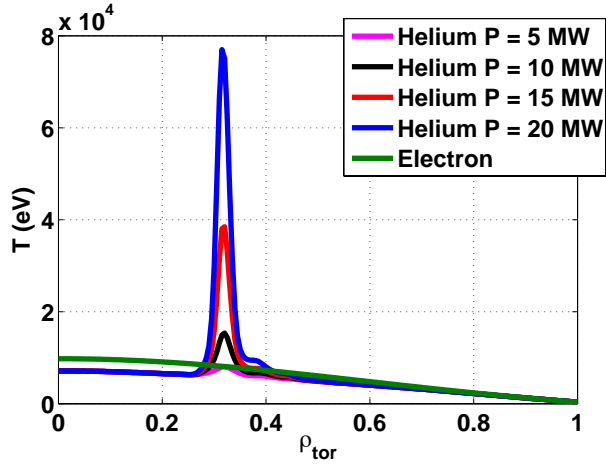


Figure 5.28: Helium temperature profile for each value of the ICRF injected power. The electron temperature is shown as reference.

formed in the electrostatic limit. Realistic kinetic profiles for the thermal species - Deuterium and Tritium - and magnetic equilibrium have been extracted from JINTRAC simulations [162]. The main plasma parameters are summarized in table 5.1. The kinetic profiles of the fast helium are consistently computed with the ICRF full-wave TORIC code interfaced with the SSFPQL Fokker-Planck solver [163, 164] for each value of the injected power. The 3He temperature profiles are shown in Fig. 5.28 for each value of the ICRF power. In Fig. 5.29 a corresponding linear and nonlinear analysis is performed for a numerical scan of the ICRF injected power at the radial position of $\rho_{\text{tor}} = 0.32$. As predicted by the wave-fast ion stabilising mechanism presented in this chapter, only a small fast ion contribution is observed for the case of $P_{\text{ICRH}} = 5\text{MW}$, i.e. where the fast ion drive is practically negligible

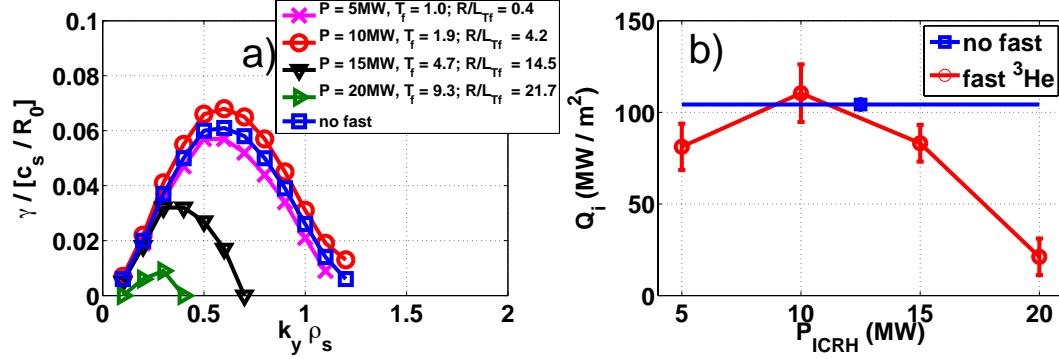


Figure 5.29: a) Growth rates and b) nonlinear main ions heat flux as a function of, respectively, $k_y \rho_s$ and injected ICRF power for an ITER standard scenario at $\rho_{tor} = 0.32$. Reproduced from [133], with the permission of IAEA.

due to the small value of the fast particle temperature gradient. An increase in the helium temperature gradients, i.e. $P_{ICRH} = 10\text{MW}$, leads to a stronger fast ion contribution in the field equation, which however becomes destabilizing since the the wave-fast-ion resonance is still in the positive region of the background drive, due to the small value of the fast particle temperature. On the contrary, a significant reduction in both linear growth rates and nonlinear fluxes can be achieved for the case of an injected power of $P_{ICRH} = 20\text{MW}$, i.e. where $T_f > 6T_e$ and the wave fast ion resonance overlaps the negative region of the background drive. For this case, fast ions add a substantial stabilising contribution to the thermal ITG drive with a consequent overall microturbulence and turbulence suppression.

5.12 Chapter summary

To summarize, the present chapter has been entirely dedicated to the physical understanding of a novel wave-fast particle resonance stabilizing mechanism. A significant fast particles active effect on the plasma micro-instability has been observed for realistic plasma parameters and geometry (based on the study shown in chapter 4) through numerical linear and nonlinear simulations. Furthermore, a theoretical simplified model has been derived. The latter can well reproduce the numerical findings and can easily be used for future extrapolations and interpretations. Fast particles have been found to strongly contribute to the main instability development, modifying the main ion response and thus the electrostatic field both in terms of magnitude

5.12 Chapter summary

and phase. In particular, fast particles can interact with the background microturbulence through a wave-particle resonance mechanism if the fast particle magnetic-drift frequency is close enough to the linear frequency of the wave. The main dependences of the resonant interaction with the magnetic geometry and on all the other physical parameters of the fast particle species have been studied. Moreover, the impact of more realistic distribution functions for modelling the energetic ion species has also been investigated. All the results presented in this chapter have also been generalized including electromagnetic fluctuations and nonlinear cross-scale coupling, which are shown not to alter significantly the resonant stabilization mechanism described before.

Chapter 6

Nonlinear electromagnetic stabilisation by energetic ions

In the previous chapter it has been shown that substantial stabilization of tokamak plasma turbulence can be achieved even in an electrostatic framework. Particularly, in certain parameter regimes, an effective energy redistribution from the background microinstability to the energetic particle species occurs if the fast particle magnetic-drift frequency is close to the linear frequency of the unstable wave. However, this resonant mechanism can only partially explain the numerical results of chapter 4 and the ones on similar discharges [83, 84, 88, 38]. These works linked the beneficial energetic particle effect to an increase of the kinetic-to-magnetic pressure ratio, β . This quantity is a measure for the relevance of electromagnetic fluctuations which typically stabilize ITG modes [155, 156, 165]. The positive impact of β on ion-scale turbulence is limited by instabilities at small toroidal mode numbers and frequencies higher than the ITG one, which are destabilized if the total plasma pressure exceeds a critical value. These modes strongly increase particle/heat fluxes [166]. In this chapter it is shown that, if this threshold is not exceeded and the electromagnetic instabilities remain submarginal, they can have a beneficial role on the overall confinement. This is demonstrated through a detailed analysis based on the frequency-spectral decomposition of the free-energy balance (introduced in chapter 2 and employed afterwards in chapter 5). These modes (identified here as TAE-like instabilities) deplete the energy content of the bulk ion-temperature-gradient ITG-driven turbulence and act as an additional catalyst for energy transfer to zonal components representing the dominant saturation channel.

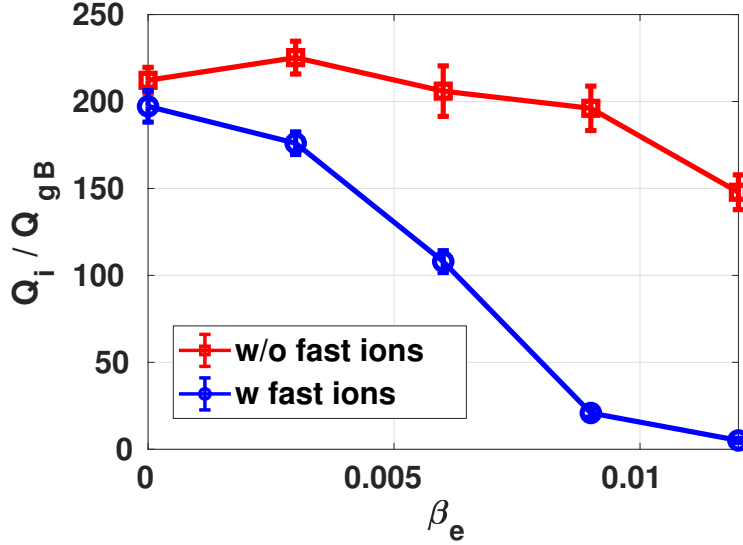


Figure 6.1: Time averaged nonlinear main ion heat fluxes in GyroBohm units for different values of β_e at $T_f/T_e = 9.8$ in simulations with/without energetic particles. Reproduced from [167], with the permission of IAEA.

6.1 Numerical simulations: parameters and results

The impact of fast ions on the electromagnetic nonlinear stabilisation of plasma turbulence is studied with GENE turbulence flux-tube simulations. The magnetic geometry and plasma parameters selected for this analysis represent a realistic JET-like scenario with thermal deuterium, electrons and externally injected neutral beam deuterium. The main parameters are inspired by the ones employed in chapter 4 and summarized in table 4.1 with the only exception of a reduced safety factor of $q = 1.2$. This choice allows us to perform a broader β_e -scan, moving the threshold of destructive MHD modes to larger values [166].

Grid resolution and plasma parameters

The numerical simulations are performed with a radial box size of $175\rho_s$ and with a minimum $k_y\rho_s$ of 0.025. The relatively small value used for $k_{y,min}$ is required to completely resolve the small k_y mode structures, which arise in the presence of energetic

6.1 Numerical simulations: parameters and results

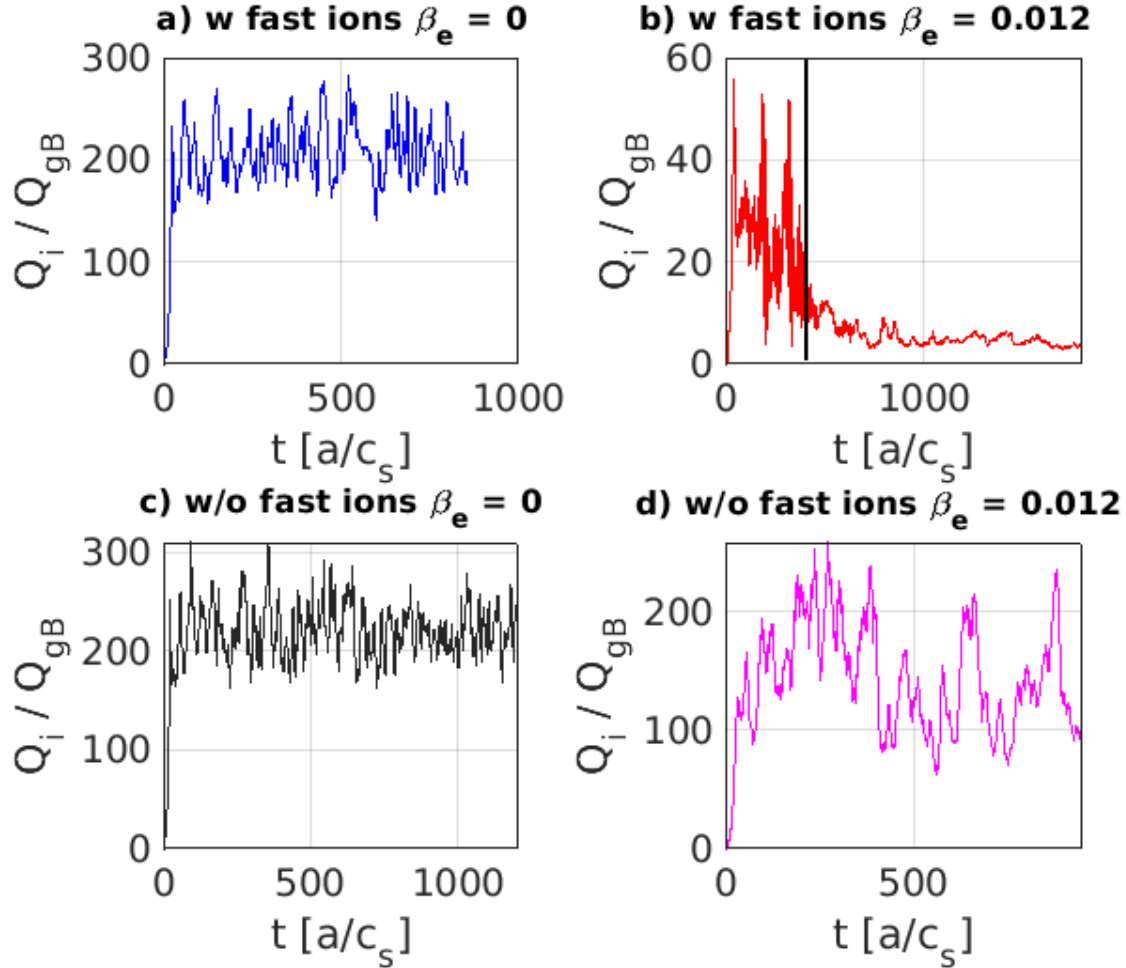


Figure 6.2: Time trace of the nonlinear main ion heat fluxes in GyroBohm units at $\beta_e = 0$ and $\beta_e = 0.012$ with/without energetic particles. The transition between Phase I and Phase II in the simulation at $\beta_e = 0.012$ with energetic particles is marked by the vertical black line.

ions and high plasma beta. The grid numbers in direct space are $192 \times (46 \text{ or } 96) \times 32$ in the radial, binormal and parallel directions while 24×32 grid points are used in the μ and the v_{\parallel} velocity space dimensions. The flux-tube description appears justified given the small Larmor-to-minor-radius ratio of $\rho_i^* = 1/450$ for thermal ions and $\rho_{fD}^* = 1/150$ for the fast deuterium. The validity of a local description for the parameters under consideration is further substantiated in section 6.5. Furthermore, for simplicity and in order to keep the computational expenses at a reasonable level, the fast particle species have been modelled with an equivalent Maxwellian distribution function. Future studies will be performed taking advantage of the non-Maxwellian GENE extension discussed in detail in chapter 2 and 3, which however requires a significant increase in the velocity space resolution.

Nonlinear β_e -scan results

To investigate the impact of energetic ions on the local turbulence levels, scans over the electron plasma beta $\beta_e = 8\pi p_e / B_0^2$ are performed. Fig. 6.1 shows the nonlinear main ion heat fluxes for different values of the electron beta contribution and are compared to the case without fast ions. The heat fluxes are normalised to $Q_{gB} = v_{th,i} \rho_i^2 n_e T_i / R_0^2$ and the results without fast ions have been obtained, similarly as done in the previous chapters, by consistently modifying the pressure gradient. A significant reduction of the main ion turbulent fluxes when fast ions and electromagnetic effects are simultaneously included in the simulations can be observed from Fig. 6.1. The main ion heat flux time traces employed to extract the averaged values of Fig. 6.1 are shown in Fig. 6.2 for the cases with/without energetic particles at $\beta_e = 0$ and $\beta_e = 0.012$. A moderate (about 25%) turbulence reduction is observed with increasing beta up to $\beta_e = 0.012$ in the absence of fast ions (red squares in Fig. 6.1). A substantial suppression of the time averaged fluxes by 95% at $\beta_e = 0.012$ is observed in the presence of fast particles (blue circles in Fig. 6.1). Moreover, two different nonlinear phases can be identified in the simulations associated to substantial energetic particle stabilization (i.e. observed for $\beta_e = 0.009$ and $\beta_e = 0.012$). A first phase (called Phase I in the remainder of this chapter) is characterized by a high-frequency modulation of the heat flux and slowly decaying transport levels. During the second phase (called Phase II), the main ion heat flux reaches a stationary state at reduced turbulence levels.

The present chapter will be dedicated to address the fundamental questions arising from the results shown already in chapter 4 and further corroborated in Figs. 6.1-6.2:

6.2 Real-space and spectral analysis of the electrostatic potential

1. What is the main role of energetic particle in the significant enhancement of turbulence suppression observed in Figs. 6.1?
2. Why does a strong turbulence stabilization arise only in the simultaneous presence of electromagnetic and nonlinear effects?
3. What are the key fast particle parameters? and would it be possible to optimize this mechanism in view of future fusion reactors?

6.2 Real-space and spectral analysis of the electrostatic potential

To further investigate the physical mechanism that is responsible for the significant fast ion turbulence suppression observed in Fig. 6.1, the electrostatic potential ϕ_1 is studied in this section for different values of the electron plasma beta. To provide a first visual qualitative picture, a snapshot of ϕ_1 at $t \sim 600c_s/a$ at the flux-tube mid plane, i.e. $\theta = 0$ is shown in Fig. 6.3 for the case with/without energetic ions for the values of $\beta_e = 0$ and $\beta_e = 0.012$. Figs. 6.3a)-c) show that small changes are observed in the ITG streamers structures for the case with/without energetic ions in the electrostatic limit. By including a finite value for the electron plasma beta of $\beta_e = 0.012$, the electrostatic potential is, however, found to create coherent structures along the bi-normal direction in the presence of energetic ions, which indicate an increase in the radial shearing rate in these simulations. The size of the turbulent eddies is correspondingly reduced (compare Fig. 6.3d) with Fig. 6.3b)). According to literature, the creation of complex shearing patterns tends to distort the ITG eddies by stretching them and naturally decreasing the streamer dimensions. This mechanism is an intrinsically stabilising effect since at smaller radial scales the dissipation is expected to become stronger. Aiming for a more quantitative comparison, the electrostatic potential is studied in Fourier space in the radial, bi-normal directions and in time by assuming periodic boundary conditions. The GENE diagnostic used to extract the frequency employs the so-called windowed Fourier transformation of the time trace (interpolated to equidistant time steps) of the electrostatic potential ϕ_1 in the time domain of the nonlinear simulations which goes from [50 – 350] in units of c_s/a . The windowed Fourier transform enables the study of non-periodic time signals by applying smoothing functions (in this case Hanning apodization functions) and removing spurious high-frequency components. The $(k_x\rho_s, \omega)$ structure of the perturbed electrostatic potential is shown in Fig. 6.4 after an average over the bi-normal wave-vectors and along the field-aligned coordinate z . The ratio between the

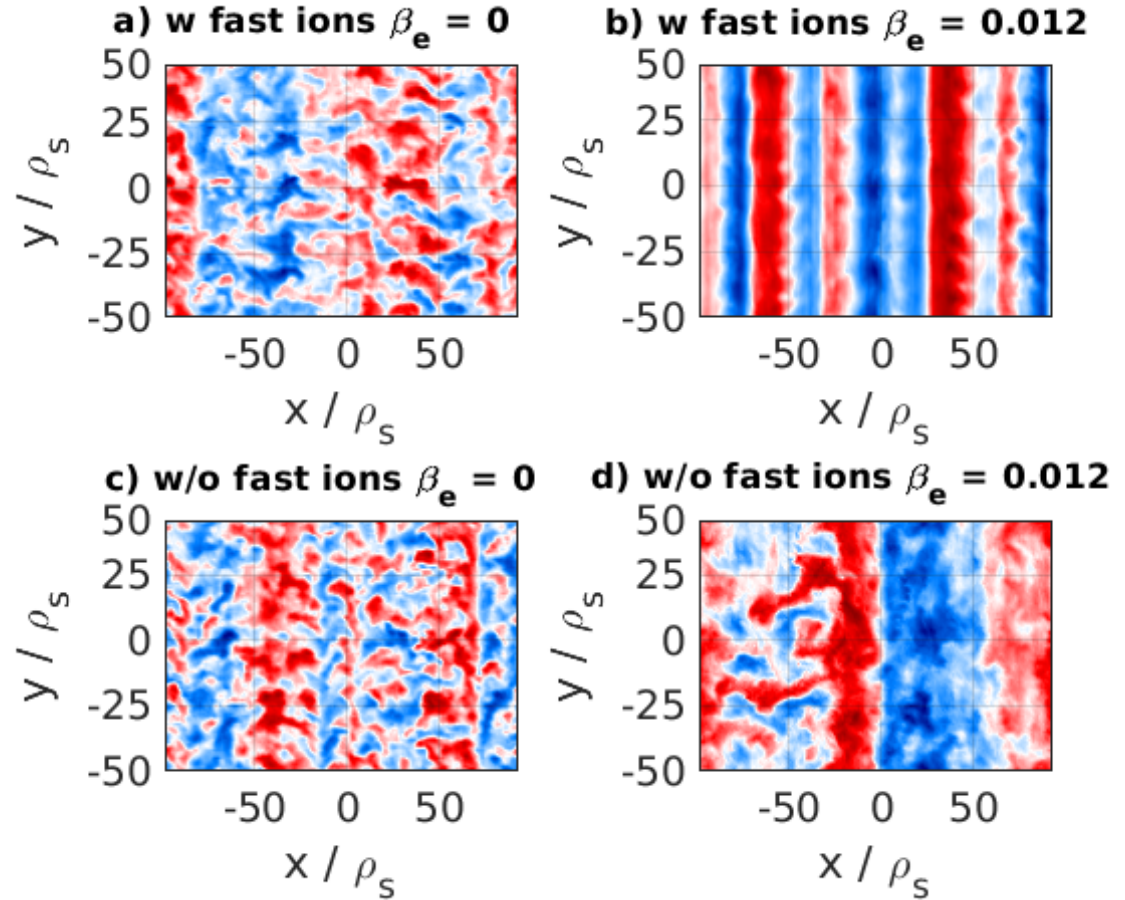


Figure 6.3: Snapshots of electrostatic potential ϕ_1 contours in the perpendicular directions during the saturated phase with (top) and without (bottom) fast ions at the flux-tube mid plane for $\beta_e = 0$ (left column) and $\beta_e = 0.012$ (right column).

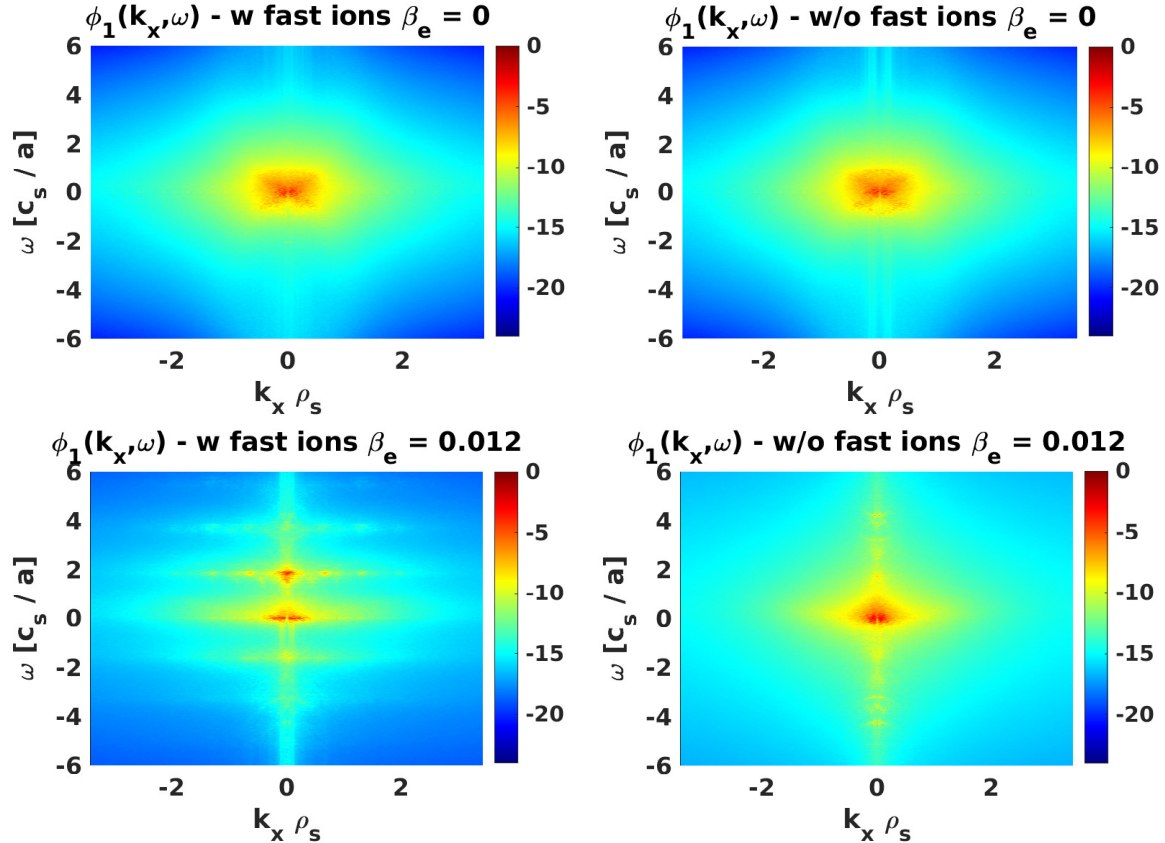


Figure 6.4: Fourier spectra of $\phi_1(\omega, k_x \rho_s)$ at $\beta_e = 0$ (upper row) and 0.012 (lower row) retaining (left column) or neglecting (right column) the energetic particle species. The electrostatic potential has been averaged over the bi-normal mode number $k_y \rho_s$, field-aligned coordinate z and in the time domain $t[a/c_s] = [50 - 350]$. The amplitude of the signal is plotted in logarithmic scale.

electron and magnetic pressure is fixed at $\beta_e = 0$ (no electromagnetic fluctuations) and $\beta_e = 0.012$ (value of β_e associated to the strongest energetic particle stabilizing effect). Fig. 6.4 reveals that in the absence of any electromagnetic effect the radial ($k_x \rho_s$) Fourier spectra of the electrostatic potential are not affected by the presence of fast ions. It peaks at $k_x \rho_s \approx 0$ as expected for ITG dominated plasma turbulence. This picture changes dramatically when EP and finite β_e are simultaneously included. In particular, Fig. 6.4 shows that at $\beta_e = 0.012$ and only in the presence of fast particles a secondary peak can be found at $\omega \sim 2c_s/a$. In the case EPs are neglected, this high-frequency peak is found to be several orders of magnitude smaller. Moreover, the sharpest peak observed at small frequencies is identified as the linear ITG mode frequency.

To identify the bi-normal mode number related to the high-frequency mode observed in Fig. 6.4, ϕ_1 is analyzed in Fig. 6.5 in the $\omega - k_y$ space. The electrostatic potential has been averaged over the field-line coordinate and $k_x \rho_s$. In all the plots of Fig. 6.5, a similar pattern, starting at small frequencies and increasing nearly linearly with k_y can be identified. This corresponds to the dispersion of the ITG mode. Only for finite β_e and in the presence of fast ions (bottom-left plot), a second branch at higher frequency can be identified. Here, it is worth mentioning that the results presented in this chapter do not depend on the straight field-line coordinate z . In the following, the impact of the energetic ions on the destabilization of the high frequency modes observed in Fig. 6.5 for $k_y \rho_s = 0$ and finite $k_y \rho_s$ is analyzed separately.

6.2.1 Observations at zero toroidal mode number

One of the main saturation mechanisms of ion-driven drift-wave turbulence is zonal flow (often associated, as previously done in chapter 4, to the shearing rate ω_{ZF}). Therefore, the study of the time evolution of the shearing rate amplitude, defined as in Eq. (4.6), gives an estimate of the degree of turbulence suppression related to an enhancement of zonal flow by energetic particle effects. Fig. 6.6 shows the shearing rate time traces for different values of β_e for the cases where the fast particle species are included or neglected in the simulations. A minor impact of energetic particles on the shearing rate levels (on the order of $\leq 10\%$) is found for $\beta_e \leq 0.006$. However, a larger and more effective shearing rate seems here always to be associated to the presence of EP. As previously observed for the main ion heat fluxes, two clearly different nonlinear phases are found for $\beta_e = 0.012$. In the first one, the zonal flow levels seem to be weakly affected by the EP presence. At the beginning of the second phase, however, a significant increase in the zonal component

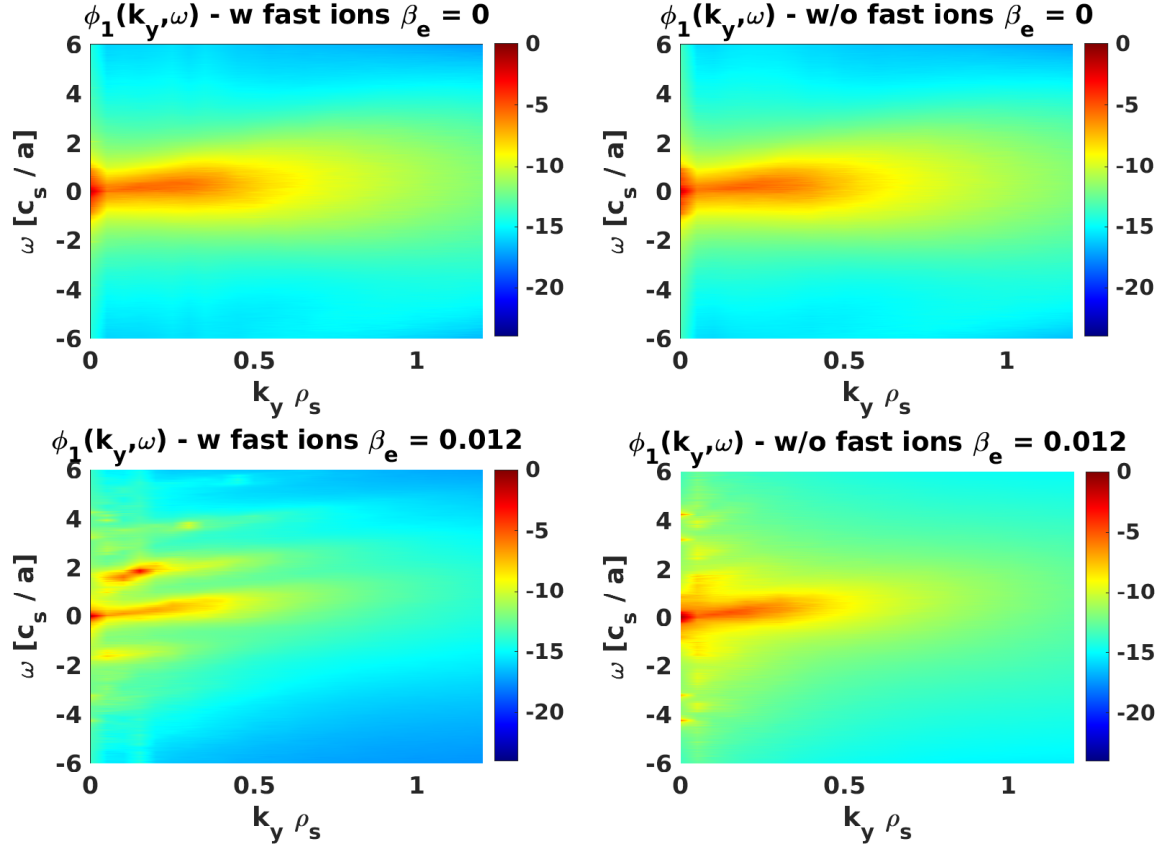


Figure 6.5: Fourier spectra of $\phi_1(\omega, k_y \rho_s)$ at $\beta_e = 0$ (upper row) and $\beta_e = 0.012$ (lower row) retaining (left column) or neglecting (right column) the energetic particle species. The electrostatic potential has been averaged over the radial mode number $k_x \rho_s$, field-aligned coordinate z and in the time domain $t[a/c_s] = [50 - 350]$. The amplitude of the signal is plotted in logarithmic scale.

6. Nonlinear electromagnetic stabilisation by energetic ions

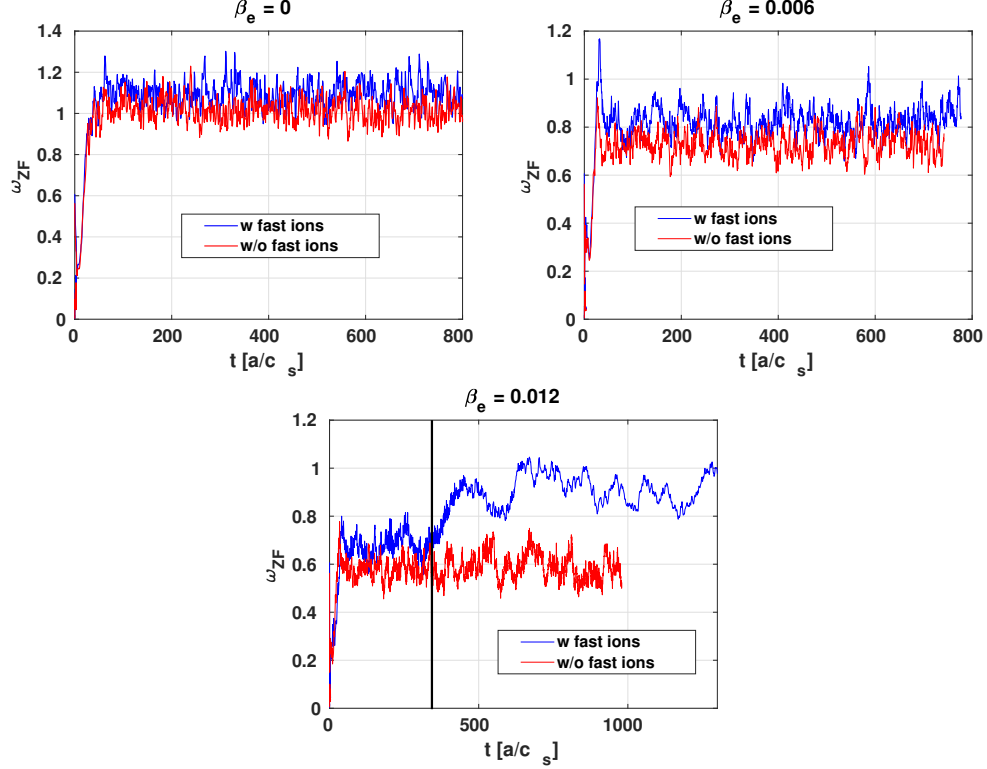


Figure 6.6: Time trace of the shearing rate amplitude ω_{ZF} in simulations with/without energetic particles for different values of the ratio between electron and magnetic pressure. The transition between Phase I and Phase II in the simulation at $\beta_e = 0.012$ with energetic particles is marked by the vertical black line.

of the potential is observed with a consequent turbulence reduction (see Figs. 6.1-6.2b)). The simulations reach a new quasi-stationary state with substantially reduced ion-scale turbulence transport which is not subject to long-time secular zonal flow evolution [168, 169] (see Ref. [170]). It is worth mentioning that the magnitude of the heat flux during this phase depends on the simulation parameters and does not necessarily imply proximity to marginality (see Ref. [170]). Similar results are e.g. observed also for the simulation with energetic particles and $\beta_e = 0.009$.

The possible contribution of energetic particles to the nonlinear excitation of zonal modes, i.e. $k_y \rho_s = 0$, at zero (zonal flow) and/or finite frequencies is investigated in the remainder of this section. To extract the frequency spectra of ϕ_1 , a Fourier transform is applied to the gyroaveraged electrostatic potential in the first nearly-

6.2 Real-space and spectral analysis of the electrostatic potential

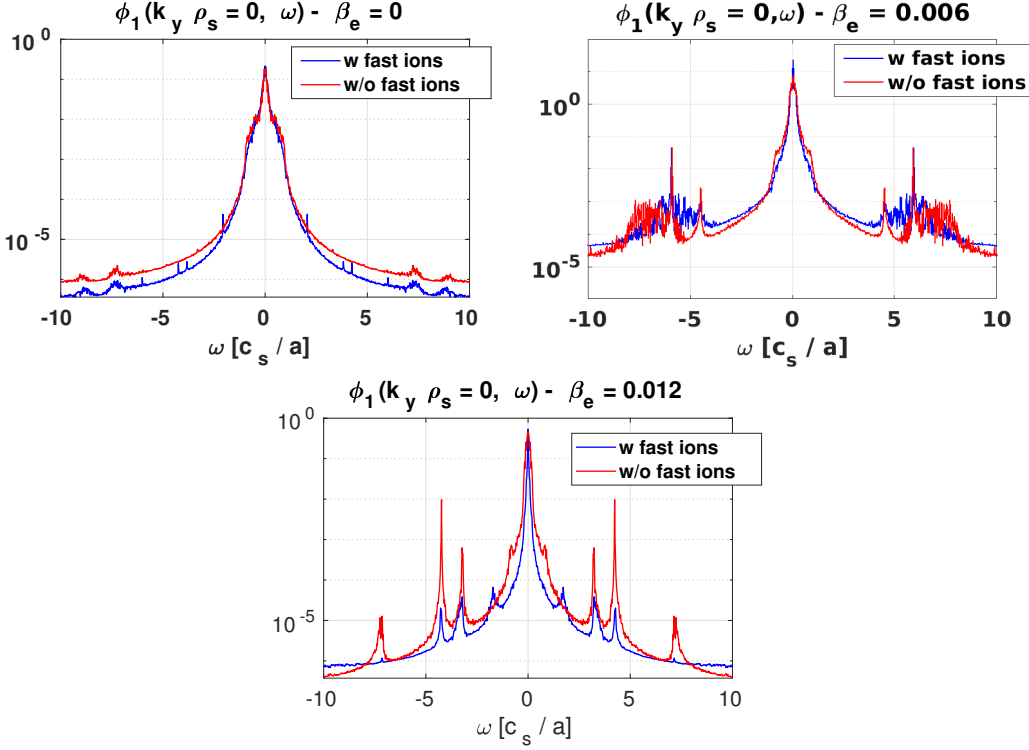


Figure 6.7: Frequency spectra of the zonal component ($k_y \rho_s = 0$) of the electrostatic potential ϕ_1 averaged over the radial mode number $k_x \rho_s$ and the field-aligned coordinate z in the time domain $t/[c_s/a] = [50 - 350]$. The Fourier spectra are obtained in simulations with/without energetic particles at different β_e .

steady state time domain (Phase I). The results of such frequency analysis are shown in Fig. 6.7 for different values of β_e and with and without fast particle species. The Fourier analysis is done by averaging over $k_x \rho_s$ and the field-aligned coordinate z in the "quasi-steady" state time domain $t/[c_s/a] = [50 - 350]$ (phase I). The presence of fast particles for each value of β_e does not significantly affect the spectra of the zonal electrostatic component for $\beta_e \leq 0.006$. The finite frequency peaks observed in the simulations with EP are also visible when only thermal species are retained with similar amplitude. However, the zero-frequency component of $\phi_1(k_y \rho_s = 0)$ slightly increases in the presence of energetic particles, consistently with the results shown in Fig. 6.6. For high- β_e simulations, on the other hand, fast ions significantly affect the amplitude of the high-frequency peaks of the zonal modes, which drop by

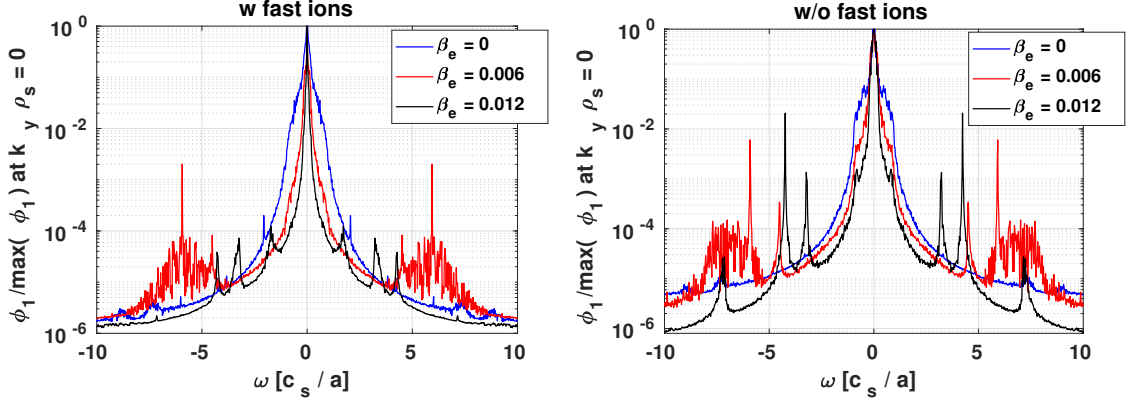


Figure 6.8: Normalized frequency spectra of the zonal component ($k_y \rho_s = 0$) of the electrostatic potential ϕ_1 averaged over the radial mode number $k_x \rho_s$ and the field-aligned coordinate z in the time domain $t/[c_s/a] = [50 - 350]$ for simulations a) with b) without fast ions.

several order of magnitude compared to the simulation where only thermal species are considered. However, the amplitude reduction of these modes does not alter the transport and zonal levels, as observed in Figs. 6.2-6.6. Furthermore, energetic particles do not affect the frequency of the zonal modes. The results shown in Fig. 6.7 are summarized in Fig. 6.8 for different values of the electron plasma beta. Fig. 6.8 reveals a dependence of the high-frequency peaks with $1/\sqrt{\beta_e}$. The excitation of the finite frequency peaks observed in the electrostatic potential spectra, can be further investigated by studying the contribution of the different terms in the free energy balance equation (see section 2.17). The dominant contribution to the overall energy increase at $k_y \rho_s = 0$ is the mode-to-mode nonlinear coupling \mathcal{NL} . As discussed in chapter 2, \mathcal{NL} is a conservative term and its contribution to the overall energy balance is always zero when summed over all the $k_x \rho_s - k_y \rho_s$ mode components. However, it may cause an energy redistribution from different scales. Typically, this nonlinear coupling between finite ITG-relevant $k_y \rho_s$ and the zonal mode components is the main saturation mechanism of ion scale-driven turbulence, as explained in detail in Ref. [131]. In particular, \mathcal{NL} is typically found to transfer energy from the ITG-scales to $k_y \rho_s = 0$ with a consequent turbulence reduction. A Fourier analysis of this term is shown in Fig. 6.9 for the different values of β_e employed previously at $k_y \rho_s = 0$ and by averaging over the field-aligned coordinate z . The time domain considered for this spectral analysis is $t[a/c_s] = [50 - 350]$. Fig. 6.9 reveals that the

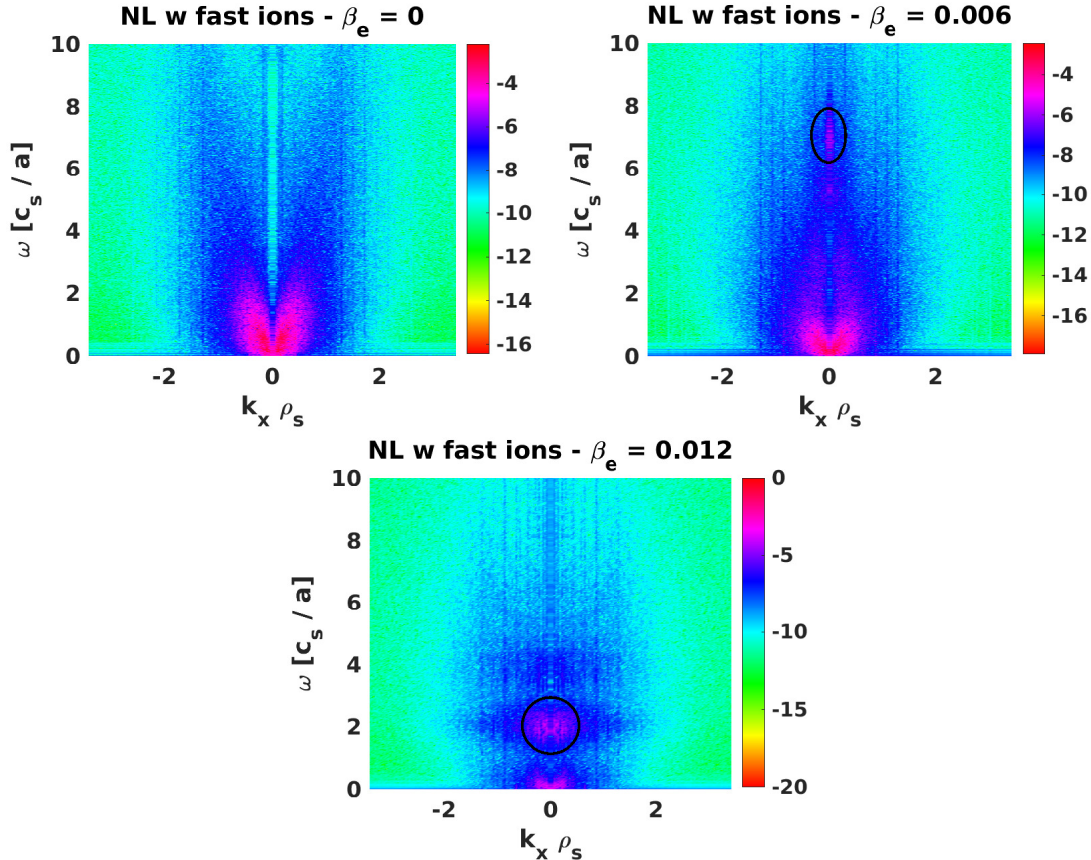


Figure 6.9: Fourier spectra of the nonlinear transfer term (defined in Eq. (2.150)) for the bi-normal mode number $k_y \rho_s = 0$ at a) $\beta_e = 0$, b) $\beta_e = 0.006$ and c) $\beta_e = 0.012$ retaining the energetic particle species. The nonlinear transfer has been averaged over the field-aligned coordinate z in the time domain $t[a/c_s] = [50 - 350]$. The amplitude of the signal is plotted in logarithmic scale.

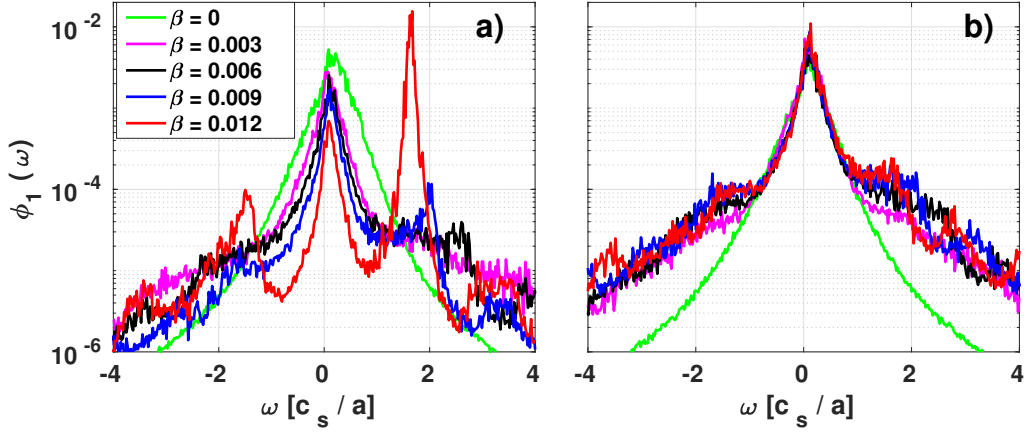


Figure 6.10: Frequency spectra of $\bar{\phi}_1$ - averaged over $k_x\rho_s$ and z - for different β_e at $k_y\rho_s = 0.1$ for simulations a) with b) without fast ions in the time range $[50-340]a/c_s$. The plots share the same legend. The ITG-frequency peaks at $\omega/[c_s/a] \sim 0.08$, while the high-frequency mode follows the relation $\omega/[c_s/a] = v_{th,i}/(2qR_0\sqrt{\beta_i})$ for each value of β_e . Reproduced from [167], with the permission of IAEA.

high frequency peaks arise from the nonlinear coupling of zonal and finite $k_y\rho_s$ mode components. However, as already mentioned before, no significant contribution of the energetic particle species to the nonlinear excitation of these high-frequency zonal modes is observed. Therefore, the transition to the second nonlinear phase identified previously for $\beta_e = 0.012$ and characterized by an increase in the shearing rate levels and a consequent reduction of the turbulent fluxes cannot be linked to a direct effect of energetic particles on the zonal mode component.

6.2.2 Observations at finite toroidal mode numbers

In all the above simulations with significant energetic particle electromagnetic effects, two different nonlinear phases could be found. A striking observation during the first phase are high-frequency modulations of the heat fluxes. In the following section, the possible relation between the finite- $k_y\rho_s$ modes observed in Fig. 6.5 and the turbulence suppression enhanced by EP during Phase I is investigated in detail.

For this purpose, a windowed Fourier transform has been applied to the gyroaveraged electrostatic potential in the first nearly-steady state time range. Fig. 6.10 shows the spectral analysis of ϕ_1 for different β_e at $k_y\rho_s = 0.1$ in all the simulations

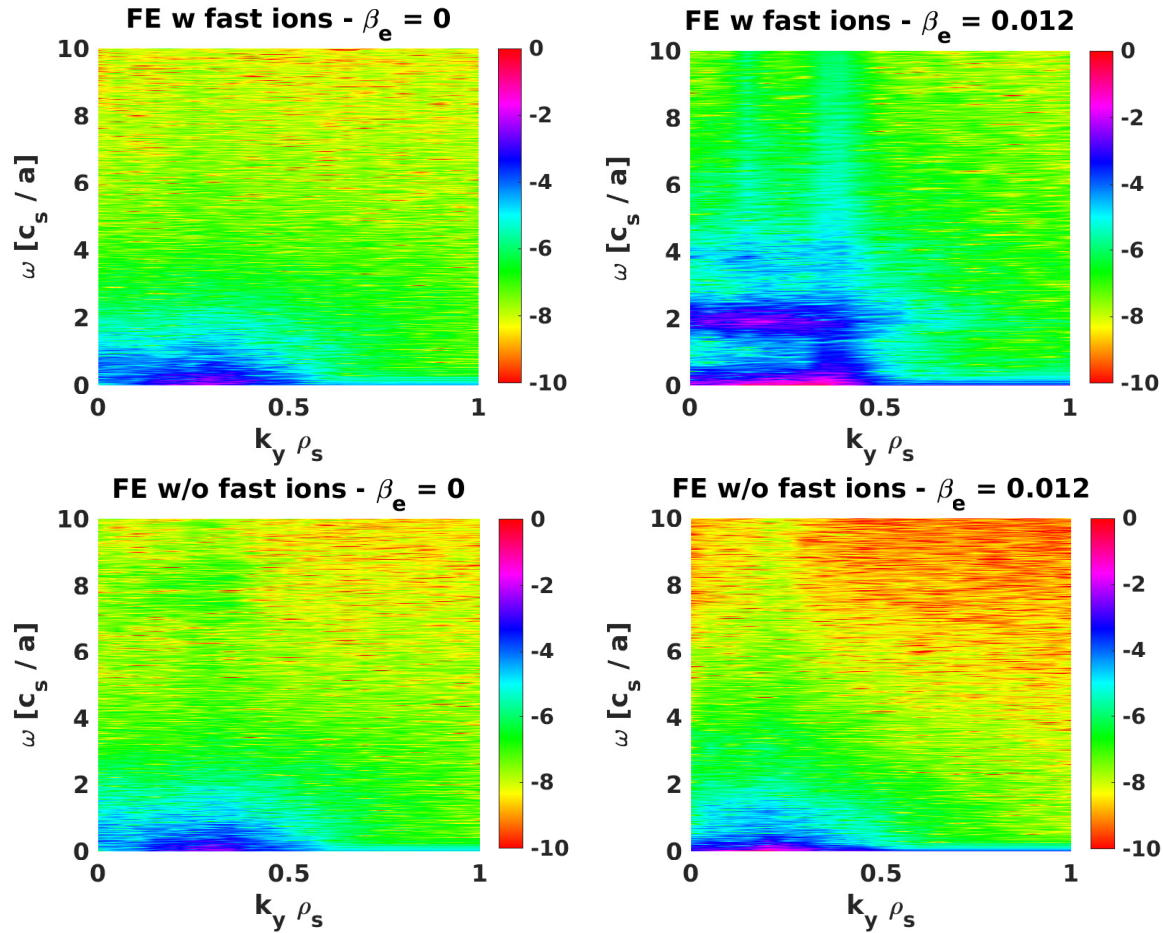


Figure 6.11: Normalized Fourier spectra of the overall free energy (FE) averaged over the field-aligned coordinate z and $k_x \rho_s$ in the time domain $t[a/c_s] = [50 - 350]$ for simulations with/without (top/bottom) energetic particles at $\beta_e = 0$ and 0.012. The amplitude of the signal is plotted in logarithmic scale.

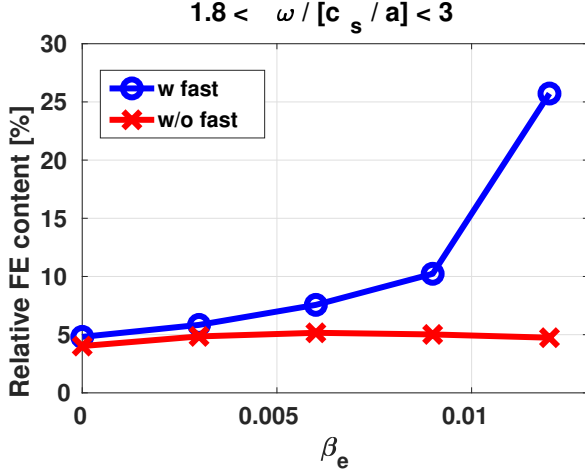


Figure 6.12: Free energy (FE) content enclosed in the high-frequency range, namely $1.3 < \omega/[c_s/a] < 3$ for different β_e in simulations with/without energetic particles.

with/without energetic particles of Fig. 6.1. Clearly, a progressive destabilization of high-frequency components with β_e can be seen at $k_y\rho_s = 0.1$ that is not observed in the absence of EP (see Fig. 6.10b)). Moreover, Fig. 6.10a) shows a corresponding reduction of the ITG-frequency domain peak ($\omega/[c_s/a] \sim 0.08$) from ca. 30% for $\beta_e = 0.003$ to ca. 85% for $\beta_e = 0.012$ with respect to the electrostatic limit, as the high-frequency component is destabilized. The presence of this mode is observed in a wide spectral ($k_y\rho_s$) range which broadens with increasing β_e . For the case $\beta_e = 0.012$, for instance, high-frequency fluctuations are observed up to ITG relevant binormal mode-numbers, namely $0.025 < k_y\rho_s < 0.2$ with a maximum at $k_y\rho_s = 0.15$.

A detailed investigation on the impact of these high-frequency modes on the background plasma turbulence can be performed by studying the overall free energy spectra for the simulations with/without EP at different β_e . Fig. 6.11 shows the Fourier analysis of the free energy term, averaged over $k_x\rho_s$ and z in the time domain $t[a/c_s] = [50 - 350]$. It reveals a significant energy redistribution from ITG-like to high-frequency modes enhanced by energetic particles and nonlinear effects. In particular, during the first nonlinear phase, the energy enclosed in the high-frequency range, namely $1.3 < \omega/[c_s/a] < 3$, increases from close to zero to about 30% as β_e is varied from 0 to 0.012, with a consequent reduction in the ITG-frequency free energy content, as shown in Fig. 6.12. These results are consistent with the progressive

6.3 Impact of the energetic-particle temperature

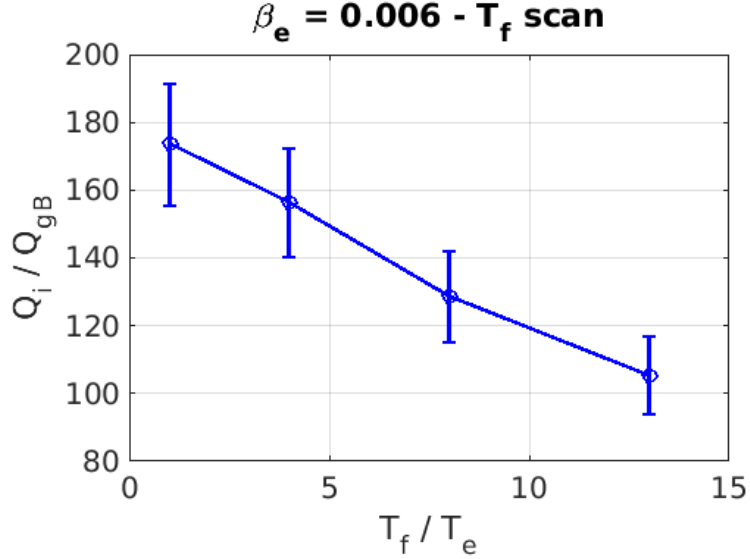


Figure 6.13: Time averaged nonlinear main ion heat fluxes in GyroBohm units for different values of T_f/T_e at $\beta_e = 0.006$.

stabilization observed in the first phases of the nonlinear simulations with β_e and energetic particles.

6.3 Impact of the energetic-particle temperature

The role of energetic particles on the nonlinear electromagnetic turbulence suppression observed in Figs. 6.1-6.2b) is related to the destabilization of high-frequency modes. As discussed in chapter 5, one of the main parameters which characterize fast particles is their large temperature T_f . Therefore, the dependence of the nonlinear excitation of these MHD modes on the fast ion temperature is investigated with nonlinear GENE flux-tube simulations at $\beta_e = 0.006$. The main plasma parameters, geometry and numerical resolution are fixed at the values previously employed and partially summarized in table 4.1. From Fig. 6.13 it is possible to observe a substantial reduction of the main ion turbulent fluxes as the fast ion temperature is increased with a relative stabilization by about 40% at $T_f = 13T_e$. Minor fast particle effects on the shearing rate levels are observed, similarly as previously shown during the nonlinear β_e -scan at $T_f = 9.8T_e$. In particular, no transition to the so-called Phase

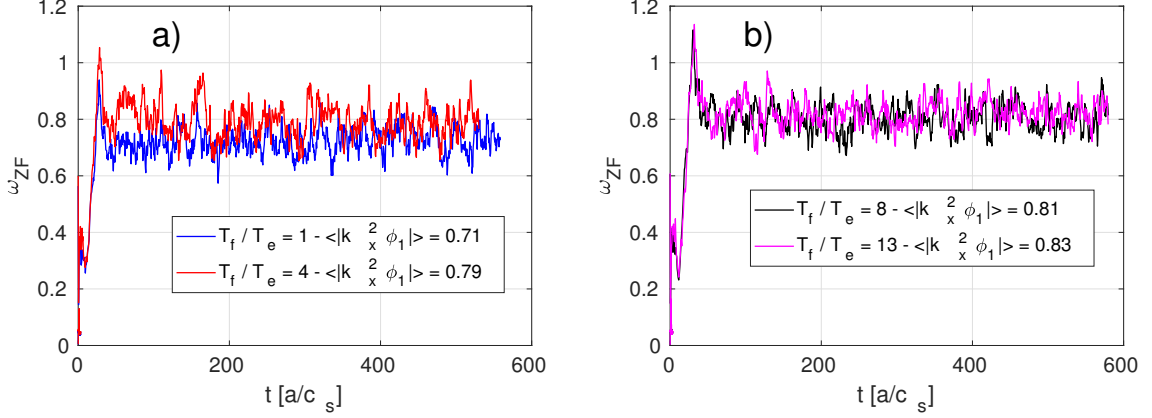


Figure 6.14: Time trace of the shearing rate amplitude ω_{ZF} for different values of the fast particle temperature at $\beta_e = 0.006$. The time averaged value of the shearing rate amplitude at each T_f/T_e is summarized in each plot legend.

II with enhanced shearing rate amplitudes is found. However, for $\beta_e = 0.006$ the increase in the energetic particle temperature leads to a slight growth of the time averaged shearing rate, as shown in Fig. 6.14. Moreover, as the main ion heat flux is reduced with T_f , a progressive enhancement in the destabilization of high-frequency modes of the electrostatic potential spectra is observed at $k_y\rho_s = 0.1$ (see Fig. 6.15). Fig. 6.15 also reveals a corresponding reduction of the negative frequency components as the amplitude of EP-driven mode increases. This observation is consistent with the three-wave-coupling frequency matching condition which needs to be satisfied to allow a resonant energy exchange (i.e. $\omega_1 = \omega_2 + \omega_3$ with $\omega_{i=1,2,3}$ the frequency of the waves involved). To extract the frequency spectra of the electrostatic potential, a Fourier transform has been applied to $\bar{\phi}_1$ in the saturated steady state time domain $t[a/c_s] = [50 - 350]$. Furthermore, by studying the overall free energy spectra (averaged over $k_x\rho_s$ and z in the time domain $t[a/c_s] = [50 - 350]$) for each value of the EP temperature, a strong energy redistribution from ITG-like to high-frequency modes is observed. In particular, as shown in Fig. 6.15b) the energy enclosed in the high-frequency range, namely $1.3 < \omega/[c_s/a] < 3$, increases from close to zero to about 10% as T_f/T_e is varied from 1 to 13 at $\beta_e = 0.006$. These results are consistent with the observations of Fig. 6.12 and with the progressive stabilization of Fig. 6.15 with T_f/T_e . More details about the nonlinear coupling between turbulent and high-frequency modes are given in section 6.6 and 6.7.

6.4 Linear analyses - mode identification

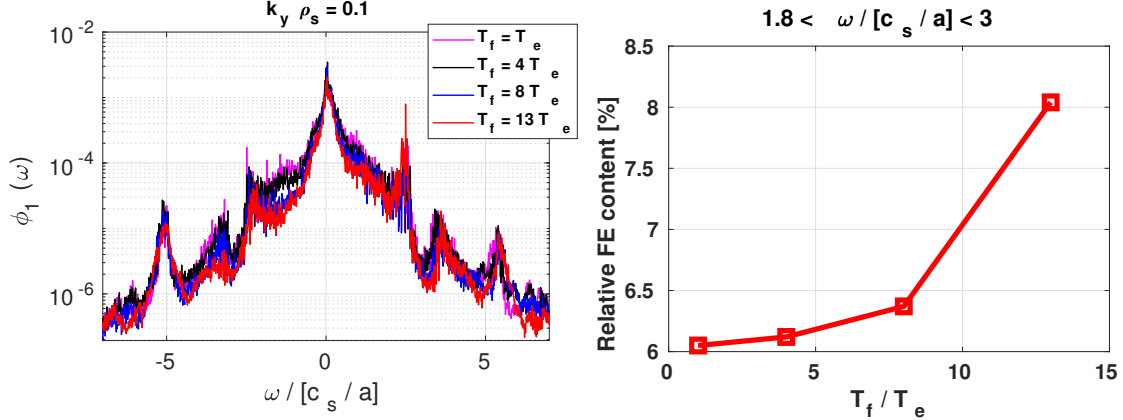


Figure 6.15: a) Frequency spectra of $\bar{\phi}_1$ - averaged over $k_x\rho_s$ and z - for different T_f/T_e at $k_y\rho_s = 0.1$ and $\beta_e = 0.006$ in the time range $[50 - 340]a/c_s$. The ITG-frequency peaks at $\omega/[c_s/a] \sim 0.08$, while the high-frequency mode follows the relation $\omega/[c_s/a] = v_{th,i}/(2qR_0\sqrt{\beta_i})$; b) Overall free energy content enclosed in the high-frequency range, namely $1.3 < \omega/[c_s/a] < 3$ for different T_f/T_e at $\beta_e = 0.006$.

6.4 Linear analyses - mode identification

The nature of the high-frequency modes identified in the spectral analysis presented above is clarified in the following section with linear single mode analyses. The main plasma parameters and magnetic geometry are the same employed for the nonlinear studies and inspired by chapter 4. We used 32 grid points in radial direction and 24 points along the field line. The bi-normal wave-number is fixed to $k_y\rho_s = 0.1$, which corresponds to a toroidal mode number of 17. In velocity space, 32 points and 24 equidistant symmetric grid points have been used for resolving, respectively, the μ and the $v_{||}$ space with a $(\mu, v_{||})$ box size of respectively (9, 3) in normalized units. The first study presented in this section concerns the linear stability analysis of the high-frequency component observed in the nonlinear GENE turbulence simulations. Since this mode appears to be destabilized in presence of electromagnetic fluctuations a scan over β_e is first performed. Fig. 6.16 shows the growth rates and frequencies of the dominant and subdominant modes at $k_y\rho_s = 0.1$. To extract the growth rates and frequency of the instability enhanced by EP, a low-frequency filter has been applied to remove the slowly-varying ITG component from the time trace of the perturbed electrostatic potential. Thereafter, the corresponding linear mode observables are

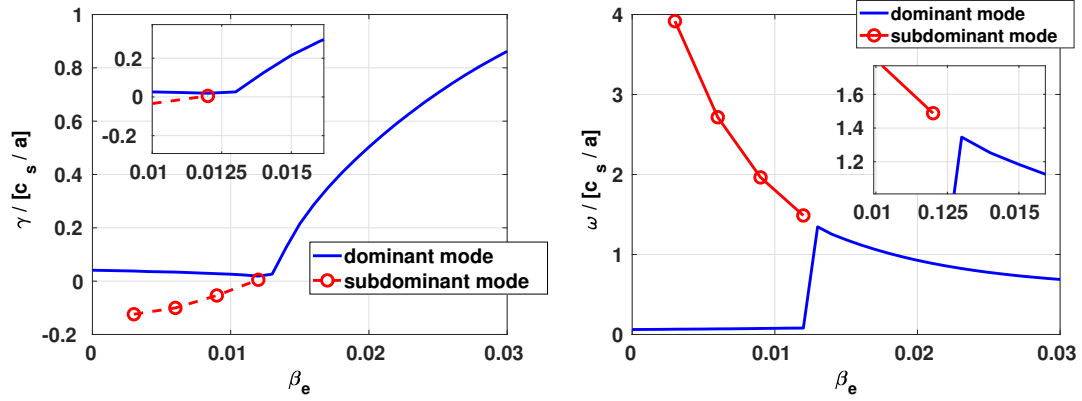


Figure 6.16: Linear growth rates a) and frequencies b) of the dominant and subdominant modes for different β_e at $k_y \rho_s = 0.1$ and $T_f = 10T_e$.

calculated by means of linear regression of the filtered logarithmic time trace of the perturbed electrostatic potential. Similar frequency analyses will also be performed in chapter 7 to extract the EGAM frequency and growth rate. Fig. 6.16 reveals that the higher-frequency mode component is linearly stable for $\beta_e < 0.013$, where ITG represents the most unstable micro-instability. The linear damping of the mode driven by EP decreases with β_e until it becomes the dominant instability. At $\beta_e \approx 0.013$ a discontinuity in $\omega / [c_s / a]$ is observed (see Fig. 6.16b)), indicating a mode transition. These high-frequency modes have the same properties as those observed in the turbulent spectra of the electrostatic potential in Fig. 6.10. They are destabilized at the same $k_y \rho_s$ scale and have similar $\omega / [c_s / a]$ values. Therefore, these modes are linearly stable in all the nonlinear simulations shown previously and brought to finite amplitude only via nonlinear mode-to-mode coupling. In the following we will refer to this instability as *linearly marginally stable* EP-driven mode. Further meaningful insights on the physical nature of this mode can be obtained by studying the poloidal mode structure of the electrostatic potential, shown in Fig. 6.17 for $\beta_e = 0.015$. All the other physical parameters and magnetic geometry are fixed to the reference values employed in the nonlinear analyses. Fig. 6.17 reveals that the electrostatic potential is characterized by 20 (inner surface) and 21 (outer surface) maxima. Therefore, the dominant poloidal mode numbers are $m = 20$ and $m = 21$. These observations lead to characterization of the high-frequency instability observed in the nonlinear GENE simulations as a TAE (toroidal-Alfvén-eigenmodes) mode. In particular, the high-frequency components of the electrostatic potential observed in Fig. 6.10-6.16

6.4 Linear analyses - mode identification

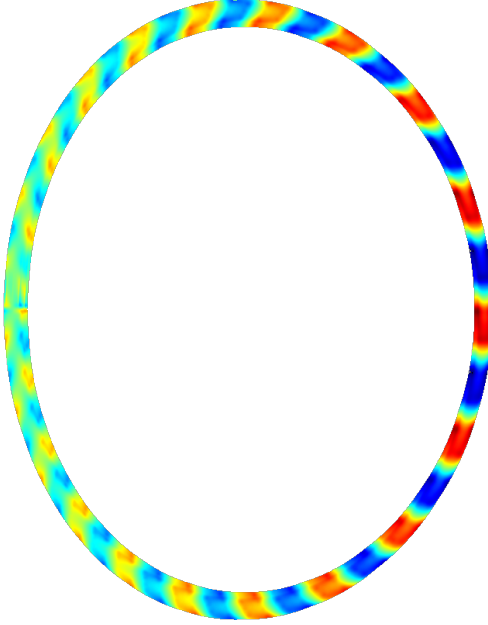


Figure 6.17: Poloidal structure of the electrostatic potential for the converged linear simulation at $k_y \rho_s = 0.1$ ($n = 17$) with $T_f = 10T_e$ and $\beta_e = 0.015$.

are well reproduced by the analytic TAE dispersion relation for each value of β_e . In particular, given a toroidal number n , as discussed in chapter 1, a TAE is located near the crossing of the m and $m + 1$ branches of the SAW (shear Alfvén wave) continuous spectrum, labelled as the continuum X point (CXP) [171, 41]. The TAE frequency can be estimated analytically with precision in the cylindrical geometry by Eq. (1.35) for $k_{\parallel} = (m - nq)/qR = 1/2qR$ as follows (in GENE normalized units)

$$\omega/[c_s/a] = \frac{v_{th,i}}{2qR_0\sqrt{\beta_i}}. \quad (6.1)$$

Here, R_0 is expressed in units of the minor radius and $\beta_i = \beta_e n_i T_i$ represents the thermal ion kinetic over magnetic pressure. Therefore, in the following, we will refer to this mode as TAE-like micro-instability. The contribution of the energetic particle species to the linear drive of the TAE-like mode is further investigated by performing scans over the fast particle temperature and β_e . The linear frequencies and growth rates are summarized in Fig. 6.18. Consistently with the nonlinear results of section 6.3, Fig. 6.18 shows that an increase in the energetic particle temperature does not affect the frequency of the TAE-like mode, which is found instead to depend on β_e

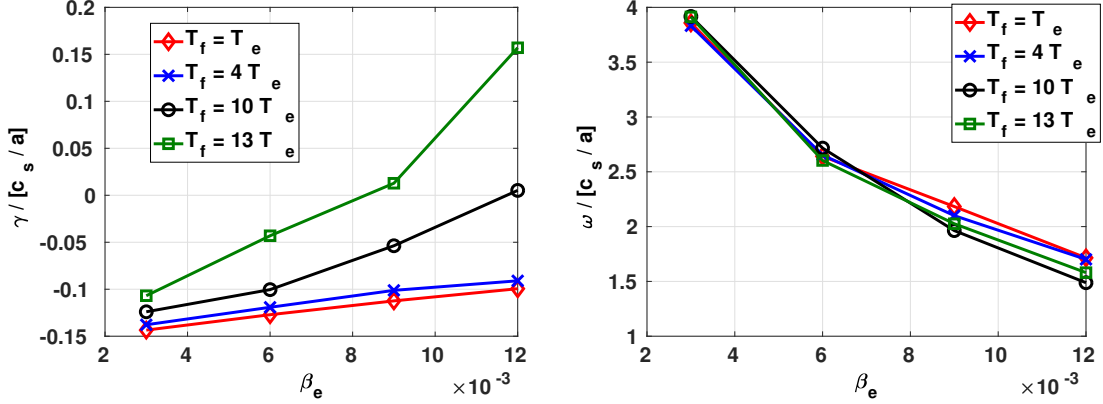


Figure 6.18: Linear growth rates a) and frequencies b) of the TAE-like modes for different β_e and energetic particle temperature at $k_y \rho_s = 0.1$.

(and on $\beta_i = \beta_e \sqrt{n_i T_i}$). On the other hand, the drive term significantly increases with T_f/T_e (as previously observed in section 6.3). In particular, it strongly impacts the threshold for the linear destabilization of this mode, which moves to smaller β_e . These results are consistent with the nonlinear observations of section 6.3 and with the well-known TAE parameter dependences [172, 173, 174, 175, 176].

6.5 Flux-tube approximation of energetic particle modes

Given the radially-global nature of energetic particle (EP) modes, local flux-tube ($1/\rho^* \rightarrow \infty$) simulations may at first sight be questionable. However, they may still provide a good approximation in certain parameter regimes as will be demonstrated in the following. Results of EP-driven modes obtained with the flux-tube gyrokinetic code GYRO have already been previously reported in Ref. [177, 178]. These studies demonstrated the feasibility of local linear and nonlinear simulations of TAE/EM modes for the GA (General Atomic) standard parameters [179]. Here, we present a first comparison between results obtained with the local version of the code GENE and well established linearly global results of TAE modes (similar/related to the ITPA benchmark case) obtained with gyrokinetic global codes at the toroidal mode number $n = 6$ [172, 173]. A detailed description of the plasma parameters can be found in Refs. [172, 173]. They are summarized in table 6.1. The

6.5 Flux-tube approximation of energetic particle modes

ITPA	benchmark	case					
R/a	\hat{s}	q	T_i/T_e	a/L_{T_i}	a/L_{T_e}	a/L_{n_i}	$\beta_e(\%)$
10	0.0	1.75	1.0	0.0	0.0	0.0	0.09
$1/\rho_i^*$	a/L_{n_e}	n_{fD}	T_{fD}/T_e	$a/L_{n_{fD}}$	$a/L_{T_{fD}}$	$1/\rho_{fD}^*$	ρ_{tor}
930	0.0012	0.0036	700	3.3	35	0.0	0.50

Table 6.1: Parameters for the ITPA benchmark case [172, 173] at $\rho_{\text{tor}} = 0.5$. Here, T denotes the temperature normalized to the electron one, $R/L_{T,n}$ the normalized logarithmic temperature and density gradients, \hat{s} the magnetic shear $\hat{s} = (\rho_{\text{tor}}/q)(dq/d\rho_{\text{tor}})$ and $\beta_e = 8\pi n_e T_e / B_0^2$ the ratio between the thermal electron and magnetic pressure.

linear TAE growth rates and frequencies as functions of the fast particle temperature and density are shown in Fig. 6.19. The flux-tube results are obtained at $\rho_{\text{tor}} = 0.5$, which corresponds to the radial position of the peak of the global electrostatic and magnetic potential structures. A good qualitative agreement is observed for each of these simulations both in the frequencies and the growth rates at $T_f < 450T_e$. The quantitative differences between the local and global codes (which are rather small in the frequencies) might be attributed to the lack of a poloidal m -filter in GENE which has been applied in the global codes and/or to the absence of "profile-averaging" effects in the flux-tube simulation which therefore experiences a stronger drive. Clearly, the flux-tube TAE description becomes less and less accurate as the ratio $\beta_f/\beta_{\text{thermal}} = T_f n_f / (T_e n_e + T_i n_i)$ increases. This would be consistent with the interpretation of a progressive mode conversion of the TAE into an energetic-particle-mode (EPM) with β_f as discussed in Ref. [172]. The latter is destabilized as the energetic particle drive contribution overcomes the stabilizing effect provided by the SAW continuum. The TAE/EPM mode conversion occurs when $\beta_f/(\beta_e + \beta_i) > 1$. In correspondence to this threshold, the TAE/EPM frequency exceeds the (upper) toroidicity continuum-gap frequency and starts to strongly interact with the SAW continuum. This interaction can only be captured by retaining a radially-global description, i.e. keeping phase-mixing effects. Therefore, the local flux-tube approximation breaks down as the EPM is destabilized. At this stage, it should be noted that the experimental scenario studied in detail in chapter 4 and above is found at $\beta_f/\beta_{\text{thermal}} < 0.29$, when even the TAE mode is linearly stable and only marginally destabilized through nonlinear coupling with the ITG turbulence. Moreover, the high-frequency modes, observed in Fig. 6.25d) and in Fig. 6.10 are consistent with the TAE linear frequency $\omega/[c_s/a] = v_{th,i}/(2qR_0\sqrt{\beta_i})$, which is significantly below the upper SAW continuum frequency and well located into the TAE gap. Therefore,

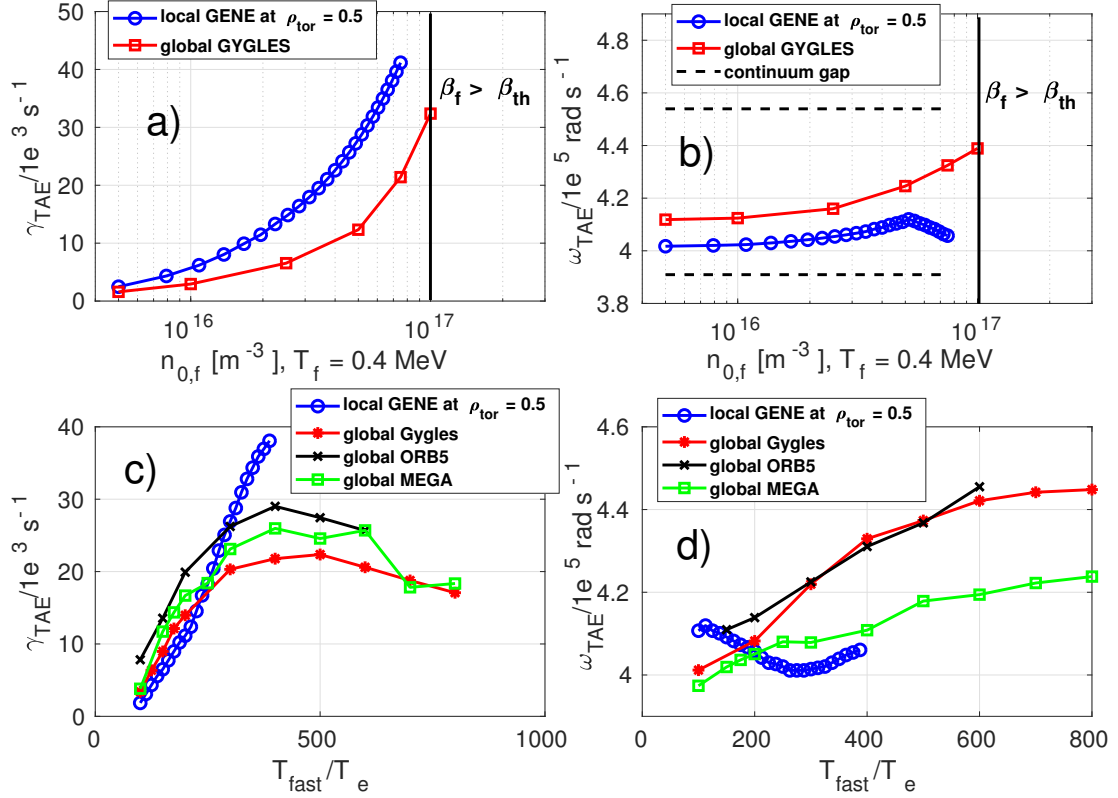


Figure 6.19: Comparison of energetic particle driven TAE a) growth rates and b) frequencies as function of n_f at the fixed fast particle temperature $T_f = 0.4 \text{ MeV}$ and c) growth rates and d) frequencies for varying temperature but fixed $n_f = 7.2 \cdot 10^{16} \text{ m}^{-3}$. The global code results and reference parameters are taken from Refs. [172, 173], the GENE flux-tube have been performed at $\rho_{tor} = 0.5$. The vertical black line in a), b) marks the energetic particle density for which $\beta_f = \beta_{thermal}$.

6.6 Nonlinear energy transfer analysis

no qualitative difference between the local and global descriptions is expected in the range of parameters employed for this analyses, and the local flux-tube gyrokinetic approximation appears to be a reasonably accurate description of energetic particle modes which lie in the SAW gaps.

6.6 Nonlinear energy transfer analysis

The numerical results shown in the previous sections strongly suggest a nonlinear destabilization of marginally stable TAE-like modes via three waves mode-to-mode coupling. Therefore, to understand the phenomenology described so far, a detailed analysis of the nonlinear energy transfer needs to be addressed more closely, e.g., by monitoring the nonlinear mode-to-mode coupling term in the free energy balance equation [131, 40, 132]. It is defined as in Eq. (2.150) as

$$\begin{aligned} \mathcal{N}_k &= \sum_{k',k''} \mathcal{T}_k^{k',k''} \\ &= \sum_{s,k',k''} \Re e \left\{ \int dz dv_{\parallel} d\mu \pi B_0 h_{1,s}^{k,*} \frac{n_s T_s}{F_{0,s}} \left[(\mathbf{k}' \times \mathbf{k}'') \cdot \frac{\mathbf{B}_0}{|B_0|} \right] \left(\bar{\xi}_{1,s}^{k'} g_{1,s}^{k''} - \bar{\xi}_{1,s}^{k''} g_{1,s}^{k'} \right) \right\}, \end{aligned} \quad (6.2)$$

with $h_{1,s}^k = f_{1,s}^k + q_s \bar{\phi}_1^k F_{0,s}/T_s$ the non-adiabatic part of the perturbed distribution function. Here, s denotes the plasma species with density n_s , temperature T_s , and charge q_s . Furthermore, $F_{0,s}$ represents the background distribution, here assumed to be Maxwellian, and $g_{1,s} = f_{1,s} + q_s v_{th,s} v_{\parallel} F_{0,s} \bar{A}_{1,\parallel}/T_s$ a modified distribution with the perturbed distribution function $f_{1,s}$, the thermal velocity $v_{th,s} = \sqrt{2T_s/m_s}$, the gyroaveraged parallel component of the vector potential $\bar{A}_{1,\parallel}$ and the field $\xi_{1,s} = \bar{\phi}_1 - v_{th,s} v_{\parallel} \bar{A}_{1,\parallel}$. The symbol $\mathcal{T}_k^{k',k''}$ represents the nonlinear energy transfer between the modes k , k' and k'' defined in chapter 2 in Eq. (2.152). It is a cubic function of $g_{1,k}$ and it can be expressed as a triadic nonlinear coupling between the modes k , k' and k'' . Since the coupling condition $k + k' + k'' = 0$ needs to be satisfied, the triad transfer is a symmetric function of k' and k'' , i.e. $\mathcal{T}_k^{k',k''} = \mathcal{T}_k^{k'',k'}$. Fig. 6.20a) shows the time evolution of the nonlinear mode-to-mode coupling term $\mathcal{N}_{k_y}(t)$ in the first nonlinear phase, summed over all radial wave-numbers for the simulation at $\beta_e = 0.012$. Here, positive and negative values indicate that a given wave-vector is receiving or losing energy through nonlinear coupling. A significant energy transfer is observed from the ITG-relevant binormal wave-vectors $0.2 < k_y \rho_s < 0.45$ to larger scales $0 < k_y \rho_s < 0.175$. Although its structure is not affected by the amplitude of the magnetic fluctuations, the nonlinear energy exchange rate $\mathcal{N}(\omega)$ significantly

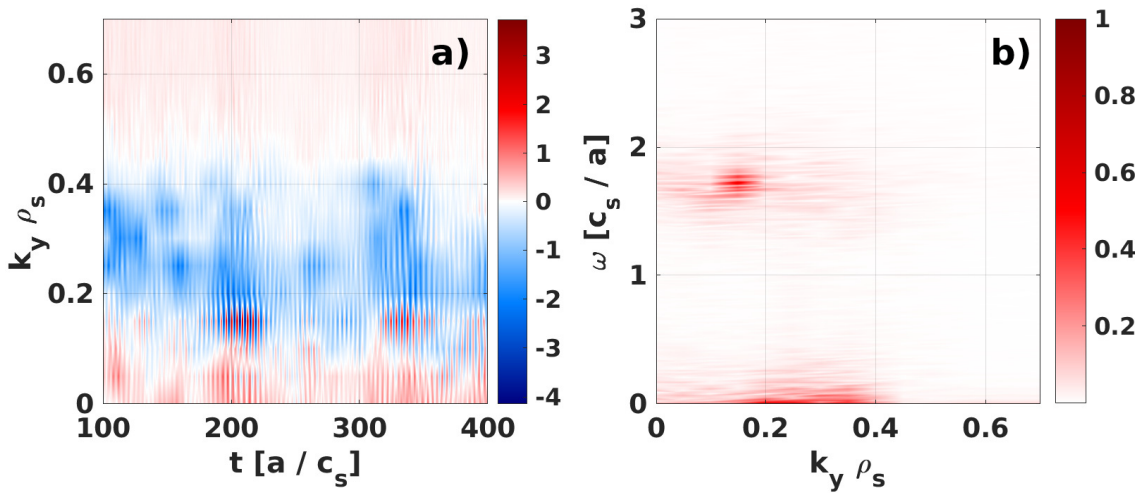


Figure 6.20: Nonlinear transfer \mathcal{N}_{k_y} at $\beta_e = 0.012$ - averaged over $k_x \rho_s$ and z - in $k_y \rho_s$ and a) in the time domain $[100 - 400]a/c_s$ and its b) frequency spectra. Positive and negative values mean, respectively, that the given wave-vector is receiving or losing energy through nonlinear coupling. Reproduced from [167], with the permission of IAEA.

6.6 Nonlinear energy transfer analysis

increases with β_e . This result is in agreement with the high-frequency modulation of the free energy observed in Fig. 6.11. By performing a Fourier decomposition in time of \mathcal{N} for each $k_y\rho_s$, fast oscillations are observed in Fig. 6.20b) for the binormal wave vector range $0.025 < k_y\rho_s < 0.2$ at the specific TAE mode frequency. The mode-to-mode coupling term transfers energy from ITG- to TAE-scales and is strongly enhanced by β_e . These results are consistent with the frequency peaking of the electrostatic potential of Fig. 6.10a).

It was noted previously that linear energy balance analyses at $k_y\rho_s = 0.1$ show that the EP-driven mode is linearly stable for $\beta_e < 0.013$, being suppressed by Landau damping mechanisms. However, as β_e increases, the curvature term contribution to the linear instability increases significantly, with a reduction of the linear damping from $\gamma_{TAE} = -0.124c_s/a$ at $\beta_e = 0.003$ to $\gamma_{TAE} = -0.005c_s/a$ at $\beta_e = 0.012$ (see Fig. 6.16). As this mode gets closer to the marginal stability, more and more energy is exchanged nonlinearly with the dominant ion-scale turbulence through mode-to-mode coupling. The interplay between nonlinear drive and damping of the EP-driven mode can be studied in detail by investigating the field component of the free energy balance (defined in chapter 2 in Eq. (2.142)) [128]

$$\frac{\partial E_w^k}{\partial t} = \sum_s \Re e \left\{ \int dz dv_{||} d\mu \pi B_0 n_s q_s \bar{\phi}_1^{k,*} \frac{\partial g_{1,s}^k}{\partial t} \right\}. \quad (6.3)$$

This analysis is reduced to the study of the curvature term - usually destabilizing - and parallel advection - related to Landau damping mechanisms. Fig. 6.21 reveals that, during the first phase, significant energy is transferred from the main deuterium to the EP curvature term, which reaches amplitudes similar to the thermal species. This interaction, identified by the oscillatory pattern of Fig. 6.21, occurs at the TAE scale, namely $k_y\rho_s \sim 0.15$ and is modulated at the TAE frequency. Moreover, Fig. 6.21 shows that EPs provide the dominant contribution to the high-frequency mode, consistently with the lack of turbulence stabilization observed in their absence in Figs. 6.1-6.2. These results explain the progressive stabilization observed in the first phases of the nonlinear simulations with β_e . In correspondence with the second nonlinear phase, the amplitude of the main deuterium curvature term decreases significantly with non-negligible EP contributions. The latter, however, sustained only through nonlinear coupling with ITG-scales, drops at a later time - $t \sim 430a/c_s$ - as well, as a consequence of the lack of cross-scale transferred energy. The "triad" coupling function $\mathcal{T}_k^{k',k''}$, defined in Eq. (6.2), is employed to investigate in detail the difference in the nonlinear interaction between EP-driven TAE and ZF in the two phases of the nonlinear simulations with energetic particles. Fig. 6.22 shows the triad wave-number spectra, normalized to the main ion heat flux, averaged over the

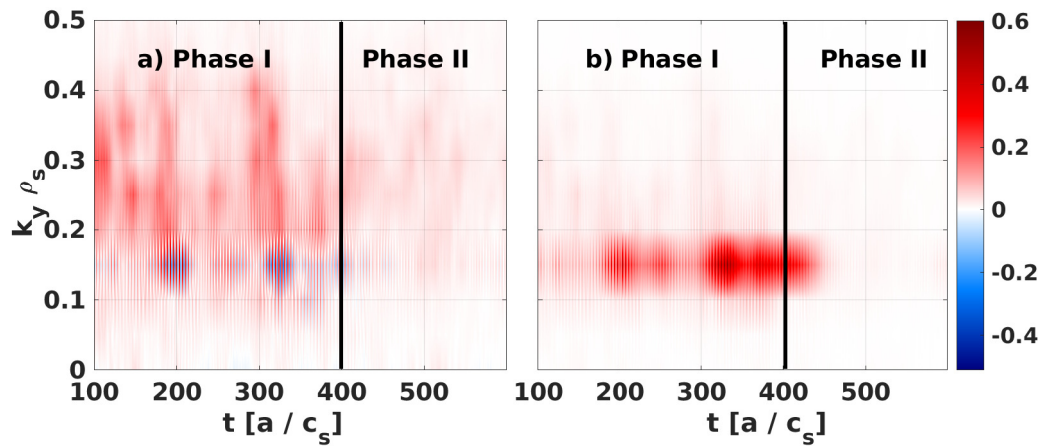


Figure 6.21: Time trace of the field component of the curvature term in the free energy balance (Eq. (2.142)) averaged over the radial mode number $k_x \rho_s$ and the field-aligned coordinate z for a) thermal deuterium and b) NBI heated deuterium - averaged over $k_x \rho_s$ and z - for different $k_y \rho_s$ at $\beta_e = 0.012$. Positive/negative values indicate a destabilizing/stabilising contribution to the overall drive at the given wave number. The black lines mark the time of the transition between phase I and II. Reproduced from [167], with the permission of IAEA.

6.6 Nonlinear energy transfer analysis

time domains of the two phases for $(k_x, k_y) \rho_s = (0.04, 0)$, i.e. for transfer to the zonal component. No significant difference is found if the radial wave-number k_x is changed. In the first phase, the selected triplet is interacting mainly with the binormal mode numbers in the range $0.2 < k_y \rho_s < 0.4$, as can be seen in Fig. 6.22a). At this scale, the ITG-drive peaks and the time-averaged EP-driven mode contribution is negligible, as confirmed by the frequency decomposition of the time trace of the overall triplet. In the first nonlinear phase, the TAE mode is not interacting significantly with zonal modes. However, as the energy is nonlinearly transferred from ITG to TAE scales, the amplitude of the EP-driven modes increases significantly and ZFs are more and more affected by the presence of these modes. In the second nonlinear phase, the whole energy transfer to the specific triplet occurs through the wave-vector $k_y \rho_s = 0.15$, where the TAE mode is dominant and it overcomes the thermal ITG contribution. The energy exchange increases by a factor of ~ 30 . The TAE mode therefore acts as an additional mediator of plasma turbulence, catalyzing energy transfer to zonal modes, strongly affecting the standard paradigm of ZF/ion-scale-turbulence interaction [131, 57].

Another striking observation is the progressive energy transfer via nonlinear three-wave coupling to zonal modes with larger radial mode number, i.e. larger $k_x \rho_s$. Fig. 6.23 shows the time averaged triad energy transfer to the modes at $(k_x, k_y) \rho_s = (0.11, 0.15)$ and $(0.32, 0.15)$ in the time domain ($t = 470 - 550 a/c_s$). This particular bi-normal scale, i.e. $k_y \rho_s = 0.15$, provides the dominant drive term contribution to the TAE-like mode, as shown previously in Fig. 6.21. By increasing the radial $k_x \rho_s$ component of the fixed triplet mode (marked in red in Fig. 6.23) one can study how the energy is successively transferred to modes at the same bi-normal scale but with larger radial mode numbers. In Fig. 6.23 this energy scattering to larger $k_x \rho_s$ is denoted by the black arrow. As explained in detail in Ref. [131] this mechanism strongly stabilizes turbulence since it increases the amplitude of the shearing rate and stronger damping occurs due to the finite gyroradius effect. This energy transfer to larger radial mode numbers is enhanced by the energetic particle driven TAE-like mode, as shown from the frequency analysis of the triplets in Fig. 6.24.

The physical mechanism described in this chapter may very well open ways for new physical interpretations of more general turbulent systems well beyond the scenarios which involve energetic ions and magnetically confined plasmas [180, 181, 182, 183, 184]. In particular, similar nonlinear effects might be observed each time sub-dominant modes approach the marginal stability threshold and are allowed to couple with both the dominant instabilities and the stable modes acting as main saturation players. Strong nonlinear reductions have, e.g., also been found in the absence of energetic ions in transitions from trapped-electron to ITG modes [185] and are an

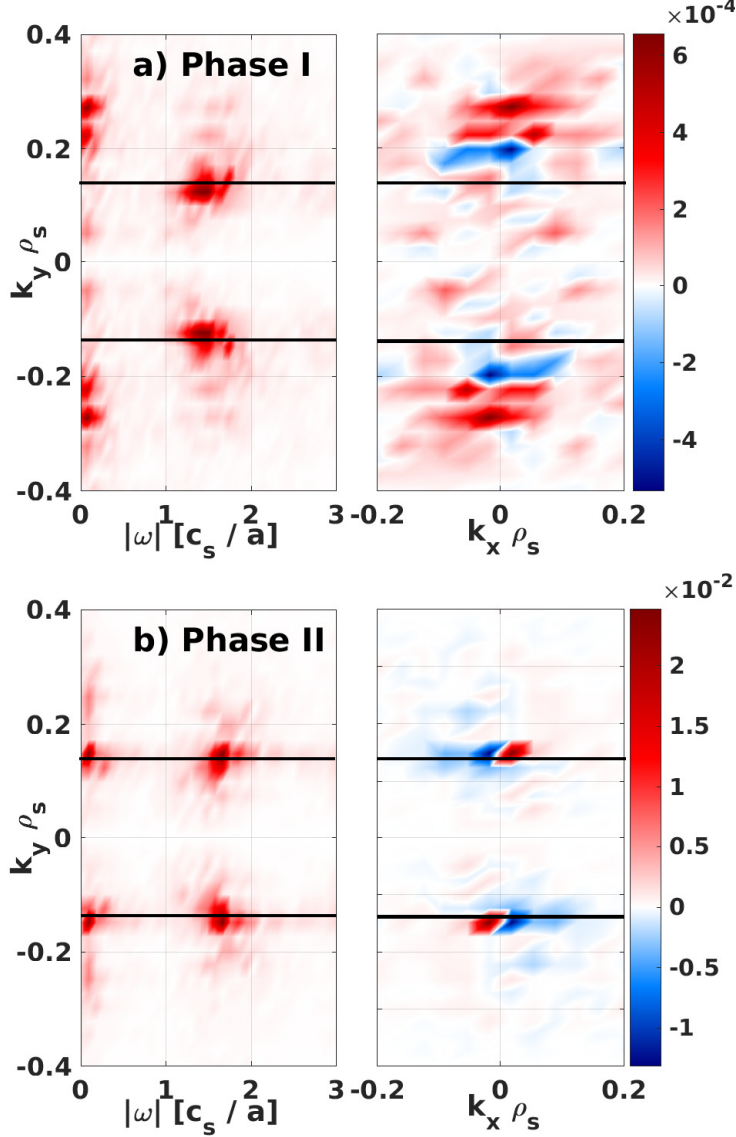


Figure 6.22: Triad energy transfer to the zonal component $T_k^{k',k''}$ normalized to the main deuterium heat flux as function of (ω, k_y) deep in the a) first ($t = 165 - 245 a/c_s$) and b) second phase ($t = 470 - 550 a/c_s$). The black line denotes the dominant TAE scale $k_y \rho_s = 0.15$. Positive/negative values indicate that a given wave-vector is receiving/losing energy through nonlinear coupling with the resonant modes. Note the difference in the colorbar, i.e. in the amplitudes in the two phases. Reproduced from [167], with the permission of IAEA.

6.6 Nonlinear energy transfer analysis

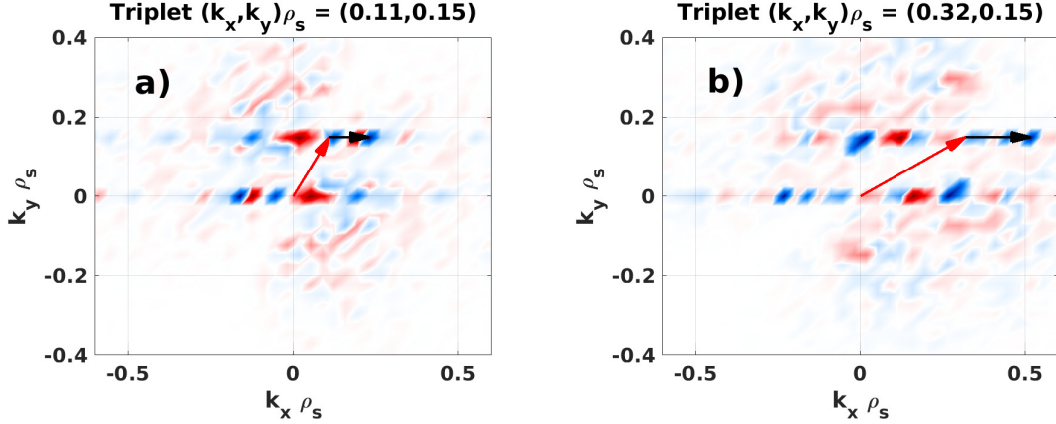


Figure 6.23: Triad energy transfer to the zonal component $\mathcal{T}_k^{k',k''}$ as function of (k_x, k_y) averaged along z and in time during the second nonlinear phase ($t = 470 - 550 a/c_s$). The red arrow denotes the fixed triplet, which represents the dominant TAE scale $k_y \rho_s = 0.15$. The scattering of energy to larger $k_y \rho_s$ is marked by the black arrow. Positive/negative values indicate that a given wave-vector is receiving/losing energy through nonlinear coupling with the resonant modes.

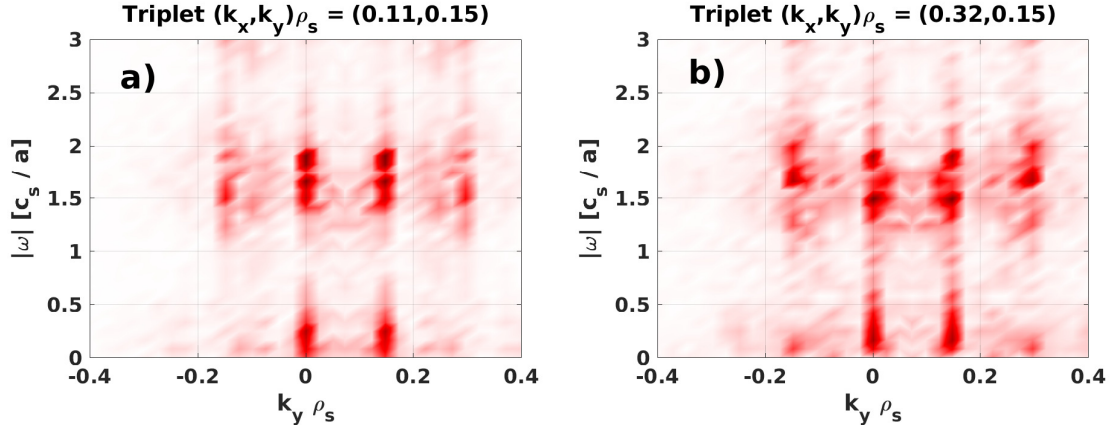


Figure 6.24: Spectral decomposition of the triad energy transfer to the zonal component $\mathcal{T}_k^{k',k''}$ as function of (ω, k_y) averaged along z and in time during the second nonlinear phase ($t = 470 - 550 a/c_s$).

JET L-mode #73224							
R/a	\hat{s}	q	T_i/T_e	R/L_{T_i}	R/L_{T_e}	R/L_{n_i}	$\beta_e(\%)$
3.1	0.52	1.74	1.0	9.3	6.8	0.02	0.33
$n_{^3He}$	n_{fD}	$T_{^3He}/T_e$	T_{fD}/T_e	$R/L_{T_{^3He}}$	$R/L_{T_{fD}}$	$R/L_{n_{^3He}}$	$R/L_{n_{fD}}$
0.07	0.06	6.9	9.8	23.1	3.2	1.6	14.8
AUG H-mode #31563							
R/a	\hat{s}	q	T_i/T_e	R/L_{T_i}	R/L_{T_e}	R/L_{n_i}	$\beta_e(\%)$
3.4	0.32	1.4	1.2	14.1	8.5	1.7	0.5
$n_{^3He}$	n_{fD}	$T_{^3He}/T_e$	T_{fD}/T_e	$R/L_{T_{^3He}}$	$R/L_{T_{fD}}$	$R/L_{n_{^3He}}$	$R/L_{n_{fD}}$
0.023	0	9.1	0	23.9	0	1.7	0
AUG H-mode #32305							
R/a	\hat{s}	q	T_i/T_e	R/L_{T_i}	R/L_{T_e}	R/L_{n_i}	$\beta_e(\%)$
3.7	0.44	1.34	0.98	8.09	6.73	3.63	1.43
$n_{^3He}$	n_{fD}	$T_{^3He}/T_e$	T_{fD}/T_e	$R/L_{T_{^3He}}$	$R/L_{T_{fD}}$	$R/L_{n_{^3He}}$	$R/L_{n_{fD}}$
0	0.14	0	7.90	0	1.39	0	4.86

Table 6.2: Parameters for the JET (Carbon-Wall) L-mode discharge #73224 at $\rho_{\text{tor}} = 0.33$, the AUG H-mode discharge #31563 with ICRH heating at $\rho_{\text{tor}} = 0.21$ and the AUG H-mode non inductive discharge #32305 at $\rho_{\text{tor}} = 0.4$. Here, T denotes the temperature normalized to the electron one, $R/L_{T,n}$ the normalized logarithmic temperature and density gradients, \hat{s} the magnetic shear $\hat{s} = (\rho_{\text{tor}}/q)(dq/d\rho_{\text{tor}})$ and $\beta_e = 8\pi n_e T_e / B_0^2$ the ratio between the thermal electron and magnetic pressure.

obvious subject for further investigations along these lines.

6.7 Similarity of different discharges

The findings discussed in this chapter are not restricted to the specific case studied above but can be observed in an increasing number of scenarios in which a substantial turbulence stabilization can be attributed to energetic particle nonlinear electromagnetic effects. To provide corresponding evidence, three different examples – the JET (Carbon-Wall) L-mode discharge #73224 with both NBI and ICRH minority heating [84], the AUG H-mode discharge #31563 with ICRH heating [186] and the AUG H-mode non-inductive discharge #32305 with only NBI heating [88] – will be studied and presented in the following. The gyrokinetic analyses are performed in the flux-tube limit at the radial position where the bulk ion temperature

6.7 Similarity of different discharges

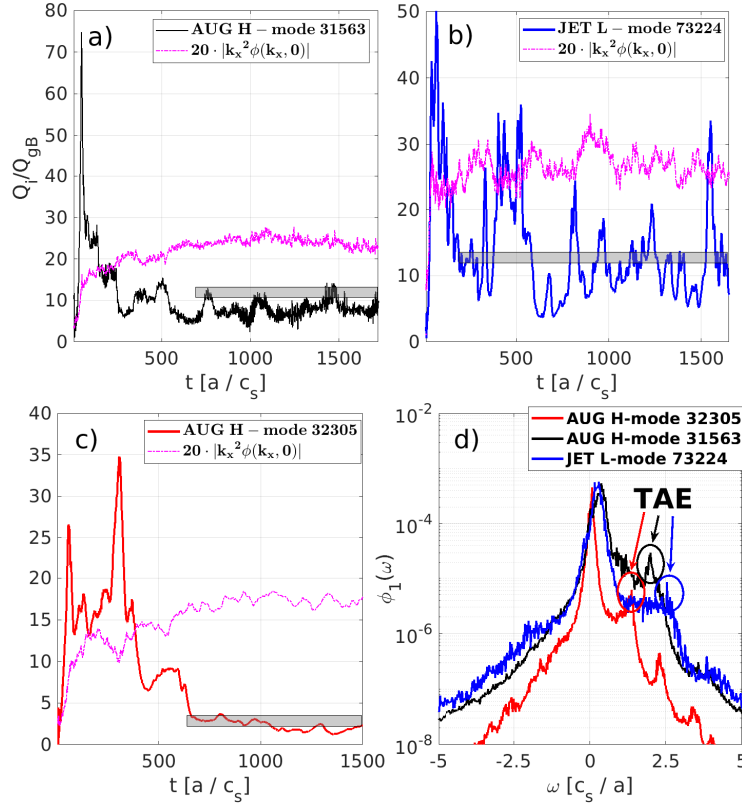


Figure 6.25: Nonlinear (a-c) main ion heat flux time trace (in GyroBohm units) and shearing rate (magenta lines) for the a) AUG H-mode discharge #31563, b) JET L-mode discharge #73224, c) AUG H-mode discharge #32305 and (b) k_x and z -averaged $\bar{\phi}_1$ frequency spectra for each discharge of table 4.1 at the $k_y \rho_s$ corresponding to the maximum of the TAE peak, identified by analyzing the frequency spectra $\phi_1(k_y, \omega)$, i.e. $k_y \rho_s = 0.125$ for the AUG H-mode discharge #32305, $k_y \rho_s = 0.1$ for the JET L-mode discharge #73224 and $k_y \rho_s = 0.175$ for the AUG H-mode discharge #31563. The gray area denotes the experimental values within error bars normalized to $Q_{gB} = v_{th,i} \rho_i^2 n_e T_i / R_0^2$. To reduce the computational cost of the nonlinear AUG H-mode #32305 and JET L-mode #73224 simulations, the heat flux output has been calculated by the GENE code only every 500 time steps. High-frequency oscillations which occur on shorter time scales are hence not visible in this figure. Reproduced from [167], with the permission of IAEA.

profile steepens. As before, the local approach is considered justified by the relatively small Larmor-to-minor-radius ratio. The main plasma parameters are summarized in table 6.2. They are the same as employed in Refs. [84, 88]. The only exceptions are the external $E \times B$ shearing rate, that it is set to zero and the absence of carbon impurities for the JET discharge #73224 to remove any turbulence reduction not related to nonlinear electromagnetic fast ion effects. The characteristic Phase I/II transition described previously (marked by a rather quick increase in the zonal flow amplitude and a substantial turbulence reduction before entering another long-term quasi-stationary state) is observed in each of these studies as shown in Fig. 6.25. It is consistent with the physics mechanism described in Ref. [167] and throughout this chapter. The frequency spectra presented in Fig. 6.25d) demonstrate the existence of high frequency components in each of the considered scenarios. These high frequencies agree well with the analytic prediction $\omega/[c_s/a] = v_{th,i}/(2qR_0\sqrt{\beta_i})$ [41] for toroidal Alfvén eigenmodes (TAE) which are, however, absent in linear simulations and thus nonlinearly destabilized. Consistent with the explanation given previously, the energy content of the bulk turbulence is depleted as the amplitude of the energetic fast particle driven TAE mode grows and the mode acts as an additional catalyst for energy transfer to zonal modes, strongly suppressing heat/particle fluxes. The differences in the bulk plasma parameters (e.g. β_e , T_i/T_e , ν^*), energetic particle heating schemes (e.g. neutral beam injection and/or ion-cyclotron resonance heating) and magnetic configurations (e.g. q , \hat{s} , a , R/a) among the selected discharges show that this phenomenology is not limited to a single particular simulation setup but it is more universal. It should be mentioned at this point that experimental signatures of the nonlinear coupling between ion-scale turbulence and high-frequency Alfvénic instabilities has also been recently observed at HL-2A in a strong NBI heated discharge [187, 188, 189].

6.8 Chapter summary

The strong transport reduction in the presence of fast ions observed in several scenarios (see for example the study shown in chapter 4) is explained in this chapter by their ability to trigger marginally stable modes which are nonlinearly excited and act as a catalyst for the main turbulence saturation mechanisms. These findings are not restricted only to TAEs and similar results could be observed each time the linear excitation threshold of subdominant modes (e.g. BAE, KBM, EPM) is approached. While already being highly relevant to plasma physics with strong heating, this study may furthermore motivate deliberate "design" of marginally stable modes in order to exploit their capability as mediators boosting nonlinear saturation mechanisms

6.8 Chapter summary

such as zonal flows.

In the core scenario discussed in this chapter, which is based on Ref. [167] – a strongly NBI-heated JET discharge with fast ion related temperature profile steepening – a two-phase process could be observed in nonlinear gyrokinetic simulations and analyzed with new spectral analyses techniques. The fast ions provide linearly marginally stable TAE modes which are nonlinearly excited by an energy redistribution from ITG to TAE spatio-temporal scales. As a result, lower transport levels corresponding to the net reduction of the ITG drive can be observed. If sufficiently populated, the fast ion modes furthermore start to increasingly affect the ZF levels which marks a second phase in the simulations. During this phase, the energy being nonlinearly transferred to the zonal modes undergoes a substantial increase in magnitude and is modulated at the TAE frequency. The increase in ZF levels directly impacts the ion-scale turbulence, strongly suppressing heat/particle fluxes. This in turns lowers the nonlinear drive of the EP modes. The system finally finds an equilibrium at a much reduced transport level. This mechanism with possibly high relevance to future plasma performance predictions is not restricted to the scenario analyzed in detail in sections 6.1-6.5, but could also be identified in different JET and ASDEX Upgrade discharges with strong heating and moreover seems to be consistent with recent experimental and analytic studies [190, 188].

Chapter 7

Effect of elongation on Energetic-Particle-Induced Geodesic Acoustic Modes

In the course of this dissertation, the impact of energetic particles on plasma turbulence has been investigated in detail. An improved understanding of previous experimental findings of a strong suppression of ion-scale instabilities [88, 157] in the presence of energetic ions has been derived and presented in chapter 5 and 6. It has been shown that fast particles can strongly reduce the background turbulent transport through electrostatic and electromagnetic effects acting mainly at finite scales ($k_y \rho_s$). However, as discussed in chapter 1, they can also excite and drive global electrostatic field oscillations at $k_y \rho_s = 0$, commonly called geodesic acoustic modes (GAM) [66, 191]. These modes are zonal flows (ZF) [56, 57] with finite frequency oscillations and are usually damped by collisionless Landau damping in the plasma core or by collisions at the edge of the device [58]. As discussed in chapter 1, energetic particles might overcome the thermal damping via inverse Landau damping mechanisms and drive energetic-particle-induced GAMs (EGAMs) [67, 68, 69, 70, 71, 72]. Since ITG turbulence mainly saturates via ZFs any modification of the latter may have a strong impact on transport levels and hence on energy confinement. Therefore, EGAMs could be another interesting player in the context of turbulence stabilization or destabilization [192]. Despite significant recent improvements in the theoretical understanding of the EGAM linear and nonlinear dynamics [77, 78, 79], several aspects still need to be addressed in order to be able to explain the whole complex turbulence/ZF nonlinear interaction. The aim of the present chapter is to contribute a piece along these lines by analyzing the impact of realistic magnetic

7. Effect of elongation on Energetic-Particle-Induced Geodesic Acoustic Modes

configurations on the linear electrostatic EGAM physics. These findings are also tested in a study of a realistic ASDEX Upgrade discharge with strongly elongated plasma. In the present chapter, results obtained in the whole radial domain (global simulations) with the extended non-Maxwellian version are presented and partially benchmarked against the gyrokinetic code ORB5 [146, 147]. ORB5 is a Lagrangian electromagnetic particle-in-cell (PIC) gyrokinetic code, which operates on the full global radial domain. Similarly to GENE, ORB5 splits the distribution function in a background component and in a fluctuating part. However, it discretizes the distribution functions with particles, so called markers, and weights. It can be initialized either as an equivalent Maxwellian background or with a double symmetric bump-on-tail distribution. The verification studies presented in this chapter represent the first radially-global numerical tests on the newly implemented equations and schemes under realistic plasma conditions.

7.1 Impact of elongation on linear EGAM dynamic

The energetic-particle-induced GAMs are resonant modes destabilized through inverse Landau damping mechanisms by the non-Maxwellian features of the energetic particle background distribution functions. Any modification of the resonance position in velocity space, e.g. due to changes in the magnetic geometry, might affect the EGAM drive. Therefore, a detailed investigation of the magnetic geometry dependences on the resonance position needs to be addressed to fully exploit and optimize any possible EGAM beneficial effect on turbulent transport. In particular, following the analytic works of Refs. [148, 149, 193], the plasma elongation is the main parameter analyzed here. Linear GENE simulations are performed with numerical CHEASE magnetic equilibria [13]. CHEASE is a code which solves the equilibrium equation for toroidal MHD equilibria and provides realistic 2D (in the poloidal plane) flux-surfaces. The new version of the non-Maxwellian code GENE is also tested against the gyrokinetic particle-in-cell (PIC) code ORB5 to further extend the benchmark effort on the newly implemented terms started already in chapter 3. These verification studies are an important and necessary step to prove the reliability of the more recent numerical schemes and analytic derivation, possibly allowing in the near future to apply the code to more realistic and complex plasma scenario. For this study an energetic ion species is included in the simulations and modelled with the (double) bump-on-tail distribution function of Eq. (3.23) with a symmetric shift of $\bar{v}_{\parallel} = 2.83$ in GENE normalised units. This value is consistent with the one previously used in several EGAM studies on similar plasma scenarios [77, 78]. As extensively discussed in chapter 3, the fast particle temperature is defined as the second order moment

7.1 Impact of elongation on linear EGAM dynamic

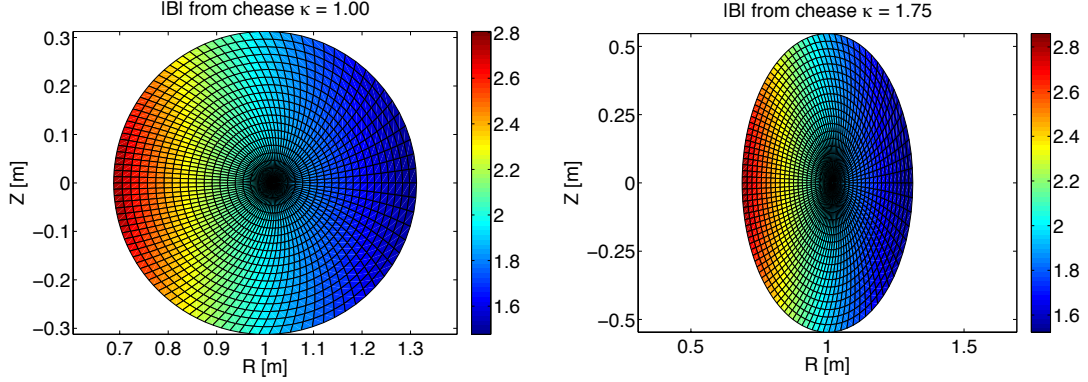


Figure 7.1: Intensity of the equilibrium magnetic field on the flux-coordinate grid for an elongation κ of a) $\kappa = 1.00$ and b) $\kappa = 1.75$. Reproduced from [139], with the permission of IAEA.

of the bump-on-tail distribution function. A local Maxwellian is maintained for the main (thermal) ion species. As discussed in chapter 3, the bump-on-tail distribution of Eq. (3.23) represents a good approximation to model energetic particles with no asymmetry in the magnetic moment direction and with the same amount of particles moving along the magnetic field lines in both directions. It is often employed in gyrokinetic simulations to describe externally injected beams at a specific energy [77, 78, 139, 194]. To facilitate the inter-code comparison, electrons are considered adiabatic in these linear simulations and at $t = 0$ a density perturbation of the form $n_1(\rho_{pol}, t_0) \sim \sin(\pi\rho_{pol})$ is initialized. The impact of kinetic electron on the EGAM dynamic has been recently studied in Ref. [194, 195]. Dirichlet boundary conditions are applied in the radial direction, which spans the range from $\rho_{pol} = [0.06, 0.94]$. Here, $\rho_{pol} = \sqrt{\psi/\psi_{edge}}$ represents the radial coordinate and ψ the poloidal flux, as defined in Eq. (1.5). The inverse aspect ratio $\epsilon (= a/R_0)$ is fixed to 0.3125, with $R_0 = 1\text{m}$ and $a = 0.3125\text{m}$. The magnetic field on axis is equal to $B_0 = 1.9\text{T}$. Furthermore, to facilitate the numerical comparison and restrict the numerical analysis to only the EGAM excitation and dynamic, flat temperature and density profiles are considered. The EP and bulk ion temperatures ($T_e = T_i = T_{EP}$) are fixed by the choice of $\rho^* = \rho_s/a$, with $\rho_s = \sqrt{T_e/m_i}/\Omega_i$ and $\Omega_i = q_i B_0/mc$. Here, $\rho^* = 1/128$ is employed. In Fig. 7.2 the EGAM growth rates and frequencies obtained for different values of the elongation and energetic ion concentrations at $\rho_{pol} = 0.5$ are compared between GENE and ORB5 for a flat q -profile $q = 2$, i.e. shear $\hat{s} = 0$. The elongation

7. Effect of elongation on Energetic-Particle-Induced Geodesic Acoustic Modes

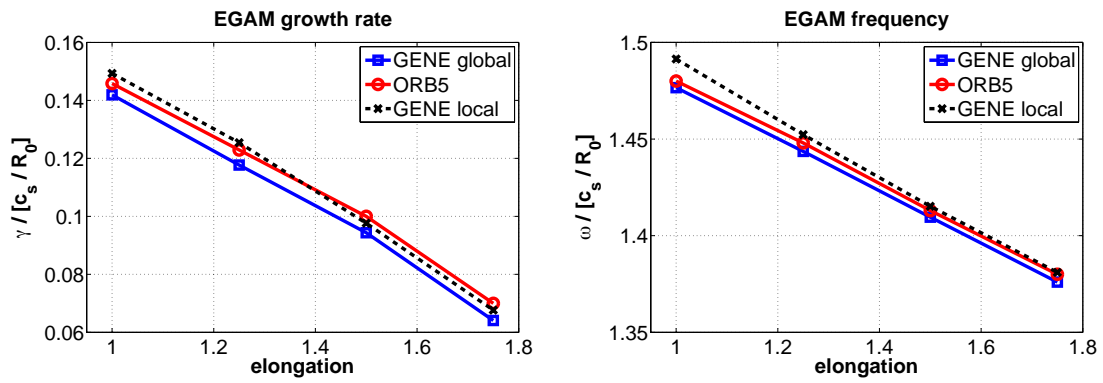


Figure 7.2: EGAM frequencies and growth rates for different values of the elongation and for $n_{EP}/n_e = 0.23$ at $\rho^* = 1/128$ for $q = 2$. Reproduced from [139], with the permission of IAEA.

is varied from $\kappa = 1$ (circular flux surfaces - see Fig. 7.1a) to $\kappa = 1.75$ (elongated plasma - see Fig. 7.1b)). From Fig. 7.2 it is possible to observe the excellent agreement between the codes GENE and ORB5 for the growth rate and frequency of the EGAM. This agreement is also confirmed by the study of the time trace of the perturbed potential ϕ_1 for different values of the plasma elongation, as can be seen in Fig. 7.3. Furthermore, we observe a pronounced dependence of the EGAM growth rate on the elongation. In the range for κ considered here, the growth rate decreases by more than a factor of 2. Only weak changes are found, instead, for the mode frequency which reduces by less than 10%. Fig. 7.2 also contain linear EGAM growth rates and frequencies obtained in the flux-tube local limit at $\rho_{pol} = 0.5$. Due to the simplified setup employed here (such as adiabatic electrons and flat profiles) the local and radially-global results agree particularly well. This good numerical agreement provides further confidence regarding the correct numerical implementation of the non-Maxwellian local and global models.

7.2 Reduced gyrokinetic model for the fast ion energy transfer terms

The relatively simple linear electrostatic setup with adiabatic electrons allows us to derive some simplified set of equations to understand and generalize the results of Figs. 7.2-7.3. The theoretical framework used for the physical interpretation of

7.2 Reduced gyrokinetic model for the fast ion energy transfer terms

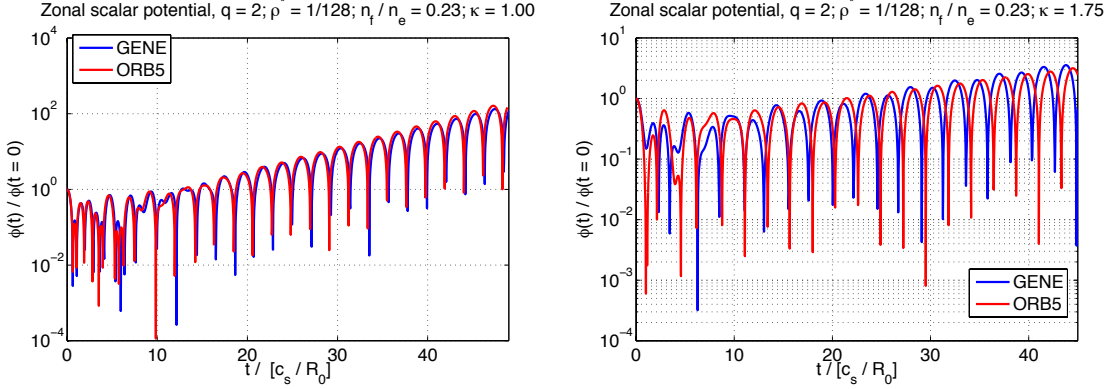


Figure 7.3: Comparison between the scalar potential normalised to $\phi(t = 0)$ obtained from GENE (blue line) and ORB5 (red line) for $n_{EP}/n_e = 0.23$ at $\rho^* = 1/128$ for $q = 2$ and a) $\kappa = 1.00$ and b) $\kappa = 1.75$. Reproduced from [139], with the permission of IAEA.

the effect of the plasma elongation on the EGAM dynamic follows the analysis of Refs. [148, 149]. The perturbed part of the linear electrostatic Vlasov equation (see Eq. (2.66)) for the bi-normal mode number $k_y \rho_s = 0$ can be written in GENE normalized units as follows

$$\begin{aligned} \frac{\partial f_{1,s}}{\partial t} = & -\frac{\mathcal{C}}{\mathcal{J}B_0} v_{||} v_{th} \left[\frac{\partial f_{1,s}}{\partial z} - \frac{q_s}{2T_{0,s}v_{||}} \partial_z \bar{\phi}_1 \frac{\partial F_{0,s}}{\partial v_{||}} \right] \\ & - \frac{T_{0,s}(\mu B_0 + 2v_{||}^2)}{q_s B_0} \mathcal{K}_x \frac{\partial f_{1,s}}{\partial x} + \frac{1}{2v_{||}} \frac{(\mu B_0 + 2v_{||}^2)}{B_0} \mathcal{K}_x \frac{\partial \bar{\phi}_1}{\partial x}. \end{aligned} \quad (7.1)$$

Here, the equilibrium background distribution is kept as a general function and the trapped particle contribution is neglected according to Refs. [148, 149]. As in chapter 2, the following geometrical coefficients $\mathcal{K}_x = -((\mathbf{B}_0 \times \nabla B_0) \cdot \hat{x})/B_0^2$, $\mathcal{C}^2 = \mathbf{B}_0 \cdot \mathbf{B}_0$ and $\mathcal{J}^{-1} = \mathbf{B}_0 \cdot \nabla z/\mathcal{C}$ in the field aligned coordinate system with x radial direction and z field aligned direction have been used. Furthermore, $\bar{\phi}_1$ denotes the gyroaveraged potential. The reference values used for normalizing Eq. (7.1) are the elementary electron charge e , the main ion mass m_i , electron temperature T_e , the magnetic field on axis B_0 and the major radius R_0 , see Ref. [196] for more details. The frequencies have been normalised to c_s/R_0 . In the following derivation, the perturbed quantities are expressed in the k_x, z and ω space through the relation

$$f_{1,s}(\mathbf{x}, z, t) = \sum_m (2\pi)^{-1} \int dk_x d\omega f_{1,s}(k_x, \omega) e^{i(mz - \omega t + k_x x_s)}, \quad (7.2)$$

7. Effect of elongation on Energetic-Particle-Induced Geodesic Acoustic Modes

where $x_s = \delta_s \cos z$, $\delta_s = \frac{\epsilon v_{th,s}}{v_{||}} (v_{||}^2 + B_0 \mu / 2)$ and $\epsilon = a/R_0$. Positive values of the real frequency identify a mode propagating in the ion direction. Employing the Jacobi-Anger expansion $e^{ik_x \delta_s \cos z} = \sum_l i^l J_l(k_x \delta_s) e^{ilz}$ and Eq. (7.2), Eq. (7.1) can be re-written as follows

$$f_{1,m,s} = \sum_{l,l'} -\frac{q_s}{2T_{0,s}v_{||}} \frac{\partial F_{0,s}}{\partial v_{||}} i^{(l'-l)} J_{l'}(k_x \delta_s) J_l(k_x \delta_s) \frac{[\omega_{ds} + (l+m)\omega_t]}{[\omega - \omega_t(l+m) + \omega_{ds}]} \phi_{1,m+l-l'}, \quad (7.3)$$

where $\omega_{ds} = \frac{T_{0,s}}{q_s B_0} (\mu B_0 + 2v_{||}^2) \mathcal{K}_x k_x$ is the radial magnetic drift frequency and $\omega_t = \frac{c}{qB_0 \mathcal{J}} v_{||} v_{th}$ is the transit frequency. Furthermore, the orthogonality relation yields $l+m = l'+m'$. For an $s-\alpha$ magnetic equilibrium, the transit frequency can be rewritten as $\omega_t = \frac{v_{||} v_{th}}{q}$, where q represents the safety factor. Since $k_{x,min} = 2\pi\rho^* \ll 1$, the toroidal drift frequency ω_{ds} can be neglected with respect to the transit frequency ω_t and Eq. (7.3) can be re-written as

$$f_{1,m,s} = \sum_{l,l'} -\frac{q_s}{2T_{0,s}v_{||}} \frac{\partial F_{0,s}}{\partial v_{||}} i^{(l'-l)} J_{l'}(k_x \delta_s) J_l(k_x \delta_s) \frac{(l+m)\omega_t}{[\omega - \omega_t(l+m)]} \phi_{1,m+l-l'}. \quad (7.4)$$

Up to the first order in m' it yields

$$f_{1,m=1,s} = -\frac{q_s J_0^2(k_x \delta_s)}{2T_{0,s}v_{||}} \frac{\partial F_{0,s}}{\partial v_{||}} \frac{\omega_t \phi_{1,m'=1}}{\omega - \omega_t} - \frac{i q_s J_1(k_x \delta_s) J_0(k_x \delta_s)}{2T_{0,s}v_{||}} \frac{\partial F_{0,s}}{\partial v_{||}} \frac{\omega_t \phi_{1,m'=0}}{\omega - \omega_t}. \quad (7.5)$$

The higher order resonance terms are here neglected. The GAM dispersion relation can be obtained from Eq. (7.4) by solving the Poisson equation. For the case of $s-\alpha$ geometry, adiabatic electrons and equivalent Maxwellian distributed particles, the dispersion relation of Ref. [148] is obtained. If a fraction of fast ions, modelled with the bump-on-tail distribution of Eq. (3.23) is considered, the dispersion relation of Ref. [78, 71] is instead derived from Eq. (7.4). The reduced Vlasov equation derived in Eq. (7.5) can be used to investigate the contribution of each particle species (s) to the overall energy exchange between the particles and the mode through the energy conservation property of the Vlasov-Poisson equations introduced already in chapters 2 and 5 [128, 135]. This analysis allows us to study and separate any fast-ion drive mechanisms from the thermal damping of the bulk plasma and will be used in the next section to identify the resonance position for each value of the plasma elongation. Thereafter, the energy exchange between the particles and the mode can be written as

$$\frac{\partial E_w}{\partial t} = \sum_s \Re \left\{ \int dz d\mu dv_{||} \pi B_0 q_s n_{0,s} \bar{\phi}_1^* \frac{\partial F_{1,s}}{\partial t} \right\}. \quad (7.6)$$

7.2 Reduced gyrokinetic model for the fast ion energy transfer terms

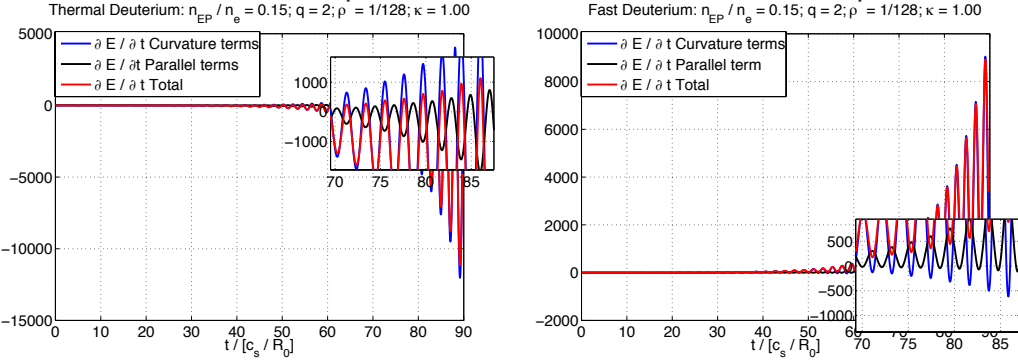


Figure 7.4: Study of the different contributions of the thermal and fast ions to the total energy transfer. Reproduced from [139], with the permission of IAEA.

where $f_{1,s}$ denotes the perturbed distribution function of the species s . This equation enables the study of the contribution of each term of the Vlasov equation to the energy exchange and hence to the mode excitation. Positive (negative) values of $\frac{\partial E_s}{\partial t}$ indicate that the plasma species considered is giving (taking) energy to (from) the electrostatic field component with a consequent growth (damping) of the mode. As shown in Ref. [128], Eq. (7.6) can be written as the sum of curvature and parallel term contributions. In Fig. 7.4 the contribution of each of these terms to the total energy derivative is displayed a) for the thermal and b) for the energetic ions at $n_{EP}/n_e = 0.15; q = 2; \rho^* = 1/128; \kappa = 1.00$. The curvature term represents the main contribution, which is consistent with fast ions exciting a geodesic acoustic mode. On the other hand, the parallel advection although overall smaller becomes significant at the minimum of the curvature term – these two different contributions oscillate, indeed, with opposite phase relation. This picture does not depend on the elongation and it is qualitatively the same between thermal and fast ions. Furthermore, we observe that the fast particles, modelled with the bump-on-tail distribution defined in chapter 3, act as a positive drive to the EGAM with a positive contribution to the particles/mode power exchange. The thermal ions, on the contrary, globally damp the fast ion driven mode, even if instantaneously they can still provide energy [78]. The overall contribution (drive-damping) to the EGAM mode determines the total mode growth rate.

7. Effect of elongation on Energetic-Particle-Induced Geodesic Acoustic Modes

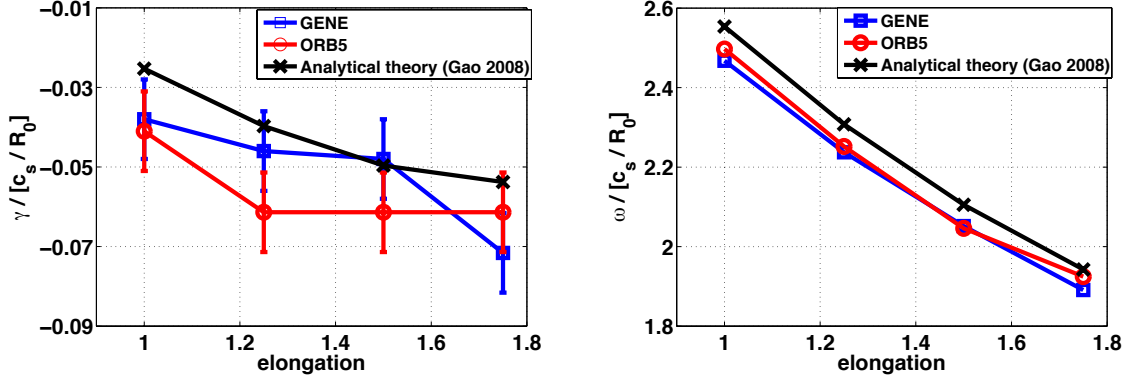


Figure 7.5: Comparison between the theoretical prediction of Ref. [193] and the GENE (blue line)/ORB5 (red line) GAM damping rate a) and frequency b) for different values of the elongation for the case $q = 2$ and $\rho^* = 1/128$. Reproduced from [139], with the permission of IAEA.

7.3 Impact of elongation on resonance position

The effect of the plasma elongation on the resonance positions for both thermal and energetic ions are studied in this section with gyrokinetic simulations and their results are compared to analytical predictions. In the small orbit drift width limit, the dominant resonance mechanism is predicted to occur between the GAM linear mode frequency and the bulk-ion parallel motion, described by the transit frequency ω_t [193]. The latter, averaged over the poloidal angle, is defined in GENE normalised units as follow [193]

$$\omega_t = \frac{v_{||} v_{th,i}}{q} \left[1 + \frac{\epsilon^2}{2} - \frac{\epsilon^2 (\kappa^2 + 1)}{4q^2} \right]. \quad (7.7)$$

Here, κ represents the value of the plasma elongation. In Fig. 7.5 a qualitatively good agreement (inside error bars) between GENE/ORB5 and the theoretical predictions of Ref. [193] can be observed for the GAM damping rate and frequency for different values of the elongation. The relatively large error bars of Fig. 7.5a) are a consequence of the significantly small GAM damping rate, which makes the corresponding analysis more challenging. The geometry and the plasma parameters are the same as employed in the previous section, i.e. $\rho^* = 1/128$ and $q = 2$. The mild dependence of the GAM damping rate on the elongation can be explained studying the $v_{||}$ structure of the energy exchange term. Inserting Eq. (7.4) in Eq. (7.6) yields the following

7.3 Impact of elongation on resonance position

simplified expression for the energy exchange power between the particles and the mode, i.e. the energy taken (negative) or given (positive) from/to the mode

$$\begin{aligned} \frac{\partial E_s}{\partial t} &= \sum_s \Re \left\{ -i\omega \int dz d\mu dv_{||} \pi B_0 q_s n_{0,s} \bar{\phi}_{1,m'=0}^* \frac{\partial F_{1,s}}{\partial t} \right\} \\ &= \sum_s \Re \left\{ i\omega \int dz d\mu dv_{||} \pi B_0 q_s n_{0,s} \bar{\phi}_{1,m'=0}^* \left[\frac{q_s J_0^2(k_x \delta_s)}{2T_{0,s} v_{||}} \frac{\partial F_{0,s}}{\partial v_{||}} \frac{\omega_t \phi_{1,m'=1}}{\omega - \omega_t} \right. \right. \quad (7.8) \\ &\quad \left. \left. + \frac{i q_s J_1(k_x \delta_s) J_0(k_x \delta_s)}{2T_{0,s} v_{||}} \frac{\partial F_{0,s}}{\partial v_{||}} \frac{\omega_t \phi_{1,m'=0}}{\omega - \omega_t} \right] \right\} \end{aligned}$$

This relation is consistent with those obtained in Ref. [70] and demonstrates that the energy transfer between the GAM/EGAM and the plasma species is proportional to the $v_{||}$ derivative of the background distribution function, i.e. $\frac{\partial F_0}{\partial v_{||}}$. If the plasma contains only thermal ions, i.e. it can be described by a Maxwellian background, the exchange power density between the wave and the ions is always negative and the mode is always naturally damped. The magnitude of the damping depends on the value of $\frac{\partial F_0}{\partial v_{||}}$ at the parallel transit motion resonance position. Larger values (in magnitude) of $\frac{\partial F_0}{\partial v_{||}}$ correspond to larger energy exchange rates and in the case of negative $v_{||}$ derivatives to stronger damping. A $\mu = 0$ and $\rho_{pol} = 0.5$ slice of the $v_{||}$ dependent energy exchange term $\epsilon_{v_{||}} = \omega_t v_{||} \frac{\partial F_0}{\partial v_{||}}$ is shown in Fig. 7.6a) in the absence of fast ions for different values of $v_{||}$. The crosses in the figure mark the different resonance conditions as defined by $\omega = \omega_t$, with ω_t given by Eq. (7.7) for each elongation value. With increasing elongation, the resonant parallel velocity moves to smaller values, i.e. for the case of Maxwellian backgrounds to more negative values of $\epsilon_{v_{||}}$ and thus to stronger damping. These findings are consistent with the elongation dependence of the total energy exchange, see Fig. 7.6b). If non-thermalised fast ions are considered, the velocity derivative of the background distribution function assumes positive values. A net energy transfer therefore occurs from the fast ions to the mode. In case the energetic particle drive overcomes the thermal damping, the mode (EGAM) is destabilized with positive values of γ . Furthermore, the EGAM growth rate is weakened with increased elongation which resembles the stronger damping in the GAM case above. This change in the γ dependence is again consistent with the corresponding change in the shape of the velocity space structure of $\epsilon_{v_{||}}$ for a bump-on-tail distribution compared to a Maxwellian background. Indeed, when the resonant transit velocity decreases with the elongation, $\epsilon_{v_{||}}$ also decreases accordingly with a consequent weakening of the wave-fast ion energy transfer. As before, this elongation dependence can also be observed in the total energy exchange, see Figs. 7.8a)-b). Further analysis can be performed studying the velocity space struc-

7. Effect of elongation on Energetic-Particle-Induced Geodesic Acoustic Modes

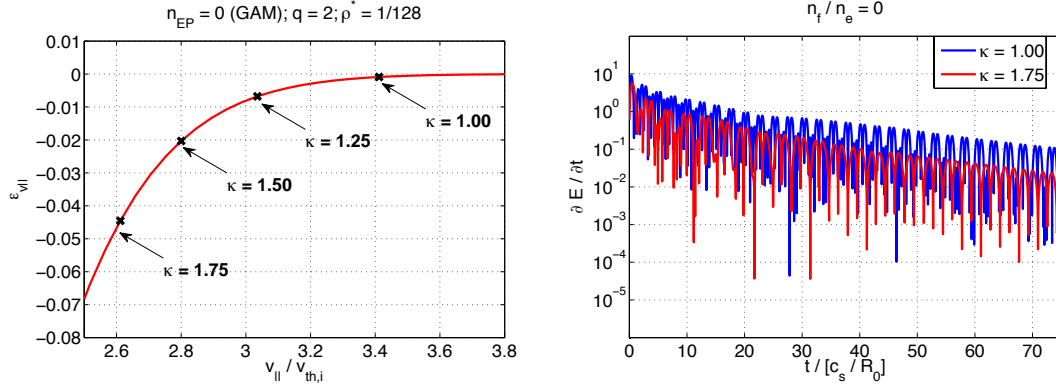


Figure 7.6: Case without fast ions: a) Slice at $\mu = 0$ of $\epsilon_{v_{\parallel}}$ for different values of v_{\parallel} . The crosses in the figure identify the value of $\epsilon_{v_{\parallel}}$ at the different resonance positions identified with Eq. (7.7) for each value of the elongation. b) Time evolution of the system energy exchange for $\kappa = 1.00$ and $\kappa = 1.75$.

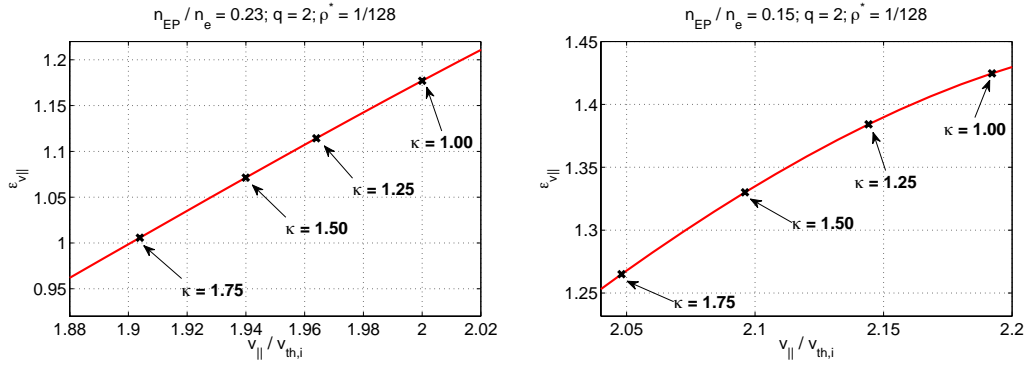


Figure 7.7: Slice at $\mu = 0$ of $\epsilon_{v_{\parallel}}$ for different values of v_{\parallel} for a) $n_f/n_e = 0.23$ and b) $n_f/n_e = 0.15$. The crosses in the figure mark the values of $\epsilon_{v_{\parallel}}$ at the resonance positions associated to different elongation values, see Eq. (7.7). Reproduced from [139], with the permission of IAEA.

7.4 AUG Experiment based studies

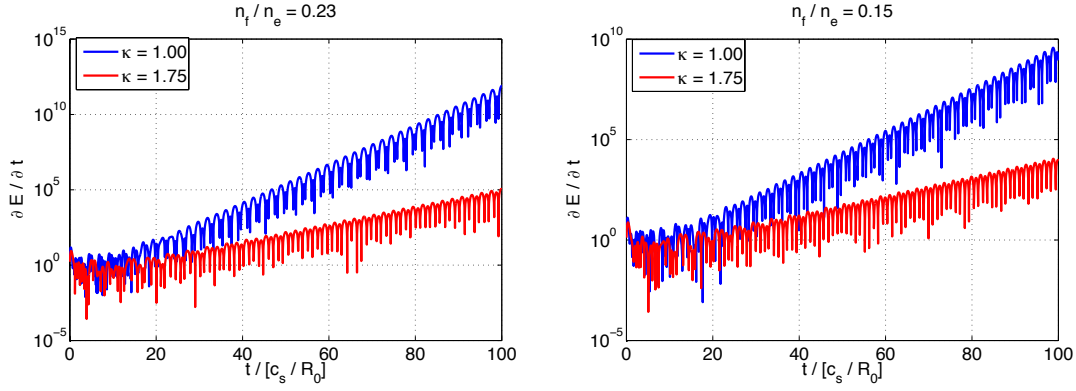


Figure 7.8: Time evolution of the total energy exchange for $\kappa = 1.00$ and $\kappa = 1.75$ for a) $n_f/n_e = 0.23$ and b) $n_f/n_e = 0.15$. Reproduced from [139], with the permission of IAEA.

ture of $\partial E/\partial t$, i.e. the energy exchange, for both different elongations, here $\kappa = 1.00$ and $\kappa = 1.75$, and energetic particle densities, $n_{EP}/n_e = 0.23$ and $n_{EP}/n_e = 0.15$. In Figs. 7.9-7.10 a slice at $\mu = 0$ and $\rho_{pol} = 0.5$ of $\partial E/\partial t$ is shown at a time step which corresponds to a maximum of the energy transfer. A phase space structure connected to the parallel transit resonance can be observed in Figs. 7.9-7.10 for both thermal and fast ions. The peak positions, i.e. the maxima of the energy exchange, occur at $v_{||}$ values predicted by Ref. [193] (black crosses in Fig. 7.9). The full velocity space integrals of the $\partial E/\partial t$ structures shown in Figs. 7.9-7.10 correspond to the values of Fig. 7.8. The results of Figs. 7.9-7.10 have been obtained performing an average over four consecutive maxima of the total energy exchange. However, it is worth mentioning here that the physical picture provided here might depend also on the velocity-space position of the symmetric bump of the energetic particle background. A corresponding investigation will be addressed in the near future.

7.4 AUG Experiment based studies

The previous analyses have shown that the main effect of the plasma elongation on the EGAM dynamics is to move the position of the parallel transit resonance in phase-space toward smaller parallel velocities. For the range of parameters previously employed, both EGAM growth rates and frequencies are therefore reduced in magnitude (with a stronger impact observed on the former). These numerical observations are also in agreement with reduced theoretical models. To further extend

7. Effect of elongation on Energetic-Particle-Induced Geodesic Acoustic Modes

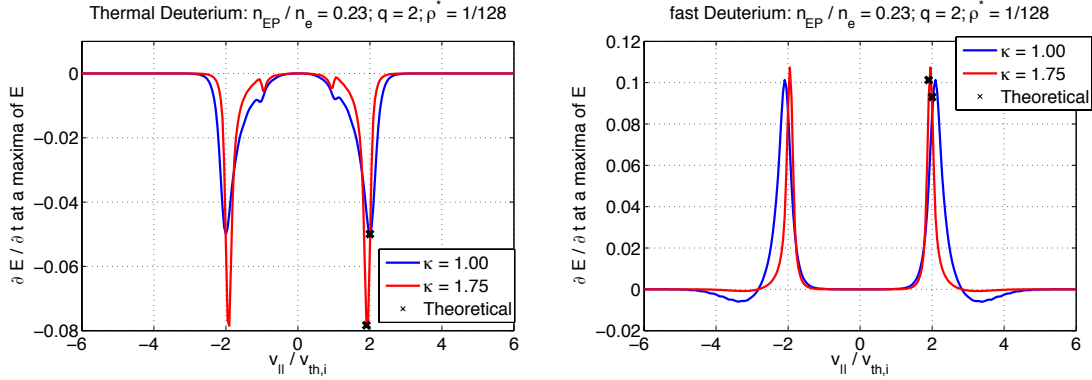


Figure 7.9: Parallel velocity structure of $\partial E / \partial t$ for thermal (left) and fast (right) deuterium at $\mu = 0$ for $\kappa = 1.00$ (blue line) and $\kappa = 1.75$ (red line) at fixed fast ion density $n_f/n_e = 0.23$. The black crosses represent the different resonance positions for each value of the elongation, see Eq. (7.7). Reproduced from [139], with the permission of IAEA.

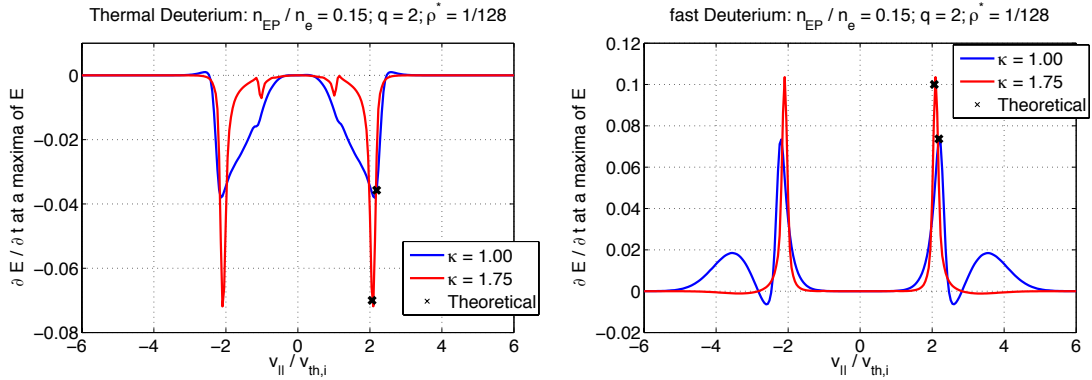


Figure 7.10: Parallel velocity structure of $\partial E / \partial t$ at $\mu = 0$ for the case $n_f/n_e = 0.15$ and $\kappa = 1.00$ (blue line), $\kappa = 1.75$ (red line). The black crosses represent the different resonance positions identified with Eq. (7.7) for each value of the elongation. Reproduced from [139], with the permission of IAEA.

7.4 AUG Experiment based studies

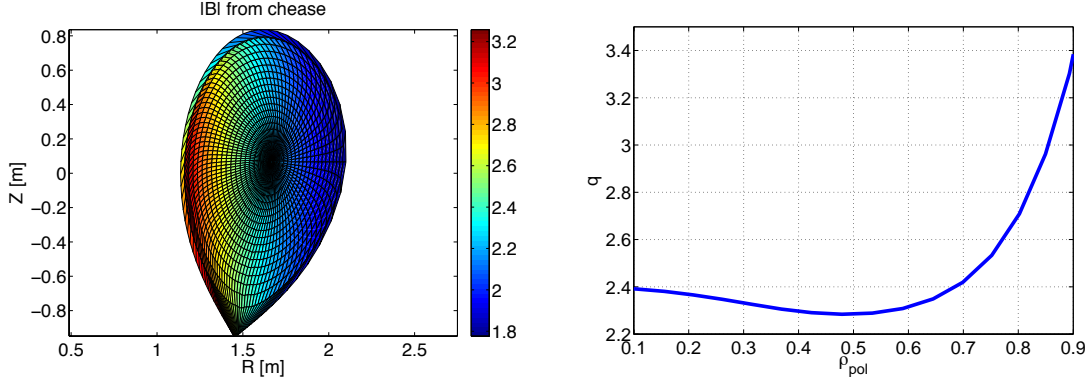


Figure 7.11: a) Intensity of the equilibrium magnetic field on the flux-coordinate grid b) safety factor profile in the AUG discharge. Reproduced from [139], with the permission of IAEA.

and generalize these findings a realistic ASDEX Upgrade experimental scenario with a strongly elongated plasma is investigated in the following section with linear electrostatic simulations studying the $k_y\rho_s = 0$ (EGAM) dynamics. This case refers to the AUG shot #31213 at 0.841s [197], which contains significant fast ion effects and fast-ion driven modes. This selected discharge is particularly relevant in the plasma physics community, since it reports the first experimental observation at ASDEX Upgrade of EGAMs driven by energetic particles. The major and minor radii are $R_0 = 1.62\text{m}$ and $a = 0.482\text{m}$. The magnetic field on axis is $B_0 = 2.2\text{T}$ and the safety factor has a reversed shear, with $q_{min}(\rho_{pol} = 0.5) = 2.3$. The plasma is composed by deuterium, electrons and is heated with $P_{NBI} = 2.5\text{MW}$ of deuterium-NBI. The tokamak magnetic geometry is provided with an experimental CHEASE equilibrium and is shown in Fig. 7.11 with the corresponding safety factor profile. The equilibrium is reconstructed from the experimental discharge via CLISTE [198] and post-processed with CHEASE for interfacing to the gyrokinetic codes. More details on the magnetic geometry and plasma parameters can be found in Refs. [197, 139, 53].

7.4.1 Flat density and temperature profiles

A first simplified setup removing any temperature and density profile effects and considering $T_i = T_e$ is analyzed in the following. In particular, $T_i = T_e = 1.603\text{keV}$ and $n_e = 1.265 \cdot 10^{19}\text{m}^{-3}$, corresponding to $\rho^* = \rho_s/a = 1/183.3$. These values have been taken from the full radial profiles at $\rho_{pol} = 0.5$. This first simplified analysis

7. Effect of elongation on Energetic-Particle-Induced Geodesic Acoustic Modes

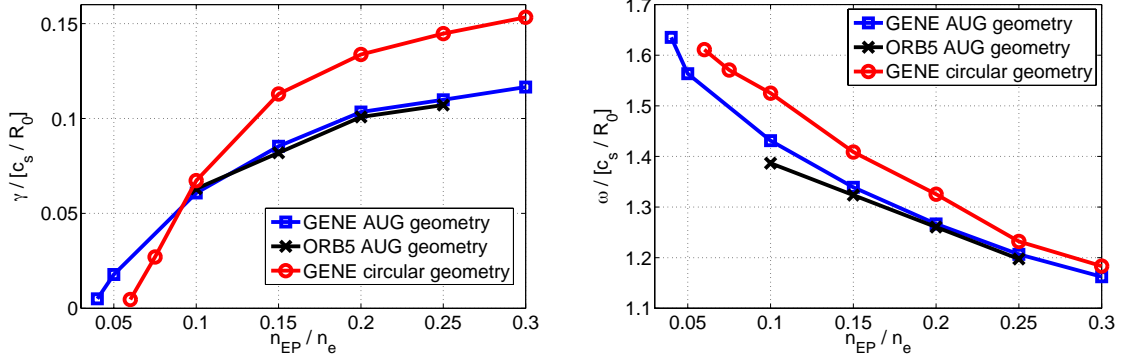


Figure 7.12: Linear EGAM growth rates a) and frequencies b) are shown for different fast ions density concentration for the realistic CHEASE and a circular equilibrium for flat density and temperature profiles. Reproduced from [139], with the permission of IAEA.

allows a reduction of the physical complexity of the system, removing phase-mixing effects while keeping those of realistic plasma geometry (and hence elongation). As before, fast ions are modelled with a bump-on-tail distribution (Eq. (3.23)) – here with $\bar{v}_{\parallel} = 2.83$ (= 4 in ORB5 units, due to a difference of a factor of $\sqrt{2}$ in the definition of the thermal velocity) in units of $v_{th,f}$ and fast ion temperature set to the main ion one, i.e. $T_{EP} = T_i$. The considered radial simulation domain covers $\rho_{pol} = [0.15, 0.85]$. For simplicity, electrons are considered adiabatic and an initial density perturbation of the form $n_1(\rho_{pol}, t_0) \sim \sin(\pi\rho_{pol})$ is initialized with Dirichlet boundary conditions. In Fig. 7.12 the linear EGAM growth rates and frequencies obtained for the realistic CHEASE equilibria with GENE and ORB5 are shown and compared to the ones of a simplified circular geometry for different fast ion density concentrations. The safety factor profile of the circular geometry case is kept the same as the experimental one, see Fig. 7.11b). The values of the growth rates and frequencies have been calculated at the radial position $\rho_{pol} = 0.25$, i.e. where the radial profile of the electrostatic potential is found to peak, as shown in Fig. 7.13.

For the nominal fast ion density $n_{EP} = 0.2n_e$ at $\rho_{pol} = 0.5$, both codes agree well on the values of the EGAM frequency and growth rate which are found to be $\omega = 1.267c_s/R_0$, i.e. $\omega/(2\pi) = 33.315\text{kHz}$ and $\gamma = 0.103c_s/R_0$ for the realistic AUG equilibrium. Fig. 7.12 furthermore demonstrates a pronounced effect of the magnetic geometry on the linear EGAM growth rates and frequencies. The plasma elongation (κ) weakens the EGAM growth rates and slightly reduces the mode frequency.

7.4 AUG Experiment based studies

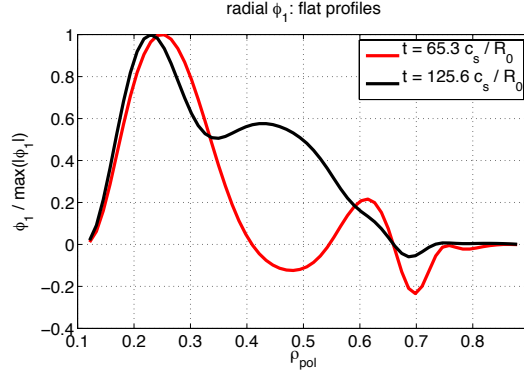


Figure 7.13: Radial structure of the electrostatic potential at different simulation times for the case of flat density and temperature profiles in the AUG discharge. Reproduced from [139], with the permission of IAEA.

Consistently with the results shown in the previous sections, the plasma elongation affects also the thermal damping, which unlike of the fast ion drive, strengthens with κ and can become dominant for the cases of weak EGAM drive. The combined effect of the elongation on the thermal damping and fast ion drive is found to significantly affect the fast ion density threshold. However, it is worth mentioning that close to the EGAM density threshold the effect of the kinetic electron damping might not be negligible anymore and should be taken into account [199]. Furthermore, the results shown in the previous sections were obtained in the case of strongly driven EGAMs. Close to the mode marginal stability the interaction between thermal damping and fast-ion drive might change significantly and affect the linear results.

7.4.2 Realistic density and temperature profiles

In the last section of this chapter, the full temperature and density profiles, shown in Fig. 7.14, are employed in the gyrokinetic analysis for each species. The fast ion population is modelled with the bump-on-tail distribution defined in Eq. (3.23), with a realistic temperature of $T_{EP} = 30\text{keV}$. The latter choice also fixes \bar{v}_{\parallel} through Eq. (3.9) (i.e. the value of the shift of the bump-on-tail distribution function), which for the parameters employed in this section is equal to $\bar{v}_{\parallel} = 1.41$ (~ 2 in ORB5 units) with respect to the thermal velocity of fast ions. As extensively discussed in chapter 3, the equivalent Maxwellian temperature imposes a constraint over the second order moment of the bump-on-tail distribution function to keep the same energy

7. Effect of elongation on Energetic-Particle-Induced Geodesic Acoustic Modes

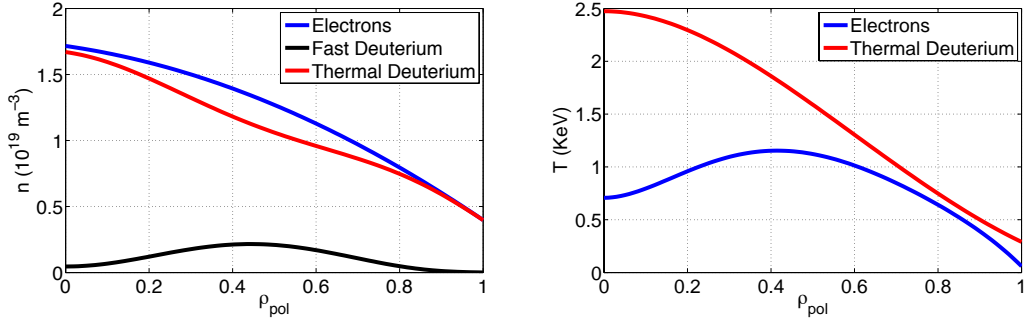


Figure 7.14: Experimental a) density and b) temperature profiles. For the NBI fast deuterium a flat temperature profile is considered at the value $T_{EP} = 30\text{keV}$. It is related to the injected energy. Reproduced from [139], with the permission of IAEA.

content. Furthermore, electrons are considered adiabatic and electrostatic simulations are performed with GENE with the radial domain covering $\rho_{pol} = [0.1, 0.9]$. The logarithmic time trace of the perturbed electrostatic potential at $\rho_{pol} = 0.5$ is shown in Fig. 7.15a). By means of linear regression, the corresponding EGAM growth rate and frequency are determined to $\gamma = 0.0465c_s/R_0$, $\omega = 2.013c_s/R_0$, i.e. $\omega/(2\pi) = 44.69\text{kHz}$. Compared to values in the previous section, the EGAM growth rate for these realistic AUG based parameters appears to be relatively small. This finding is consistent with the analytic energy exchange formula, Eq. (7.8), which predicts an inverse proportionality between the mode/ion energy exchange term and the fast ion temperature. We also observe a significant increase in the EGAM mode frequency. It is also possible to compare the experimentally measured frequency of the $n = 0$ modes at $t = 0.841\text{s}$ and $\rho_{pol} = 0.5$ with the values obtained by GENE with realistic density and temperature profiles. Despite the simplified setup - adiabatic electrons, no nonlinear coupling and electrostatic simulations -, Fig. 7.15b) displays a surprisingly good agreement between the measurement of the EGAM frequency in the first linear phase and the simulation value. At later times, the EGAM mode enters a nonlinear chirping phase, which cannot be described with linear simulations. The particularly good agreement with the experimental frequency is achieved only by reasonably modelling the fast ion temperature. For the case of $T_{EP} = T_e$, shown in the previous section, an underprediction of the mode frequency is observed. Moreover, a comparison of the linear results obtained with an ad-hoc circular equilibrium and with the realistic MHD geometry reveals that the latter is also a crucial ingredient for achieving a good EGAM frequency agreement. The growth rate ob-

7.4 AUG Experiment based studies

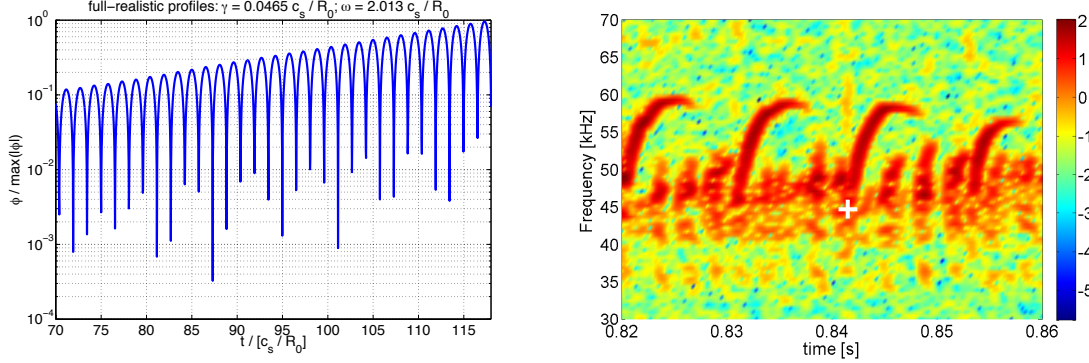


Figure 7.15: a) Time trace of the perturbed electrostatic potential in logarithmic scale with the corresponding values of the EGAM growth rate and frequency for realistic density and temperature profiles; b) experimental time evolution of the frequency spectra of the AUG discharge #31213. The white cross refers to the EGAM frequency obtained from GENE simulations. Reproduced from [139], with the permission of IAEA.

tained with the circular equilibrium is found to increase by more than 50% up to $\gamma = 0.0763 c_s / R_0$. The mode frequency, on the other hand, has a weaker dependence on the plasma elongation and it is found to increase by a factor of $\sim 15\%$ up to $\omega = 2.327 c_s / R_0$. In dimensional units, the mode frequency is $\omega / (2\pi) = 51.66$ kHz, which is still qualitatively close to the experimental measurements. However, a quantitative agreement is achieved only by considering a more sophisticated model for the magnetic equilibrium which includes - among others - elongation effects. This finding is well in line with the dedicated analysis mentioned in Sec. 7.2 - 7.3. Furthermore, the radial structure of the electrostatic potential is also analyzed at different simulation times, corresponding to maxima of ϕ_1 . As can be seen in Fig. 7.16, the mode is already localized around the maximum fast ion density at $\rho_{pol} = 0.5$ at an early stage of the simulation. For different radial positions, the fast ion density decreases and the drive, which is already significantly weak at $\rho_{pol} = 0.5$ barely overcomes the thermal damping and the mode is strongly weakened. However, for a more realistic comparison with the experimental measurements of the EGAM radial structure [53] - measured at $\rho_{pol} \sim 0.3$ - , a more accurate description of the fast ion background distribution function and of the nonlinear physics needs to be considered.

7. Effect of elongation on Energetic-Particle-Induced Geodesic Acoustic Modes

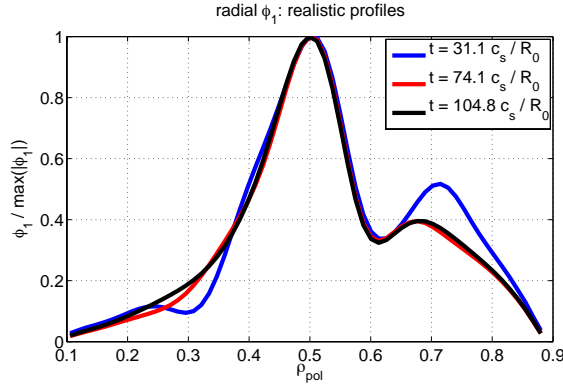


Figure 7.16: Radial structure of the electrostatic potential at different simulation times for the case of realistic density and temperature profiles of the AUG discharge. Reproduced from [139], with the permission of IAEA.

7.5 Chapter summary

In the present chapter, first results obtained with the global version of the gyrokinetic code GENE which supports non-Maxwellian backgrounds are shown and successfully benchmarked against the global gyrokinetic code ORB5. The linear analyses reveal differences between both codes in the EGAM growth rates and frequencies of the order of $\leq 5\%$ for realistic magnetic geometries extracted from the code CHEASE. By taking advantage of these recent developments in GENE, a joint investigation with ORB5 is performed by studying the effect of the plasma elongation on the EGAM dynamics with both numerical simulations and reduced analytical models. To facilitate the comparison between theory and simulations, adiabatic electrons and electrostatic fluctuations are considered. Furthermore, a symmetric double bump distribution function is chosen for modelling the energetic ion population, while Maxwellian bulk ions are considered. It is found that the plasma elongation significantly weakens the EGAM growth rates, barely modifying the respective mode frequency. It introduces small order corrections on the parallel transit resonance position which affect the energy exchange between the fast ions and the mode, i.e. it modifies the phase space position in which the inverse Landau damping occurs. In particular, the resonant transit velocity decreases with the elongation, which, for the choice of parameters here considered, moves through regions in phase space where the shape of the fast ion distribution is less favourable to exchange energy with the mode, with a consequent reduction of the linear growth rate. Finally, these findings have been applied

7.5 Chapter summary

to an ASDEX Upgrade discharge with strongly elongated geometry. For this analysis realistic density and temperature profiles have been considered. Despite the approximations taken in our simulations regarding the EP distribution function and the adiabatic model for the electrons, a good agreement of the linear frequency obtained with numerical simulations and the onset of the EGAM frequency chirping cycle is found. Moreover, a significant effect of the plasma elongation on the EGAM instability threshold has been observed.

7. Effect of elongation on Energetic-Particle-Induced Geodesic Acoustic Modes

Chapter 8

Conclusions

8.1 Summary

In the course of this work, turbulence in magnetized plasmas has been investigated with the primary goal to improve the theoretical understanding of the stabilizing effect of energetic particles observed in many experiments and simulations. A key issue for efficient magnetic fusion devices is to increase the energy confinement time, mainly limited by plasma turbulence. Therefore, any mechanism limiting turbulent transport development can be considered an important step along understanding and optimizing nowadays magnetic confinement experiments as well as improving future ITER or DEMO predictions. In this context, in this thesis, realistic scenarios of the currently running experiment JET and ASDEX Upgrade have been studied in detail and the main effects of energetic particles on plasma micro-turbulence have been identified. The main results obtained in this work are summarized in the following.

Upgrading GENE to the study of non-thermalized species

The interaction between energetic particles and plasma turbulence has been studied with numerical simulations performed with the state-of-the-art gyrokinetic code GENE. To improve the modelling of fast ion species, GENE and its underlying equations have been extended to account for highly non-thermalised species. In tokamak experiments, they are usually generated by external auxiliary heating schemes while in future reactors they will also arise from fusion reactions between deuterium and tritium atoms. In particular, the often employed assumption in the gyrokinetic δf -theory to model the equilibrium distribution of each plasma species with a Maxwellian is relaxed. More flexible backgrounds can now be considered, which

might be either analytical or obtained from numerical models. Thanks to these code modifications, more realistic energetic particle analyses can be accomplished with GENE.

Numerical tests and benchmark studies

Extensive verification studies and benchmarks against other codes have been presented in the course of this thesis to test the correct analytic derivation of the more general gyrokinetic equations and the proper numerical implementation. Convergence analyses have revealed that to fully capture individual asymmetries and anisotropies in the distribution function of the energetic particle species, a larger velocity grid discretization is required.

Energetic particle effects on ion-dominated plasma turbulence

A particular plasma with significant fast ion effects obtained experimentally in the largest European fusion device (JET) has been studied with the new GENE code capabilities, performing single-mode (linear) and multi-mode (nonlinear) analyses. In agreement with the experimental observations, a reduction in the energetic-particle stabilization of turbulence has been observed with the more realistic distribution functions. Depending on the particular heating scheme employed experimentally, e.g. NBI and/or ICRH, and therefore on the nature of fast-ion velocity distributions, a substantial difference in the numerical findings has been observed.

This peculiar result has been investigated in detail in the course of this dissertation and attributed to a wave-fast particle resonance stabilizing mechanism whose role had been neglected so far. It has been found that energetic ions can exchange energy with the background micro-instabilities if the fast particle magnetic-drift frequency is close enough to the linear frequency of the wave. The direction and magnitude of this energy redistribution (from the fast particles to the wave or vice versa) depends on the shape of the energetic particle profiles (density and temperature) and velocity space structures of their background. In particular, it was explained why this resonant stabilization of the turbulence is observed when ICRH-heated ions are included, while it is absent in the case of NBI-ions. All these findings have been reproduced with a theoretical simplified model, which might be used in the near future to extrapolate these results to different reactor relevant parameters. The consequences of such mechanisms on the overall energy balance has also been modelled with a simplified expression for the energetic particle field and kinetic energy terms. The capabilities of such models to capture the modifications of the resonant interac-

8.1 Summary

tion due to changes in the fast particle charge, mass and magnetic shear have also been shown.

Another turbulence suppression mechanism associated to the improved confinement of the JET discharge partially analyzed previously is related to the combination of nonlinear, electromagnetic effects with fast particles. In particular, the amplitude of the outboard propagating turbulent transport reduces by almost two orders of magnitude compared to simulations when only thermal species are considered. These results are not only limited to this specific JET scenario, but are also found in many different experimental devices and simulations. The mechanism responsible for this particularly strong fast particle nonlinear turbulence stabilisation remained elusive for almost a decade despite its high relevance to plasma performance predictions and turbulent systems in general. It has been clarified for the first time in the course of this thesis work. It has been found that linearly marginally stable modes - here, fast ion pressure driven toroidal-Alfvén-eigenmodes (TAEs) - are excited nonlinearly and (i) deplete the energy content of the bulk ion-temperature-gradient (ITG)-driven turbulence and (ii) act as an additional catalyst for energy transfer to zonal modes representing the dominant saturation channel. The resulting signatures – high-frequency oscillations of the perturbed electrostatic potential and increase in the zonal flow amplitude – have been found in a number of simulations for different JET and ASDEX Upgrade scenarios with reduced transport levels attributed to energetic particle effects. This mechanism might be extremely valuable for future fusion reactors such as ITER where a large fraction of supra-thermal ions will be inherently present in the form of α -particles as a direct result of the fusion reaction.

Energetic-particle-induced geodesic acoustic modes

The direct impact of energetic particles on the finite-frequencies zonal flow components has also been investigated in this thesis work. The excitation of coherent radially global oscillations called EGAM (energetic-particle-induced geodesic acoustic mode) via resonant interaction with the fast particle species has been studied employing the new features of the code GENE, which enables the use of realistic non-Maxwellian distribution functions for the fast particle population. A joint investigation with another gyrokinetic code with similar capabilities called ORB5 has been performed to further verify the analytic derivation and implementation performed in this thesis. The impact of the magnetic plasma elongation on the EGAM dynamics has been investigated with numerical simulations and reduced models. A careful analysis of the energy balance equation revealed that the elongation moves

the resonance through regions where the shape of the fast ion distribution is less favourable for an exchange of energy with the mode, with a consequent reduction of the linear growth rate. Finally, these findings have been applied to an ASDEX Upgrade discharge with strongly elongated geometry. A good agreement between the linear mode frequency obtained with numerical simulations and the one measured experimentally has been found only by retaining the realistic elongated plasma geometry.

8.2 Outlook

Resonant interaction of energetic ions with plasma micro-turbulence

The finding of electrostatic energetic particle effects on the bulk ion-driven turbulence - apart from dilution - constitutes an important step along understanding and optimizing nowadays and future fusion devices. Further investigations can still be addressed in future works. In particular, the extension of these results to radially global gyrokinetic turbulence simulations might provide valuable insights. According to the reduced model described in chapter 5, to efficiently reduce the main ion thermal micro-instability and associated turbulent transport, it is required at the same time that (i) the minimum of the background drive term is negative (this being controlled by the ratio of the fast particle temperature and density gradients) and (ii) the wave-fast-ion resonance and this negative region of the background drive overlap in phase space (this being controlled by the fast particle temperature). Therefore, energetic particle might impact the thermal micro-instability differently in a global framework depending on the radial position selected, generating outward or inward particle and heat fluxes. These non-local effects might lead to the formation of radially localized domains where turbulence is highly suppressed (typically called internal transport barriers). These analyses might be extremely challenging from the computational point of view. To account for this issue, first analyses might be performed assuming adiabatic electrons. The wave-fast ion resonant interaction mechanism here presented is not assumed to be significantly affected by the electron dynamics.

Moreover, the impact of this fast particle stabilizing mechanism on the experimentally observed stiffening of the main ion temperature profiles might be addressed with dedicated simulations with reduced quasi-linear transport models, such as QuaLiKiz [200, 201, 202], ASTRA/TGLF [203, 204, 205]. These codes can study the evolution of macroscopic observables, such as temperature and density profiles due to turbulence effects.

8.2 Outlook

Finally, the new GENE code capabilities of modelling energetic particle species with more realistic non-thermalized backgrounds might be employed to assess the impact of velocity space anisotropies and symmetries on the wave-fast ion resonant interaction.

Nonlinear electromagnetic stabilisation by energetic ions

The theoretical investigation of the impact of energetic particles on ion-scale dominated turbulence could be further extended by developing reduced analytic models to describe the nonlinear coupling between TAE/ITG and TAE/ITG/ZF. Such a simplified model would be required to further optimize the nonlinear turbulence stabilizing mechanism discussed in chapter 6 to future fusion reactors like ITER and DEMO.

The prominent role of MHD energetic particle driven modes in the nonlinear electromagnetic turbulent stabilization discussed in chapter 6 raises the question of how accurate the flux-tube model is in capturing such instabilities. In the present thesis, preliminary comparisons between local/global linear results are shown for the so-called TAE-ITPA benchmark case. It represents a simplified plasma scenario employed for inter-code radially global verification studies. A good agreement was achieved with GENE flux-tube simulations. However, a more systematic investigation needs to be performed in the near future for more realistic reactor relevant parameters.

A natural extension of the results presented in chapter 6 would require nonlinear electromagnetic simulations in a radially global framework. However, these analyses are extremely expensive from the numerical point of view and might only be addressed with state-of-the-art supercomputers.

Moreover, the impact of energetic particle background energy asymmetries and anisotropies on the nonlinear mode-to-mode coupling between EP-driven modes, ion-scale turbulence and zonal flows might also be addressed with the novel GENE code non-Maxwellian features.

Effect of elongation on Energetic Geodesic Acoustic Modes

Another project which could be further investigated in the near future concerns the nonlinear interaction between EGAMs and ion-scale driven turbulence. This analysis might be first addressed with flux-tube simulations, which enables a more sophisticated treatment of the free energy balance equation, and only afterwards extended to a global framework. The radially global results might be compared to

the ones recently obtained in Ref. [192, 206]. Moreover, the linear and the nonlinear EGAM dynamics can be studied by modelling the energetic particle distribution function with more realistic equilibrium backgrounds, such as numerical backgrounds extracted from state-of-the-art heating codes.

Code optimization

Finally, it is worth to emphasize that most of the analyses previously suggested will significantly increase the computational cost of the nonlinear GENE simulations. In particular, a combination of the global effects with the more costly realistic distribution functions is hence so far beyond reach. To overcome this numerical issue, a numerical code optimization is required. In particular, species dependent velocity space grids – similarly to what has been done in Ref. [207] for radially dependent velocity space structures, will need to be implemented in the present version of the non-Maxwellian code GENE to significantly speed up the numerical calculations.

Bibliography

- [1] D. Told, “Gyrokinetic microturbulence in transport barriers,” *PhD thesis, University ULM*, 2012.
- [2] H. W. Bartels, H. S. Bosch, R. Brakel, H. J. Hartfuss, D. Hartmann, R. Hippler, D. H. H. Hoffmann, R. Kleiber, A. Könies, K. Krieger, A. Melzer, A. G. Peeters, R. Schneider, B. D. Scott, W. Suttrop, and H. Zohm, “IPP summer university for plasma physics,” 2005.
- [3] ITER Physics Basis Editors *Nucl. Fusion*, vol. 39, p. 2175, 1999.
- [4] “ITER - the way to a new energy,” www.iter.org, 03/03/2020sien.
- [5] J. J. Sakurai, “Modern Quantum Mechanics. Prentice Hall, 1993.,” *book*, 1993.
- [6] J. D. Lawson, “Some criteria for a Power Producing Thermonuclear Reactor,” *Physical Society B*, vol. 70, p. 6, 1957.
- [7] J. Wesson, “Tokamaks. Oxford Engineering Science Series No 48, 1997.,” *book*, 1997.
- [8] N. Bonanomi, “Experimental investigation and gyro-kinetic modelling of turbulent transport in thermonuclear plasmas,” *PhD thesis, University of Milano-Bicocca*, 2017.
- [9] S. Li, H. Jiang, Z. Ren, and C. Xu, “Optimal tracking for a Divergent-Type Parabolic PDE System in Current Profile Control,” *Abstr. Appl. Anal*, vol. 940965, p. 8, 2014.
- [10] W. Dhaeseleer, W. Hitchon, J. D. Callen, and J. Shohet, “Flux coordinates and magnetic field structure (Springer-Verlag, Berlin, 1991),” *book*, 1991.
- [11] T. Görler, “Multiscale effects in plasma microturbulence,” *PhD thesis, University ULM*, 2009.

BIBLIOGRAPHY

- [12] R. Miller, M. Chu, J. Greene, Y. Lin-Liu, and R. Waltz, “Noncircular, finite aspect ratio, local equilibrium model,” *Phys. Plasmas*, vol. 5, p. 979, 1998.
- [13] H. Lütjens, A. Bondeson, and O. Sauter, “The CHEASE code for toroidal MHD equilibria,” *Comp. Phys. Comm.*, vol. 97, p. 219, 1996.
- [14] A. Pochelon, P. Angelino, R. Behn, S. Brunner, S. Coda, N. Kirneva, S. Y. Medvedev, H. Reimerdes, J. Rossel, O. Sauter, L. Villard, D. Wágner, A. Bottino, Y. Camenen, G. P. Canal, P. K. Chattopadhyay, B. P. Duval, A. Fasoli, T. P. Goodman, S. Jollet, A. Karpushov, B. Labit, A. Marinoni, J.-M. Moret, A. Pitzschke, L. Porte, M. Rancic, V. S. Udintsev, and the TCV Team, “Recent tcv results - innovative plasma shaping to improve plasma properties and insight,” *Plasma and Fusion Research*, vol. 7, pp. 2502148–2502148, 2012.
- [15] M. E. Austin, A. Marinoni, M. L. Walker, M. W. Brookman, J. S. deGrassie, A. W. Hyatt, G. R. McKee, C. C. Petty, T. L. Rhodes, S. P. Smith, C. Sung, K. E. Thome, and A. D. Turnbull, “Achievement of reactor-relevant performance in negative triangularity shape in the dIII-d tokamak,” *Phys. Rev. Lett.*, vol. 122, p. 115001, Mar 2019.
- [16] G. Merlo, S. Brunner, O. Sauter, Y. Camenen, T. Görler, F. Jenko, A. Marinoni, D. Told, and L. Villard, “Investigating profile stiffness and critical gradients in shaped TCV discharges using local gyrokinetic simulations of turbulent transport,” *Plasma Physics and Controlled Fusion*, vol. 57, p. 054010, apr 2015.
- [17] G. Merlo, “Flux-tube and global grid-based gyrokinetic simulations of plasma microturbulence and comparisons with experimental TCV measurements,” *PhD thesis, École Polytechnique FéDÉrale de Lausanne*, 2016.
- [18] D. R. Nicholson, “Introduction to Plasma Theory. Wiley, 1983.,” *book*, 1983.
- [19] J. P. Freidberg, “Ideal MHD. Cambridge University Press, 2014.,” *book*, 2014.
- [20] W. Horton, “Drift waves and transport,” *Rev. Mod. Phys.*, vol. 71, p. 735, 1999.
- [21] C. Angioni, “Theoretical and experimental research on particle and impurity transport in the core of tokamak plasmas,” *Habilitation thesis*, 2010.
- [22] J. Weiland, A. B. Jármán, and H. Nordman, “Diffusive particle and heat pinch effects in toroidal plasmas,” *Nucl. Fusion*, vol. 29, p. 10, 1989.

BIBLIOGRAPHY

- [23] H. Nordman, J. Weiland, and A. Jarmén, “Simulation of toroidal drift mode turbulence driven by temperature gradients and electron trapping,” *Nucl. Fusion*, vol. 30, p. 983, 1990.
- [24] W. Horton, D. Choi, and W. M. Tang, “Toroidal drift modes driven by ion pressure gradients,” *Physics of Fluids*, vol. 24, p. 1077, 1981.
- [25] F. Romanelli, “Ion temperature-gradient-driven modes and anomalous ion transport in tokamaks,” *Physics of Fluids B*, vol. 1, pp. 1018–1025, May 1989.
- [26] W. Horton and B. G. Hong, “Toroidal electron temperature gradient driven drift modes,” *Physics of Fluids*, vol. 31, p. 2971, 1988.
- [27] F. Jenko, W. Dorland, M. Kotschenreuther, and B. N. Rogers, “Electron temperature gradient driven turbulence,” *Phys. Plasmas*, vol. 7, pp. 1904–1910, May 2000.
- [28] W. Dorland, F. Jenko, M. Kotschenreuther, and B. N. Rogers, “Electron temperature gradient turbulence,” *Phys. Rev. Lett.*, vol. 85, pp. 5579–5582, Dec 2000.
- [29] E. Mazzucato, D. R. Smith, R. E. Bell, S. M. Kaye, J. C. Hosea, B. P. LeBlanc, J. R. Wilson, P. M. Ryan, C. W. Domier, N. C. Luhmann, H. Yuh, W. Lee, and H. Park, “Short-scale turbulent fluctuations driven by the electron-temperature gradient in the national spherical torus experiment,” *Phys. Rev. Lett.*, vol. 101, p. 075001, Aug 2008.
- [30] H. Biglari, P. H. Diamond, and M. N. Rosenbluth, “Toroidal ionpressuregradientdriven drift instabilities and transport revisited,” *Physics of Fluids B*, vol. 1, p. 109, 1989.
- [31] X. Garbet and J. Chinardet, “Ionic instability thresholds in tokamaks,” *Physics of Fluids B*, vol. 4, p. 136, 1992.
- [32] S. C. Guo and F. Romanelli, “The linear threshold of the iontemperaturegradientdriven mode,” *Physics of Fluids B*, vol. 5, p. 520, 1993.
- [33] B. Coppi and F. Pegoraro, “Theory of the ubiquitous mode,” *Nucl. Fusion*, vol. 17, p. 5, 2018.
- [34] M. N. Rosenbluth and C. L. Longmire, “Stability of plasmas confined by magnetic fields,” *Annal. of Physics*, vol. 1, p. 120, 1957.

- [35] A. Casati, C. Bourdelle, X. Garbet, and F. Imbeaux, “Temperature ratio dependence of ion temperature gradient and trapped electron mode instability thresholds,” *Phys. Plasmas*, vol. 15, p. 042310, 2008.
- [36] F. L. Hinton and R. D. Hazeltine, “Theory of plasma transport in toroidal confinement systems,” *Rev. Mod. Phys.*, vol. 48, pp. 239–308, Apr 1976.
- [37] S. Ejima, T. Petrie, A. Riviere, T. Angel, C. Armentrout, D. Baker, F. Blau, G. Bramson, N. Brooks, R. Callis, R. Chase, J. DeBoo, J. DeGrassie, E. Fairbanks, R. Fisher, R. Groebner, C. Hsieh, J. Hugill, G. Jahns, J. Lohr, J. Luxon, M. Mahdavi, F. Marcus, N. Ohyabu, P. Petersen, W. Pfeiffer, R. Seraydarian, A. Sleeper, R. Snider, R. Stambaugh, T. Tamano, T. Taylor, R. Waltz, J. Wesley, and S. Wojtowicz, “Scaling of energy confinement with minor radius, current and density in doublet III ohmically heated plasmas,” *Nucl. Fusion*, vol. 22, pp. 1627–1649, dec 1982.
- [38] N. Bonanomi, P. Mantica, J. Citrin, T. Görler, B. Teaca, and JET Contributors, “Impact of electron-scale turbulence and multi-scale interactions in the JET tokamak,” *Nucl. Fusion*, vol. 58, p. 124003, 2018.
- [39] T. Görler and F. Jenko, “Scale separation between electron and ion thermal transport,” *Phys. Rev. Lett.*, vol. 100, p. 185002, May 2008.
- [40] S. Maeyama, Y. Idomura, T.-H. Watanabe, M. Nakata, M. Yagi, N. Miyato, A. Ishizawa, and M. Nunami, “Cross-Scale Interactions between Electron and Ion Scale Turbulence in a Tokamak Plasma,” *Phys. Rev. Lett.*, vol. 114, p. 255002, 2015.
- [41] L. Chen and F. Zonca, “Physics of alfvén waves and energetic particles in burning plasmas,” *Rev. Mod. Phys.*, vol. 88, p. 015008, Mar 2016.
- [42] P. Lauber, “Super-thermal particles in hot plasmas - kinetic models, numerical solution strategies, and comparison to tokamak experiments,” *Physics Reports*, vol. 533, no. 2, pp. 33 – 68, 2013. Superthermal particles in hot plasmas - kinetic models, numerical solution strategies, and comparison to Tokamak experiments.
- [43] F. Zonca, “Continuum damping of toroidal Alfvén eigenmodes in finite- β tokamak equilibria,” *PhD thesis, Princeton*, 1993.
- [44] G. Vlad, F. Zonca, and S. Briguglio, “Dynamics of Alfvén Waves in Tokamaks,” *Rivista del Nuovo Cimento*, vol. 22, pp. 1–97, 1999.

BIBLIOGRAPHY

- [45] A. Hasegawa and L. Chen, “Plasma heating by alfvén-wave phase mixing,” *Phys. Rev. Lett.*, vol. 32, pp. 454–456, Mar 1974.
- [46] H. L. Berk, “Continuum damping of Low-n Toroidicity-Induced shear Alfvén eigenmodes,” *PhD thesis, University of Texas at Austin*, 1991.
- [47] M. N. Rosenbluth and P. H. Rutherford, “Excitation of alfvén waves by high-energy ions in a tokamak,” *Phys. Rev. Lett.*, vol. 34, pp. 1428–1431, Jun 1975.
- [48] A. Mikhailovskii, “Thermonuclear drift instabilities,” *Zh. Eksp. Teor. Fiz. (USSR)*, vol. 68:5, 1975.
- [49] K. T. Tsang, D. J. Sigmar, and J. C. Whitson, “Destabilization of low mode number alfvén modes in a tokamak by energetic or alpha particles,” *The Physics of Fluids*, vol. 24, no. 8, pp. 1508–1516, 1981.
- [50] G. Y. Fu and J. W. Van Dam, “Excitation of the toroidicity-induced shear alfvén eigenmode by fusion alpha particles in an ignited tokamak,” *Physics of Fluids B: Plasma Physics*, vol. 1, no. 10, pp. 1949–1952, 1989.
- [51] A. Biancalani, N. Carlevaro, A. Bottino, G. Montani, and Z. Qiu, “Nonlinear velocity redistribution caused by energetic-particle-driven geodesic acoustic modes, mapped with the beam-plasma system,” *Journal of Plasma Physics*, vol. 84, no. 6, p. 725840602, 2018.
- [52] D. Zarzoso, D. del Castillo-Negrete, D. Escande, Y. Sarazin, X. Garbet, V. Grandgirard, C. Passeron, G. Latu, and S. Benkadda, “Particle transport due to energetic-particle-driven geodesic acoustic modes,” *Nuclear Fusion*, vol. 58, p. 106030, aug 2018.
- [53] L. Horváth, G. Papp, P. Lauber, G. Por, A. Gude, V. Igochine, B. Geiger, M. Maraschek, L. Guimarais, V. Nikolaeva, G. I. Pokol, and The ASDEX Upgrade Team, “Experimental investigation of the radial structure of energetic particle driven modes,” *Nucl. Fusion*, vol. 56, p. 112003, 2016.
- [54] A. Melnikov, L. Eliseev, F. Castejón, C. Hidalgo, P. Khabanov, A. Kozachek, L. Krupnik, M. Liniers, S. Lysenko, J. de Pablos, S. Sharapov, M. Ufimtsev, V. Zenin, H. Group, and T.-I. Team, “Study of NBI-driven chirping mode properties and radial location by the heavy ion beam probe in the TJ-II stellarator,” *Nuclear Fusion*, vol. 56, p. 112019, aug 2016.

BIBLIOGRAPHY

- [55] J. Zhu, Z. Ma, and G. Fu, “Nonlinear frequency chirping of toroidal alfvén eigenmodes in tokamak plasmas,” *Nuclear Fusion*, vol. 54, p. 123020, nov 2014.
- [56] M. N. Rosenbluth and F. L. Hinton, “Poloidal flow driven by ion-temperature-gradient turbulence in tokamaks,” *Phys. Rev. Lett.*, vol. 80, pp. 724–727, Jan 1998.
- [57] P. H. Diamond, S. I. Itoh, K. Itoh, and T. S. Hahm, “Zonal flows in plasmaa review,” *Plasma Phys. Control. Fusion*, vol. 47, 2005.
- [58] Z. Gao, “Collisional damping of the geodesic acoustic mode,” *Phys. Plasmas*, vol. 20, p. 032501, 2013.
- [59] Z. Qiu, I. Chavdarovski, A. Biancalani, and J. Cao, “On zero frequency zonal flow and second harmonic generation by finite amplitude energetic particle induced geodesic acoustic mode,” *Phys. Plasmas*, vol. 24, p. 072509, 2017.
- [60] R. May, “Stability and Complexity in Model Ecosystems; Cambridge: Cambridge University Press, 1974.,” *book*, 1974.
- [61] P. H. Diamond, Y.-M. Liang, B. A. Carreras, and P. W. Terry, “Self-regulating shear flow turbulence: A paradigm for the l to h transition,” *Phys. Rev. Lett.*, vol. 72, pp. 2565–2568, Apr 1994.
- [62] K. Itoh, S.-I. Itoh, M. Yagi, and A. Fukuyama, “Dynamic structure in self-sustained turbulence,” *Plasma Physics and Controlled Fusion*, vol. 38, pp. 2079–2096, dec 1996.
- [63] K. Itoh, S.-I. Itoh, and A. Fukuyama, “Transport and Structural Formation in Plasmas; Bristol: Institute of Physics Publishing, 1999.,” *book*, 1999.
- [64] M. A. Malkov and P. H. Diamond, “Bifurcation and scaling of drift wave turbulence intensity with collisional zonal flow damping,” *Physics of Plasmas*, vol. 8, no. 9, pp. 3996–4009, 2001.
- [65] P. W. Terry, “Suppression of turbulence and transport by sheared flow,” *Rev. Mod. Phys.*, vol. 72, pp. 109–165, Jan 2000.
- [66] N. Winsor, L. Johnson, and M. Dawson, “Geodesic Acoustic Waves in Hydro-magnetic Systems,” *Phys. Plasmas*, vol. 11, p. 2448, 1968.
- [67] G. Y. Fu, “Energetic-Particle-Induced Geodesic Acoustic Mode,” *Phys. Rev. Lett.*, vol. 101, p. 185002, 2008.

BIBLIOGRAPHY

- [68] Z. Qiu, F. Zonca, and L. Chen, “Nonlocal theory of energetic-particle-induced geodesic acoustic mode,” *Plasma Phys. Control. Fusion*, vol. 52, p. 095003, 2010.
- [69] Z. Qiu, F. Zonca, and L. Chen, “Nonlocal theory of energetic-particle-induced geodesic acoustic mode,” *Plasma Science Tech.*, vol. 12, p. 257, 2011.
- [70] D. Zarzoso, X. Garbet, Y. Sarazin, R. Dumont, and V. Grandgirard, “Fully kinetic description of the linear excitation and nonlinear saturation of fast-ion-driven geodesic acoustic mode instability,” *Phys. Plasmas*, vol. 19, p. 022102, 2012.
- [71] J.-B. Girardo, D. Zarzoso, R. Dumont, X. Garbet, Y. Sarazin, and S. Sharapov, “Relation between energetic and standard geodesic acoustic modes,” *Phys. Plasmas*, vol. 21, p. 092507, 2014.
- [72] A. Biancalani, I. Chavdarovski, Z. Qiu, A. Bottino, D. Del Sarto, A. Ghizzo, Ö. D. Gürcan, P. Morel, and I. Novikau, “Saturation of energetic-particle-driven geodesic acoustic modes due to wave-particle nonlinearity,” *J. Plasma Phys.*, vol. 83, p. 725830602, 2017.
- [73] R. Nazikian, G. Y. Fu, M. E. Austin, H. L. Berk, R. V. Budny, N. N. Gorelenkov, W. W. Heidbrink, C. T. Holcomb, G. J. Kramer, G. R. McKee, M. A. Makowski, W. M. Solomon, M. Shafer, E. J. Strait, and M. A. Van Zeeland, “Intense Geodesic Acousticlike Modes Driven by Suprathermal Ions in a Tokamak Plasma,” *Phys. Rev. Lett.*, vol. 101, p. 185001, 2008.
- [74] T. Ido, M. Osakabe, A. Shimizu, T. Watari, M. Nishiura, K. Toi, k. Ogawa, K. Itoh, I. Yamada, R. Yasuhara, y. Yoshimura, and S. Kato, “Identification of the energetic-particle driven GAM in the LHD,” *Nucl. Fusion*, vol. 55, p. 083024, 2015.
- [75] H. L. Berk, C. J. Boswell, D. Borba, A. C. A. Figueiredo, T. Johnson, M. F. F. Nave, S. D. Pinches, S. E. Sharapov, and JET EFDA contributors, “Explanation of the JET $n = 0$ chirping mode,” *Nucl. Fusion*, vol. 46, pp. S888–S897, 2006.
- [76] X. T. Chen, W. Ding, L. M. Yu, X. Q. Ji, J. Q. Dong, Q. W. Yang, Y. Liu, L. W. Yan, Y. Zhou, W. Li, X. M. Song, S. Y. Chen, Z. B. Shi, and X. R. Duan, “EGAM induced by energetic electrons and nonlinear interactions among

- EGAM, BAEs and tearing modes in a toroidal plasma,” *Phys. Lett. A*, vol. 377, pp. 387–390, 2013.
- [77] A. Biancalani, A. Bottino, P. Lauber, and D. Zarzoso, “Numerical validation of the electromagnetic gyrokinetic code NEMORB on global axisymmetric modes,” *Nucl. Fusion*, vol. 54, p. 104004, 2014.
- [78] D. Zarzoso, A. Biancalani, A. Bottino, P. Lauber, E. Poli, J.-B. Girardo, X. Garbet, and R. Dumont, “Analytic dispersion relation of energetic particle driven geodesic acoustic modes and simulations with NEMORB,” *Nucl. Fusion*, vol. 54, p. 103006, 2014.
- [79] H. Wang, Y. Todo, and C. Kim, “Hole-Clump Pair Creation in the Evolution of Energetic-Particle-Driven Geodesic Acoustic Modes,” *Phys. Rev. Lett.*, vol. 110, p. 155006, 2013.
- [80] G. Tardini, J. Hobirk, V. G. Igochine, C. F. Maggi, P. Martin, D. McCune, A. G. Peeters, A. C. C. Sips, A. Stäbler, J. Stober, and ASDEX Upgrade Team, “Thermal ions dilution and ITG suppression in ASDEX Upgrade ion ITBs,” *Nucl. Fusion*, vol. 47, pp. 280–287, 2007.
- [81] M. Romanelli, A. Zocco, F. Crisanti, and JET Contributors, “Fast ion stabilization of the ion temperature gradient driven modes in the Joint European Torus hybrid-scenario plasmas: a trigger mechanism for internal transport barrier formation,” *Plasma Phys. Controlled Fusion*, vol. 52, p. 045007, 2010.
- [82] C. Holland, C. C. Petty, L. Schmitz, K. H. Burrell, G. R. McKee, T. L. Rhodes, and J. Candy, “Progress in GYRO validation studies of DIII-D H-mode plasmas,” *Nucl. Fusion*, vol. 52, no. 11, p. 114007, 2012.
- [83] J. Citrin, J. Garcia, T. Görler, F. Jenko, P. Mantica, D. Told, C. Bourdelle, D. R. Hatch, G. M. D. Hogeweij, T. Johnson, M. J. Pueschel, and M. Schneider, “Electromagnetic stabilization of tokamak microturbulence in a high- β regime,” *Plasma Phys. Controlled Fusion*, vol. 57, p. 014032, Jan. 2015.
- [84] J. Citrin, F. Jenko, P. Mantica, D. Told, C. Bourdelle, J. Garcia, J. W. Haverkort, G. M. D. Hogeweij, T. Johnson, and M. J. Pueschel, “Nonlinear Stabilization of Tokamak Microturbulence by Fast Ions,” *Phys. Rev. Lett.*, vol. 111, p. 155001, Oct. 2013.

BIBLIOGRAPHY

- [85] C. Bourdelle, G. Hoang, X. Litaudon, C. Roach, T. Tala, for the ITPA Topical Group on Trans Physics, and the International ITB Database Work Group, “Impact of the α parameter on the microstability of internal transport barriers,” *Nuclear Fusion*, vol. 45, pp. 110–130, feb 2005.
- [86] R. Bravenec, J. Citrin, J. Candy, P. Mantica, T. Görler, and JET Contributors, “Benchmarking the GENE and GYRO codes through the relative roles of electromagnetic and EB stabilization in JET high-performance discharges,” *Plasma Phys. Controlled Fusion*, vol. 58, Nov. 2016.
- [87] N. Bonanomi, P. Mantica, A. Di Siena, E. Delabie, T. Johnson, E. Lerche, S. Menumir, M. Tsalas, D. Van Eester, and JET Contributors, “Turbulent transport stabilization by ICRH minority fast ions in low rotating JET ILW L-mode plasmas,” *Nucl. Fusion*, vol. 58, p. 5, 2018.
- [88] H. Doerk, A. Bock, A. Di Siena, E. Fable, T. Görler, F. Jenko, J. Stober, and The ASDEX Upgrade Team, “Turbulence in high-beta ASDEX upgrade advanced scenarios,” *Nucl. Fusion*, vol. 58, p. 016044, 2018.
- [89] A. Di Siena, T. Görler, H. Doerk, R. Bilato, J. Citrin, T. Johnson, M. Schneider, E. Poli, and JET Contributors, “Non-Maxwellian fast particle effects in gyrokinetic GENE simulations,” *Phys. Plasmas*, vol. 25, p. 042304, 2018.
- [90] A. Di Siena, T. Görler, E. Poli, R. Bilato, H. Doerk, and A. Zocco, “Resonant interaction of energetic ions with bulk-ion plasma micro-turbulence,” *Phys. Plasmas*, vol. 1, p. 1, 2019.
- [91] A. J. Brizard and T. S. Hahm, “Foundations of nonlinear gyrokinetic theory,” *Rev. Mod. Phys.*, vol. 79, p. 421, 2007.
- [92] E. A. Frieman and L. Chen, “Nonlinear gyrokinetic equations for lowfrequency electromagnetic waves in general plasma equilibria,” *The Physics of Fluids*, vol. 25, no. 3, pp. 502–508, 1982.
- [93] F. Mertz, “Gyrokinetic simulation of multimode plasma turbulence,” *PhD thesis, Universität Münster*, 2008.
- [94] P. Astfalk, T. Görler, and F. Jenko, “Dshark: A dispersion relation solver for obliquely propagating waves in bi-kappa-distributed plasmas,” *Journal of Geophysical Research: Space Physics*, vol. 120, no. 9, pp. 7107–7120, 2015.

- [95] P. Astfalk and F. Jenko, “Parallel and oblique firehose instability thresholds for bi-kappa distributed protons,” *Journal of Geophysical Research: Space Physics*, vol. 121, no. 4, pp. 2842–2852, 2016.
- [96] P. Astfalk and F. Jenko, “Leopard: A gridbased dispersion relation solver for arbitrary gyrotropic distributions,” *Journal of Geophysical Research: Space Physics*, vol. 122, no. 1, pp. 89–101, 2017.
- [97] T. M. Antonsen and B. Lane, “Kinetic equations for low frequency instabilities in inhomogeneous plasmas,” *The Physics of Fluids*, vol. 23, no. 6, pp. 1205–1214, 1980.
- [98] G. Rewoldt and W. M. Tang, “Beam-ion and alpha particle effects on microinstabilities in tokamaks,” *The Physics of Fluids*, vol. 26, no. 12, pp. 3619–3623, 1983.
- [99] C. Angioni and A. G. Peeters, “Gyrokinetic calculations of diffusive and convective transport of α particles with a slowing-down distribution function,” *Phys. Plasmas*, vol. 15, p. 052307, May 2008.
- [100] G. J. Wilkie, I. G. Abel, E. G. Highcock, and W. Dorland, “Validating modeling assumptions of alpha particles in electrostatic turbulence,” *J. Plasma Phys.*, vol. 81, Jan. 2015.
- [101] R. Waltz and E. Bass, “Prediction of the fusion alpha density profile in ITER from local marginal stability to alfvén eigenmodes,” *Nuclear Fusion*, vol. 54, p. 104006, oct 2014.
- [102] A. Di Siena, T. Görler, H. Doerk, J. Citrin, T. Johnson, M. Schneider, E. Poli, and JET Contributors, “Non-Maxwellian background effects in gyrokinetic simulations with GENE,” *J. Phys. Conf. Ser.*, vol. 775, p. 012003, 2016.
- [103] M. Schneider, L. G. Eriksson, I. Jenkins, J. F. Artaud, V. Basiuk, F. Imbeaux, T. Oikawa, JET-EFDA contributors, and ITM-TF contributors, “Simulation of the neutral beam deposition within integrated tokamak modelling frameworks,” *Nucl. Fusion*, vol. 51, p. 063019, 2011.
- [104] J. Hedin, T. Hellsten, L. G. Eriksson, and T. Johnson, “The influence of finite drift orbit width on ICRF heating in toroidal plasmas,” *Nucl. Fusion*, vol. 42, pp. 527–540, 2002.

BIBLIOGRAPHY

- [105] M. Brambilla, “Quasi-linear ion distribution function during ion cyclotron heating in tokamaks,” *Nucl. Fusion*, vol. 34, pp. 1121–1143, 1994.
- [106] M. Brambilla, “Finite Larmor radius wave equations in Tokamak plasmas in the ion cyclotron frequency range,” *Plasma Phys. Controlled Fusion*, vol. 31, pp. 723–757, 1989.
- [107] A. Brizard, “Nonlinear gyrokinetic Maxwell-Vlasov equations using magnetic coordinates,” *Journal of Plasma Physics*, vol. 541, p. 41, 1989.
- [108] D. H. E. Dubin, J. A. Krommes, C. Oberman, and W. W. Lee, “Nonlinear gyrokinetic equations,” *Physics of Fluids*, vol. 3524, p. 26, 1983.
- [109] T. S. Hahm, W. W. Lee, and A. Brizard, “Nonlinear gyrokinetic theory for finite-beta plasmas,” *Physics of Fluids*, vol. 1940, p. 31, 1988.
- [110] T. S. Hahm, “Nonlinear gyrokinetic equations for tokamak microturbulence,” *Physics of Fluids*, vol. 2670, p. 31, 1988.
- [111] R. G. Littlejohn, “Variational principles of guiding centre motion,” *Journal of Plasma Physics*, vol. 29, pp. 111–125, 1983.
- [112] A. Brizard, “Nonlinear gyrokinetic Vlasov equation for toroidally rotating axisymmetric tokamaks,” *Phys. Plasmas*, vol. 2, p. 459471, 1995.
- [113] T. Dannert, “Gyrokinetische Simulation von Plasmaturbulenz mit gefangenen Teilchen und elektromagnetischen Effekten,” *PhD thesis, Technische Universität München*, 2005.
- [114] R. G. Littlejohn, “Hamiltonian perturbation theory in noncanonical coordinates,” *Journal of Mathematical Physics*, vol. 23, p. 742, 1982.
- [115] J. R. Cary and R. G. Littlejohn, “Noncanonical Hamiltonian mechanics and its application to magnetic field line flow,” *Annal. of Physics*, vol. 151, pp. 1–34, 1983.
- [116] J. Candy, R. E. Waltz, S. E. Parker, and Y. Chen, “Relevance of the parallel non-linearity in gyrokinetic simulations of tokamak plasmas,” *Phys. Plasmas*, vol. 13, p. 074501, 2006.
- [117] Y. Idomura, M. Ida, S. Tokuda, and L. Villard, “New conservative gyrokinetic full-f Vlasov code and its comparison to gyrokinetic f particle-in-cell code,” *Journal of Computational Physics*, vol. 226, p. 244, 2006.

- [118] S. Jolliet, “Gyrokinetic particle-in-cell global simulations of ion-temperature-gradient and collisionless-trapped-electron-mode turbulence in tokamaks,” *PhD thesis, École Polytechnique FéDÉrale de Lausanne*, 2009.
- [119] T. Dannert and F. Jenko, “Gyrokinetic simulation of collisionless trapped-electron mode turbulence,” *Phys. Plasmas*, vol. 12, p. 072309, 2005.
- [120] T. Görler, X. Lapillonne, S. Brunner, T. Dannert, F. Jenko, F. Merz, and D. Told, “The global version of the gyrokinetic turbulence code GENE,” *Journal of Computational Physics*, vol. 230, pp. 7053–7071, Aug. 2011.
- [121] R. Balescu, “Transport Processes in Plasmas Vol. 1: Classical Transport; Vol. 2: Neoclassical Transport. New York, USA: North-Holland Press, 1988..,” *book*, 1988.
- [122] F. Jenko, “Numerische Modellierung von stoßfreier Driftwellenturbulenz,” *PhD thesis, Technische Universität München*, 1998.
- [123] Z. Lin, T. S. Hahm, W. W. Lee, W. M. Tang, and P. H. Diamond, “Effects of collisional zonal flow damping on turbulent transport,” *Phys. Rev. Lett.*, vol. 83, p. 3645, 1999.
- [124] H. Doerk, “Gyrokinetic Simulation of Microtearing Turbulence,” *PhD thesis, University ULM*, 2012.
- [125] J. D. Huba, “NRL (Naval Research Laboratory) plasma formulary, 2007,” 2007.
- [126] H. Sugama, T. H. Watanabe, and M. Nunami, “Linearized model collision operators for multiple ion species plasmas and gyrokinetic entropy balance equations,” *Phys. Plasmas*, vol. 16, p. 112503, 2009.
- [127] P. Crandall, D. Jarema, H. Doerk, Q. Pan, G. Merlo, T. Görler, A. Bañón Navarro, D. Told, M. Maurer, and F. Jenko, “Multi-spacies collisions for delta-f gyrokinetic simulations: implementation and validation with gene,” *submitted to Plasma Phys. Controlled Fusion*.
- [128] A. Bañón Navarro, P. Morel, M. Albrecht-Marc, D. Carati, F. Merz, T. Görler, and F. Jenko, “Free energy balance in gyrokinetic turbulence,” *Phys. Plasmas*, vol. 18, p. 092303, Sept. 2011.
- [129] A. Bañón Navarro, P. Morel, M. Albrecht-Marc, D. Carati, F. Merz, T. Görler, and F. Jenko, “Free Energy Cascade in Gyrokinetic Turbulence,” *Phys. Rev. Lett.*, vol. 106, p. 055001, 2011.

BIBLIOGRAPHY

- [130] A. Bañón Navarro, “Gyrokinetic Large Eddy Simulations,” *PhD thesis, University Bruxelles*, 2012.
- [131] M. Nakata, T.-H. Watanabe, and H. Sugama, “Nonlinear entropy transfer via zonal flows in gyrokinetic plasma turbulence,” *Phys. Plasmas*, vol. 19, p. 022303, 2012.
- [132] S. Maeyama, T.-H. Watanabe, and A. Ishizawa, “Suppression of Ion-Scale Microtearing Modes by Electron-Scale Turbulence via Cross-Scale Nonlinear Interactions in Tokamak Plasmas,” *Phys. Rev. Lett.*, vol. 119, p. 195002, 2017.
- [133] A. Di Siena, T. Görler, H. Doerk, E. Poli, and R. Bilato, “Fast-ion stabilization of tokamak plasma turbulence,” *Nucl. Fusion*, vol. 58, p. 054002, 2018.
- [134] R. Hatzky, T. M. Tran, A. Könies, R. Kleiber, and S. J. Allfrey, “Energy conservation in a nonlinear gyrokinetic particle-in-cell code for ion-temperature-gradient-driven modes in θ -pinch geometry,” *Phys. Plasmas*, vol. 9, pp. 898–912, Mar. 2002.
- [135] P. Manas, Y. Camenen, S. Benkadda, W. A. Hornsby, and A. G. Peeters, “Enhanced stabilisation of trapped electron modes by collisional energy scattering in tokamaks,” *Phys. Plasmas*, vol. 22, p. 062302, June 2015.
- [136] J. D. J. Gaffey, “Energetic ion distribution resulting from neutral beam injection in tokamaks,” *J. Plasma Phys.*, vol. 16, pp. 149–169, 1976.
- [137] C. Estrada-Mila, J. Candy, and R. E. Waltz, “Turbulent transport of alpha particles in reactor plasmas,” *Phys. Plasmas*, vol. 13, p. 112303, Nov. 2006.
- [138] T. Dannert, S. Günter, T. Hauff, F. Jenko, X. Lapillonne, and P. Lauber, “Turbulent transport of beam ions,” *Phys. Plasmas*, vol. 15, p. 062508, June 2008.
- [139] A. Di Siena, A. Biancalani, T. Görler, H. Doerk, I. Novikau, P. Lauber, A. Bottino, and E. Poli, “Effect of elongation on energetic particle-induced geodesic acoustic mode,” *Nucl. Fusion*, vol. 58, p. 106014, 2018.
- [140] A. M. Dimits, G. Bateman, M. A. Beer, B. Cohen, W. Dorland, G. W. Hammett, C. Kim, J. E. Kinsey, M. Kotschenreuther, A. H. Kritz, L. L. Lao, J. Mandrekas, W. M. Nevins, S. E. Parker, A. J. Redd, D. E. Shumaker, R. Sydora, and J. Weiland, “Comparisons and physics basis of tokamak transport models and turbulence simulations,” *Phys. Plasmas*, vol. 7, p. 969, 2000.

BIBLIOGRAPHY

- [141] M. Kotschenreuther, G. Rewoldt, and W. M. Tang, “Comparison of initial value and eigenvalue codes for kinetic toroidal plasma instabilities,” *Comput. Phys. Commun.*, vol. 88, p. 128, 1995.
- [142] A. G. Peeters and D. Strintzi, “Electron temperature gradient turbulence,” *Phys. Plasmas*, vol. 11, p. 3748, 2004.
- [143] A. Peeters, Y. Camenen, F. Casson, W. Hornsby, A. Snodin, D. Strintzi, and G. Szepesi, “The nonlinear gyro-kinetic flux tube code gkw,” *Comput. Phys. Commun.*, vol. 180, no. 12, pp. 2650 – 2672, 2009.
- [144] T. Hein, C. Angioni, E. Fable, and J. Candy, “Gyrokinetic study of the role of β on electron particle transport in tokamaks,” *Phys. Plasmas*, vol. 17, p. 102309, 2010.
- [145] C. Angioni, Y. Camenen, F. J. Casson, E. Fable, R. M. McDermott, A. G. Peeters, and J. E. Rice, “Off-diagonal particle and toroidal momentum transport: a survey of experimental, theoretical and modelling aspects,” *Nucl. Fusion*, vol. 52, p. 114003, 2012.
- [146] S. Jolliet, A. Bottino, P. Angelino, R. Hatzky, T. M. Tran, B. F. Mcmillan, O. Sauter, K. Appert, Y. Idomura, and L. Villard, “A global collisionless PIC code in magnetic coordinates,” *Comput. Phys. Comm.*, vol. 177, p. 409, 2007.
- [147] A. Bottino and E. Sonnendrücker, “Monte Carlo particle-in-cell methods for the simulation of the VlasovMaxwell gyrokinetic equations,” *J. Plasma Phys.*, vol. 81, p. 435810501, 2015.
- [148] H. Sugama and T.-H. Watanabe, “Erratum: Collisionless damping of geodesic acoustic modes [J. Plasma Physics (2006) 72, 825,” *J. Plasma Phys.*, vol. 74, pp. 139–140, 2008.
- [149] H. Sugama and T.-H. Watanabe, “Collisionless damping of geodesic acoustic modes,” *J. Plasma Phys.*, vol. 72, pp. 825–828, 2006.
- [150] X. Lapillon, S. Brunner, T. Dannert, S. Jolliet, A. Marinoni, L. Villard, T. Görler, F. Jenko, and F. Merz, “Clarifications to the limitations of the s- α equilibrium model for gyrokinetic computations of turbulence,” *Phys. Plasmas*, vol. 16, p. 032308, 2009.

BIBLIOGRAPHY

- [151] P. Mantica, D. Strintzi, T. Tala, C. Giroud, T. Johnson, H. Leggate, E. Lerche, T. Loarer, A. G. Peeters, A. Salmi, S. Sharapov, D. Van Eester, P. C. de Vries, L. Zabeo, and K.-D. Zastrow, “Experimental Study of the Ion Critical-Gradient Length and Stiffness Level and the Impact of Rotation in the JET Tokamak,” *Phys. Rev. Lett.*, vol. 102, p. 175002, May 2009.
- [152] P. Mantica, C. Angioni, C. Challis, G. Colyer, L. Frassinetti, N. Hawkes, T. Johnson, M. Tsalas, P. C. de Vries, J. Weiland, B. Baiocchi, M. N. A. Beurskens, A. C. A. Figueiredo, C. Giroud, J. Hobirk, E. Joffrin, E. Lerche, V. Naulin, A. G. Peeters, A. Salmi, C. Sozzi, D. Strintzi, G. Staebler, T. Tala, D. Van Eester, and T. Versloot, “A Key to Improved Ion Core Confinement in the JET Tokamak: Ion Stiffness Mitigation due to Combined Plasma Rotation and Low Magnetic Shear,” *Phys. Rev. Lett.*, vol. 107, p. 135004, Sept. 2011.
- [153] J. F. Artaud, “The CRONOS suite of codes for integrated tokamak modelling,” *Nucl. Fusion*, vol. 50, p. 043001, 2010.
- [154] J. Citrin, F. Jenko, P. Mantica, D. Told, C. Bourdelle, R. Dumont, J. Garcia, J. W. Haverkort, G. M. D. Hogeweij, T. Johnson, M. J. Pueschel, and JET-EFDA contributors, “Ion temperature profile stiffness: non-linear gyrokinetic simulations and comparison with experiment,” *Nucl. Fusion*, vol. 54, p. 023008, 2014.
- [155] J. Weiland and A. Hirose, “Electromagnetic and kinetic effects on the ion temperature gradient mode,” *Nuclear Fusion*, vol. 32, pp. 151–155, jan 1992.
- [156] A. Hirose, “On finite β stabilization of the toroidal ion temperature gradient mode,” *Physics of Plasmas*, vol. 7, no. 2, pp. 433–436, 2000.
- [157] J. Citrin, F. Jenko, P. Mantica, D. Told, C. Bourdelle, J. Garcia, J. W. Haverkort, G. M. D. Hogeweij, T. Johnson, and M. J. Pueschel, “Nonlinear Stabilization of Tokamak Microturbulence by Fast Ions,” *Phys. Rev. Lett.*, vol. 111, p. 155001, Oct. 2013.
- [158] F. Jenko and A. Kendl, “Radial and zonal modes in hyperfine-scale stellarator turbulence,” *Phys. Plasmas*, vol. 9, pp. 4103–4106, 2002.
- [159] M. J. Pueschel, D. R. Hatch, T. Görler, W. M. Nevins, F. Jenko, P. W. Terry, and D. Told, “Properties of high- microturbulence and the non-zonal transition,” *Phys. Plasmas*, vol. 20, p. 102301, 2013.

BIBLIOGRAPHY

- [160] T. Hauff and F. Jenko, “Mechanisms and scalings of energetic ion transport via tokamak microturbulence,” *Phys. Plasmas*, vol. 15, p. 112307, Nov. 2008.
- [161] J. Candy and R. E. Waltz, “An Eulerian gyrokinetic-Maxwell solver,” *Journal of Computational Physics*, vol. 186, pp. 545–581, 2003.
- [162] V. Parail, R. Albanese, R. Ambrosino, J.-F. Artaud, K. Besseghir, M. Cavinato, G. Corrigan, J. Garcia, L. Garzotti, Y. Gribov, F. Imbeaux, F. Koechl, C. Labate, J. Lister, X. Litaudon, A. Loarte, P. Maget, M. Mattei, D. McDonald, E. Nardon, G. Saibene, R. Sartori, and J. Urban, “Self-consistent simulation of plasma scenarios for ITER using a combination of 1.5D transport codes and free-boundary equilibrium codes,” *Nucl. Fusion*, vol. 53, p. 113002, 2013.
- [163] M. Brambilla and R. Bilato, “Advances in numerical simulations of ion cyclotron heating of non-maxwellian plasmas,” *Nucl. Fusion*, vol. 49, p. 085004, 2009.
- [164] R. Bilato, M. Brambilla, O. Maj, L. D. Horton, C. F. Maggi, and J. Stober, “Simulations of combined neutral beam injection and ion cyclotron heating with the toric-ssfpql package,” *Nucl. Fusion*, vol. 51, p. 103034, 2011.
- [165] G. G. Whelan, M. J. Pueschel, and P. W. Terry, “Nonlinear electromagnetic stabilisation of plasma microturbulence,” *Phys. Rev. Lett.*, vol. 120, p. 175002, 2018.
- [166] M. J. Pueschel and Jenko, “Transport properties of finite- β microturbulence,” *Phys. Plasmas*, vol. 17, p. 102310, May 2010.
- [167] A. Di Siena, T. Görler, E. Poli, A. Bañón Navarro, A. Biancalani, and F. Jenko, “Electromagnetic turbulence suppression by energetic particle driven modes,” *Nuclear Fusion*, vol. 59, p. 124001, sep 2019.
- [168] F. Rath, A. G. Peeters, R. Buchholz, S. R. Grosshauser, P. Migliano, A. Wikl, and D. Strintzi, “Comparison of gradient and flux driven gyro- kinetic turbulent transport,” *Phys. Plasmas*, vol. 23, p. 052309, 2016.
- [169] A. G. Peeters, F. Rath, R. Buchholz, Y. Camenen, J. Candy, F. J. Casson, S. R. Grosshauser, W. A. Hornsby, D. Strintzi, and A. Wikl, “Gradient-driven flux-tube simulations of ion temperature gradient turbulence close to the non-linear threshold,” *Phys. Plasmas*, vol. 23, p. 082517, 2016.

BIBLIOGRAPHY

- [170] A. Di Siena, T. Görler, E. Poli, A. Bañón Navarro, A. Biancalani, and F. Jenko, “Electromagnetic turbulence suppression by energetic particle driven modes,” *Supplemental material to "Electromagnetic turbulence suppression by energetic particle driven modes"*, 2019.
- [171] C. Z. Cheng and M. S. Chance, “Low-n shear Alfvén spectra in axisymmetric toroidal plasmas,” *Physics of Fluids B*, vol. 29, p. 3695, 1986.
- [172] A. Mishchenko, A. Könies, and R. Hatzky, “Global particle-in-cell simulations of fast- particle effects on shear Alfvén waves,” *Phys. Plasmas*, vol. 16, p. 082105, 2009.
- [173] A. Könies, S. Briguglio, N. Gorelenkov, T. Fehér, M. Isaev, P. Lauber, A. Mishchenko, D. A. Spong, Y. Todo, W. A. Cooper, R. Hatzky, R. Kleiber, M. Borchardt, G. Vlad, A. Biancalani, A. Bottino, and ITPA EP TG, “Benchmark of gyrokinetic, kinetic MHD and gyrofluid codes for the linear calculation of fast particle driven TAE dynamics,” *Nuc. Fusion.*, vol. 58, p. 126027, 2018.
- [174] S. Hu and L. Chen, “Discrete alfvén eigenmodes in high- β toroidal plasmas,” *Physics of Plasmas*, vol. 11, no. 1, pp. 1–4, 2004.
- [175] A. Bierwage, L. Chen, and F. Zonca, “Pressure-gradient-induced alfvén eigenmodes: I. ideal MHD and finite ion larmor radius effects,” *Plasma Physics and Controlled Fusion*, vol. 52, p. 015004, nov 2009.
- [176] F. Zonca and L. Chen, “Theory on excitations of drift alfvén waves by energetic particles. ii. the general fishbone-like dispersion relation,” *Physics of Plasmas*, vol. 21, no. 7, p. 072121, 2014.
- [177] E. M. Bass and R. E. Waltz, “Gyrokinetic simulations of mesoscale energetic particle-driven Alfvénic turbulent transport embedded in microturbulence,” *Phys. Plasmas*, vol. 17, p. 112319, 2010.
- [178] H. Sheng, R. E. Waltz, and G. M. Staebler, “Alfvén eigenmode stability and critical gradient energetic particle transport using the Trapped-Gyro-Landau-Fluid model,” *Phys. Plasmas*, vol. 24, p. 072305, 2017.
- [179] R. E. Waltz, G. D. Kerbel, and J. Milovich, “Bulk ion heating with ICRF waves in tokamaks,” *Phys. Plasmas*, vol. 1, p. 2229, 1994.

BIBLIOGRAPHY

- [180] A. T. Lin, K. R. Chu, C. C. Lin, C. S. Kou, D. B. McDermott, and N. C. Luhmann Jr, “Marginal stability design criterion for gyro-TWTs and comparison of fundamental with second harmonic operation,” *Int. J. Electron.*, vol. 72, p. 873, 1992.
- [181] Q. S. Wang, D. B. McDermott, and N. C. Luhmann, “Demonstration of Marginal Stability Theory by a 200-kW Second-Harmonic Gyro-TWT Amplifier,” *Phys. Rev. Lett.*, vol. 75, p. 23, 1995.
- [182] W. van Saarloos, “Front propagation into unstable states. II. Linear versus nonlinear marginal stability and rate of convergence,” *Phys. Rev. D*, vol. 39, p. 6367, 1989.
- [183] R. G. Cai, X. He, H. F. Li, and H. Q. Zhang, “Phase transitions in AdS soliton spacetime through marginally stable modes,” *Phys. Rev. D*, vol. 84, p. 046001, 2011.
- [184] S. S. Gubser, “Breaking an Abelian gauge symmetry near a black hole horizon,” *Phys. Rev. D*, vol. 78, p. 065034, 2008.
- [185] F. Merz and F. Jenko, “Nonlinear interplay of TEM and ITG turbulence and its effect on transport,” *Nucl. Fusion*, vol. 50, p. 054005, 2010.
- [186] M. J. Mantiseni, R. Bilato, V. V. Bobkov, A. Kappatou, R. M. McDermott, M. Nocente, T. Odstril, G. Tardini, M. Bernert, R. Dux, T. Hellsten, P. Mantica, M. Maraschek, S. K. Nielsen, J.-M. Noterdaeme, J. Rasmussen, F. Ryter, M. Stejner, J. Stober, M. Tardocchi, the ASDEX Upgrade Team, and the EUROfusion MST1 Team, “Bulk ion heating with ICRF waves in tokamaks,” *AIP Conf. Proc.*, vol. 1689, p. 030005, 2015.
- [187] W. Chen, R. R. Ma, Y. Y. Li, Z. B. Shi, H. R. Du, M. Jiang, L. M. Yu, B. S. Yuan, Y. G. Li, Z. C. Yang, P. W. Shi, X. T. Ding, J. Q. Dong, Z. X. Wang, Y. Liu, M. Xu, Y. H. Xu, Q. W. Yang, and X. R. Duan, “Alfvénic ion temperature gradient activities in a weak magnetic shear plasma,” *EPL (Europhysics Letters)*, vol. 116, p. 45003, Nov. 2016.
- [188] W. Chen, M. Jiang, Y. Xu, P. W. Shi, L. M. Yu, X. T. Ding, Z. B. Shi, X. Q. Ji, D. L. Yu, Y. G. Li, Z. C. Yang, W. L. Zhong, Z. Y. Qiu, J. Q. Li, J. Q. Dong, Q. W. Yang, Y. Liu, L. W. Yan, M. Xu, and X. R. Duan, “Experimental observation of multi-scale interactions among kink/tearing modes and high-frequency fluctuations in the HL-2A core NBI plasmas,” *Nuc. Fusion*, vol. 57, p. 114003, 2017.

BIBLIOGRAPHY

- [189] W. Chen, D. Yu, R. Ma, P. Shi, Y. Li, Z. Shi, H. Du, X. Ji, M. Jiang, L. Yu, B. Yuan, Y. Li, Z. Yang, W. Zhong, Z. Qiu, X. Ding, J. Dong, Z. Wang, H. Wei, J. Cao, S. Song, X. Song, Y. Liu, Q. Yang, M. Xu, and X. Duan, “Kinetic electromagnetic instabilities in an ITB plasma with weak magnetic shear,” *Nuclear Fusion*, vol. 58, p. 056004, mar 2018.
- [190] A. M. Balk, “Mode generation via interaction,” *Phys. Rev. E.*, vol. 98, p. 062208, 2018.
- [191] F. Zonca and L. Chen, “Radial structures and nonlinear excitation of geodesic acoustic modes,” *Europhysics Lett.*, vol. 83, p. 35001, 2008.
- [192] D. Zarzoso, Y. Sarazin, X. Garbet, R. Dumont, A. Strugarek, J. Abiteboul, T. Cartier-Michaud, G. Dif-Pradalier, V. Grandgirard, G. Latu, C. Passeron, and O. Thomine, “Impact of Energetic-Particle-Driven Geodesic Acoustic Modes on Turbulence,” *Phys. Rev. Lett.*, vol. 110, p. 125002, 2013.
- [193] Z. Gao, P. Wang, and H. Sanuki, “Plasma shaping effects on the geodesic acoustic mode in toroidally axisymmetric plasmas,” *Phys. Plasmas*, vol. 15, p. 074502, 2008.
- [194] I. Novikau, A. Biancalani, A. Bottino, A. Di Siena, P. Lauber, E. Poli, E. Lanti, N. Villard, L. Ohana, and ASDEX Upgrade Team, “Implementation of energy transfer technique in ORB5 to study collisionless wave-particle interactions in phase-space.,” *submitted*.
- [195] I. Novikau, A. Biancalani, A. Bottino, G. G. Conway, Ö. D. Gürcan, P. Manz, P. Morel, A. Poli, E. Di Siena, and ASDEX Upgrade Team, “Linear gyrokinetic investigation of the geodesic acoustic modes in realistic tokamak configurations,” *Phys. Plasmas*, vol. 24, p. 122117, 2017.
- [196] T. Görler, X. Lapillonne, S. Brunner, T. Dannert, F. Jenko, F. Merz, and D. Told, “The global version of the gyrokinetic turbulence code GENE,” *Journal of Computational Physics*, vol. 230, pp. 7053–7071, Aug. 2011.
- [197] P. Lauber *Off-axis NBI heated discharges at ASDEX Upgrade: EGAMs, RSAEs and TAE bursts. Presentation at the 13th Energetic Particle Physics TG Meeting, Padua, Italy 2014* <https://portal.iter.org/departments/POP/ITPA/EP/EP/Documents/13/Presentation/01-01-Lauber.pdf>.

- [198] P. J. Mc Carthy, P. Martin, and W. Schneider, “The CLISTE interpretative equilibrium code,” *Report IPP 5/85*, 1999.
- [199] I. Novikau, A. Biancalani, A. Bottino, G. D. Conway, Ö. D. Gürcan, P. Manz, P. Morel, E. Poli, and A. Di Siena, “Linear gyrokinetic investigation of the geodesic acoustic modes in realistic tokamak configurations,” *Phys. Plasmas*, vol. 24, p. 122117, 2017.
- [200] C. Bourdelle, X. Garbet, F. Imbeaux, A. Casati, N. Dubuit, R. Guirlet, and T. Parisot, “A new gyrokinetic quasilinear transport model applied to particle transport in tokamak plasmas,” *Physics of Plasmas*, vol. 14, no. 11, p. 112501, 2007.
- [201] C. Bourdelle, J. Citrin, B. Baiocchi, A. Casati, P. Cottier, X. Garbet, and F. I. and, “Core turbulent transport in tokamak plasmas: bridging theory and experiment with QuaLiKiz,” *Plasma Physics and Controlled Fusion*, vol. 58, p. 014036, dec 2015.
- [202] J. Citrin, C. Bourdelle, F. J. Casson, C. Angioni, N. Bonanomi, Y. Camenen, X. Garbet, L. Garzotti, T. Görler, Ö. D. Gürcan, F. Koechl, F. Imbeaux, O. Linder, K. van de Plassche, P. Strand, and G. S. and, “Tractable flux-driven temperature, density, and rotation profile evolution with the quasilinear gyrokinetic transport model QuaLiKiz,” *Plasma Physics and Controlled Fusion*, vol. 59, p. 124005, nov 2017.
- [203] G. V. Pereverzev and P. N. Yushamanov, “ASTRA automated system for transport analysis in a tokamak,” *Report IPP 5/98*, 2002.
- [204] E. Fable, C. Angioni, A. A. Ivanov, K. Lackner, O. Maj, S. Y. Medvedev, G. Pautasso, G. V. Pereverzev, and W. T. and, “Dynamical coupling between magnetic equilibrium and transport in tokamak scenario modelling, with application to current ramps,” *Plasma Physics and Controlled Fusion*, vol. 55, p. 074007, jun 2013.
- [205] J. E. Kinsey, G. M. Staebler, and R. E. Waltz, “The first transport code simulations using the trapped gyro-landau-fluid model,” *Physics of Plasmas*, vol. 15, no. 5, p. 055908, 2008.
- [206] D. Zarzoso, P. Migliano, V. Grandgirard, G. Latu, and C. Passeron, “Nonlinear interaction between energetic particles and turbulence in gyro-kinetic simulations and impact on turbulence properties,” *Nuclear Fusion*, vol. 57, p. 072011, jun 2017.

BIBLIOGRAPHY

- [207] D. Jarema, H. Bungartz, T. Görler, F. Jenko, T. Neckel, and D. Told, “Block-structured grids in full velocity space for eulerian gyrokinetic simulations,” *Computer Physics Communications*, vol. 215, pp. 49 – 62, 2017.

Acknowledgement

The work presented in this thesis would not have been possible without the support provided by a number of people to whom I owe my most sincere acknowledgements. First of all, I would like to thank Tobias Görler and Emanuele Poli for their outstanding supervision. They gave me the unique possibility of studying an extremely interesting and exciting topic, granting me always the freedom to follow my research interests. I am very grateful to Tobias for all the time spent to explain and clarify to me each of my doubts spanning from the code GENE to the most disparate physics and general questions. Tobias has always been extremely kind and professional knowing always the right answer. A very special thanks goes to Emanuele Poli for his constant and encouraging guidance throughout all my work, for always being available for any kind of advice and for the excellent feedbacks and ideas provided. I have learned a lot from them, both from the professional and human points of view and I believe I could have not asked for better supervisors.

I am very gratefully to Frank Jenko, which despite the numerous commitments, always found some time to provide valuable suggestions to further improve and consolidate the main results. Moreover, Frank gave me the possibility to participate in several international conferences and meetings which allowed me to create new collaborations and meet scientists from many other research institutes.

Another special thanks goes to Hauke Doerk for all the precious help that he gave me at the beginning (but not only!) of my PhD. I particularly enjoyed all our discussions about the different aspects of the energetic particle physics but also about climate changes, pollution and global warming, which contributed to expand my horizons.

I also would like to thank Silvio Sergio Cerri for the very nice and friendly working (and not) environment. I particularly remember our participation in a Magic draft game with all the cards in German without knowing or understanding even a single word.

Among those who provided valuable scientific help to my thesis I would love to acknowledge Alessandro Biancalani, Philip Lauber, Alberto Bottino and Ivan Novikau for the very nice and interesting collaboration with the ORB5 and energetic particle

groups. I have learned a lot from all of you and I really enjoyed all our discussions. They helped me a lot in developing a deeper understanding on the energetic particle physics.

Moreover, a special thanks goes also to Alejandro Bañón Navarro, Roberto Bilato and Jonathan Citrin for all the physics conversations (during conferences and/or at the IPP) and for all the excellent comments and suggestions. Alejandro was also very supportive in the various attempts to submission to PRL with the prophetic words: "This paper is gonna be accepted".

I would also like to acknowledge Mireille Schneider for the NEMO/SPOT data and Thomas Johnson for the SELFO one, which were essential for the numerical analyses shown in chapter 4. I am also very grateful to Clemente Angioni, Paola Mantica and Alessandro Zocco for the interest in the results of my work and for all the bright suggestions always provided.

David Laurine and Nicola Bonanomi also deserve an acknowledgement for the time spent in and outside the work environment. Moreover, I am very grateful to my (current and ex) office mates Karen Pommois, Andres Cathey, Daniel Groselj, Francisco Matos, Victor Artigues and all the other PhD students. Special thanks go to Francois Orain, Tilman Lunt and Simon Freethy for all the time that we spent together playing basketball, I really enjoyed it!

For the proofreading of the manuscript and their helpful comments concerning language and content, Karl Stimmel and Maurice Maurer deserve special thanks.

I heartily thank my parents Gabriella, Lello and my brother Andrea for their constant and unconditional support. If I managed to accomplish whatever I have done so far it is only thanks to them. They always gave me the possibility to follow my interests and they always motivated me to aim higher. I could never thank you enough for that!

Last but not least, my deepest thanks go to the love of my life, Saria for the full support and devotion that she always bought me. During these four years we have been the pillar to each other even being thousand of kilometers far apart. We shared every single difficulties and achievements that we encountered (maybe this balance is more in favour of the difficulties), making everything less discouraging and more rewarding. I really love to immensely thank you for that and for each moment spent together.

Declaration

I declare that the work presented in this thesis is my own except where stated otherwise, and was carried out at the Max Planck Institute for Plasma Physics in Garching under the supervision of Prof. Dr. Emanuele Poli and Dr. Tobias Görler. Parts of the work reported in this thesis have been published in peer reviewed journals, as listed below:

1. A. Di Siena, T. Görler, H. Doerk, J. Citrin, T. Johnson, M. Schneider, E. Poli and JET Contributors, "Non-Maxwellian background effects in gyrokinetic simulations with GENE", *J. Phys. Conf. Ser.*, **775**, 012003, 2016.
2. A. Di Siena, T. Görler, H. Doerk, R. Bilato, J. Citrin, T. Johnson, M. Schneider, E. Poli and JET Contributors, "Non-Maxwellian fast particle effects in gyrokinetic GENE simulations", *Phys. Plasmas*, **25**, 042304, 2018.
3. A. Di Siena, T. Görler, H. Doerk, E. Poli, and R. Bilato, "Fast-ion stabilization of tokamak plasma turbulence", *Nucl. Fusion*, **58**, 054002, 2018.
4. A. Di Siena, T. Görler, E. Poli, R. Bilato, H. Doerk, A. Zocco, "Resonant interaction of energetic ions with bulk-ion plasma micro-turbulence", *Phys. Plasmas (invited APS special edition)*, **26**, 052504, 2019.
5. A. Di Siena, T. Görler, E. Poli, A. Bañón Navarro, A. Biancalani and F. Jenko, "Electromagnetic turbulence suppression by energetic particle driven modes", *Nucl. Fusion*, **59**, 124001, 2019.
6. A. Di Siena, A. Biancalani, T. Görler, H. Doerk, I. Novikau, P. Lauber, A. Bottino, and E. Poli, "Effect of elongation on energetic particle-induced geodesic acoustic mode", *Nucl. Fusion*, **58**, 106014, 2018.

Publication 1 and 2 in the above list are the basis of chapter 2 and 3 of this thesis. Publication 2 is the basis of chapter 4 of this thesis. Publications 3 and 4 in the

above list are the basis of chapters 5. Publications 5 in the above list is the basis of chapters 6. Publications 6 in the above list is the basis of chapters 7.

List of publications

Publications in peer-reviewed journals

1. A. Di Siena, T. Görler, H. Doerk, J. Citrin, T. Johnson, M. Schneider, E. Poli and JET Contributors, "Non-Maxwellian background effects in gyrokinetic simulations with GENE", *J. Phys. Conf. Ser.*, **775**, 012003, 2016.
2. A. Di Siena, T. Görler, H. Doerk, E. Poli, and R. Bilato, "Fast-ion stabilization of tokamak plasma turbulence", *Nucl. Fusion*, **58**, 054002, 2018.
3. A. Di Siena, T. Görler, H. Doerk, R. Bilato, J. Citrin, T. Johnson, M. Schneider, E. Poli and JET Contributors, "Non-Maxwellian fast particle effects in gyrokinetic GENE simulations", *Phys. Plasmas*, **25**, 042304, 2018.
4. A. Di Siena, A. Biancalani, T. Görler, H. Doerk, I. Novikau, P. Lauber, A. Bottino, and E. Poli, "Effect of elongation on energetic particle-induced geodesic acoustic mode", *Nucl. Fusion*, **58**, 106014, 2018.
5. A. Di Siena, T. Görler, E. Poli, R. Bilato, H. Doerk, A. Zocco, "Resonant interaction of energetic ions with bulk-ion plasma micro-turbulence", Accepted to publication in *Phys. Plasmas* (invited APS special edition), 2019.
6. A. Di Siena, T. Görler, E. Poli, A. Bañón Navarro, A. Biancalani and F. Jenko, "Electromagnetic turbulence suppression by energetic particle driven modes", Submitted to *Phys. Rev. Lett.*, 2019.
7. C. Castaldo, A. Di Siena, R. Fedele, F. Napoli, L. Amicucci, R. Cesario, G. Schettini, "Influence of collisions on parameteric instabilities induced by lower hybrid waves in tokamak plasmas", *Nucl. Fusion*, **56**, 106003, 2016.
8. I. Novikau, A. Biancalani, A. Bottino, G. G. Conway, Ö. D. Gürcan, P. Manz, P. Morel, E. Poli, A. Di Siena and The ASDEX Upgrade Team, "Linear gyrokinetic investigation of the geodesic acoustic modes in realistic tokamak configurations", *Phys. Plasmas*, **24**, 122117, 2017.

-
9. H. Doerk, A. Bock, A. Di Siena, E. Fable, T. Görler, F. Jenko, J. Stober, The ASDEX Upgrade Team, "Turbulence in high-beta ASDEX upgrade advanced scenarios", Nucl. Fusion, **58**, 106044, 2018.
 10. N. Bonanomi, P. Mantica, A. Di Siena, E. Delabie, T. Johnson, E. Lerche, S. Menumir, M. Tsalas, D. Van Eester JET Contributors, "Turbulent transport stabilization by ICRH minority fast ions in low rotating JET ILW L-mode plasmas", Nucl. Fusion, **58**, 056025, 2018.
 11. I. Novikau, A. Biancalani, A. Bottino, A. Di Siena, Ph. Lauber, E. Poli, E. Lanti, L. Villard, N. Ohana and The ASDEX Upgrade Team, "Implementation of energy transfer technique in ORB5 to study collisionless wave-particle interactions in phase-space", Submitted to Computer Physics Communications, 2019.
 12. N. Bonanomi, C. Angioni, C. F. Maggi, P. A. Schneider, P. C. Crandall, A. Di Siena, The ASDEX Upgrade Team, The EUROFusion MST1 Team and JET Contributors, "Effect of the isotope mass on the turbulent transport at the edge of L-mode plasmas in ASDEX Upgrade and JET-ILW", Submitted to Nucl. Fusion, 2019.

Published conference proceedings

1. A. Di Siena, T. Görler, H. Doerk, R. Bilato, J. Citrin, T. Johnson, M. Schneider, E. Poli and JET Contributors, "Impact of realistic fast ion distribution function in gyrokinetic GENE simulations", Proceedings of the 44th EPS Conference on Plasma Physics, Belfast, Northern Ireland (UK), 2017.
2. T. Görler, A. Di Siena, H. Doerk, T. Happel, A. Bañón Navarro, R. Bilato, A. Bock, G. D. Conway, F. Jenko, E. Poli, E. Sonnendruecker, J. Stober, I.-G. Farcas, T. Neckel, J. Citrin, S. J. Freethy, A. J. Creely, A. E. White, P. Hennequin, T. Johnson, C. Lechte, M. Schneider, The ASDEX Upgrade Team and JET Contributors, "En route to high-performance discharges: insights and guidance from high-realism gyrokinetics", Proceedings of the 27th IAEA Conference on Fusion Energy, Gandhinagar, India, 2018
3. A. Biancalani, A. Bottino, A. Di Siena, T. Görler, I. Novikau, Ö. D. Gürcan, P. Morel, F. Jenko, E. Lanti, N. Ohana, L. Villard, G. Merlo, A. Mishchenko, Z. Qiu, "Self-consistent gyrokinetic description of the interaction between Alfvén modes and turbulence", Proceedings of the 27th IAEA Conference on Fusion Energy, Gandhinagar, India, 2018

Invited talks and oral conference contributions

1. A. Di Siena, T. Görler, H. Doerk, J. Citrin, T. Johnson, M. Schneider, E. Poli and JET Contributors, "Effect of non-Maxwellian background distributions on fast ion stabilisation in GENE", IPP Theory Meeting, Schloss Ringberg (Germany), 2016 (oral presentation).
2. A. Di Siena, T. Görler, H. Doerk, E. Poli, R. Bilato, N. Bonanomi and P. Mantica, "On the role of fast ions in turbulence simulations", IPP Theory Meeting, Berlin (Germany), 2017 (oral presentation).
3. A. Di Siena, T. Görler, H. Doerk, E. Poli and R. Bilato, "New insights into fast ion induced turbulence stabilization", DPG-Frühjahrstagung 2019 , Erlangen (Germany), 2017 (oral presentation).
4. A. Di Siena, T. Görler, H. Doerk, R. Bilato, J. Citrin, T. Johnson, M. Schneider, E. Poli and JET Contributors, "Non-Maxwellian fast particle effects on (electromagnetic) GENE turbulence simulations", ITPA Transport and Confinement, Helsinki (Finland), 2017 (oral presentation).
5. A. Di Siena, T. Görler, H. Doerk, R. Bilato, J. Citrin, T. Johnson, M. Schneider, E. Poli, A. Biancalani, A. Bottino, I. Novikau, Ph. Lauber, JET Contributors and The ASDEX Upgrade Team, "Non-Maxwellian fast particle effects in GENE turbulence simulations", IPP E2M Meeting, Schloss Ringberg (Germany), 2018 (oral presentation).
6. A. Di Siena, T. Görler, H. Doerk, R. Bilato, J. Citrin, T. Johnson, M. Schneider, E. Poli and JET Contributors, "New insights into fast ion induced turbulence stabilisation", Joint EU-US Transport Task Force Workshop, Seville (Spain), 2018 (oral presentation).
7. A. Di Siena, T. Görler, R. Bilato, H. Doerk, E. Poli, N. Bonanomi, P. Mantica, J. Citrin, T. Johnson, M. Schneider, A. Bañón Navarro, JET Contributors and The ASDEX Upgrade Team, 60th Annual Meeting of the Division of Plasma Physics of the American Physical Society, Portland (Oregon), 2018 (invited presentation).